Preventing infections in an ageing population: new nano/microcarriers for antibacterial coatings

Ana Maria Ferreira

A thesis submitted in partial fulfilment of the requirements of Nottingham Trent University for the degree of Doctor of Philosophy

February 2023

Copyright statement

Acknowledgements

I am grateful to the European Union and Nottingham Trent University for funding my doctoral studies through the Marie Skłodowska-Curie fellowship program, and to the Doctoral Training Alliance for their continuous support. I also would like to thank Dmitry Volodkin for offering me the chance to pursue this PhD and for his continuous support and valuable guidance.

I am thankful to Gareth Cave for all his help and for introducing me to his research group, where I made some amazing friends. I would like to thank Valeria Puddu for her support and helpfulness during my PhD journey. Her positive spirit, and warmheartedness, have made a meaningful impact on my experience. I am also grateful to Michael Loughlin for his generosity and for taking the time to teach me the ropes, always paying close attention to detail and ensuring that I had a solid understanding.

I would like to acknowledge my lab mate, Jack, for making my experience in the lab an easy and enjoyable one. A big shout-out to all the wonderful microbiology PhD students who put me at ease in the microbiology lab and shared precious tips. I am grateful to Kinana, for all the help and being an unwavering example of resilience, and to Dinga for lighting up the room.

I am deeply thankful to both Mohamed and Muhammad for bringing a spark of happiness to the lab, and to Soojin for all the mouth-watering treats and being a warm presence.

I am deeply grateful to all the technicians who helped me throughout my studies, including Barbara, Graham, Dom, Kath, Shaff, David and Kieran.

My heartfelt thanks go to Andrew and Corinne for being my first home in the UK and providing me with a truly British experience, from a warm cup of tea to holidays in Norfolk.

The warmest thanks to Jonny, for being the lighthouse in the sometimes-turbulent PhD waters and keeping me well-fed with over 700 breakfasts.

And finally, I would like to thank my family. My mum Isabel, who is the epitome of hard work; my sisters Elisabete, Ângela, Lúcia and Marta, who shaped who I am today and always provided unwavering support; and my dad Diamantino, who gave me the genes of curiosity.

Publications, presentations and awards

Publications

List of Publications attained during the doctoral studies:

Ferreira, A., Vikulina, A., Cave, G., Loughlin, M., Puddu, V., Volodkin D. Vaterite-nanosilver hybrids with antibacterial properties and pH-triggered release. *Materials Today Chemistry* 30, 101586, (2023). https://doi.org/10.1016/j.mtchem.2023.101586.

Ferreira, A., Vikulina, A., Loughlin, V., Volodkin D. How similar is the antibacterial activity of silver nanoparticles coated with different capping agents? RSC Advances 13, 10542-10555, (2023). https://doi.org/10.1039/D3RA00917C

Ferreira, A., Vikulina, A., Cave, G., Loughlin, M., Puddu, V., Volodkin, D. Vaterite vectors for the protection, storage and release of silver nanoparticles. *Journal of Colloid and Interface Science* 631, 165-180, (2023). https://doi.org/10.1016/j.jcis.2022.10.094

Campbell, J., Ferreira, A., Bowker, L., Hunt, J., Volodkin, D., Vikulina, A. Dextran and its derivatives: biopolymer additives for the modulation of vaterite $CaCO_3$ crystal morphology and adhesion to cells. *Advanced Materials Interfaces* 9, 2201196, (2022). https://doi.org/10.1002/admi.202201196

Ferreira, A., Vikulina, A., Volodkin, D. $CaCO_3$ crystals as versatile carriers for controlled delivery of antimicrobials. *Journal of Controlled Release* 328, 470-489, (2020). https://doi.org/10.1016/j.jconrel.2020.08.061

Submissions for Publication

List of submissions in scientific journals undergoing peer review:

Ferreira, A., Vikulina, A., Loughlin, V., Volodkin D. Development of antimicrobial coatings based on $CaCO_3$-nanosilver hybrids. *Advanced Composites and Hybrid Materials*. *Under Review*.

Presentations

Ferreira, A., Vikulina, A., Cave, G., Loughlin, M., Puddu, V., Volodkin D. Calcium carbonate vectors for silver nanoparticles protection and controlled delivery. **Poster Presentation**. 13th Global Drug Delivery & Formulation Summit**, Berlin, Germany**, 27 – 29 July **2022**. **Presenting author**.

Ferreira, A., Cave, G., Loughlin, M., Puddu, V., Volodkin D. Development of vaterite-nanosilver antimicrobial carriers. **Oral Presentation**. STAR Conference**, Nottingham, UK**, 8 – 9 June **2021**. **Presenting author**.

Ferreira, A., Cave, G., Puddu, V., Volodkin D. Vaterite microcarriers for encapsulation and controlled release of stabilized nanosilver. **Oral Presentation**. Dynamic self-assembly and quorum effects in chemistry and biology predicted by non-linear modelling algorithms meeting**, Liverpool, UK**, 20 – 23 October **2019**. **Presenting author**.

Ferreira, A., Campbell, J., Polytarchou C., Volodkin D., Vikulina, A. $CaCO_3$ crystals as promising vectors for intracellular delivery via pH-mediated recrystallization. **Poster Preparation.** International Conference on Materials Research and Nanotechnology, **Rome, Italy.** 10-12 June **2019.**

Awards

Research Development Grant (application D22-8117137082). Funded by the Royal Society of Chemistry. June, 2022.

Table of contents

List of figures

List of tables

List of abbreviations

AA	Antimicrobial agent
ACC	Amorphous calcium carbonate
AgNPs	Silver nanoparticles
AL	Alginate lyase
ATCC	American type culture collection
ATR	Attenuated total reflectance
BC	Bactericidal concentration
BDMDAC	Benzyldimethyldodecylammonium chloride
BGI	Biofilm growth inhibition
BZN	Benznidazole
C_0	Initial concentration of silver
CA	Cellulose acetate
$CaCO_3$/AgNPs	Hybrids of calcium carbonate and silver nanoparticles
CFU	Colony-forming unit
C_i	Initial concentration
CIP	Cold isostatic pressing
Citrate	Trisodium citrate
CL	Cardiolipin
Cl-DMH-UA	3-chloro-4,4-dimethylhydantoin undecanoic acid
Coating A	Coatings composed of $CaCO_3$/AgNPs hybrids
Coating B	Coatings composed of CaCO3/AgNPs hybrids, PVP and mucin
CP	Colloidal precipitation
Dex	fluorescein isothiocyanate–dextran/dextran
DEX^{CM}	Fluorescein isothiocyanate–carboxymethyl–dextran/carboxymethyl–dextran
Dex^{DEAE}	Fluorescein isothiocyanate–diethylaminoethyl–dextran/diethylaminoethyl–dextran
DLS	Dynamic light scattering

DMEM	Dulbecco's modified eagle medium
DNA	Deoxyribonucleic acid
DNAse	Deoxyribonuclease
DOXY	Doxycycline hyclate
E. coli	*Escherichia coli*
EDS	Energy-dispersive X-ray spectroscopy
EDTA	Ethylenediaminetetraacetic acid
EG	Ethylene glycol
EPS	Exopolysaccharides
FBS	Foetal bovine serum
FDA	Food and drug administration agency
FTIR	Fourier transform infrared
GI	Growth inhibition
hBM-MSC	Bone marrow mesenchymal stem cell line
HMDS	Hexamethyldisiloxane
HPH	High pressure homogenizer
I	Intensity
ICP-MS	Inductively coupled plasma mass spectrometry
L	Length
LB	Lennox broth base
LbL	Layer-by-layer
LC_{50}	Lethal Concentration that causes the death of 50% of the organisms
LE	Loading efficiency
MBC	Minimum bactericidal concentration
MBEC	Minimum biofilm eradication concentration
MHA-S	Mueller Hinton agar Sigma
MHB-O	Mueller Hinton broth Oxoid
MHB-S	Mueller Hinton broth Sigma
MHB-Sc	Mueller Hinton broth Sigma control

MIBC	Minimum inhibitory biofilm concentration
MIC	Minimum inhibitory concentration
mix.	Mixing
MNP	Mineralized nanoparticles
MOI	Molecules of interest
MRSA	methicillin-resistant Staphylococcus aureus
MSC	Mesenchymal stem cell growth medium
MTT	3-(4,5-Dimethylthiazol-2-yl)-2,5-Diphenyltetrazolium Bromide
n.d.	Not defined
NB	Nutrient Broth
NCTC	National collection of type cultures
NHDFs	Normal human dermal fibroblasts
NTUCC	Nottingham Trent University cultures collection
OD_{600}	Optical densities at 600 nm
P. aeruginosa	*Pseudomonas aeruginosa*
PAA	Polyacrylic acid
PAH	Poly(allylamine hydrochloride)
PBS	Phosphate buffered saline
PEG	Polyethylene glycol
PEG-PAsp	Poly(ethylene glycol)-poly(aspartic acid)
PEI	Polyethyleneimine
Poly(L-asp)	Poly(L-aspartic acid) sodium salt
PSS	Poly(sodium 4-styrenosulfonate)
PVA	Poly(vinyl alcohol)
PVP	Polyvinylpyrrolidone
RNA	Ribonucleic acid
RT	Room temperature
SA	Similar antimicrobial activity
SDS	Sodium dodecyl sulphate

SEM	Scanning electron microscopy
SERS	Surface-enhanced raman scattering
SR	Survival ratio
TBS	Tris buffer saline
TBSc	Tris buffer saline control
TEM	Transmission electron microscopy
T	Temperature
TGA	Thermogravimetric analysis
UV-vis	Ultraviolet-visible spectroscopy
W	Width
XRD	X-ray diffraction
ZI	Zone of inhibition

Abstract

Infection diseases are responsible for high mortality and morbidity in the elderly, with the treatment of a single resistant infection being extremely costly due to the extended hospitalization periods and additional treatment costs. Contaminated surfaces are associated with the spread of pathogenic microorganisms, being a dangerous transmission route in hospital settings, where the incidence of antimicrobial-resistant infections has reached alarming levels. Surfaces coated with antimicrobial agents have allowed the production of safe surfaces that can prevent the spread of microorganisms, with silver nanoparticles (AgNPs) being widely used due to their broad spectrum of bioactivity. Nevertheless, the colloidal instability of AgNPs and adverse effects on living organisms have driven the search for materials able to stabilize and control silver release. Vaterite $CaCO_3$ crystals have extensively been studied as drug carriers due to their facile synthesis, biocompatibility, porous structure and pH-sensitive properties.

The work presented in this thesis aims to develop hybrids composed of vaterite and AgNPs for antibacterial coatings. The work focuses on the stabilization of AgNPs, the mechanisms of AgNPs loading and release, the design of antibacterial coatings and the antimicrobial activity of the developed materials against *Escherichia coli*, methicillin-resistant *Staphylococcus aureus* and *Pseudomonas aeruginosa*, three bacteria responsible for numerous nosocomial infections.

Five different capping agents were tested as stabilizing agents for AgNPs: trisodium citrate (Citrate), polyvinylpyrrolidone (PVP), dextran (Dex), diethylaminoethyl–dextran (Dex^{DEAE}) and carboxymethyl–dextran (Dex^{CM}). The results showed that the capping agents substantially impact the antibacterial activity of the AgNPs. The AgNPs coated with the Dex and Dex^{CM} presented the best antibacterial activity due to their better stability which resulted in the release of more silver ions, better interactions with the bacteria and diffusion into the biofilms.

The stabilized AgNPs were then loaded into vaterite *via* co-precipitation in order to protect, store and control their release, resulting in $CaCO_3$/AgNPs hybrids composed of up to 4% weight content of nanoparticles. The loading mechanism was well-described by the Langmuir adsorption model. The dissolution of $CaCO_3$ was found to be the primary release mechanism at acid pH, while at neutral and basic pH the recrystallisation into non-porous

calcite was responsible for the release of AgNPs. The pH-dependent release was then effectively regulated with poly(4-styrenesulfonic acid) to achieve a burst and sustained release. The antibacterial studies demonstrated that the hybrids protect the AgNPs without affecting their antibacterial activity.

Coatings of $CaCO_3$/AgNPs hybrids were designed by a simple drop-casting technique. PVP and mucin were used as additives to control the hybrids distribution, ensure coating mechanical integrity, and prevent the undesired release of AgNPs. Strong antibacterial performance was demonstrated at surface concentration of hybrids between 15 and 30 $\mu g/cm^2$. The *in vitro* cytotoxicity studies demonstrated that the hybrids at bactericidal concentrations do not affect the viability of human cells, and in some cases, even decrease the toxicity of AgNPs.

The findings presented in this thesis open new ways to stabilise, protect, store and release AgNPs, shedding light on the release mechanisms of AgNPs from vaterite and helping to foresee the release profiles of other active agents. The developed coating also demonstrates the enormous potential of the hybrids as active components for antibacterial surfaces, crucial to tackling the current antimicrobial resistance crisis.

Chapter 1

Introduction

The literature review in Section 3 has been published in 2020 as a review article titled "$CaCO_3$ crystals as versatile carriers for controlled delivery of antimicrobials" in the Journal of Controlled Release, Volume 328, pages 470 to 489[1].

1. Research overview, aims and objectives

Each year, about 3.8 million people acquire a healthcare-associated infection in acute care hospital units in European Union countries, Norway and Iceland[2]. The treatment of a single resistant infection has been estimated to cost €8,500 to €34,000 more than a non-resistant infection due to extended hospitalization periods and additional treatment costs[2].

A high number of deaths in over 65 years old individuals result from infection diseases[3,4]. Changes in the immune system associated with ageing, comorbidities, and alterations in the organism functions can increase the risk and severity of infections[3]. Moreover, the longer time spent in hospitals or other care facilities increases the risk of this age group acquiring a multi-drug-resistant infection[4].

The scarcity of drugs to tackle the increasing number of resistant microorganisms has intensified the need for solutions to control the spread of dangerous microbes, potentiate the activity of current antimicrobial agents, and control their spread in the environment.

Vaterite crystals are calcium carbonate ($CaCO_3$) inorganic porous particles of spherical shape with nano to micrometre sizes[5]. Vaterite is one of the three crystalline polymorphs of $CaCO_3$ and the least stable when compared to calcite and aragonite[5]. Vaterite crystals are biocompatible, have a porous structure, high loading capacity[5,6], tuneable recrystallization kinetic and can be simply prepared at a low cost, making them good microcarriers for antimicrobials.

Silver nanoparticles (AgNPs) are one of the most commercialised nanomaterials due to their attractive physical-chemical and biological properties, being found in many

applications, such as antimicrobial products and electronics1. Due to AgNPs broad-spectrum of activity against pathogenic microbes, they have been extensively commercialized and used to produce a wide range of goods with antimicrobial properties[8,9]. Nonetheless, the intensive use of AgNPs has raised concerns about their accumulation in the environment and potential adverse effects on different living organisms[10]. Moreover, the stability of AgNPs can easily be disrupted, decreasing the overall antimicrobial activity[11].

Based on vaterite properties and antimicrobial activity of AgNPs, this thesis aims to develop stable hybrids composed of vaterite and AgNPs ($CaCO_3$/AgNPs) with antibacterial activity and controlled silver release, for the production of functional coatings with antibacterial activity. To achieve the research aims, the following objectives have been set:

1. Investigate the stabilization of AgNPs with different capping agents and study the impact of the AgNPs surface identity on the antibacterial activity.

2. Produce AgNPs/$CaCO_3$ hybrids and study the loading mechanism of AgNPs.

3. Identify the release mechanisms of AgNPs from the hybrids and assess the antibacterial activity against pathogenic bacteria.

4. Develop and characterize coatings composed of AgNPs/$CaCO_3$ hybrids, test their antibacterial activity and *in vitro* cytotoxicity.

2. Thesis outline

The present thesis consists of six chapters. A brief overview of each chapter is presented below:

Chapter 1: *Literature Review*. This chapter summarizes the findings related to $CaCO_3$ synthesis, the factors that affect the crystal properties, the loading techniques, and a compilation of previous works on the controlled delivery of antimicrobials using $CaCO_3$ crystals as vectors. Overall, this chapter presents the background knowledge needed for developing $CaCO_3$ carriers for antimicrobial delivery, being the thesis pillars.

Chapter 2: *Silver nanoparticles synthesis and characterization*. This chapter is focused on the development of the antimicrobial agent/cargo, *i.e.*, AgNPs. AgNPs with different

surface properties are synthesized and characterised, and their stability and antibacterial activity assessed.

Chapter 3: *Design of hybrids of vaterite and silver nanoparticles*. This chapter is centred on the loading of AgNPs into vaterite via co-precipitation, presenting the nanoparticle loading/adsorption mechanism, the impact of AgNPs capping agents on the affinity to $CaCO_3$, and the stability of AgNPs before and after loading. Overall, this chapter studies whether vaterite $CaCO_3$ crystals can be used as effective carriers/supporting matrices to store, protect and deliver AgNPs.

Chapter 4: *Study of silver nanoparticles release from the hybrids and antibacterial activity assessment*. In this chapter, the recrystallization of the hybrids composed of $CaCO_3$ vaterite and AgNPs ($CaCO_3$/AgNPs) is studied in more detail and polymers are used to halt the conversion of vaterite into calcite and control the release of AgNPs. The hybrids are characterized, and the release mechanisms of AgNPs are extensively studied. The antibacterial activity of the $CaCO_3$/AgNPs hybrids is also tested against *Escherichia coli*, methicillin-resistant *Staphylococcus aureus* and *Pseudomonas aeruginosa*, three bacterial isolates responsible for a high number of infections.

Chapter 5: *Antibacterial coatings based on $CaCO_3$/AgNPs hybrids*. In this chapter, a formulation is developed to produce coatings composed of $CaCO_3$/AgNPs hybrids. The coatings are characterized, and their antibacterial activity assessed against *Escherichia coli*, methicillin-resistant *Staphylococcus aureus* and *Pseudomonas aeruginosa*.

Chapter 6: *Conclusion and Future Work*. This last chapter presents the concluding remarks and an overview of the original contributions to knowledge and suggestions for future work.

3. Literature review

The discovery of the first antibiotics marked a turning point in the history of medicine. The prospects of cure for patients with bacterial infections changed radically for the best. However, the heavy and sometimes incorrect use of antimicrobials promoted the appearance of alarming levels of resistance. Antibiotic-resistant infections cause per year at least 25,000 deaths in the European Union[12] and 35,000 in the United States of America[13], with the prospects of causing 10 million deaths globally per year by 2050 if nothing is done

to address the problem[14]. The lack of new classes of antibiotics in the market, and the lower interest of pharmaceutical companies in developing new drugs (low success and profits) accentuates the severity of the problem[15–17].

The rational use of antibiotics is essential to tackle the levels of bacterial resistance. Numerous campaigns and discussion groups have been created to raise the attention of healthcare practitioners and the general public, nonetheless there is still a long way to go.

Drug delivery systems are extremely important to improve the pharmacokinetics of the antimicrobial agents, increase the antimicrobial activity, patients' adherence to treatment programs, decrease the side effects, and supress the appearance of new resistance mechanisms[18–21].

The antibiotics used clinically today present some drawbacks such as limited stability, solubility, bioavailability, distribution/penetration in the target tissue, and short half-lifes[17,21,22]. Moreover, new therapeutic agents such as antimicrobial peptides, are sensitive to enzymatic decomposition[23].

In an attempt to improve drug delivery effectiveness and the chemotherapeutic outcomes, new carriers have been developed to effectively deliver antimicrobials. These include mesoporous silica, liposomes, quantum dots, dendrimers, solid lipid nanoparticles, nano- and micro-emulsions, gels, carbon nanomaterials, magnetic nanoparticles, microneedles and polymeric microparticles[24–28]. The most common polymer-based carriers are typically made of polymers such as chitosan, alginate, gelatin, albumin, collagen, polyvinyl pyrrolidone, polyacrylic acid, poly(vinyl alcohol), poly(methyl methacrylate), polyurethanes, polystyrene, poly(lactic-co-glycolic) acid, poly(lactic acid) and polyglycolic acid, with the last three being the most studied[27–30]. Some of the delivery carriers enumerated are already used in commercialized products[29,30]. However, the often intricate and multi-step production, cytotoxicity, recognition by the immune system, and significant loss of bioactivity in the complex biological media retards their further clinical translation and urges the search for alternative carriers that can bypass these limitations[24,31].

$CaCO_3$ is a versatile mineral with different applications such as in construction (limestone), production of bone cements, dental implants and scaffolds, and as a filler for paints, coatings, paper, pigments and plastics[32–35]. $CaCO_3$ is also included in different pharmacopoeias and is widely commercialized for pharmaceutical use in oral formulations as an excipient/active substance (antacids and medicines for the treatment of calcium deficiency). More recently it has been employed as a vector for drug delivery and as a

decomposable template for assembly of multilayer capsules[32,33,36,37]. $CaCO_3$ availability, low price, biocompatibility, biodegradability, high surface area, simple synthesis, tuneable and stimuli-responsive properties, make it an excellent candidate for storage and controlled release of various drugs[38]. Importantly, the use of calcium carbonate as a food and pharmaceutical additive/ingredient is approved by the Food and Drug Administration Agency (FDA). Recently, the European Food Safety Agency Panel on Food Additives and Nutrient Sources added to Food re-evaluated $CaCO_3$ usage taking into account the latest available toxicological data and confirmed that there are not toxicological concerns related to its use[39]. Numerous works have reported the use of $CaCO_3$, mainly the vaterite polymorph, for biomedical applications, e.g., for encapsulation of enzymes, hormones, deoxyribonucleic acid (DNA), growth factors, and drugs[32,40–52]. The employment $CaCO_3$ crystals as carriers for delivery of antimicrobials was demonstrated for the first time about two decades ago and was followed by several scientific reports demonstrating the advantages of $CaCO_3$ crystals for antimicrobials delivery over other drug delivery systems. $CaCO_3$ protects the antimicrobial agents from the external environment and can be designed to release the cargo in a controlled way and on demand. One of the most interesting characteristics of the $CaCO_3$ crystals is their sensitivity to different pH values which allows the cargo to be released on specific sites or conditions without affecting the antimicrobial activity. Moreover, the easily adjustable properties of $CaCO_3$ crystals (size, solubility, shape, composition) makes them attractive and dynamic drug delivery systems for different targets, microenvironment conditions and routes of administration.

This literature review summarises the use of nano- and micro-crystals of $CaCO_3$ as versatile carriers for the delivery of antimicrobials in a controlled and programmed manner, as highly desired for multiple drug delivery applications. The first part of this review intends to look at the main synthesis routes of $CaCO_3$ crystals and the factors that affect the crystal properties (e.g., size, morphology, structure) and that can be used to fine tune their properties. In the second part, the approaches for loading/release antimicrobial agents into/from the crystals and the antimicrobial performance of the $CaCO_3$ crystals are addressed.

3.1. $CaCO_3$ crystals

$CaCO_3$ is a mineral that occurs in three anhydrous crystalline forms: aragonite, vaterite and calcite; and two less common hydrated phases: ikaite and monohydrocalcite[53,54]. $CaCO_3$ can also occur as amorphous $CaCO_3$ (ACC), which is highly unstable and rapidly transforms into the metastable or stable polymorphs. Calcite is the most thermodynamically stable polymorph at standard conditions, and like the other anhydrous polymorphs, ACC precedes its formation[54,55].

Each $CaCO_3$ anhydrous polymorph has a typical morphology. Aragonite presents a needle-like shape, while vaterite and calcite have spherical and rhombohedral morphologies, respectively (**Figure 1-1**)[56]. Nonetheless, this shape can be changed by altering different synthesis conditions[33].

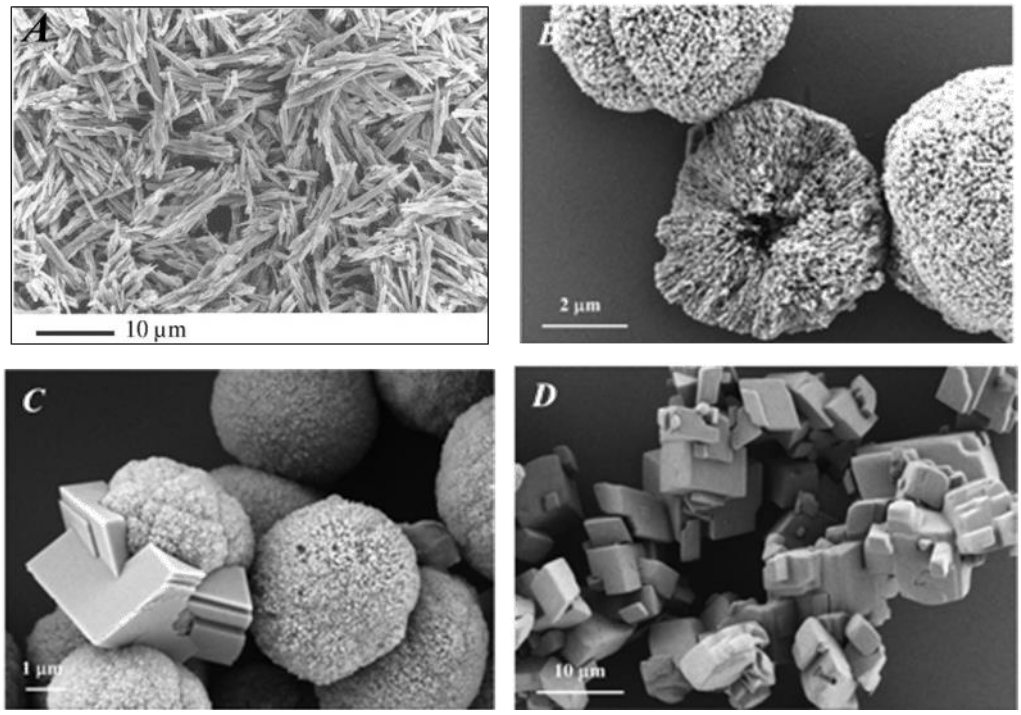

Figure 1-1. Scanning electron microscopy (SEM) images of aragonite (A), broken vaterite (B), vaterite and vaterite recrystallizing to calcite (C) and calcite (D). Image A adapted from Lucas A. et al.[57] and Image B, C e D adapted from Volodkin D. et al.[58]. Copyright 2001, with permissions from Elsevier (Image A) and Copyright 2004, with permission from American Chemical Society (Image B, C and D).

Bare vaterite crystals are unstable in aqueous solutions recrystallizing into calcite within some hours or a few days. However, the recrystallization kinetics can be changed with additives like polymers[32,33,59,60]. Despite this, vaterite porous structure, high surface area, tuneable morphology and size, which can range from tens of nanometres to tens of micrometres, makes it an attractive drug carrier[5,32]. From all the $CaCO_3$ polymorphs vaterite

presents some of the best properties for drug delivery, nonetheless, being a metastable phase between ACC and calcite, it poses some challenges and opportunities. These are related with vaterite instability and recrystallization into calcite, which can be used to trigger the cargo release.

3.2. Main routes of $CaCO_3$ synthesis

There are four main $CaCO_3$ synthesis methods: CO_2 bubbling, slow carbonation, reverse emulsion and solution precipitation (**Figure 1-2**)[61,62]. CO_2 bubbling or carbonation is the main industrial method and consists of bubbling CO_2 into a $Ca(OH)_2$ solution (Eq. 3 and Eq. 4) obtained from limestone calcination (Eq. 1) followed by hydration (Eq. 2)[63–65]. This method results mainly in nano-sized calcite crystals[33,66], nonetheless the size, polymorphism, morphology and properties of the formed particles can be controlled with additives, varying the Ca^{2+} concentration, or the operating conditions such as liquid or gas flow rate, CO_2 pressure and temperature[33].

$$CaCO_3(\text{limestone}) \rightleftharpoons CaO + CO_2 \qquad T \sim 900\ °C \qquad (1)$$
$$CaO + H_2O \rightleftharpoons Ca(OH)_2 \qquad (2)$$
$$CO_2 + H_2O \rightleftharpoons H_2CO_3 \qquad (3)$$
$$H_2CO_3 + Ca(OH)_2 \rightleftharpoons CaCO_3(\text{crystals}) + 2H_2O \qquad (4)$$

Slow carbonation reaction is a less common carbonation method. It consists of producing carbonate ions through the dissolution of CO_2 resultant from the slow decomposition of salts like ammonium carbonate (Eq. 5) or the hydrolysis of dimethyl carbonate under alkaline conditions[33,67–69].

$$(NH_4)_2CO_3 \rightleftharpoons 2NH_3 + CO_2 + H_2O \qquad (5)$$

Reverse emulsion (water in oil or W/O) synthesis comprises a system composed of a hydrophobic continuous phase with dispersed hydrophilic droplets (CO_3^{2-} or Ca^{2+} solutions) stabilized by a surfactant. $CaCO_3$ is formed when the emulsions are mixed, and the micelles containing CO_3^{2-} and Ca^{2+} ions collide, forming "micro-reactors". This method allows the synthesis of nano- and micro-particles with narrow size distributions. $CaCO_3$ polymorphism, size and morphology can be controlled by adding different additives, changing the pH, temperature, reaction time as well as the molar ratios of water to oil, water to surfactant, and Ca^{2+} to CO_3^{2-} [33,70].

The solution route, also known as solution precipitation method or mixing method[71], is the main method used on a lab-scale for the synthesis of $CaCO_3$, and consists of mixing

supersaturated solutions of CO_3^{2-} and Ca^{2+} containing salts with or without additives. It is the simplest and quickest method to produce $CaCO_3$ when compared with the carbonation or reverse emulsion. Moreover, the simple adjustment of the synthesis variables allows to quickly tune the size, shape, and polymorphism of the crystals. Up to the best of our knowledge, this is the only method that has been up scaled for the commercial fabrication of vaterite microcrystals (e.g. PlasmaChem GmbH, Germany). In relation to the encapsulation of antimicrobials, the solution precipitation method has been the most used up to now.

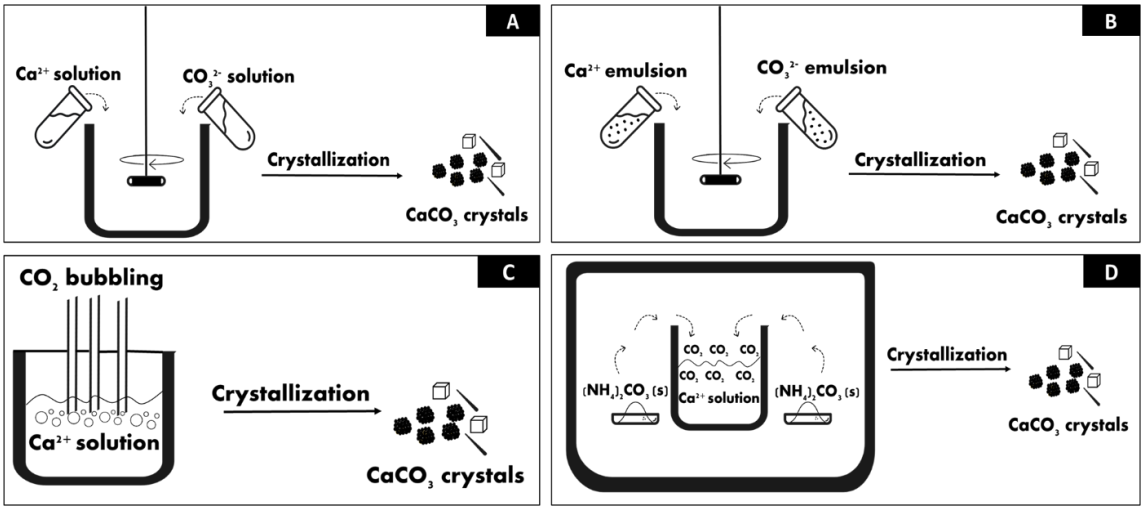

Figure 1-2. Main $CaCO_3$ synthesis methods: (a) solution precipitation method; (b) reverse emulsion (W/O) method; (c) CO_2 bubbling method and (d) slow carbonation method. Figure redrawn based on the work of Boyjoo Y. et al.[33].

3.3. Effect of the synthesis conditions on $CaCO_3$ crystals properties

Various synthesis conditions like presence of additives, solvent type, pH, rate and mode of mixing, temperature and precursor concentrations can significantly affect the properties of the crystals. Notably, the effect of most of these synthesis conditions, like pH, supersaturation, temperature, mixing mode and solvents, are transversal to the majority of the synthesis/loading methods. Most of these variables have been extensively studied, and the best conditions to produce crystals with a specific size, polymorphism, or other properties have been determined. In the sections below, the effect of these variables will be addressed in more detail, with a special focus on the solution precipitation method, due to its widespread use and the high number of detailed studies.

3.3.1. pH

The main effect of pH during the synthesis of $CaCO_3$ is on the availability of carbonate ions. When the pH is equal to 8 or drops to lower values, carbonate ions are protonated forming bicarbonate, which decreases the concentration of CO_3^{2-}, and consequently the precipitation of $CaCO_3$. Therefore, pH values above 8 are necessary for $CaCO_3$ synthesis. However, within the basic pH range, very high pH values create high nucleation rates, promoting uncontrolled crystal growth and the formation of large and irregular crystals[33].

The pH value also governs the effect of some additives, mainly when they possess ionizable groups. Additives with carboxylic groups are an example, as they are ionized at basic pH originating sites able to interact with Ca^{2+} and therefore controlling the crystals formation. Interestingly, additives with carboxylic groups are associated with the formation of particles with more uniform size distributions[33].

Oral et al.[72] studied the influence of pH during $CaCO_3$ synthesis at room temperature, through the solution precipitation method in the presence of ethylene glycol (EG). The results demonstrated that when the pH of the precursor solutions was 8 and 10 the vaterite particles formed independently of the $[Ca^{2+}]$:$[CO_3^{2-}]$ ratio. However, above pH 10, the ratio between the salts started playing a role on the type of polymorph formed. Oral and co-workers also verified that the size of $CaCO_3$ particles increased when the pH of the precursor solutions was higher.

Clifford Y. et al.[73] studied the effect of different synthesis conditions, including pH, on the polymorphism of $CaCO_3$. The experiment comprised mixing solutions of $CaCl_2$ with Na_2CO_3 at constant conditions. The authors demonstrated that pH affects the crystals polymorphism, with vaterite being more predominant at pH values between pH 8.5 and 10.

Han Y. et al.[74] studied the effect of pH on the polymorphism of $CaCO_3$ synthesized *via* carbonation and concluded that higher pH values resulted in lower contents of the vaterite (**Figure 1-3**) in favour of calcite.

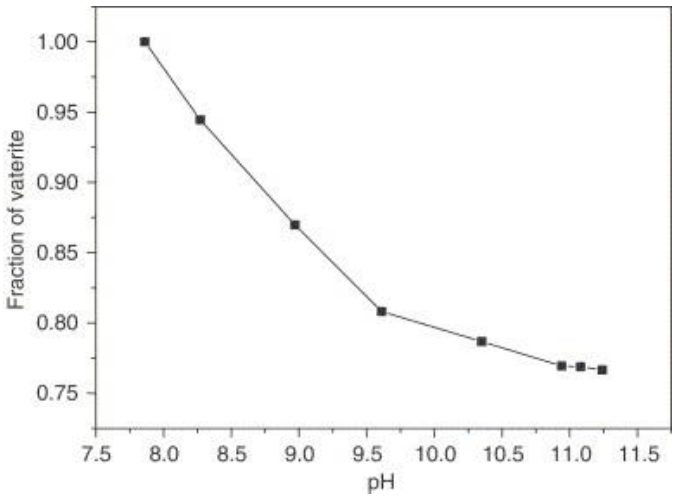

Figure 1-3. Fraction of vaterite synthesized *via* carbonation at different pH values. Adapted from Han Y. et al.[74]. Copyright 2006, with permission from Elsevier.

3.3.2. Temperature

Temperature is an important factor when synthesizing $CaCO_3$ crystals, as it influences the polymorphism of the particles produced[75]. Ogino T. et al.[76] synthesized $CaCO_3$ particles by mixing $CaCl_2$ (1.93×10^{-2} M) with Na_2CO_3 (9.26×10^{-3} M) at a molar ratio of 2 to 1, respectively, and studied the effect of temperature on the type of polymorph formed. Ogino T. and co-workers verified that at low temperatures (≤ 20°C) calcite was the main polymorph formed, while at temperatures between 30 and 40°C vaterite was produced at higher contents, and at temperatures around 70°C aragonite was the predominant polymorph. Similar findings were reported by Chen J. et al.[77], who synthesized $CaCO_3$ by mixing $CaCl_2$ (0.25 M) and NH_4HCO_3 (0.25 M) (**Figure 1-4**). Nonetheless, in contrast to the work of Ogino et al.[76], the formation of vaterite was also observed at 60°C. Ševčík R. et al.[78], also reported the synthesis of vaterite at 60°C by mixing equal molar ratios of $CaCl_2$ (2.0 M) and K_2CO_3 (2.0 M). This difference can be explained by the higher molar ratios used by Ševčík R. et al.[78] and Chen J. et al[77]. This demonstrates that the initial concentration of the reagents can modulate the temperature effect on the type of polymorph formed. This effect was previously reported by Ma M. et al[79].

Interestingly, the temperature also affects the mesoporous internal structure of vaterite. Feoktistova N. et al.[36], verified that vaterite crystals synthetized without additives at 45°C presented larger pores, a feature that can be crucial for many bio-applications.

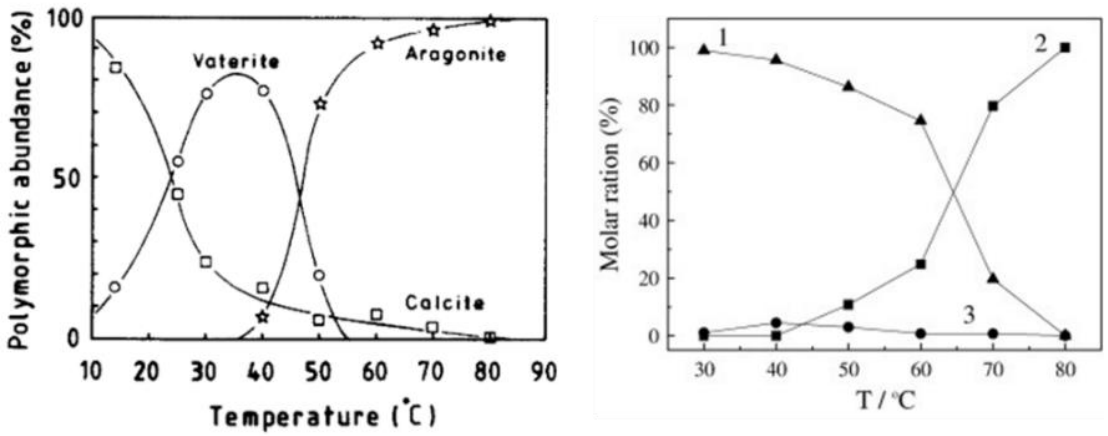

Figure 1-4. Polymorphic abundance (%) of crystalline carbonates at the early metastable stages as a function of temperature.1 - vaterite; 2 - aragonite and 3 - calcite. Adapted from Ogino T. et al. [76] (left) and Chen J. et al.[77] (right). Copyright 1987 and 2009, respectively, with permission from Elsevier.

3.3.3. Supersaturation and $[Ca^{2+}]:[CO_3^{2-}]$ ratio

The concentration of the precursor salts and the $[Ca^{2+}]:[CO_3^{2-}]$ ratio affect the synthesis duration, type and size of the polymorph formed. The crystallization takes place just when the supersaturation is reached. The high supersaturation results in higher nucleation ratios and lower induction times[80]. According to the "Ostwald's step rule" at a low supersaturation the stable polymorph (calcite) is preferentially precipitate while at a high supersaturation the metastable polymorph (vaterite and aragonite) tends to form[81,82]. Kitamura M.[81] verified this tendency when synthesizing $CaCO_3$ by mixing $CaCl_2$ and Na_2CO_3 solutions at different concentrations. It was shown that vaterite tended to precipitate at high concentrations (200 mM) while calcite mainly precipitated at lower concentration (50 mM)[81]. The same trend was verified by Ma M. et al.[79] and Ogino T. et al[76], who reported that the relative abundance of vaterite increased with the concentrations of Ca^{2+} and CO_3^{2-} ions at 25°C. Nonetheless, it has been demonstrated that when the supersaturation of ACC is lower than 1, *i.e.* the ion activity product of the initially supersaturated solution is lower than the solubility product of ACC at 25°C, only vaterite crystals with a peculiar hexagonal plate-like shape are formed[76,83]. Moreover, the synthesis of these vaterite crystals implies longer induction times (time needed for the detection of the first newly created particles) due to the low initial concentrations (c_i) of the salts solutions[83]. The supersaturation rate also influences the size of $CaCO_3$ crystals. Higher supersaturation promotes the formation of smaller crystals due to the occurrence of more nucleation centres at the same total mass of the precipitate[5,71,81]. Finally, the ratio of the precursor salt affects mainly the size and shape of the crystals. Nonetheless, at a very high pH values it can also affect the polymorphism[72]. It has been demonstrated that concentrations of CO_3^{2-} higher than that of Ca^{2+} result in the formation

of crystals with more ellipsoidal geometries, while lower concentrations promote the formation of isotropic spherical particles (**Figure 1-5**)[72,84].

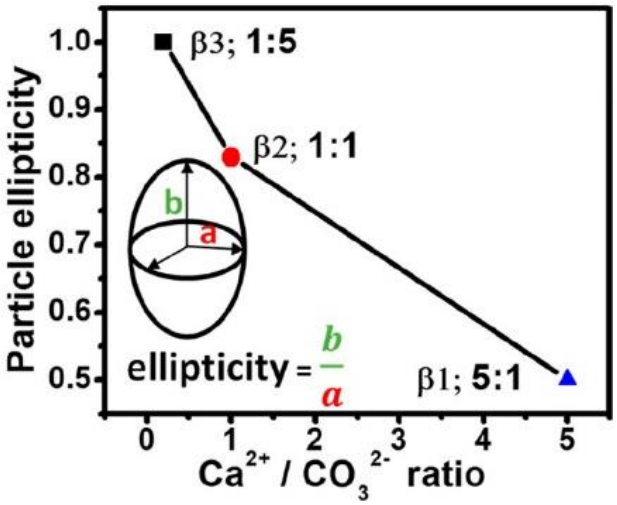

Figure 1-5. Dependence of particle ellipticity on the $[Ca^{2+}]$:$[CO_3^{2-}]$ ratio. $CaCO_3$ crystals were synthesized at room temperature by mixing $CaCl_2$ and Na_2CO_3 solutions. Adapted from Bahrom H. et al.[84]. Copyright 2019, with permission from American Chemical Society.

3.3.4. Reagents mixing

The reagents mixing order and stirring speed affect mainly the morphology, size and size distribution of the crystals[33]. Volodkin D. et al.[85] tested the effect of stirring time (15, 20, 30 and 40 s) and speed (400, 650 and 900 rpm) on the properties of $CaCO_3$ synthetized *via* the solution precipitation route. They concluded that higher stirring times and speeds lead to the formation of more nuclei and, as a result, smaller crystals. Just by varying the stirring time and speed, the authors were able to synthesize particles with sizes ranging between 3 and 20 µm. Other authors have also reported similar results[48,86].

Ševčík et al.[78] and Mori Y. et al.[87] verified that when mixing precursor solutions with very high concentrations (1-2M) the stirring speed affects the type of the polymorph formed. Inadequate stirring creates different local concentrations in the same solution/gel, promoting the formation of calcite. On the other hand, a homogenous and continuous agitation results in an even bulk concentration and higher contents of vaterite.

The reagents mixing order also affects the characteristics of the crystal. Wang et al.[88] demonstrated that adding the CO_3^{2-} to the Ca^{2+} solution (quick mixing or dropwise) results in smaller crystals with uniform size distribution. However, with the opposite mixing order, the crystals become larger and have a non-uniform size distribution. This effect is more pronounced when the Ca^{2+} solution is added dropwise to the CO_3^{2-} solution. The different results are related to the different pH values of the precursor solutions[88,89]. When a Ca^{2+}

containing salt solution (pH 6.41 to 8.83 for $CaCl_2$ at 2 to 800 mM [79]) is added to a CO_3^{2-} containing salt solution (pH 11.0 for Na_2CO_3 at 2 mM to 800 mM[79]) the transitory initial pH value, before reaching the equilibrium, is higher than when the opposite is done. This results in high nucleation rates with uncontrolled crystal growth and the formation of large crystals with inhomogeneous size distribution[33,88].

3.3.5. Solvent

Water is the primordial, most used, and most studied solvent for the synthesis of $CaCO_3$. Nonetheless, mixtures of water with other solvents have also been used to produce $CaCO_3$ crystals[56,59,84,90,91], including ethanol, propan-1-ol, methanol, polyethylene glycol (PEG), glycerine, N,N-dimethylformamide and EG[56,59,84,90–92]. Overall, the solvents decrease the solubility of $CaCO_3$ which results in higher supersaturation and the formation of smaller particles. Some of these solvents like PEG, glycerine and EG also increase the density of the reaction media which diminishes the molecular diffusion and reduces the crystal growth rate and the probability of nucleation[84,90]. Moreover, low, or even no water, results in the stabilization of the $CaCO_3$ particles formed during the early stages of the synthesis[84].

Solvents can also affect the type of polymorph formed. Sand K. et al.[56] demonstrated that the combination of water (50%) with ethanol (50%) promotes the formation of aragonite at 24°C, which usually just occurs at high temperatures in aqueous solutions.

3.3.6. Additives

Numerous articles have reported the effect of additives on the properties of $CaCO_3$ crystals, with their selection being mainly empirical. Moreover, the effect on the properties of the crystals can vary with the concentration of the additive or other experimental conditions[93]. The type of additives tested on $CaCO_3$ synthesis includes surfactants, synthetic polymers, biomolecules, biopolymers, and inorganic compounds. These additives affect the crystallization process (cluster formation, prenucleation, nucleation, and growth), polymorphism and recrystallization kinetics. Moreover, it can lead to the formation of crystals with different sizes and shapes (flower, peanut, pyramid-like etc.)[32,33,93,94]. The incorporation of additives attempts to mimic the capacity of different organisms to build and control the formation of different $CaCO_3$ structures using organic or inorganic compounds (biomineralization)[33,95].

Various review papers present summarized information about the effect of additives on the properties of $CaCO_3$ and can be found elsewhere[32,33,59]. Despite the large number of variables when studying the effect of additives, it has been reported that synthetic

polymers, at the right concentration, usually induce the formation of vaterite spheres with a uniform size distribution. Both polyacrylic acid and polystyrene sulfonate are reported to be some of the most effective polymers in promoting the retention of the vaterite spherical shape[33,59]. Biopolymers and biomolecules such as cellulose, soluble starch, ovalbumin, bovine serum albumin, and dopamine are also known to promote the formation and/or stabilization of vaterite by adsorbing to the surface of the crystals and retarding the dissolution/recrystallization into calcite[32,33,59].

3.4. Loading approaches for $CaCO_3$ crystals

The three main approaches for loading molecules of interest (MOI) into the $CaCO_3$ crystals are adsorption, infiltration and co-precipitation[5,96,97]. More recently, freezing-induced loading, which can be considered a sub-type of infiltration, has also been proposed as an efficient loading route[38].

3.4.1. Adsorption

The adsorption loading method consists in adsorbing the MOI on the crystals through molecular interactions (**Figure 1-6**)[5]. This method is usually carried out by mixing $CaCO_3$ crystals with a solution containing the MOI[96]. pH is an important parameter when adsorbing proteins into $CaCO_3$ as it affects the net charge of proteins and $CaCO_3$, and consequently the electrostatic interactions as well as the activity of the proteins[41,58]. Interestingly, despite the electrostatics forces governing the protein-$CaCO_3$ interactions, the inter-protein interactions in the bulk solution also affect the loading efficiency into vaterite[98]. This is due to the inter-protein interactions promoting the formation of protein aggregates which affect the proteins diffusion into porous vaterite and the loading efficiency as a whole[98].

The adsorption approach is straightforward loading method, although long mixing periods might be required which can affect the stability of the $CaCO_3$ crystals, even more if metastable polymorphs are used. Moreover, the adsorption loading method presents a limited loading capacity[96].

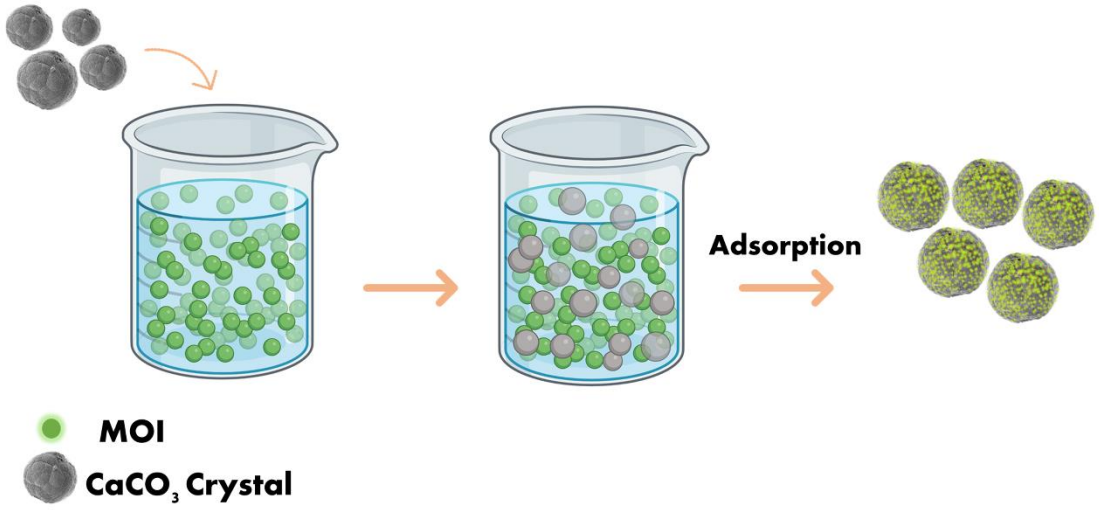

Figure 1-6. Schematic representation of $CaCO_3$ crystals loading *via* adsorption. MOI - molecule of interest. Created with BioRender.com

3.4.2. Infiltration

The infiltration loading method consists in mixing $CaCO_3$ crystals with the MOI followed by decreasing the solubility of the cargo by altering the pH or promoting the solvent evaporation (**Figure 1-7**)[5,99]. As well as the adsorption method, infiltration can be carried out with $CaCO_3$ crystals synthetised *via* different methods. However, this loading approach results in a better loading efficiency as the empty pores of the crystals can be completely loaded with the MOI[5,100,101].

Freezing-induced loading can be considered a sub-type of infiltration. This method involves mixing $CaCO_3$ crystals with the solution containing the MOI, which is then submitted to freezing/thawing cycles under agitation[38]. Gorin D. et al[38] demonstrated that by controlling the number of cycles is possible to load three to four times more nanoparticles and proteins, respectively, than *via* the co-precipitation and adsorption methods.

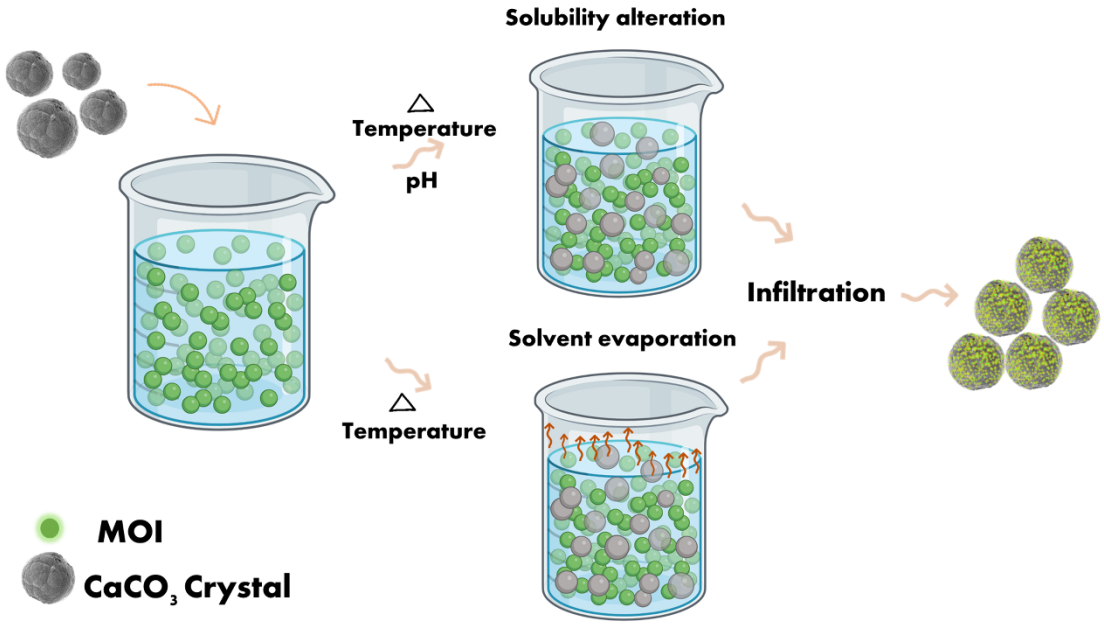

Figure 1-7. Schematic representation of $CaCO_3$ crystals loading via infiltration. MOI - molecule of interest. Created with BioRender.com

3.4.3. Co-precipitation

The co-precipitation is based on capturing the MOI into the crystals during the synthesis of $CaCO_3$ by adding the MOI to the precursor salts solutions (**Figure 1-8**)[5,96]. This approach is widely used to load MOI into crystals synthetized *via* solution precipitation and reverse emulsion. This is also the most popular method for loading $CaCO_3$ as it is quick, simple and allows to load very high contents of MOI with a uniform distribution and at mild synthesis conditions[5,42,96]. Nonetheless, the MOI added during the synthesis might affect the crystallization process (nucleation rate, polymorphism, crystal size and shape) and stability of $CaCO_3$. Furthermore, while this approach can result in a high loading efficiency (more than 60% w/w for catalase), the synthesis conditions (precursor salts and pH) can affect the activity of some sensitive MOIs like enzymes and proteins[43,102–104]. The loading of small molecules might also be problematic as they can easily diffuse through the pores of vaterite which are tens of nm. However, this can be suppressed by combining them with macromolecules[5]. The associating of mucin with vaterite crystals is an example, as mucin increases the charge into the cavity of the porous crystals which increases the retention of small drugs like doxorubicin[105–107].

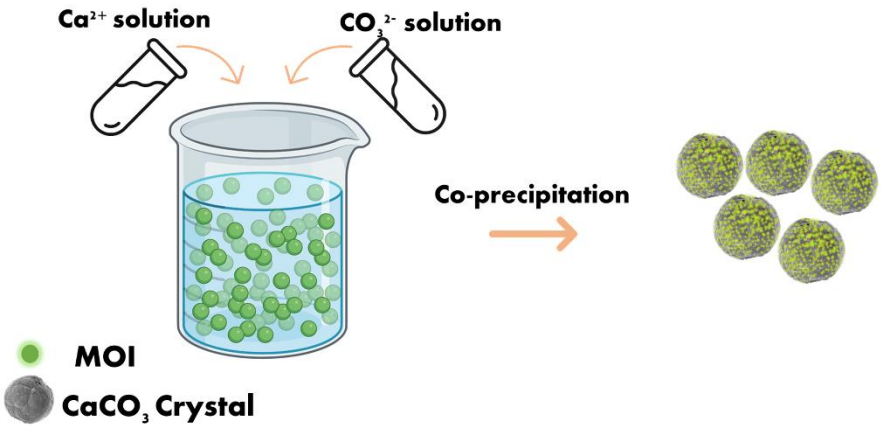

Figure 1-8. Schematic representation of $CaCO_3$ crystals loading *via* co-precipitation. MOI - molecule of interest. Created with BioRender.com

3.5. $CaCO_3$ hybrids

The addition of additives during the synthesis of $CaCO_3$ can be applied to control the nucleation process and crystal stability, but also to improve the MOI loading efficiency and release profile. Coating $CaCO_3$ crystals with different polymers after synthesis can also be used to load, retain and control MOI release in a stimuli-responsive manner. Polyelectrolyte multilayers prepared by the layer-by-layer (LbL) deposition have been reported as an effective way to synthesize hybrid vectors composed of polymers and $CaCO_3$ for drug delivery.

Polyelectrolyte multilayers are very attractive coatings that can endow multiple functions including cellular adhesion and other bio-related activities serving as reservoirs for MOI[108–110]. The multilayers can reach thicknesses of micrometres and more[111], and host a very high amount of MOI including small charged molecules[112], large biomacromolecules such as proteins[113], and polysaccharides with low charge[114]. The multilayers performance can easy be tuned by changing the number of deposited layers, the type of polyelectrolytes used, including their combination, and the deposition conditions such as temperature[115]. Potentially any decomposable particle (core) can be used for the production of multilayer structures[116–118]. $CaCO_3$ crystals have been used as sacrificial cores for the formation of free-standing multiplayer capsules, as they can be easily decomposed with acidic compounds or Ca^{2+} chelating agents. The capsules can be stained by fluorescent probes bound to polyelectrolytes and the multilayers can be effective for protecting a loaded MOI

and adjusting its release kinetics[119]. In general, the hybrid structures made of $CaCO_3$ crystals, polyelectrolyte multilayers, and soft polymer-based structures sensitive to external triggers[120], can serve as mimics of biological structures such as the extracellular matrix and the intracellular environment[121], or even be a key part of tailor-made polymer-based scaffolds used for tissue engineering[122–125]. These hybrids demonstrate the potential of $CaCO_3$ crystals for the design of structures with advanced drug delivery properties.

3.6. $CaCO_3$ crystals as vectors for antimicrobials delivery

$CaCO_3$ presents a set of characteristics that makes it an excellent candidate for drug delivery including the delivery of antimicrobials, as some of these therapeutic agents present limited stability, solubility, bioavailability, distribution/penetration, and short half-life. Different research works have explored the use of $CaCO_3$ as a vector for antimicrobials delivery. **Table 1-1** to **Table 1-4** present a summary of the published work in this research topic including the synthesis conditions, loading method, and properties of the final $CaCO_3$ carriers. In the next sections, the application of $CaCO_3$ for the delivery of antimicrobials is discussed in more detail.

Table 1-1. Summary of $CaCO_3$ synthesis conditions by carbonation and characteristics of the $CaCO_3$ crystals loaded with the antimicrobial agents. EDTA: Ethylenediaminetetraacetic acid; RT: Room Temperature; AgNPs: Silver nanoparticles; C_i: Initial concentration; mix: Mixing; n.d.: Not defined. [a] Weight percentage of the antimicrobial agent in the total weight of the loaded $CaCO_3$ particles. [b] Calculated/assumed based on the data/information presented in the article.

	Synthesis Conditions						**Antimicrobials**		**Crystals Characteristics**		
Ref.	**Synthesis Method**	**Reagents (C_i before mix.)**	**T (°C)**	**pH**	**Reaction Time**	**Additives**	**Antimicrobial Agent**	**Loading Method**	**Morphology**	**Polymorph**	**Size**
Pan X. et al. [126]	Carbonation	$Ca(OH_2)$ (n.d.) CO_2- 40ml.min^{-1}	RT[b]	-	-	EDTA (n.d.)	Gentamicin Sulfate (31.17 ± 1.66 to 50.05 ± 1.85 wt% [a])	Adsorption	Chain-like	Calcite	62.5 nm
Sahoo P. et al. [127]	Carbonation	$CaCl_2$ (0.3 M) NH_4OH (5 M) CO_2 (99 %)-1.5 L.min^{-1}	RT[b]	-	30 min	Microalgae cells (1.8 wt%)	AgNPs (20-25nm; 3.7 wt% [a])	AgNPs *in situ* synthesis	Spherical	Calcite, Vaterite	5 µm

Table 1-2. Summary of $CaCO_3$ synthesis conditions by reverse microemulsion, and characteristics of the $CaCO_3$ crystals loaded with the antimicrobial agents. RT: Room Temperature; C_i: initial concentration; mix: Mixing; T.: Temperature; n.d.: Not defined. [a] Weight percentage of the antimicrobial agent in the total weight of the loaded $CaCO_3$ particles. [b] Calculated/assumed based on the data/information presented in the article.

	Synthesis Conditions						Antimicrobials		Crystals Characteristics		
Ref.	**Synthesis Method**	**Reagents (C_i before mix.)**	**T (°C)**	**pH**	**Reaction Time**	**Additives**	**Antimicrobial Agent**	**Loading Method**	**Morphology**	**Polymorph**	**Size**
Qian K. et al. [128]	Reverse Microemulsion	$CaCl_2$ (1 M) Na_2CO_3 (1 M)	RT[b]	-	-	-	Validamycin (11.1 to 19.3 wt%[a])	co-Precipitation	Spherical	Calcite	57.5 -199.7 nm
Dizaj S. et al. [19]	Reverse Microemulsion	$CaCl_2$ (5 M) Na_2CO_3 (2 M)	RT[b]	-	24 h	-	Ciprofloxacin HCl (20.49 ± 0.09 wt% [a])	co-Precipitation or Adsorption (10 min)	Spherical	Calcite, Vaterite	90 nm (Adsorption) 116 nm (co-Precipitation)
Dizaj S. et al. [22]	Reverse Microemulsion	$CaCl_2$ (5 M) Na_2CO_3 (2 M)	25	-	24 h	-	Gentamicin Sulfate (25.3 ± 2.5 wt% [a])	co-Precipitation or Adsorption (10 min)	Spherical	Calcite, Vaterite	90 nm (Adsorption) 113 nm (co-Precipitation)
Memar Y. et al. [129]	Reverse Microemulsion	$CaCl_2$ (5 M) Na_2CO_3 (2 M)	25	-	24 h	-	Gentamicin Sulfate (25.3 ± 2.5 wt% [a])	co-Precipitation	Spherical	Calcite, Vaterite	113 nm

Table 1-3. Summary of $CaCO_3$ synthesis conditions by solution/colloidal precipitation, and characteristics of the $CaCO_3$ crystals loaded with the antimicrobial agents. RT: Room Temperature; C_i: initial concentration; mix: Mixing; T: Temperature; n.d.: not defined; AL: Alginate lyase; CP: Colloidal precipitation; CIP: Cold isostatic pressing; L-Length; W-With; DNase: deoxyribonuclease; Poly(L-asp): Poly(L-aspartic acid) sodium salt; PLL: Poly-L-lysine hydrobromide; PAH: Poly(allylamine hydrochloride); AgNPs: Silver nanoparticles; PSS: Poly(sodium 4-styrenesulfonate); SDS: Sodium dodecyl sulphate; PEG-PAsp: poly(ethylene glycol)-poly(aspartic acid). [a] Weight percentage of the antimicrobial agent in the total weight of the loaded $CaCO_3$ particles. [b] Calculated/assumed based on the data/information presented in the article. [c] Synthesis temperature is not specified, but the use of an ice bath is reported.

	Synthesis Conditions						Antimicrobials		Crystals Characteristics		
Ref.	**Synthesis Method**	**Reagents (C_i before mix.)**	**T (°C)**	**pH**	**Reaction Time**	**Additives**	**Antimicrobial Agent**	**Loading Method**	**Morphology**	**Polymorph**	**Size**
Islan G. et al. [130]	Colloidal Precipitation followed by AL treatment (48h)	Na_2CO_3 (0.30M) $CaCl_2$ (0.29M)	-[c]	10	5 min (CP) 48 h (AL treatment)	Glycine buffer; Sodium Alginate and/ or Pectin (6.5-23.6 wt%)	Levofloxacin (1.21 ± 0.01 to 1.40 ± 0.06 wt% [b])	Adsorption (24h)	Spherical	Vaterite	3.6-4.6 µm
Islan G. et al. [131]	Colloidal Precipitation followed by AL treatment (48h)	Na_2CO_3 (0.30M) $CaCl_2$ (0.29M)	-[c]	10	5 min (CP) 48 h (AL treatment)	Glycine buffer; Sodium Alginate(n.d.) and DNase (1.15-2.71 wt%)	Levofloxacin (7.41 wt% [b])	Adsorption (24h)	Spherical	Vaterite	3-5 µm
Lucas A. et al. [57]	Solution Precipitation	$KHCO_3$ (0.1M) $CaCl_2$ (0.1M)	100	-	-	-	Gentamicin Sulfate (n.d.); Metronidazole (n.d)	Integration by CIP and Sublimation	Needle-like	Aragonite	5-10 µm (L) 1 to 2 µm (W)
Lucas A. et al. [132]	Solution Precipitation	$KHCO_3$(0.1M) $CaCl_2.2H_2O$ (0.1M)	100	-	-	-	Gentamicin Sulfate: Integration (5.5 ± 0.2 to 11.2 ± 0.6 wt% [a]); adsorption (0.35 ± 0.02 to 0.40 ± 0.02 wt% [a])	Integration by CIP (5 min 600MPa) and Sublimation; Adsorption	Needle-like	Aragonite	5-10 µm (L) 1 to 2 µm (W)
Yan H. et al. [133]	Solution Precipitation	$CaCl_2$ (2mM) Na_2CO_3 (2 mM)	0, 20, 40	-	24h	Guar Gum (n.d.)	Vancomycin Hydrocholoride (24.3 to 46 wt%[a])	Adsorption (12h)	Spherical	Calcite,Vaterite	1 µm
Dizaj S. et al. [86]	Solution Precipitation	Na_2CO_3(n.d.): $CaCl_2$ (n.d.) molar ratios - 1:1; 3:1.5; 5:2	RT[b]		15 min	-	Gertamicin Sulfate (n.d.)	co-Precipitation	-	-	80.0-300.12 nm
Begum G. et al. [37]	Solution Precipitation	$(NH_4)_2CO_3$(n.d.): $CaCl_2$ (n.d.) molar ratios - 1:1	RT	-	30 min	Poly(L-asp) and PLL (n.d.)	Tetracycline (n.d.)	co-Precipitation	Spherical	Vaterite, Amorphous	0.5 – 1 µm
Mihai M. et al. [134]	Solution Precipitation	Na_2CO_3(0.05M) $CaCl_2.2H_2O$ (0.10M)	RT	10.5	9 h	PAH and/or Pectins (n.d.)	Tetracycline hydrocholoride (15.28-39.90 wt% [b])	Adsorption (4h)	Rhombohedral and Spherical	Calcite, Vaterite	4.85 – 7.76 µm

Table 1-3. *(Continuation)*

	Synthesis Conditions						Antimicrobials		Crystals Characteristics		
Ref.	**Synthesis Method**	**Reagents (C_i before mix.)**	**T (°C)**	**pH**	**Reaction Time**	**Additives**	**Antimicrobial Agent**	**Loading Method**	**Morphology**	**Polymorph**	**Size**
Racovita S. et al.[135]	Solution Precipitation	Na_2CO_3 (0.05M) $CaCl_2.2H_2O$ (0.10M)	RT	10.5	8 h	PAH and/or Pectins (n.d.)	Streptomycin (3.54-15.79 wt% [b]); kanamycin (4.43-29.52 wt %[b])	Adsorption (4h)	Rhombohedral and Spherical	Calcite, Vaterite	~ 5 – 8 µm
Said F. et al [136]	Solution Precipitation	Na2CO3 (0.33M) CaCl2 (0.33M)	RT[b]	-	3 min	-	Penicillin; Ampicillin; Ciprofloxacin (>5 wt% [a])	Adsorption (24h)	Spherical	Calcite, Vaterite	5 µm
Matei C. et al. [137]	Solution Precipitation	Na_2CO_3 (0.4M) $CaCl_2$ (0.4M)	10	-	30 min	*Ulva lacuna* extract (n.d.)	Ag/AgCl (n.d.)	co-Precipitation	Spherical or Rhombohedral	Calcite	-
Długosz M. et al. [138]	Solution Precipitation	Na_2CO_3 (0.03M) $Ca(NO_3)$ (0.03M)	25	-	5 min	PSS and PAH (after synthesis) (n.d.)	AgNPs (30-50 nm; 0.015wt% [a])	co-Precipitation	Spherical	-	2 µm
Baldassarre F. et al. [139]	Solution Precipitation	$NaHCO_3$ (0.125M) $CaCl_2$ (0.083M)	-	-	-	-	Caffeic acid; N-acetylcysteine (n.d.)	Adsorption (overnight)	-	-	50-75 nm
Tessarolo L. et al. [140]	Solution Precipitation	$CaCl_2$ (0.025M) Na_2CO_3 (0.05M)	30	-	72 h	SDS and Pluronic F-68 (n.d.)	Benznidazole (25 wt%[a])	co-Precipitation	Spherical	-	41.81nm
Min K. et al. [141]	Solution Precipitation	$CaCl_2$ (0.044M)[c] Na_2CO_3 (0.044M)[c]	RT	8	16 h	PEG-PAsp (n.d.)	Doxycycline hyclate (2.35 wt% [a])	co-Precipitation	Spherical	Vaterite	312.5nm
Xue J. et al. [142]	Solution Precipitation	$CaCl_2$ (0.2M) Na_2CO_3 (0.2M)	RT[b]	-	30 min	β-cyclodextrins; casein and Fe_3O_4 nanoparticles (n.d.)	Minocycline (n.d.)	Adsorption (24h)	Spherical	Vaterite	2 – 5 µm

Table 1-4. Summary of the fabrication conditions for the top-down method or previously acquired $CaCO_3$ crystals, and characteristics of the $CaCO_3$ crystals loaded with the antimicrobial agents. CA: $CaCO_3$ acquired from and external supplier ; RT: Room Temperature; T: Temperature; n.d.: Not defined; AgNPs: Silver nanoparticles; HPH: High pressure homogenizer; PSS: Poly(sodium 4-styrenesulfonate); Cl-DMH-UA: 3-chloro-4,4-dimethylhydantoin undecanoic acid; LbL: Layer by Layer; PEI: Polyethyleneimine. [a] Weight percentage of the antimicrobial agent in the total weight of the loaded $CaCO_3$ particles. [b] Calculated/assumed based on the data/information presented in the article.

	Fabrication Conditions				**Antimicrobials**		**Crystals Characteristics**		
Ref.	**Method**	**Material**	**T (°C)**	**Additives**	**Antimicrobial Agent**	**Loading Method**	**Morphology**	**Polymorph**	**Size**
Isa T. et al. [143]	Top-Down, Microemulsion (O/W) milling with HPH	Dried cockle shells-$CaCO_3$ powder	RT[c]	-	Ciprofloxacin HCl (5.9 wt% [a])	Adsorption (overnight)	Spherical	Aragonite	13.94-23.95 nm
Padmanabhuni R. et al. [144]	CA	$CaCO_3$	-	-	Cl-DMH-UA (n.d.)	Adsoprtion of the Cl-DMH-UA precursor (2h), Cl-DMH-UA *In situ* synthesis (1h) (n.d.)	Scalenoheral	Calcite[b]	2-4 µm
Apalangya V. et al. [145]	Top-Down	Eggshells	100	-	AgNPs (5-20nm) (n.d.)	Adsorption and *In situ* AgNPs synthesis (2h)	-	Calcite	Micron range
Tiimob B. et al. [146]	Top-Down	Eggshells	-	-	AgNPs (10-15nm) (n.d.)	Adsorption and *In situ* AgNPs synthesis (≥5h)	-	Calcite	-
Ferreira C. et al. [147]	CA	$CaCO_3$	-	PSS and PEI (n.d.)	Benzyldimethyldodecylammonium chloride (n.d.)	LbL adsorption	Spherical	-	2-4 µm

3.6.1. $CaCO_3$ vectors production

As previously referred, there are different approaches for the synthesis of $CaCO_3$ crystals. In the research works compiled in this literature review the most frequent method for $CaCO_3$ synthesis was the solution precipitation. The microemulsion and carbonation methods were also reported, although not to such a great extent. Some works also presented a top-down approach for the production of micro- and nanoparticles of $CaCO_3$ where cockle shells and eggshells were used as the starting material[143,145,146]. Isa T. et al.[143] produced aragonite nanoparticles from cockle shells through a microemulsion (O/W) system using a high-pressure homogenizer for milling the particles. The particles were then loaded with ciprofloxacin *via* adsorption and tested against *Salmonella Typhimurium* (American Type Culture Collection (ATCC) 14028) through the disc diffusion susceptibility assay. The results demonstrated that the encapsulated ciprofloxacin presented higher antibacterial activity against *Salmonella Typhimurium* than the pristine ciprofloxacin with inhibitions zones of 18.6 ± 0.5 mm and 11.7 ± 0.9 mm, respectively. Another interesting top-down approach was reported by Apalangya V. et al. [145] who used eggshells waste for the extraction of $CaCO_3$ and proteins, followed by *in situ* synthesis of silver nanoparticles (AgNPs) by ball milling. This method allowed to decrease the size of $CaCO_3$ particles and the simultaneous reduction of Ag^+ to Ag^0 by the eggshell proteins (**Figure 1-9**) also responsible for the stabilization of the AgNPs.

The different routes of $CaCO_3$ synthesis, and their easy implementation and modification, broadens the spectrum of applications of $CaCO_3$ and highlights their suitability and adaptability for the encapsulation of different types of drugs.

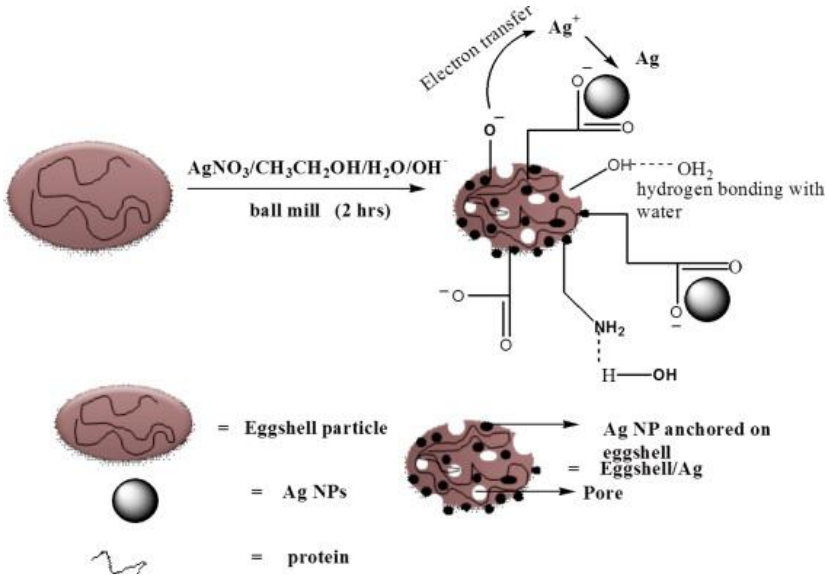

Figure 1-9. Proposed mechanism of $CaCO_3$-AgNPs nanocomposites formation. Adapted from Apalangya V. et al.[145]. Copyright 2014, with permission from Elsevier.

3.6.2. Antimicrobials loading

Table 1-1 to 1-4 show various methods for loading antimicrobials into the $CaCO_3$ crystals. The most reported methods were adsorption and co-precipitation due to their straightforwardness, efficiency and mild loading conditions.

The efficiency of antimicrobials loading is presented in the tables and ranged between 0.015[138] and 50 wt%[126]. This wide range is explained by the vast number of conditions that can influence the loading capacity of the crystals including the crystal synthesis conditions, loading method, additives used, crystals size, surface area and the antimicrobial agent properties.

Despite the advantages of the adsorption and co-precipitation loading methods, some works have reported very different and interesting loading approaches. To the best of our knowledge, Luca A. et al.[57,132,148] was the first group to report the use of $CaCO_3$ crystals as vectors for controlled delivery of antibiotics. In the various works published by the group, aragonite crystals were first synthesized and then the antimicrobials loaded through integration by a cold isostatic pressing and sublimation process. As depicted in **Figure 1-10**, the process starts by mixing aragonite powder with a pore-making agent (naphthalene) and the antibiotic of interest. Then the mixture is submitted to a cold isostatic pressing followed by heating under vacuum at 80°C for the pore former elimination and the macroporosity induction[132,148]. The authors also tested loading gentamicin after aragonite processing with naphthalene. Nonetheless, the loading efficiency (**Table 1-1**) and

release profiles were not satisfactory: 4 days against 8 to 12 days when gentamicin was incorporated during the aragonite processing[132].

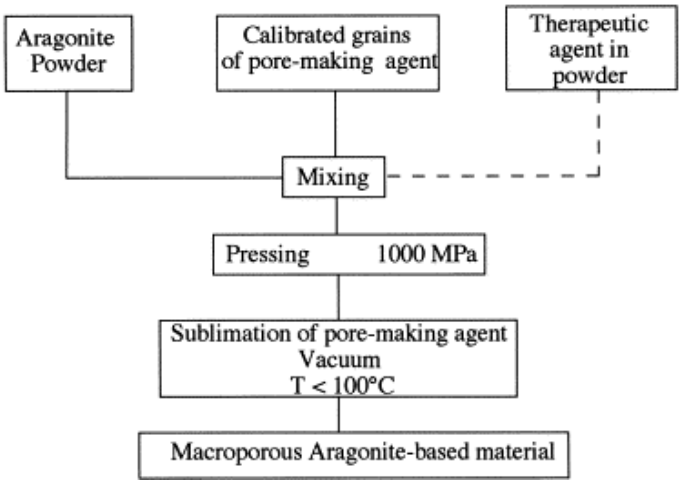

Figure 1-10. Steps for the fabrication of porous aragonite-based materials. Adapted from Luca A. et al.[57] Copyright 2001, with permission from Elsevier.

Ferreira C. et al.[147] used a loading method that resembles the LbL assembly approach to produce multilayer capsules (**Figure. 1-11**). It consisted in coating the $CaCO_3$ crystals with the biocide benzyldimethyldodecylammonium chloride (BDMDAC) after pre-coating the crystals with positively charged polymers PSS and polyethyleneimine (PEI). The antimicrobial activity of the assembled particles was tested against *Pseudomonas fluorescens* due to its ability to form disinfectant-resistant biofilms. The $CaCO_3$ crystals coated with BDMDAC promoted a reduction of viable counts between 81.9 and 93.3% for 6.33 and 11.75 mg/l of BDMDAC, respectively. Similar results were obtained with free BDMDAC (84.9% for 6.33 mg/l, and 91.3% for 11.75 mg/l) demonstrating that $CaCO_3$ did not affect the antibacterial activity of BDMDAC against *P. fluorescens*.

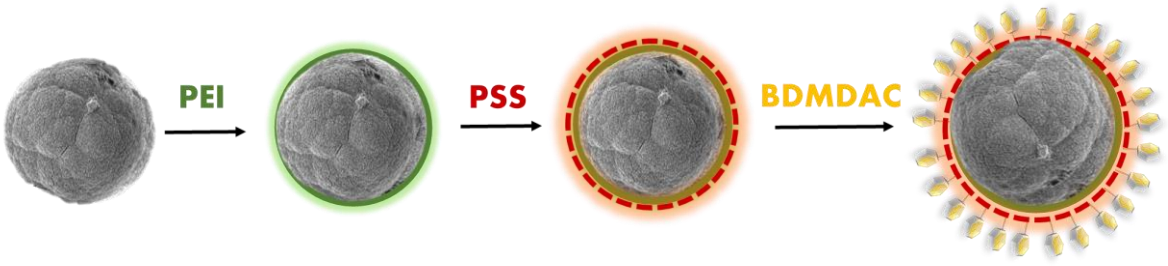

Figure. 1-11. Representation of the layer-by-layer assembly method used to produce $CaCO_3$ microparticles coated with BDMDAC. Figure redrawn based on the work of Ferreira C. et al.[147].

Sahoo P. et al. [127] fabricated and loaded AgNPs into $CaCO_3$ crystals ($CaCO_3$-AgNPs), previously synthesized by carbonation and using microalgae as bio-templates (**Figure 1-12**). The synthesized $CaCO_3$-AgNPs particles were then mixed with paints and tested

against *Escherichia coli*, *Psychrobacter alimentarius*, and *Staphylococcus equorum* using the zone of inhibition test. The results demonstrated that while the unmodified paint did not present any antimicrobial activity, the paint mixed with $CaCO_3$-AgNPs did.

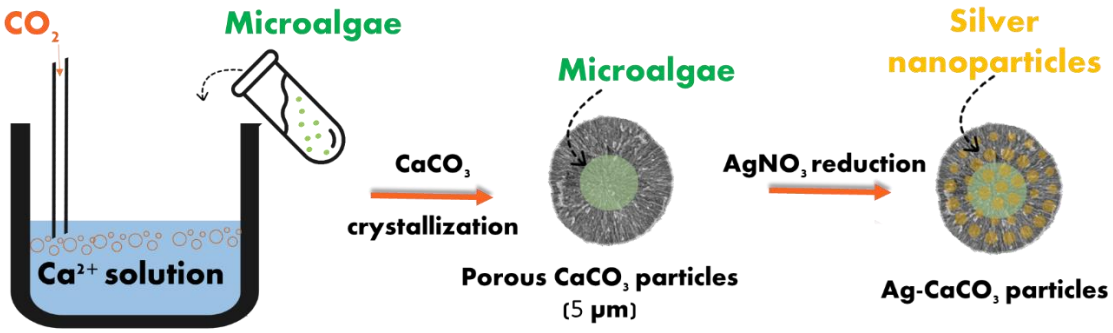

Figure 1-12. Synthesis steps of porous $CaCO_3$ microsphere by carbonation in the presence of microalgae. Silver nanoparticles were synthesized on the porous microparticles by reducing $[Ag(NH_3)]^+$ with D-maltose. Figure redrawn based on the work of Sahoo P. et al.[127].

Padmanabhuni R. and co-workers[144] reported a particular loading approach by combining adsorption with *in situ* synthesis. The research group coated $CaCO_3$ microcrystals with 4,4-dimethylhydantoin undecanoic acid (DMH- UA) and then treated the particles with diluted bleach for the synthesis of the antimicrobial agent 3-chloro-4,4-dimethylhydantoin undecanoic acid (Cl-DMH-UA) which presented antibacterial activity.

All the works discussed in this section demonstrate the versatility of the $CaCO_3$ loading routes, and that different approaches can be applied.

3.6.3. $CaCO_3$ vectors properties

$CaCO_3$ crystals can be presented as three different anhydrous polymorphs (calcite, vaterite and aragonite) and their size can be tuned by playing with the synthesis variable. The works reported in **Table 1-1 to Table 1-4** show that the crystals loaded with antimicrobials present different characteristic due to $CaCO_3$ sensitivity to the synthesis conditions such as the type of additive, pH, temperature, reagents ratios and concentrations. $CaCO_3$ crystals loaded with antimicrobials presented spherical, rhombohedral, needle-like, chain-like, and scalenohedral morphologies, with the spherical shape being the most frequently reported. The three types of polymorphs were used as carriers with some articles reporting both vaterite and calcite polymorphs.

The synthesis and loading conditions, including their duration, are critical factors that influence the type of polymorph produced. The long synthesis and loading times reported in some of the works presented might explain, in some cases, the predominance of calcite

and calcite/vaterite mixtures over pure vaterite crystals, as bare vaterite and aragonite crystals recrystallize into calcite within hours *via* the dissolution and recrystallization pathways[149,150].**Table 1-1 to 1-4** show that the size of $CaCO_3$ crystals loaded with antimicrobial agents ranged between ca 14 nm and 10 µm. Vector size is an important parameter that can affect the pharmacokinetics of the whole system including the carrier distribution, extravasation/diffusion, endocytosis, flow properties, and clearance[151]. Therefore, the size of the crystals should be controlled based on their application especially if developed for human or animal use. Microparticles for subcutaneous or intramuscular administration should present diameters up to 50 µm[152], nonetheless, for intravenous administration the particles should have sizes between 30 to 300 nm as particles smaller than 10 nm are rapidly excreted by the kidneys and particles larger than 300 nm can promote thrombosis and be rapidly eliminated[153]. For pulmonary drug administration, the carriers optimum size ranges between 1 and 5 µm[151]. Smaller delivery systems present cytotoxic effects and are easily exhaled without promoting any therapeutic action. On the other side, particles with diameters larger than 5 µm are removed by the mucociliary clearance mechanism, not fulfilling their action[151]. The easy adjustment of $CaCO_3$ crystals size by simply changing production parameters like reagents concentration, stirring speed and time, makes these crystals attractive as dynamic drug delivery systems for different targets and routes of administration.

Islan G. and co-workers[130,131] published two works where $CaCO_3$ crystals with the optimal size for pulmonary delivery were developed. The hybrid vaterite microparticles, with sizes between 3 and 5 µm, were also composed of sodium alginate (120 kDa) and/or high methoxyl pectin (70-75% esterification degree)[130,131]. A summary of the synthesis conditions and particle characteristic are present in **Table 1-3.** After synthesis, the crystals were treated with alginate lyase (AL) for alginate cleavage (**Figure 1-13**) resulting in particles with a much higher surface area (71.6 to 74.9 m^2/g) than the bare $CaCO_3$ (16.4 m^2/g) or untreated crystals (34.9 to 51.4 m^2/g)[130]. The developed particles were loaded with levofloxacin or levofloxacin and deoxyribonuclease (DNase) and tested against *Pseudomonas Aeruginosa* (ATCC 15442). The results demonstrated that the microparticles treated with AL presented a potent bacterial activity resultant from the particles increased surface area and consequent higher levofloxacin content. Further *in vivo* experiments were carried out in mice to study the distribution and preclinical pharmacokinetics of the particles administrated in the lungs *via* nebulization and dry powder inhalation. The results

showed that the particles presented a good penetration, resulting in higher levels of levofloxacin in comparison with the administration of the free drug form[131].

The tuneable properties of $CaCO_3$ crystals demonstrate their versatility to deliver drugs into different targets and the possibility to finely adjust the pharmacokinetic and release mechanism.

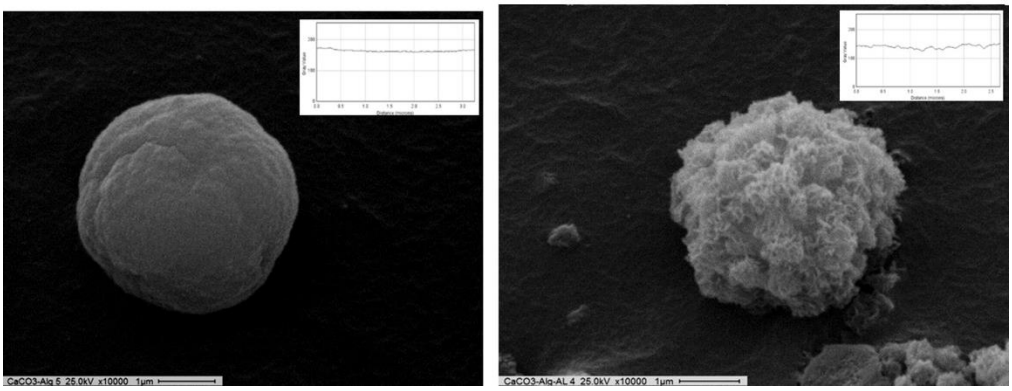

Figure 1-13. SEM images of $CaCO_3$-sodium alginate microparticles before (left) and after (right) being treated with alginate lyase. Figure adapted from Islan C. et al.[130]. The plot profile of the microparticles surface is shown in the top right corner of the images. Copyright 2015, with permission from Elsevier.

3.6.4. Release of antimicrobials

The antimicrobials currently used for the treatment of infectious diseases present some problems including short half-life, limited stability and solubility. Moreover, the therapeutic range of some drugs is narrow, as high concentrations can be toxic whereas low concentrations can promote the development of antimicrobial resistance[154,155]. Drug delivery systems can improve the pharmacokinetics of antimicrobial drugs by protecting and controlling their release and ultimately decreasing the dosage frequency, side effects and improving the therapeutic effect.

Drug delivery systems release the cargo through diffusion and/or a response to an intrinsic stimuli like pH, temperature, redox conditions or the presence of specific enzymes. An external stimuli like magnetic field, heat, light and ultrasound can also be applied to trigger the cargo release[156].

$CaCO_3$ carriers can release the cargo *via* three ways: diffusion, dissolution and recrystallization of the metastable polymorphs (vaterite and aragonite) to the more stable form, i.e., calcite. The release mechanisms can occur concomitantly, although the carrier and cargo properties and interactions, allied with the medium conditions (pH, chemical composition and temperature) will define the primary release mechanism.

pH drastically affects the solubility of $CaCO_3$. At low pH values $CaCO_3$ crystals dissolve and release the cargo, as CO_3^{2-} reacts with free protons forming HCO_3^-. pH has been used

as a trigger for $CaCO_3$ cargo release in acidic tumour microenvironments and inflammation sites[97,141,157].

Bacterial infection sites usually present low pH due to the increased contents of organic acids resultant from the anaerobic fermentation carried out by some bacteria and the host immune system response[158–160]. Together, the bacterial metabolism and the immune response can decrease the pH up to 5.5[159]. Some of the works reporting the use of $CaCO_3$ crystals as antimicrobial carriers uses the pH sensitivity to trigger the drug release.

Min K. and co-workers[141] synthesized $CaCO_3$ nanoparticles loaded with doxycycline hyclate (DOXY) by co-precipitation using PEG-PA co-polymer as a mineralization template (**Figure 1-14**). The goal was to synthesize pH-sensitive nanoparticles selective to the acidic microenvironment of bacterial biofilms. The drug release was tested at pH 7.4, 6.5, 5.5 and 4.0 resulting in ca. 20, 60, 90 and 100%, respectively, of free drug after 24h (**Figure 1-16**). The results demonstrated a pH-dependent release behaviour of the carrier, with the acidic pH triggering the release of DOXY due to the dissolution of $CaCO_3$. The nanoparticles were tested against *Prevotella intermedia* (ATCC 49046), an anaerobic gram-negative bacterium known to cause oral diseases. The experiments were done at uncontrolled (~7.4-5.3) and controlled pH (~7.4-6.5) and with free and encapsulated DOXY. The results showed that the loaded ($CaCO_3$-DOXY) and free DOXY, at uncontrolled pH and after 25 h, had similar antibacterial activity, both presenting the same bactericidal concentration (1 µg/ml). On the other hand, at controlled pH, the drug loaded into $CaCO_3$ had a bactericidal effect at 2 µg/ml, demonstrating the nanoparticles sensitivity to pH. The crystal violet staining assay was also performed to investigate the inhibitory effect of DOXY-$CaCO_3$ on *Prevotella intermedia* biofilm formation. Once again, the pH-sensitivity was demonstrated with half of the antibiotic concentration significantly decreasing the biofilm formation at lower pH.

Qian K. et al.[128], synthetized calcite crystals loaded with validamycin by the reverse microemulsion method. The main synthesis conditions and crystals properties are present in **Table 1-2**. The release behaviour and stability of the free and encapsulated validamycin forms were tested at three different pH values: 5; 7 and 9. The results showed that validamycin loaded into $CaCO_3$ crystals presented better stability and a controlled release profile. At pH 5 and 9 almost all validamycin was released after 7 and 14 days ,respectively, demonstrating a pH-dependant release behaviour.

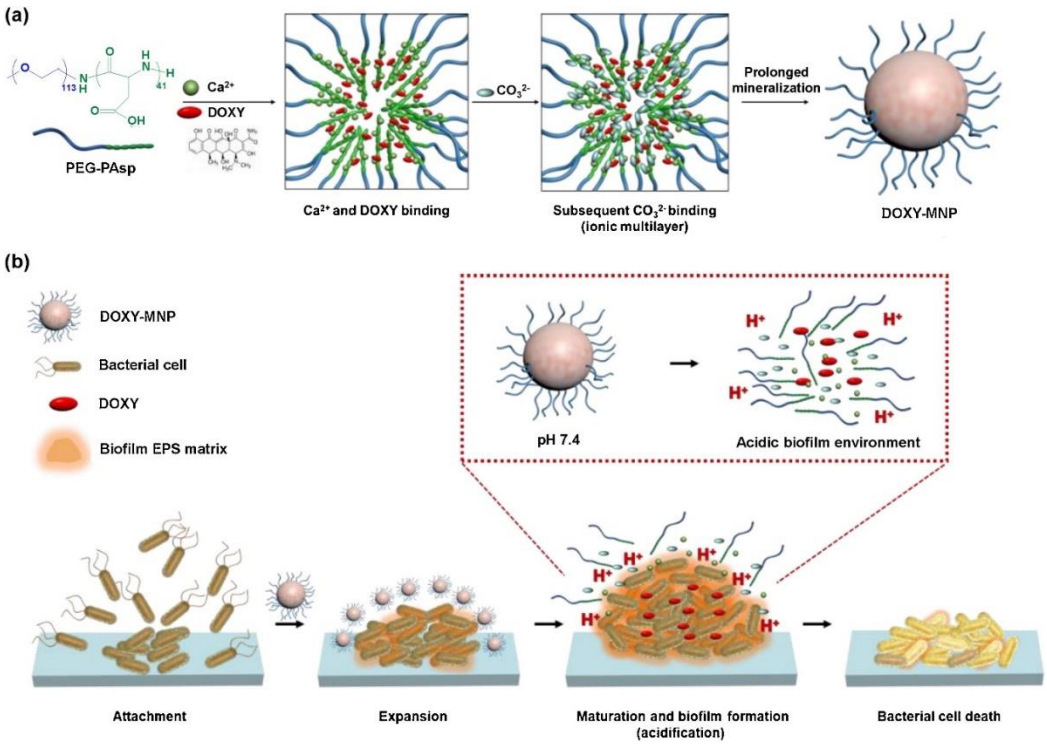

Figure 1-14. Illustration of DOXY-loaded $CaCO_3$ mineralized nanoparticles (DOXY-MNPs) synthesis pathway (a) and DOXY release mechanism from the MNPs triggered by the acidic microenvironment of the biofilm (b). EPS: exopolysaccharides. Adapted from Min K. et al.[141]. Copyright 2019, with permission from Elsevier.

Długosz M. and co-workers[138] fabricated $CaCO_3$ vectors loaded with AgNPs by co-precipitation and then used the particles for coating down feathers. The AgNPs release profile from $CaCO_3$ particles was evaluated at pH 6.8 and 5.4 over 14 days (**Figure 1-16**). The results demonstrated a slow and pH-dependant release of silver and, as expected, at pH 5.4 silver was released more quickly.

Begum G. and co-workers[37] developed $CaCO_3$ structures using poly(L-aspartic acid) sodium salt (poly(L-asp)), and poly-L-lysine hydrobromide (PLL) as templates for spherical particles formation, and tetracycline entrapment (**Figure 1-15**).

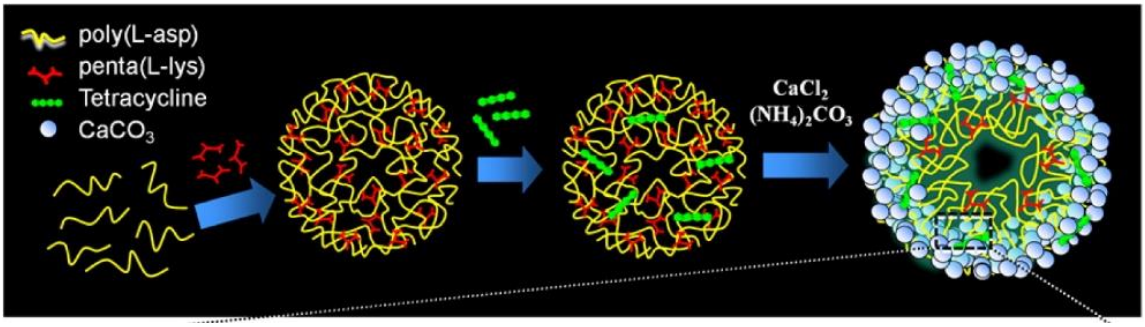

Figure 1-15. Tetracycline entrapment process and $CaCO_3$ mineralization and assembly. Adapted from Begum G. et al.[37]. Copyright 2016, with permission from American Chemical Society.

Tetracycline release behaviour was evaluated over 15 days at pH 4.5, 6.0 and 7.4 at 37°C (**Figure 1-16**). Regardless of the pH, an initial burst release of the drug was verified followed by a controlled release of almost all the loaded antibiotic within 24 h at pH 4.5 (100% released) and 360 h at pH 6 (94% released). The drug release at pH 7.4 was comparatively slower with 61% of the drug being released after 360 h. This and the other research works presented in this section demonstrate the pH-sensitivity of $CaCO_3$ carriers, with low pH values being able to trigger $CaCO_3$ dissolution and consequent drug release.

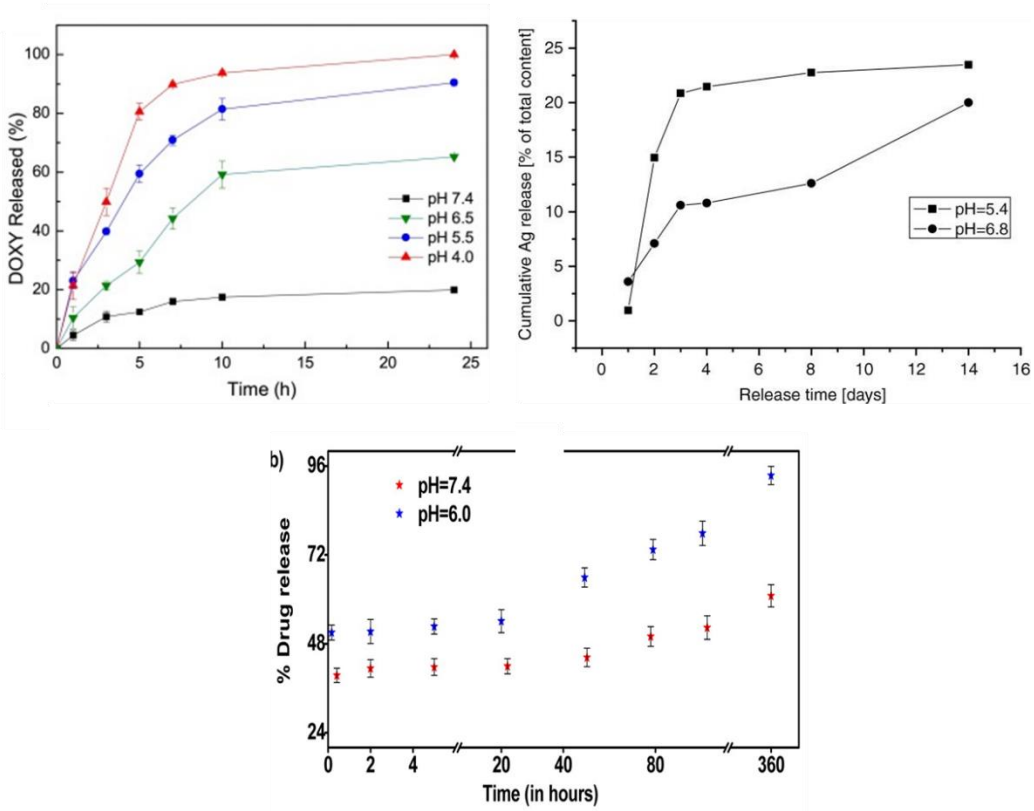

Figure 1-16. pH-responsive release of doxycycline (top left), AgNPs (top right) and tetracycline (bottom) from $CaCO_3$ carriers. Adapted from Min K. et al.[141], Długosz M. et al.[138], and Begum G. et al[37], respectively. Copyright 2019, 2012 and 2016, with permission from Elsevier, Springer Nature and American Chemical Society, respectively.

3.6.5. $CaCO_3$ vectors biocompatibility and cytotoxicity

The safety of drug delivery systems needs to be demonstrated and their biocompatibility assessment is of utmost importance.

Up to now, all *in vitro* studies suggest no cytotoxicity of bare vaterite crystals[161] even when used at high concentrations[162]. Despite the limited number of *in vivo* studies, all of them support the safety of $CaCO_3$ particles as drug carriers *via* different routes, e.g. ocular[43], intranasal[163], pulmonary[164] or transdermal[165]. Interestingly, it has been demonstrated that bolus intravenous injections of bare $CaCO_3$ crystals can alter the extracellular pH and can

be used to inhibit tumour growth *in vivo*[166]. Besides, different works have tested the biocompatibility of $CaCO_3$ carriers loaded with antimicrobials. Memar M. et al.[129] synthetized $CaCO_3$ nanoparticles loaded with gentamicin sulfate by a reverse microemulsion method and tested their biocompatibility and cytotoxicity. Biocompatibility was assessed using three assays: i) hemolysis assay on human red blood cells, ii) erythrocyte sedimentation rate assay and iii) protein interaction between loaded $CaCO_3$ and human blood plasma. The toxicity was tested by the 3-(4,5-Dimethylthiazol-2-yl)-2,5-diphenyltetrazolium bromide (MTT) viability assay on a bone marrow mesenchymal stem cell line (hBM-MSC). The reported results demonstrated that the $CaCO_3$ nanoparticles loaded with gentamicin sulfate displayed a favourable biocompatibility and low toxicity.

Isa T. et al.[143] tested the biocompatibility and cytotoxicity of aragonite particles loaded with ciprofloxacin in a Macrophages J774A.1 cell line using three different tests: i) MTT (viability test), ii) bromo-21-deoxyuridine assay (genotoxicity test) and iii) interleukin 1 beta cellular expression assessment by ribonucleic acid (RNA) extraction and reverse transcriptase-polymerase chain reaction, (immunogenicity assessment). The results demonstrated that the loaded nanoparticles presented cytocompatibility without the upregulation of the immune system response.

The *in vivo* biocompatibility, resorption and bone ingrowth of aragonite microparticles was evaluated by Lucas A. et al.[57]. The results demonstrated an excellent biocompatibility, resorption and osteoconduction, with the porosity degree largely affecting the last two properties. Overall, the results demonstrated the enormous potential of this type of material as a resorbable bone substitute and its good biocompatibility.

3.6.6. Antimicrobial performance

The key goals when using delivery systems for antimicrobial drugs are to protect the cargo from degradation, decrease the toxicity and promote a controlled release while assuring a therapeutic concentration at the site of infection.

Table 1-5 presents a comparison between the antimicrobial activity of the free and immobilized antimicrobial agents. In most of the reported studies the compounds loaded into $CaCO_3$ crystals presented similar or better antimicrobial activity than the free form. Several factors can alter the antimicrobial activity of the agents loaded into $CaCO_3$ particles such as the size and morphology of the crystals, presence of additives, affinity between the $CaCO_3$ and the antimicrobials, type of microorganism, microenvironment conditions (pH, temperature, composition and ionic strength) and even the type of antimicrobial assay used.

Apalangya V. et al.[145] produced $CaCO_3$ particles with embedded AgNPs and tested the free and loaded AgNPs against *Escherichia coli* (ATCC 11775) by a modified Kirby-Bauer disc diffusion assay. The results indicated a superior antibacterial activity of the AgNPs loaded into $CaCO_3$ particles. The authors explained this effect by a better dispersion and interaction of the particles with *E. coli* improved by the hydrophilic groups of the eggshell proteins present in the vectors. Isa T. et al.[143] also reported better antimicrobial activity of ciprofloxacin loaded into aragonite against *Salmonella Typhimurium* (ATCC 14028). The authors proposed that the higher antibacterial activity resulted from a better diffusion of the nanoparticles through the bacteria. Tessarolo L. et al.[140] published one of the few works where an antiparasitic drug, benznidazole (BZN), is encapsulated into $CaCO_3$ crystals (BZN-$CaCO_3$). The encapsulated and free drug were tested against *Trypanosoma cruzi* strain Y, a parasite responsible for the Chagas disease. The results demonstrated a higher potency of BZN-$CaCO_3$ particles against the three forms of *Trypanosoma cruzi* (epimastigote, trypomastigote and amastigote). The authors proposed that the better activity of BZN-$CaCO_3$ particles resulted from an increased cell permeability when compared with the free BZN form. Pan X et al.[126] produced calcite nanoparticles loaded with gentamicin sulfate and tested the antibacterial activity of bare calcite, free and encapsulated gentamicin against *Bacillus subtillis*. The results demonstrated a synergistic effect between $CaCO_3$ and gentamicin sulfate. The authors propose that the drug delivery system increased the damage of the bacterial cells wall and enhanced the permeability of the cell membranes. The synergistic effect was not reported by Dizaj S. et al. [19] and Memar et al.[129] who also studied the encapsulation of gentamicin in $CaCO_3$ particles and verified that the bare antibiotic presented similar and better antibacterial properties, respectively. The different results can be explained by the different properties of the carriers (size, morphology, porosity), experimental conditions and bacterium strain.

Min K. et al. [141] and Padmanabhuni R. et al.[144] also reported inferior antibacterial activity of the antimicrobial agents loaded into $CaCO_3$ particles at some of the experimental conditions studied. In the case of Min K. et al[141] the lower bactericidal activity of the encapsulated doxycycline hyclate was verified at a higher pH value (7.4-6.5) but not at lower pH (7.4-5.3) as discussed in **Section 3.6.4.**. Regarding the work of Padmanabhuni R. et al.[144], the inferior antibacterial activity was related with the limited mobility of the antimicrobial agent in the $CaCO_3$ particles, with free Cl-DMH-UA presenting better results due to higher mobility. Nonetheless, when free and encapsulated Cl-DMH-UA were

incorporated into cellulose acetate films as antimicrobial fillers, both presented similar activity against *S. aureus* regardless of the concentration, and against *E. coli* at 5% w/w. Moreover, both systems presented a similar biofilm growth inhibition.

Overall, $CaCO_3$ crystals have a great potential as vectors for the delivery of antimicrobial agents as they can protect and promote a controlled release without affecting the antimicrobial activity.

Table 1-5. Summary of the antimicrobial activity of free and $CaCO_3$-encapsulated antimicrobial agents. AA: Antimicrobial Agent; SA: Similar Antimicrobial Activity; (-): Inferior Antimicrobial Activity; (+) Superior Antimicrobial Activity; GI: Growth Inhibition; MIC: Minimum Inhibitory Concentration; MBC: Minimum Biofilm Inhibitory Concentration; ZI: Zone of Inhibition; IC_{50}: Inhibitory Concentration that inhibits 50% of growth; LC_{50}: Lethal Concentration that causes the death of 50% of the microorganisms; BC: Bactericidal Concentration; SR: Survival Ratio; CA: Cellulose Acetate (free and encapsulated forms used as cellulose acetate additive); Cl-DMH-UA: 3-chloro-4,4-dimethylhydantoin undecanoic acid; BGI: Biofilm Growth Inhibition. [a] Cl-DMH-UA weight percentage on the total weight of the cellulose acetate film.

Ref.	Microorganism	Antimicrobial Agent (AA)	Antimicrobial activity (Free-AA)	Antimicrobial activity ($CaCO_3$-AA)	Result Type
Pan X. et al. [126]	*B. subtillis*	Gentamicin Sulfate	-	+	GI
Qian K. et al. [128]	*Rhizoctonia solani*	Validamycin	+ (2^{nd} day) - (7^{th} day)	- (2^{nd} day) + (7^{th} day)	GI
Dizaj S. et al. [19]	*S. aureus*	Ciprofloxacin HCl	SA	SA	MIC
Dizaj S. et al. [22]	*S. aureus*	Gentamicin Sulfate	SA	SA	MIC
Memar Y. et al.[129]	*P. Aeruginosa*	Gentamicin Sulfate	+	-	MIC
			SA	SA	MBC
Begum G. et al. [37]	*B. subtilis*, *S. aureus*, *S. epidermidis*, *E. coli*, *K. pneumoniae*, and *P. aeruginosa*	Tetracycline	SA	SA	MIC and ZI
Tessarolo L. et al. [140]	*Trypanosoma cruzi* strain Y	Benznidazole	- (24h) SA (72h)	+ (24h) SA (72h)	IC_{50}
			-	+	LC_{50}
Min K. et al. [141]	*Prevotella intermedia*	Doxycycline hyclate	SA	SA	BC (pH 7.4-5.32)
			+	-	BC (pH 7.4-6.5)
Isa T. et al. [143]	*Salmonella Typhimurium*	Ciprofloxacin HCl	-	+	ZI
Padmanabhuni R. et al. [144]	*S. aureus* and *E. coli*	Cl-DMH-UA	+	-	SR
			SA (*S. aureus*) + (*E. coli*:1-3 wt%[a]) SA (*E. coli*: 5wt %[a])	SA (*S. aureus*) - (*E. coli*: 1-3 wt%[a]) SA (*E. coli*: 5wt %[a])	SR (CA)
			SA	SA	BGI
Apalangya V. et al. [145]	*E. coli*	AgNPs (5-20nm)	-	+	ZI
Ferreira C. et al. [147]	*Pseudomonas fluorescens*	Benzyldimethyldodecylammonium chloride	SA	SA	SR

3.7. Concluding remarks

$CaCO_3$ crystals present an enormous potential as carriers for antimicrobial agents. By adjusting different affecters during $CaCO_3$ synthesis such as pH, temperature, reagents ratios and additives, crystals with different sizes, morphologies, surface area and physical-chemical properties can be produced. The capacity to host and protect high contents of antimicrobials and to deliver them in a controlled way, and in some cases, in a stimuli-response fashion proves the versatility of the crystals as modern and advanced drug delivery systems. Several works have explored the use of $CaCO_3$ as carriers for the delivery

of antimicrobial agents with studies demonstrating a pH-dependent controlled release without affecting the antimicrobial activity and, in some cases, even improving it. The use of $CaCO_3$ as carriers for multiple drugs opens new avenues for combating drug resistance, which is nowadays one of the major obstacles for a successful treatment. The different approaches reported so far for loading antimicrobials into $CaCO_3$ particles also demonstrate their high versatility, with the synthesis variations being almost endless. Moreover, the simple production methods and affordable reagents, make $CaCO_3$ crystals highly attractive when compared with carriers that require long, complex and expensive fabrication methods. The good biocompatibility results anticipate their safety in humans, a determinant factor for their introduction in the market as drug delivery systems.

Chapter 2

Silver nanoparticles synthesis and characterization

All the content presented in this chapter has been published in 2023 as a research article titled "How similar is the antibacterial activity of silver nanoparticles coated with different capping agents?" in the journal RSC Advances, Volume 13, pages 10542 to 10555.

1. Introduction

Silver nanoparticles (AgNPs) are one of the most commercialised nanomaterials due to their attractive physical-chemical and biological properties, being found in a diverse number of applications, such as antimicrobial products and electronics[7]. AgNPs can be produced through different routes: chemical, physical and biological, with the chemical route being one the most commonly used[7,167]. In the chemical reduction method, AgNPs are synthesised by reducing ionic silver with a reducing agent, like sodium borohydride or sodium citrate. The synthesis of AgNPs through this route is quick, cost-effective and simple, with the properties of the nanoparticles, including size, being adjusted with additives or by changing the reagent ratios, synthesis temperature, pH or stirring speed[168,169]. Despite the simplicity of this route, tight control is required to prevent the overgrowth of the nanoparticles. Within seconds, the nanoparticles can transform into large sub-micron particles or form nanoparticle aggregates. To help control the growth of the AgNPs, and assure long-term stability, capping agents are used. These agents are usually added during synthesis and adsorb on the surface of the nanoparticles, endowing stability *via* decreasing the surface energy and promoting repulsion forces (electrostatic, van der Waals or hydration) or steric hindrance[170]. The repulsive forces can co-exist with steric hindrance, and both can prevent the over-growth and agglomeration between adjacent particles[170,171]. Numerous capping agents are applied as stabilisers for AgNPs, with polyvinylpyrrolidone (PVP) and trisodium citrate (Citrate) being two of the most used ones, due to their good stabilisation properties and safety[172]. Dextran (Dex) and the

derivatised forms diethylaminoethyl–dextran (Dex^{DEAE}) and carboxymethyl–dextran (Dex^{CM}) have also been used as capping agents, although to a much lower extent than PVP and Citrate[173–181].

The selection of the capping agent is crucial to assure that the AgNPs do not agglomerate when exposed to destabilisers, like electrolytes, and lose their unique properties and biocidal activity. The antimicrobial activity of AgNPs is size-dependent. Smaller nanoparticles present better antibacterial activity, as they release more silver ions (Ag^+), and more easily interact and penetrate the cell membranes[182,183]. The toxicity mechanisms of AgNPs are not fully understood but it is believed that the release of Ag^+ from the nanoparticles is crucial to kill the bacteria. Ag^+ can disrupt the membrane, and once uptaken by the cell, interact with disulfide or sulfhydryl groups of intracellular enzymes leading to the disruption of metabolic processes like adenosine triphosphate release, and increasing the production of reactive oxygen species[167,182]. Alongside that, Ag^+ can interact with the DNA, affecting DNA replication and cell propagation, and denature the cytoplasmic ribosomal components hindering protein synthesis[167,182]. It is believed that the AgNPs also play a role in killing the bacteria through denaturation of the membrane and modification of the cell wall structure, which can lead to leakage of cellular contents and cell death[167,182]. Nonetheless, Xiu et al. [183], have shown that the antibacterial activity of AgNPs against *Escherichia coli* mainly relies on Ag^+ release, highlighting the role of the ions over the particles in eradicating the bacteria.

Based on the antibacterial mechanisms of the AgNPs, the capping agents play an important role in assuring and potentiating the antibacterial activity, mainly by preventing the formation of clusters, but also by endowing new characteristics that can change the interactions with the bacteria and release rate of Ag^+.

In this work, AgNPs were synthesised and stabilised with five different capping agents: Citrate, PVP, Dex, Dex^{DEAE} and Dex^{CM}. Bare nanoparticles were also synthesised for comparison. The produced AgNPs were characterised through various techniques, to investigate the effect of the capping agents on the physicochemical properties of the AgNPs, as well as on the stability in different media. The antibacterial activity of the AgNPs was assessed against *E. coli*, methicillin-resistant *Staphylococcus aureus* (MRSA) and *Pseudomonas aeruginosa* (*P. aeruginosa*) to study how the capping agents influence the antibacterial activity.

Overall, this work presents a comparative study where the role of the capping agents, their properties and sensitivity to external factors are investigated in an attempt to highlight the importance of a holistic approach in the design of stable AgNPs.

2. Materials and methods

2.1. Materials

Silver nitrate ($AgNO_3$, extra pure crystals, ≥99%), sodium borohydride ($NaBH_4$, ≥99% pure), polyvinylpyrrolidone 40 kDa (PVP), trisodium citrate dihydrate (Citrate, $C_6H_5Na_3O_7 \cdot 2H_2O$, ≥99% pure), fluorescein isothiocyanate–dextran 40 kDa (Dex), fluorescein isothiocyanate–diethylaminoethyl–dextran 40 kDa (Dex^{DEAE}), fluorescein isothiocyanate–carboxymethyl–dextran 40 kDa (Dex^{CM}), dehydrated Mueller Hinton broth Sigma 70192 (MHB-S), Mueller Hinton agar Sigma 70191 (MHA-S), phosphate buffered saline (PBS) tablets, Triton™ X-100, and TraceCERT® 1 ppm Silver ICP-MS standard in 2% nitric acid, were obtained from Sigma-Aldrich (Steinheim, Germany). Calcium dichloride dihydrate ($CaCl_2.2H_2O$, ≥99%), disodium carbonate (Na_2CO_3, ≥99.5%), tris buffer saline 10X solution (TBS), 99% ethanol, 70% nitric acid (HNO_3, analytical grade), 37% hydrochloric acid (HCl, analytical grade), dehydrated Mueller Hinton Broth Oxoid CM0405B (MHB-O), dehydrated Nutrient Broth Oxoid CM0001B (NB), dehydrated Lennox Broth Base 12780-052 Thermo Fisher Scientific (LB) and crystal violet ($C_{25}H_{30}N_3Cl$, pure), were obtained from Fisher Scientific (Loughborough, United Kingdom).

2.2. Methods

2.2.1. Synthesis of silver nanoparticles

AgNPs were synthesised *via* a modified chemical reduction methodology adapted from Nau E.et al.[9]. Briefly, freshly prepared $NaBH_4$ (40 mL, 0.01 M) in ultrapure, type I water was added dropwise (*ca*. 2 drops/sec) using a burette to $AgNO_3$ (2 mL, 0.1 M) at room temperature in a 1 L flat glass media bottle under constant stirring (850 rpm) using a magnetic stirrer plate and a PTFE-coated magnetic stir bar. Before adding the $NaBH_4$ solution, the $AgNO_3$ solution was mixed with ultrapure, type I water (158 mL) and the capping agent (trisodium citrate, PVP, Dex, Dex^{DEAE} or Dex^{CM}). The final capping agent concentration in 200 mL final volume was 0.20, 0.38 and 0.06 $mg.ml^{-1}$ for trisodium citrate, PVP and all the dextrans, respectively. The final capping agent/$AgNO_3$ ratios (w/w) were

11.8, 22.1 and 3.7 for trisodium citrate, PVP and all the dextrans, respectively. The trisodium citrate concentration was chosen based on the work of Izak-Nau, E. et al.[9]. The PVP and Dex^{DEAE} concentrations were selected based on preliminary studies, where AgNPs were synthesised with different concentrations of PVP (0.09 to 1.50 $mg.ml^{-1}$) and Dex^{DEAE} (0.02-0.25 $mg.ml^{-1}$) and then compared. After the synthesis, AgNPs were filtered and then washed with ultrapure, type I water by centrifugation (5000 *g* for 30 min) using Pierce™ Protein Concentrators PES with a 50K molecular weight cut-off membrane (Thermo Fisher Scientific, Germany). The particles were then resuspended in ultrapure, type I water, and the silver concentration was determined by inductively coupled plasma mass spectrometry (ICP-MS) as described below.

2.2.2. Silver nanoparticles characterisation

Ultraviolet-visible (UV-vis) spectroscopy: AgNPs present size-dependent optical properties, making UV-vis analysis a simple and highly sensitive method to evaluate AgNPs formation, size, and stability[184,185].Before analysis , AgNPs were diluted with ultrapure, type I water to an absorbance below one, and then the UV-vis extinction spectra were recorded in a NanoDrop One spectrophotometer (Thermo Scientific, USA) between 190 and 850 nm. The UV-vis spectra were normalised between 300 and 600 nm for better comparison between samples.

Transmission electron microscopy (TEM): AgNPs stock colloidal dispersions were diluted with ultrapure, type I water, and then 7 µl were poured on top of a holey carbon film copper grid (Agar Scientific Ltd, UK) and the excess removed with filter paper. The grid was left drying overnight before analysis on a JEM-2100 Plus transmission electron microscope (Jeol, Japan) using an operating voltage of 200 kV. The diameter of 300 particles was measured to estimate the particle size and distribution using the ImageJ software (NIH, USA).

Dynamic light scattering (DLS) analysis: DLS analysis was performed to determine the hydrodynamic size and zeta-potential of the AgNPs in ultrapure, type I water (pH 5.28) using a Zetasizer Nano ZS instrument (Malvern, UK). The hydrodynamic size data corresponds to an average of 30 runs, and the zeta potential to the calculated mean value to an average of 50 runs.

Fourier transform infrared (FTIR) spectroscopy: The AgNPs were analysed by FTIR spectroscopy (Spectrum Two FTIR spectrometer, PerkinElmer, Uberlingen, Germany) after being washed. The colloids of concentrated AgNPs were poured on top of the ATR crystal and then dried with a Dexter® heat air gun before analysis until no water peaks were detectable. 32 scans were run for each sample between 500 and 4000 cm^{-1}, with a resolution of 4 cm^{-1}. The ATR (attenuated total reflectance) technique was used in all the measurements. The spectra were normalised for better comparison between samples.

X-ray diffraction (XRD): The crystalline structure of the AgNPs was analysed in a SmartLab SE X-Ray diffraction system from Rigaku Co. Ltd. (Tokyo, Japan) with a Kβ filter for cupper ($\lambda = 0.1392$ nm). Layers of concentrated AgNPs colloids were dried with a Dexter® heat air gun on a zero-background sample holder and then scanned with a $\theta/2\theta$ scan axis. The scan range varied between 20° and 80°, and the scan mode and speed were 1D and 5°/min, respectively.

Thermogravimetric analysis (TGA): Approximately 3 mg of dried AgNPs were heated in an open porcelain crucible from 30 to 850°C, under a nitrogen atmosphere at a heating rate of 10°C/min on a thermogravimetric analyser (TGA 4000, (PerkinElmer). The capping agents were also analysed at the same conditions for comparison.

Determination of silver concentration by ICP-MS: AgNPs colloidal dispersions in ultrapure, type I water were digested with a fresh mixture of one part of 70% HNO_3 and three parts of 37% HCl (v/v) to ensure the formation of soluble silver chloride complexes [$AgCl_x^{1-x}$] instead of insoluble AgCl salts. All the digested samples presented a concentration of silver lower than 10 $\mu g.ml^{-1}$ and an HCl content higher than 10% (v/v). The samples were digested at room temperature in the dark for over 1 hour and then 7 to 14 µl of the digested samples were diluted with 1 ml of 2% HNO_3 before analysis. A calibration curve was obtained for each independent ICP analysis with silver concentrations ranging between 3 $\mu g\ L^{-1}$ to 800 $\mu g\ L^{-1}$. The coefficient of determination of the standards calibration curve was always superior to 0.99.

2.2.3. Stability of the AgNPs

The stability of all the synthesised AgNPs was analysed after being stored at 4°C for 9 months. Fresh and 9-months old AgNPs were analysed by UV-vis spectroscopy and pictures taken to assess the sedimentation of AgNPs. The stability of the different AgNPs

was also analysed in PBS, and different types of broths used for bacterial growth/maintenance (MHB-S, MHB-O, LB and NB). Briefly, 25 µl of pre-washed AgNPs were mixed with 250 µl of ultrapure, type I water (control), PBS or broth, and then analysed by UV-vis spectroscopy, before and after incubation at 37°C for approx. 20 hours. The AgNPs were also analysed under the microscope (Life Technologies EVOS FL, Invitrogen, USA) to detect the formation of micro-size clusters. Ultrapure, type I water, PBS, MHB-S, MHB-O, LB and NB without AgNPs were used as the respective blanks. The UV-vis spectra were normalised between 300 and 600 nm, and zero was defined as $y \leq 0.043$ to eliminate the effect of background noise.

2.2.4. Assessment of the antibacterial activity

The antibacterial activity of the AgNPs was determined against *Escherichia coli* O157:H7 (*E. coli*), methicillin-resistant *Staphylococcus aureus* (MRSA) and *Pseudomonas aeruginosa* PA01 (*P. aeruginosa*). The *E. coli*, MRSA and *P. aeruginosa* isolates were obtained from the American Type Culture Collection (ATCC 43888), National Collection of Type Cultures (NCTC 12493) and Nottingham Trent University Cultures Collection (NTUCC 876), respectively.

2.2.4.1. Inoculum preparation

The bacterial isolates were streaked onto MHA-S plates and incubated at 37°C for 18 to 20 hours. For each isolate, three to four isolated colonies of the same morphological appearance were transferred into a tube containing 5 ml of MHB-S and then incubated for 18-20 hours in a shaker at 35°C and 225 rpm. Just before exposing the bacteria to the AgNPs, overnight cultures were diluted to 1×10^6 CFU.ml^{-1}.

2.2.4.2. Minimum inhibitory concentration (MIC) and minimum bactericidal concentration (MBC)

The MIC was determined using the broth microdilution method adapted from Wiegand I. *et al*.[186], with some modifications. Briefly, the different AgNPs were serially diluted in a 96-wells microplate with MHB-S. Then 50 µl of *E. coli*, MRSA or *P. aeruginosa*, previously diluted with MHB-S to 1×10^6 CFU.ml^{-1}, were added to each well. The concentrations of the AgNPs ranged between 480 and 0.47 µg.ml^{-1}. The final bacterial inoculum density was approximately 5×10^5 CFU.ml^{-1}. Bacteria in MHB-S at the same density were used as growth controls (positive control) and the medium with and without

AgNPs as sterility controls (negative control). Replicates of the controls were included in all the plates. The microplates were incubated at 37°C for 18 to 20 hours and then read visually by observing the presence or absence of turbidity. The MIC was defined as the lowest concentration that inhibited the visible growth of the bacteria in all the replicate wells. The MBC was determined after reading the MIC and consisted of plating 10 µl of the wells without visible turbidity onto MHA-S plates. The agar plates were incubated at 37°C for 24 hours and then read visually. The lowest dilution without macroscopic bacterial growth was defined as the MBC. The experiment was repeated three times, with three replicates per repetition.

2.2.4.3. Growth curves

Bacterial isolates were grown for 18-20 hours and then diluted to 1×10^6 CFU.ml^{-1} with MHB-S. After that, 50 µl of the diluted bacterial isolates were added to the wells of a 96-well microplate containing 50 µl of AgNPs in MHB-S. The concentration of the AgNPs against *E. coli* and MRSA was 30 µg.ml^{-1} and against *P. aeruginosa* 7.5 µg.ml^{-1}. The bacterial growth was analysed in a microplate reader (Cytation 3, BioTek, Vermont, USA) over 21 h. The microplate was kept at 37°C under mainly static conditions, and the optical density was measured every 20 min at 600 nm. Before each measurement, the microplate was gently stirred in orbital movements for 20 sec. The experiment was carried out in triplicate, and untreated samples were used as growth controls. Sterility controls composed of the media and AgNPs without bacteria were also included in the experiment and used as blanks. To prevent condensation on the lid and the "edge effect" during incubation, the outer wells of the microplate were filled with PBS, and the lid was treated with 0.05% Triton X-100 in 20% ethanol as described by Brewster J.[187] with some minor modifications. Briefly, 5 mL of 0.05% Triton X-100 in 20% ethanol, pre-filtered with a 0.2 µm syringe-tip filter (Fisherbrand™, Loughborough, United Kingdom), was poured on the microplate lid and tilted several times to ensure even coverage of the inner surface. The lid was then left for about 15 min inside a biosafety cabinet to prevent any contamination. After that, the Triton X-100 in 20% ethanol was poured off, and the lid was shaken to remove most of the liquid. Finally, the lid was leaned against a vertical surface inside the biosafety cabinet and allowed to air-dry.

2.2.4.4. Minimum biofilm eradication concentration (MBEC)

The MBEC determination method was adapted from Ivanova A. et al.[188] with some modifications. Briefly, bacterial isolates of MRSA and *P. aeruginosa* were grown for 18-20 hours and then diluted to 1×10^6 CFU.ml^{-1} with MHB-S. Then 100 µl of bacteria were added to the wells of a 96-well microplate. The plates were then incubated for 24 hours at 37°C under static conditions to promote biofilm formation. After incubation, the planktonic cells were removed by gently washing the wells two times with 150 µl of PBS. Between washes, the microplate was shaken at 100 rpm for 5 min. After washing, 120 µl of AgNPs at concentrations between 3.5 and 960 µg.ml^{-1}, previously diluted with MHB-S, were added to the wells and then the microplate was incubated for 24 hours at 37°C under static conditions. After incubation, the non-adhered bacterial cells were removed by gently washing the wells two times with 150 µl of sterile PBS (between washes the microplate was shaken at 100 rpm for 5 min). After that, the biofilms were fixated by heating at 60°C for 1 hour and then stained with 150 µl crystal violet (0.1% w/v) for 1 hour at room temperature. After staining, the wells were washed three times with 150 µl of sterile PBS. Between washes, the microplate was shaken at 100 rpm for 5 min. The crystal violet was then dissolved with 200 µl per well of 30% v/v acetic acid. 100 µl of the dissolved crystal violet was then transferred into a 96-well microplate, and the absorbance read at 595 nm. The experiment was carried out in triplicate, and untreated biofilms were used as positive controls. Sterility controls of MHB-S medium were also carried out throughout the whole experiment and used as blank.

3. Results and Discussion

3.1. AgNPs characterisation

3.1.1. Effect of the capping agents on the optical properties of the AgNPs and synthesis reproducibility

The production of AgNPs via the chemical route requires the use of capping agents to prevent the growth over nanoscale dimensions and endow stability by preventing their agglomeration and formation of large clusters of nanoparticles. The capping agents stabilise the nanoparticles via adsorption on the surface, decreasing the surface energy and promoting repulsion forces and steric hindrance[170,171]. Numerous capping agents are used as stabilisers for AgNPs, including dextrans, PVP and trisodium citrate, with the last two

being the most common ones[172]. The selection of the capping agent is an important step, as it affects the properties, stability and consequently the final activity of the nanoparticles.

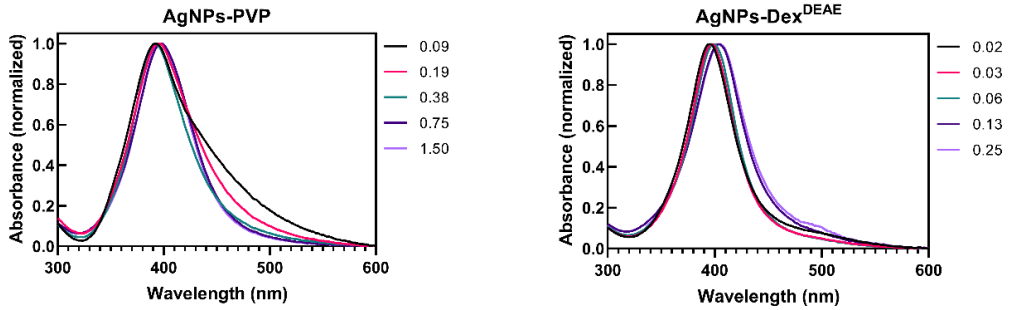

Figure 2-1. UV-vis spectra of AgNPs synthesised with different concentrations of PVP (left) and Dex^{DEAE} (right). Labels correspond to the final concentration of the capping agent in $mg.ml^{-1}$.

In this work PVP, Citrate and Dex^{DEAE} were chosen as capping agents to stabilise the AgNPs. The concentration of Citrate was defined as 0.2 mg ml^{-1} based on the work of Izak-Nau, E. et al.[9], and the final concentration of PVP and Dex^{DEAE} was selected based on preliminary studies (**Figure 2-1**), where AgNPs were synthesised with different concentrations of PVP and Dex^{DEAE} and then analysed by UV-vis spectroscopy. This method is a good option for analysing AgNPs as it is highly sensitive to their size, shape and polydispersity[189]. Spherical AgNPs with sizes around 10 nm, and with low polydispersity, tend to present a narrow peak with maximum absorbance in the 400 nm region, due to the surface plasmon resonance of the AgNPs[189]. As shown in **Figure 2-1** increasing the PVP concentration from 0.09 to 0.38 $mg.ml^{-1}$ resulted in AgNPs with lower polydispersity, as indicated by the narrower peaks. This can be explained by the increment of the surface coverage with PVP, which increased the stability of the AgNPs through more steric hindrance *via* its bulky structure and repulsive forces created by the hydrophobic carbon chains[190]. At concentrations above 0.38 $mg.ml^{-1}$ no changes were verified in the spectra, which indicates the saturation of the AgNPs with PVP. Interestingly, the AgNPs synthesised with Dex^{DEAE} required lower concentrations of Dex^{DEAE} to stabilise the AgNPs (0.02 to 0.06 $mg.ml^{-1}$), indicating good affinity between Dex^{DEAE} and the AgNPs. Based on the results presented in **Figure 2-1**, the PVP and Dex^{DEAE} concentrations were set at 0.38 and 0.06 $mg.ml^{-1}$, respectively, as at these ratios, the AgNPs presented narrow peaks with maximum absorbance around 400 nm.

Two other dextrans with the same molecular weight (40k), Dex and Dex^{CM}, were also tested as stabilising agents to further evaluate the effect of dextrans charge on the properties of the AgNPs. The concentration of Dex and Dex^{CM} was also set at 0.06 $mg.ml^{-1}$, as at this

concentration stable AgNPs with a narrow size distribution were formed. The chemical structures of all the capping agents are presented in **Figure 2-2.**

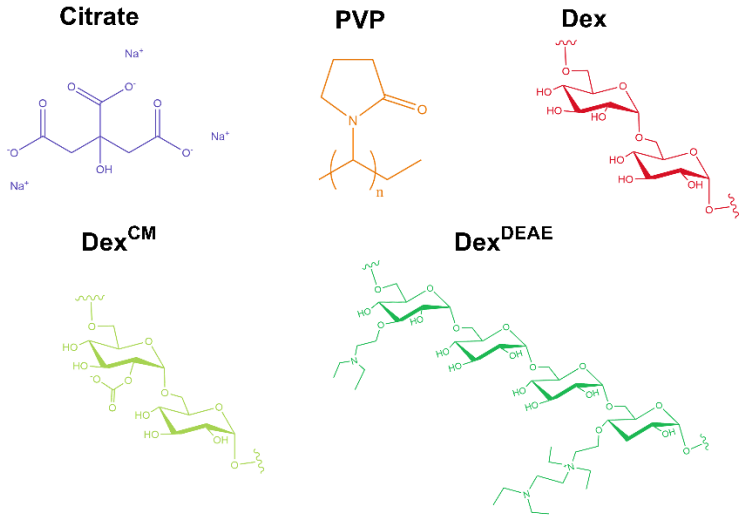

Figure 2-2. Chemical structure of the capping agents used to stabilise the AgNPs.

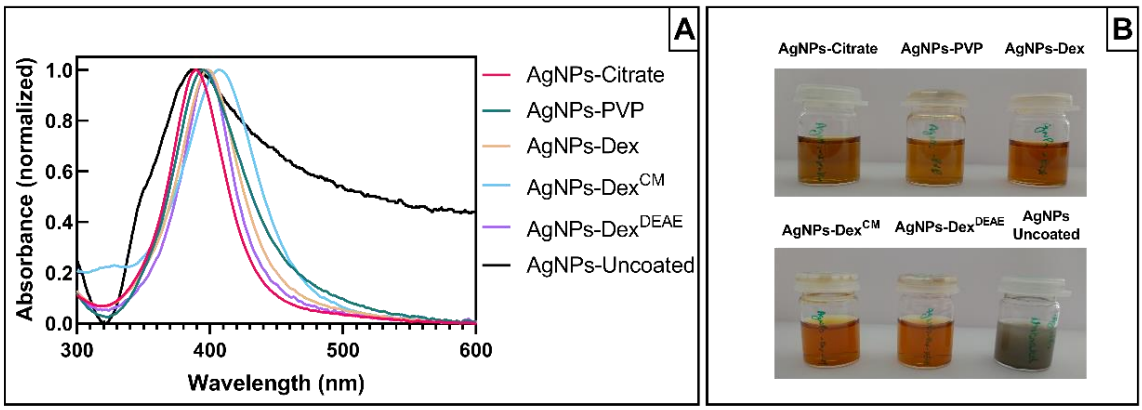

Figure 2-3. UV-vis absorbance spectra of the bare AgNPs (AgNPs-Uncoated) and the AgNPs coated with different capping agents after washing (A), and the colloidal dispersions of all AgNPs after synthesis (B).

Figure 2-3 presents the UV-vis absorbance spectra of the AgNPs synthesised without any capping agent (AgNPs-Uncoated) and with Citrate (AgNPs-Citrate), PVP (AgNPs-PVP), Dex (AgNPs-Dex), Dex^{CM} (AgNPs-Dex^{CM}), and Dex^{DEAE} (AgNPs-Dex^{DEAE}) as stabilisers. All the AgNPs presented a maximum absorbance between 385 and 406 nm (**Table 2-1**), proving the formation of AgNPs. While the AgNPs synthesised with capping agents presented narrow peaks and colloidal dispersions with a characteristic amber colour

(**Figure 2-3**, **B**), the uncoated AgNPs had a broad absorbance peak, distinctive of highly polydisperse colloids, and presented a greyish colour, an indicator of nanoparticles with bigger sizes and the formation of cluster.

Table 2-1. Maximum absorbance wavelength (λ_{max}) of the AgNPs after washing.

AgNPs	λmax (nm)
AgNPs-Citrate	389.0
AgNPs-PVP	394.5
AgNPs-Dex	398.0
AgNPs-DexCM	398.0
AgNPs-Dex^{DEAE}	406.0
AgNPs-Uncoated	388.5

To demonstrate the reproducibility of the AgNPs production between synthesis, three independent batches of AgNPs were analysed by UV-vis spectroscopy. As presented in **Figure 2-4**, the absorbance spectra between the batches of coated AgNPs were very similar, with the maximum absorbance peak around 400 nm, demonstrating the reproducibility of the synthesis method and the formation of AgNPs with sizes around 10 nm. The AgNPs synthesised without stabiliser also presented similar absorbance spectra between batches, although with some differences, showing that the synthesis reproducibility is harder to achieve.

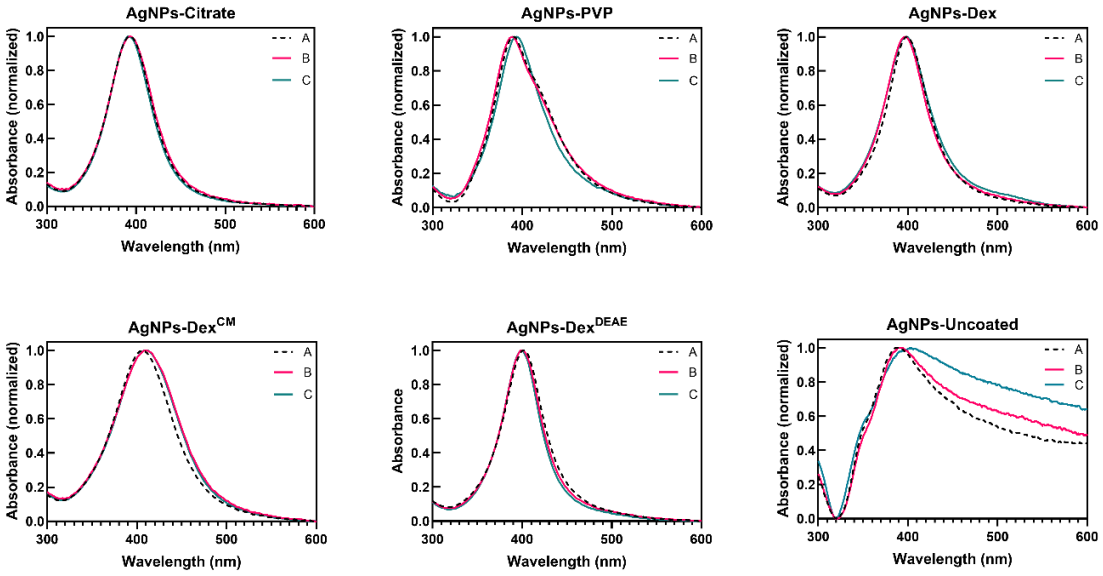

Figure 2-4. UV-vis spectra of different batches of AgNPs. The different batches are labelled with different letters (A, B or C). The batches were prepared on different days from fresh reagent solutions.

3.1.2. Size distribution

The size of the AgNPs is one of the most important characteristics as it drastically affects the antibacterial activity, with smaller nanoparticles being associated with better antimicrobial activity[182].

The size of the synthesised nanoparticles was studied by TEM and DLS. **Figure 2-6** depicts the TEM images and size distribution histograms of all the AgNPs. The AgNPs-Citrate, AgNPs-PVP, AgNPs-Dex, AgNPs-Dex^{CM}, AgNPs-Dex^{DEAE} and AgNPs-Uncoated presented the following average diameters determined by TEM: 9.7 ± 2.0; 13 ± 4.4; 8.1 ± 2.9, 7.8 ± 3.0; 9.5 ± 2.9 and 33.1 ± 32.0 nm, respectively. The data shows that all the nanoparticles coated with a stabilising agent presented an average size around 10 nm with a Gaussian-like distribution. On the other hand, the uncoated AgNPs presented larger sizes and broad distribution, as shown by the size distribution histogram and TEM images, where it is possible to see particles with diameters of 10 and 300 nm.

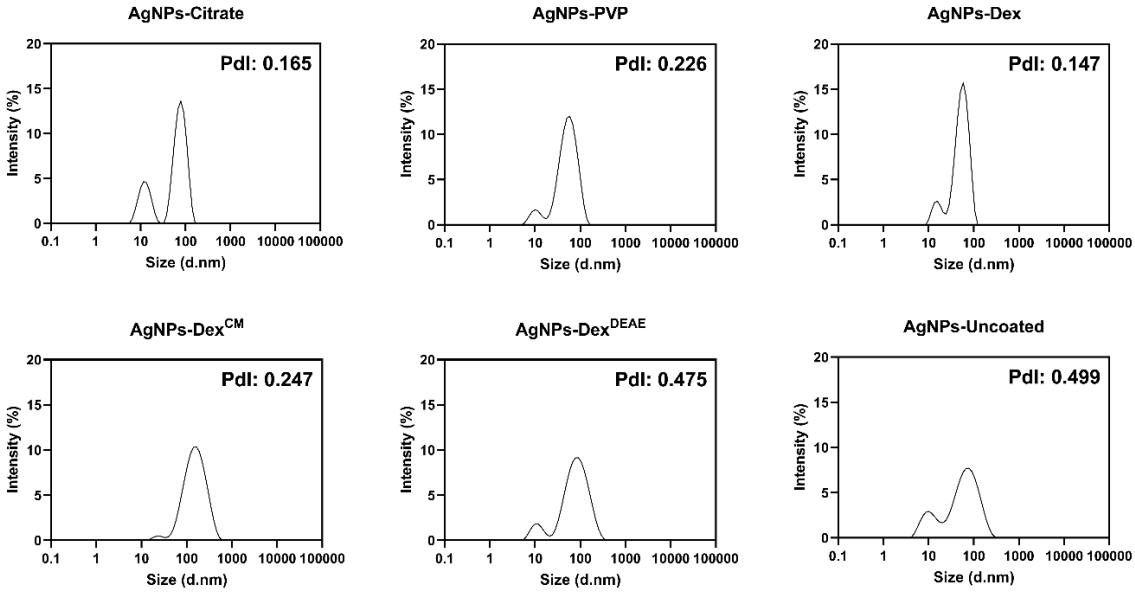

Figure 2-5. Size distribution and polydispersity index (PdI) of the AgNPs determined by DLS.

While TEM mainly gives information about the diameter of the inorganic core of metallic nanoparticles, as it is more sensitive to electron-dense regions, DLS provides information about the hydrodynamic size of the nanoparticles, which corresponds to the inorganic core, capping agent and adsorbed solvent layer[191,192]. **Figure 2-5** presents the hydrodynamic diameter of the nanoparticles measured by DLS (intensity weighted). All the AgNPs presented two size clusters, one with maximum intensity around 10 nm and the other at 70 nm, except for the AgNPs coated with Dex^{CM}, which presented maximum intensity for the first and second peaks around 22 and 140 nm, respectively. This data shows that the AgNPs hydrodynamic diameters have a bimodal distribution, with the average diameters determined by TEM coinciding with the first peak. The second peak, around 70-140 nm, can be explained by four different reasons: 1) the fact that DLS reflects the hydrodynamic diameter; 2) the AgNPs not being perfectly monodisperse; 3) the lower accuracy of DLS analysis for bimodal distributions, and 4) the distortion effect of larger nanoparticles on DLS results, as the diameter of larger nanoparticles is heavily weighted, and therefore, even if larger nanoparticles are present in lower numbers they will result in much higher intensities, due to the intensity of scattered light being proportional to the sixth power of the radius[193,194]. Interestingly, the DLS analysis did not detect the large nanoparticles found

by TEM on the uncoated AgNPs sample, which can be explained by the sedimentation of these nanoparticles/clusters during DLS analysis.

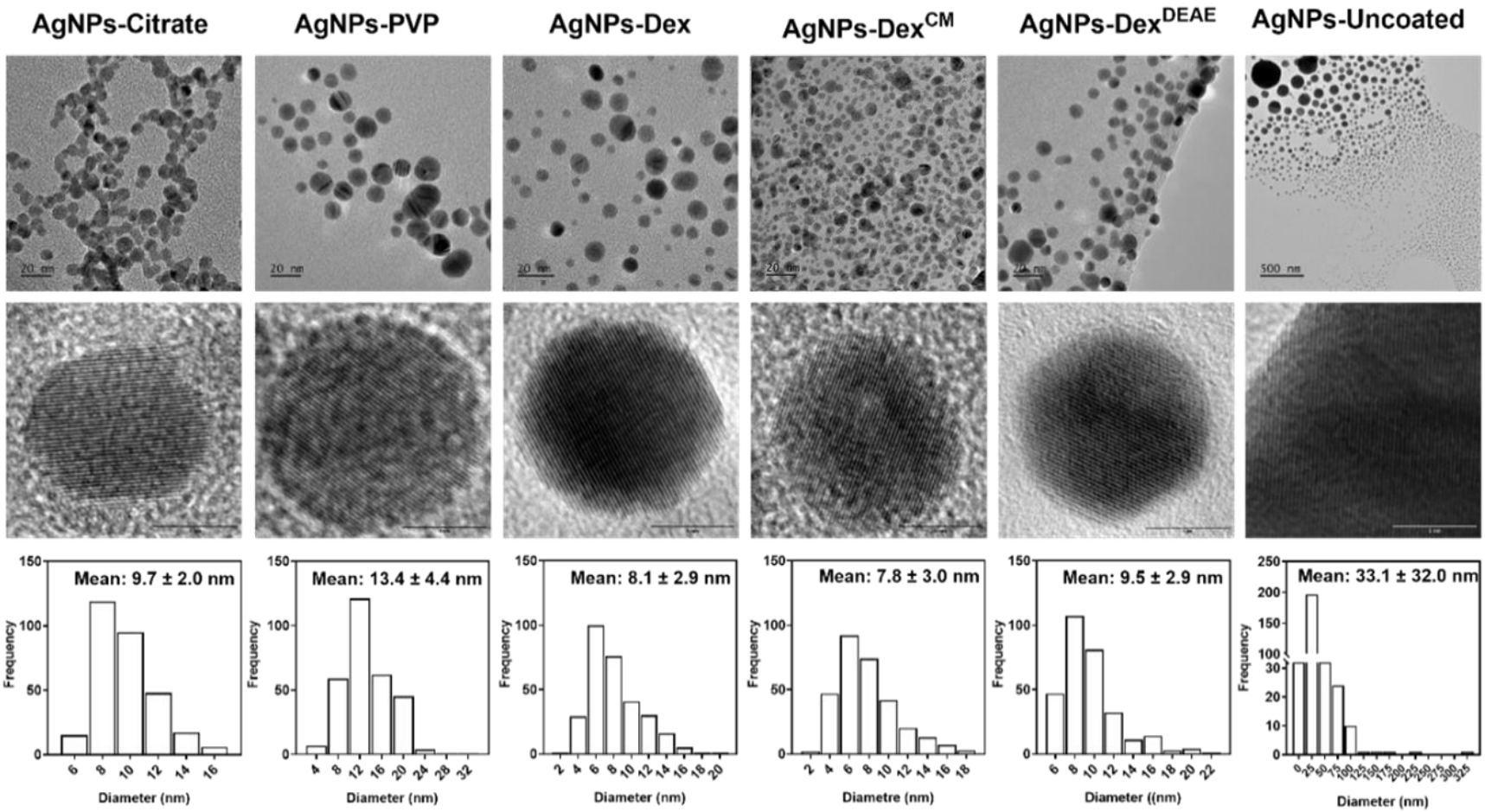

Figure 2-6. TEM images of the synthesised AgNPs and corresponding size distribution histograms.

3.1.3. Crystalline structure

The crystalline structure of the AgNPs was studied by powder XRD. **Figure 2-7** depicts the diffraction pattern of all the produced AgNPs. Regardless of the type of capping agent, or absence of stabiliser, all the AgNPs presented a face-centred cubic crystal structure with the characteristic peaks of silver metallic nanoparticles around 38, 44, 64 and 77°, assigned to the crystal planes (111), (200), (220) and (311) (Card No.:9008459, Rigaku database). The crystalline structure of the AgNPs is also evidenced in the TEM images (**Figure 2-6**, **middle row**), where it is possible to see the lattices in all AgNPs. The absence of the main silver oxide crystals peaks on the diffraction pattern at 32.17, 37.31, 53.79, 64.08 and 67.29° (Card No. 7109246, Rigaku database) also indicates that the nanoparticles were pure silver.

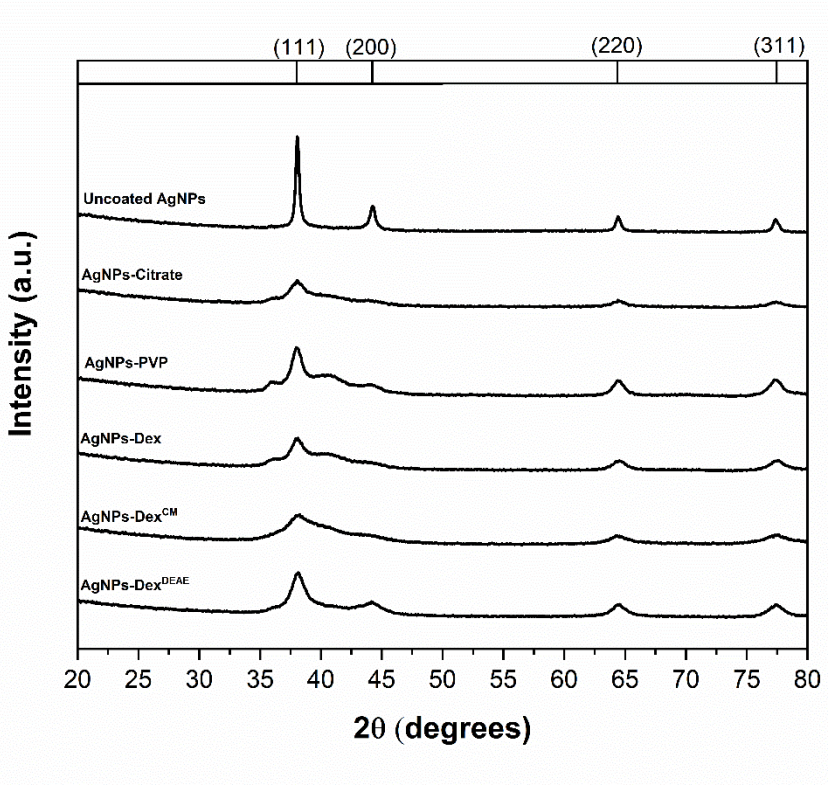

Figure 2-7. X-ray diffraction pattern of the AgNPs.

Two of the major differences between the XRD pattern of the uncoated AgNPs and the stabilised ones are the peaks intensities and broadening. The uncoated AgNPs presented more intense and narrow peaks than the stabilised AgNPs, where in some cases, some of the peaks are difficult to discern. This is due to the size of the nanoparticles. The smaller the AgNPs, the higher the peak broadening and the lower the signal-to-noise ratio[195]. These

results are in agreement with the UV-vis and TEM data, which show that the uncoated nanoparticle colloids present particles with larger diameters.

3.1.4. Surface charge and chemistry

The stabilisation of nanoparticles with capping agents implies the alteration of the surface chemistry to create repulsion forces and steric hindrance that prevents the agglomeration of the particles upon collision with one another. **Table 2-2** presents the zeta potential of the AgNPs in ultrapure, type I water. All the nanoparticles, except for the AgNPs-Dex^{DEAE}, had a negative zeta potential (-21.9 to -36.4 mV) due to the polyanionic nature of some of the capping agents, i.e., citrate ions and Dex^{CM}, and the presence of electrons on the surface of the metallic nanoparticles, which are sufficient to endow a negative charge due to the low mass of the AgNPs[196,197]. The AgNPs coated with Dex^{DEAE}, were the only nanoparticles that presented a positive potential (ca. 45 mV), due to positively charged diethylaminoethyl moieties on the derivatised dextran.

The charge on the surface of the nanoparticles helps to promote their stability through repulsion forces. Allied with that, the stability of the coated AgNPs is increased by steric hindrance promoted by the bulky structures of the capping agents.

Table 2-2. Zeta potential of the AgNPs in ultrapure, type I water. The values correspond to the average of 50 runs.

AgNPs	**Zeta potential (mV)**
AgNPs-Citrate	-30.6 ± 5.3
AgNPs-PVP	-24.0 ± 8.0
AgNPs-Dex	-21.9 ± 7.0
AgNPs-Dex^{CM}	-36.4 ± 6.0
AgNPs-Dex^{DEAE}	45.2 ± 6.9
AgNPs-Uncoated	-32.5 ± 9.9

Figure 2-8 presents the infrared spectra of the coated AgNPs and the pure capping agents (Citrate, PVP, Dex, Dex^{CM} and Dex^{DEAE}). The data shows that the capping agents are responsible for the spectral signatures of the nanoparticles. All the AgNPs presented

characteristic peaks of the capping agent, with shifts in the wavelength being present due to the interactions with the AgNPs surface. In the case of the AgNPs coated with Citrate, the nanoparticles presented bands with strong intensities at 1553 and 1376 $cm^{-1,}$ which corresponded to the asymmetric and symmetric stretching vibration of the carboxylate groups, respectively[198,199].

The AgNPs coated with PVP presented the characteristic bands of PVP, with an intense band at 1660 cm^{-1} resulting from C=O stretching, and two other bands at 1290 and 1020 cm^{-1} resulting from C-N stretching. The redshifts of these bands demonstrate the interaction of PVP with silver, as these interactions occur through the carbonyl group and nitrogen atom of the pyrrolidone ring[172]. It has been reported that PVP also interacts with silver through Van der Waals attraction and direct binding, which explains the redshifts and different intensities of the bands attributed to C–H bending at 1490-1420 cm^{-1} [172].

All the AgNPs coated with dextran, or derivatised dextran, presented similar spectra due to their chemical similarity. The AgNPs presented the characteristic bands resultant from the glycosidic bonds at 1149-1151 cm^{-1}, 1021-1024 cm^{-1} and 916-918 cm^{-1}[200,201]. Interestingly, the spectra of the AgNPs coated with dextrans presented a more evident band at ca. 1040 cm^{-1}. This band has been associated with a more-ordered structure[201], and seems to indicate that the dextrans adsorbed on the surface of the AgNPs present a well-organised structure. The AgNPs coated with dextrans also presented more intense bands at ca. 1419-1386 cm^{-1}, assigned to in-plane bending of the C-H bond[202], and seems to have resulted from the interactions of the dextrans with the nanoparticles.

Overall, the data shows that the capping agents adsorbed on the surface of the nanoparticles resulted in AgNPs with different charges and spectral identities.

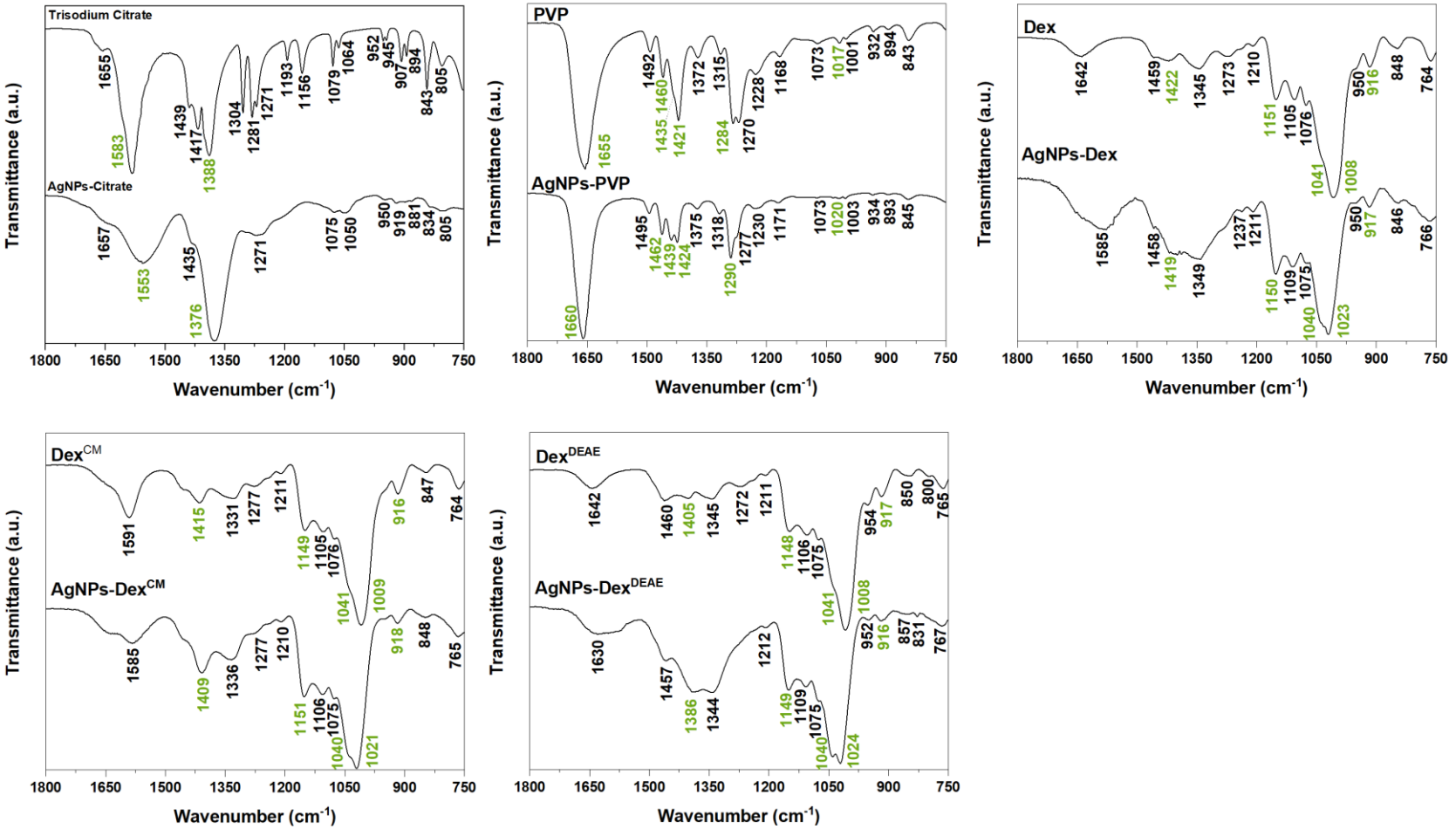

Figure 2-8. FTIR spectra of the AgNPs and respective capping agents.

3.1.5. Capping agent content

Thermogravimetric analysis was carried out to study the thermal stability of the AgNPs and the content of the capping agent adsorbed on the nanoparticles. Uncoated AgNPs and pure capping agents were used as controls. As depicted in **Figure 2-9**, all the coated AgNPs presented a weight variation below 5% between 30 and 200°C, resulting from the evaporation of the water adsorbed on the nanoparticles. All the capping agents showed an almost complete degradation at 600-700°C, except for Citrate. Regarding the amount of capping agent adsorbed on the nanoparticles, this varied between ca. 5 and 50%. The percentage of citrate ions adsorbed on the surface of the nanoparticles was predicted to be above 4.9% and below 14.9%. The last value was determined considering that the weight loss (4.9%) accounted for 32.8% of the total content of the capping agent. This value is overestimated, as the capping agent corresponds to only citrate ions provided by the dissolution of trisodium citrate dihydrate salt. Nonetheless, this estimation helps to determine a percentage range of the citrate content adsorbed on the nanoparticles. The AgNPs-PVP presented a high content of adsorbed PVP (49.4%), corresponding to almost 50% of the total mass of the nanoparticles. The AgNPs-Dex, AgNPs-Dex^{CM} and AgNPs-Dex^{DEAE} presented the following percentages of adsorbed capping agent: 24.3, 35.6 and 40.4%, respectively. The different percentages demonstrate that the dextrans have different affinities to the nanoparticles, with Dex and Dex^{DEAE} presenting the lowest and highest affinity, respectively. These results show that the diethylaminoethyl and carboxymethyl moieties on the derivatised dextran, increase the affinity to the nanoparticles, possibly by creating more interactions with the nanoparticles surface. This data also explains why lower concentrations of dextran solutions (0.06 $mg.ml^{-1}$, or below) in comparison with PVP (0.38 $mg.ml^{-1}$, or above) resulted in stable AgNPs even when stabilised with Dex. The high affinity between the dextrans and the AgNPs increased their adsorption, with low concentrations being enough to form a stabilising layer.

The different capping agents contents on the surface of the AgNPs were also reflected on the DLS data (**Figure 2-5**). The AgNPs with lower percentages of capping agent (AgNPs-Citrate and AgNPs-Dex) presented slightly more narrow distributions (lower polydispersity index) with the peak centred around 10 nm being more intense in comparison to the AgNPs coated with PVP, Dex^{CM} and Dex^{DEAE}.

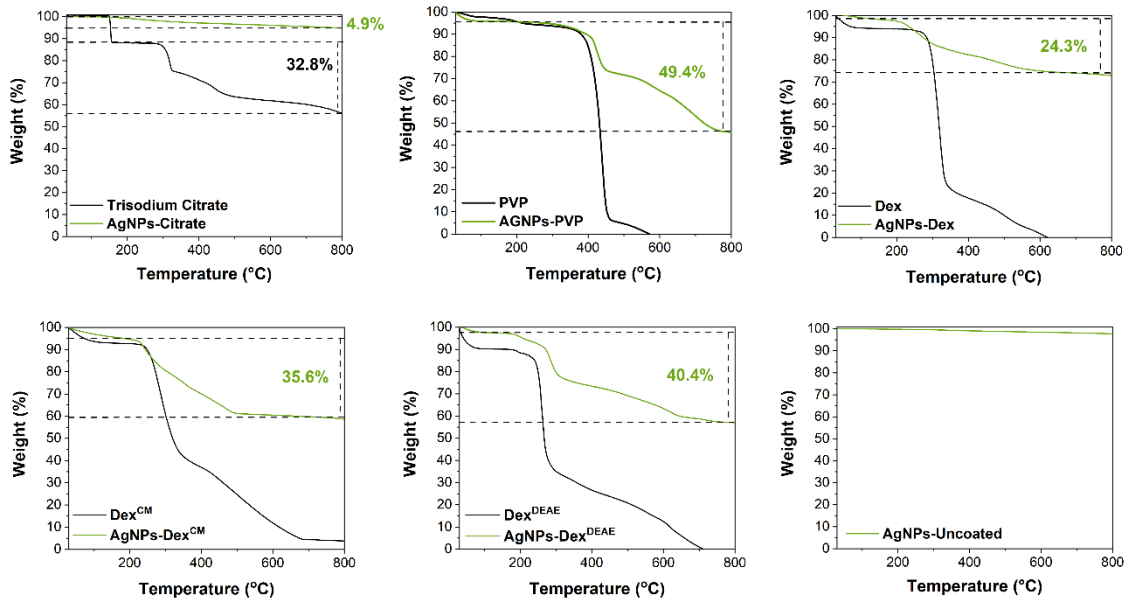

Figure 2-9. TGA curve of the AgNPs and corresponding capping agents.

3.2. Stability of the AgNPs

The antibacterial activity and optical properties of the AgNPs are size-dependent, and therefore is of utmost importance to monitor their size during storage and application. In the next sections, the stability of AgNPs after storage, and the effect of different media on their properties, are studied.

3.2.1. Storage stability

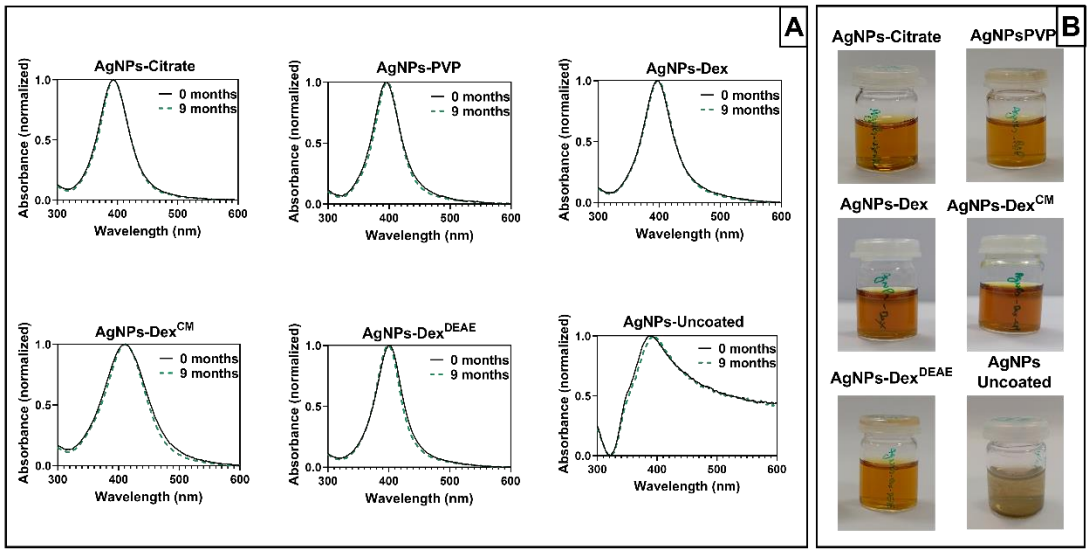

Figure 2-10. UV-vis spectra of the AgNPs after synthesis (0 months) and after being stored for 9 months at 4°C (9 months) (A), and appearance of the colloidal dispersions after storage for 9 months (B).

The colloidal stability of the AgNPs, when stored at 4°C for 9 months, was assessed to study the capacity of the different capping agents to maintain the colloidal stability of the nanoparticles. **Figure 2-10A** presents the UV-vis spectra of the AgNPs, with and without coating, before (0 months) and after being stored for 9 months (9 months). The UV-vis is a good method to monitor the stability of the AgNPs, as the peak around 400 nm is sensitive to the size of the nanoparticles. The data shows that the size of the AgNPs did not change substantially over time, as the UV-vis spectra are identical before and after storage.

The images of the AgNPs dispersions after storage (**Figure 2-10B**) show that the coated AgNPs kept their colloidal stability as there was no detectable sedimentation of the nanoparticles on the bottom of the flask. On the other hand, the uncoated AgNPs presented the formation of a deposit, highlighting their limited colloidal stability and the importance of the capping agents to prolong the storage stability.

3.2.2. Stability in bacterial growth media

The culture media used to perform the antibacterial tests present rich compositions to provide all the nutrients required for bacterial growth. Their composition varies according to the type of medium and can include starch, casein hydrolysate, peptone, meat infusions, meat/yeast extracts, and salts. While these components promote optimal bacterial growth, some adsorb on the surface of the nanoparticles forming a corona that changes the biological identity of the nanoparticles[203]. This corona can help to increase the stability of

the nanoparticles but also changes their activity[11]. Other components present in culture media, like salts and charged biomolecules, can also disrupt the stability of the nanoparticles and promote the formation of clusters, reducing the total surface area, and consequently the antibacterial activity[11]. Moreover, chloride salts, like NaCl, which are found in a vast number of media, can either decrease or increase the activity of AgNPs by reacting with free Ag^+ forming insoluble precipitates of AgCl or soluble silver chloride complexes $AgCl_x^{(x-1)-}$. The formation of AgCl salt or $AgCl_x^{(x-1)-}$ complexes is dependent on the concentration of Cl^-, with higher concentrations favouring the formation of silver chloride complexes, which increases the toxicity of the AgNPs[204]. Due to the complexity of the culture media, and the myriad of formulations existent in the market containing components that can affect the stability, surface charge, release and availability of Ag^+, comparisons between antibacterial tests reported by different research groups are challenging[11].

Figure 2-11 and **Figure 2-12** present the UV-vis spectra and transmittance images of the AgNPs in different culture media and PBS before and after incubation at 37°C, respectively. The composition of the culture media and PBS are presented in **Table 2-3**, and the images of the nanoparticles dispersions before and after incubation, are present in **Figure 2-13**, as the colour change of the dispersions is a quick and reliable indicator of the AgNPs stability.

Table 2-3. Composition of PBS buffer, MHB-O, MHB-S, LB and NB media. Values in brackets represent the concentration of the salt.

	Salts ($g.L^{-1}$)	**Dehydrated infusion from beef ($g.L^{-1}$)**	**Meat extract ($g.L^{-1}$)**	**Casein hydrolysate ($g.L^{-1}$)**	**Starch ($g.L^{-1}$)**	**Yeast extract ($g.L^{-1}$)**	**Peptone**
PBS	NaCl (8) Na_2HPO_4/KH_2PO_4 (1) KCl (10)		-	-	-	-	-
MHB-O	-	300	-	17.5	1.5	-	-
MHB-S	-	-	2	17.5	1.5	-	-
LB	NaCl (5)	-	-	-	-	5	10
NB	NaCl (5)	-	1	-	-	2	5

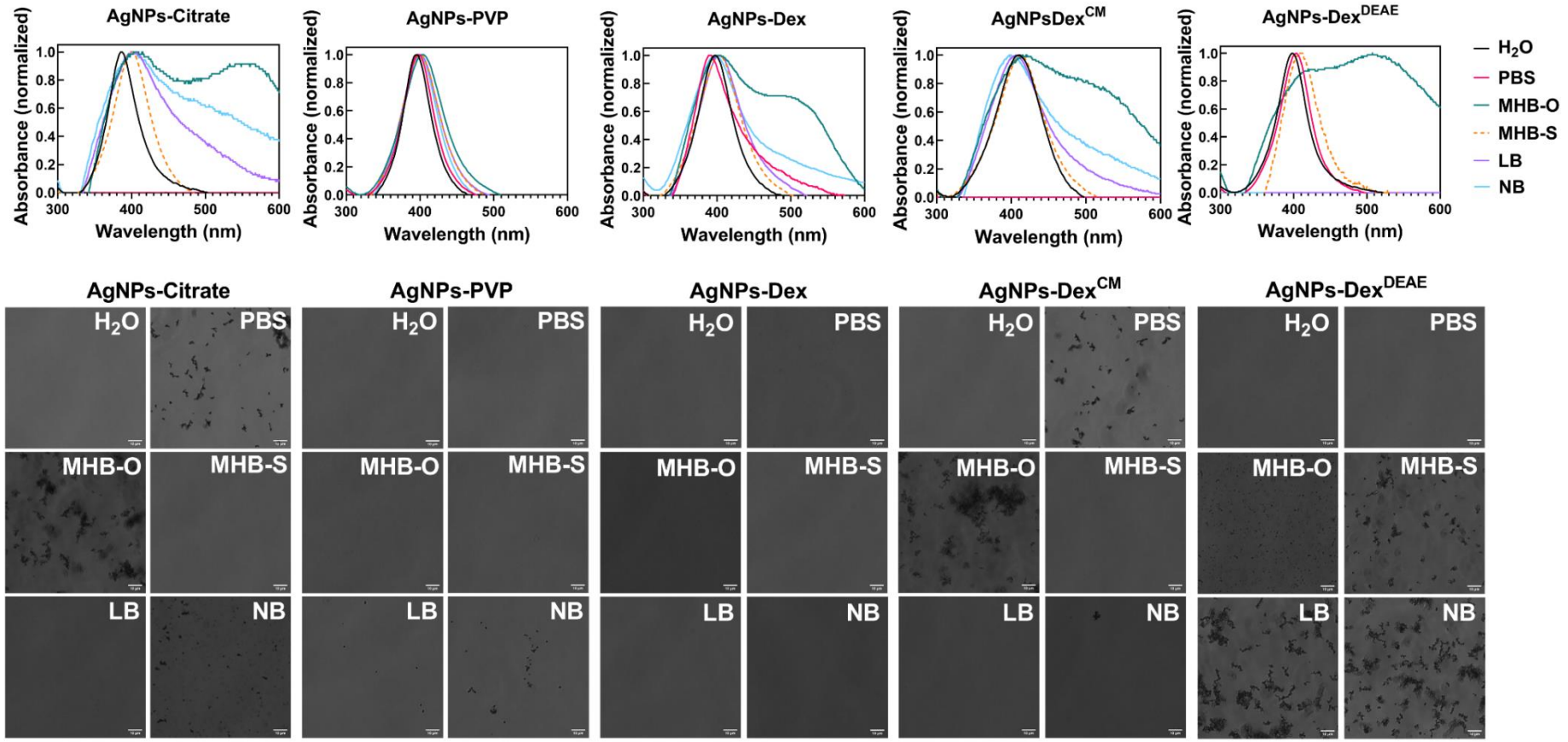

Figure 2-11. UV-vis spectra and respective transmittance images of the AgNPs in ultrapure, type I water (H_2O), PBS and different broths used for bacterial growth: MHB-O, MHB-S, LB and NB.

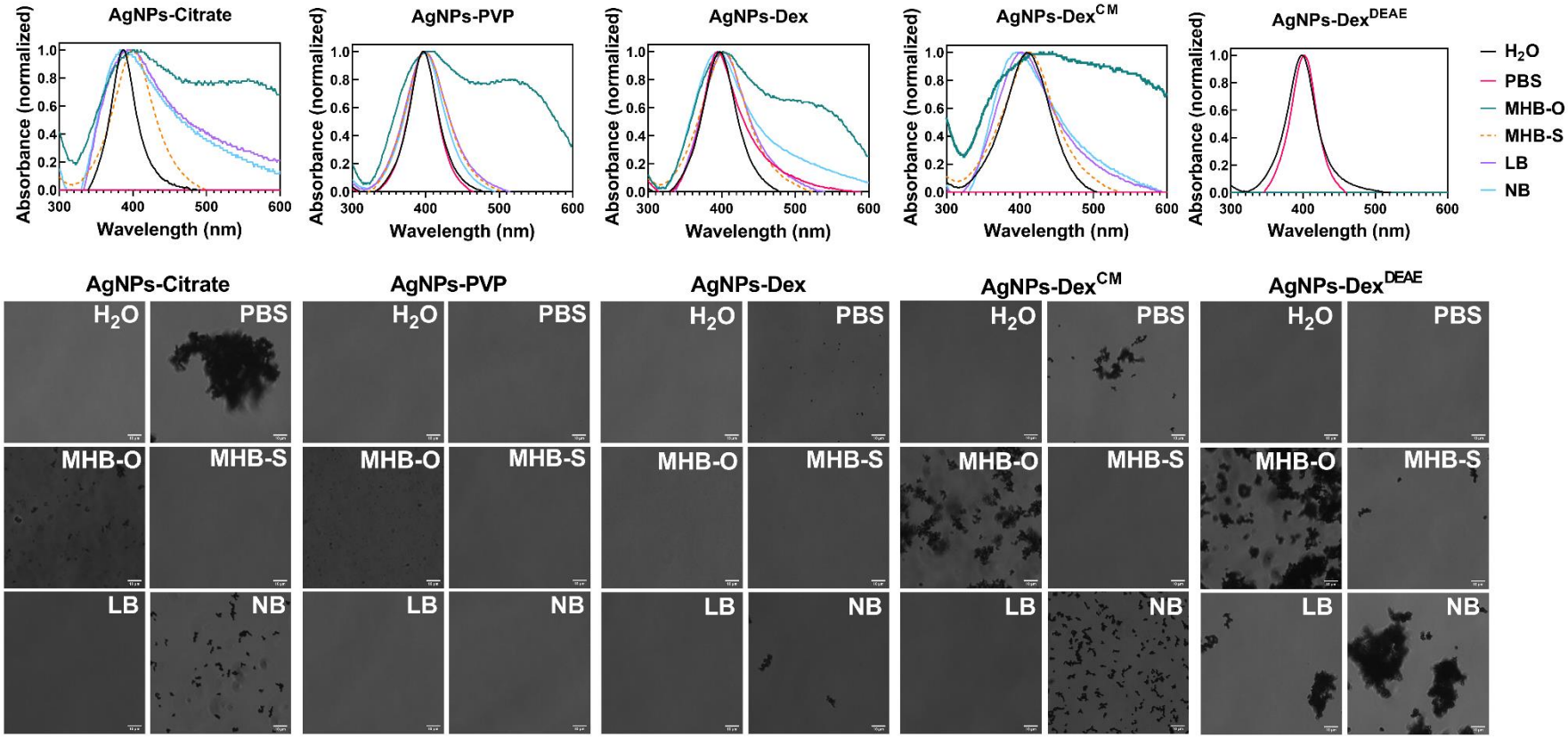

Figure 2-12. UV-vis spectra and respective transmittance images of the AgNPs in ultrapure, type I water (H_2O), PBS and different broths used for bacterial growth: MHB-O, MHB-S, LB and NB after mixing and overnight incubation at 37°C.

Overall, the data shows that the AgNPs stability varies with the type of media, with the AgNPs coated with PVP being the most stable nanoparticles across all the media tested. Nonetheless, after overnight incubation at 37°C, micro-sized clusters of AgNPs-PVP formed in MHB-O, as demonstrated in **Figure 2-12**. The AgNPs coated with Dex^{DEAE} were extremely unstable in all the media tested, which was enhanced during incubation at 37°C. As shown in **Figure 2-11** and **Figure 2-12**, the maximum absorbance band around 400 nm disappeared due to the formation of large silver clusters and the nanoparticles flocculation. On the other hand, the AgNPs-Dex^{DEAE} presented good stability in PBS, demonstrating that the instability was triggered by the interaction of the biomolecules in the media with Dex^{DEAE}, promoting the coating displacement from the surface of the AgNPs.

The AgNPs coated with Citrate, Dex, and Dex^{CM} showed some degree of instability in PBS, with the AgNPs coated with Citrate and Dex^{CM} immediately clustering and losing their surface plasmon resonance properties (**Figure 2-11**). As shown in **Figure 2-13**, the colour of the nanoparticles dispersions in PBS changed from amber to grey and then became clear due to the flocculation of the nanoparticles. This was caused by the salts present in PBS, which destabilised the electric repulsions created by the citrate ions and Dex^{CM} negative charges, triggering the irreversible agglomeration of the nanoparticles. Another mechanism of destabilization may be related to the competition of phosphate ions, also negatively charged, with citrate ions and Dex^{CM} for adsorption on the surface of the AgNPs. Phosphate ions can partially or completely replace the capping agents and reduce the colloidal stability of the AgNPs by forming a less organized diffuse layer of ions.

All the nanoparticles after incubation presented some degree of instability in MHB-O, which can be explained by the high content of dehydrated infusion from meat (300 $g.L^{-1}$). On the other hand, MHB-S was the media that less disturbed the stability of the AgNPs, and for that reason, was selected for the antibacterial tests.

Overall, the data shows that the AgNPs are highly sensitive to the composition of the media and buffers, with positively charged nanoparticles being extremely unstable in culture media. The higher the content of electrolytes and meat infusion or extracts, the higher the chance of disrupting the stability of the nanoparticles, with the nanoparticles stabilised through electrostatic repulsions being more susceptible.

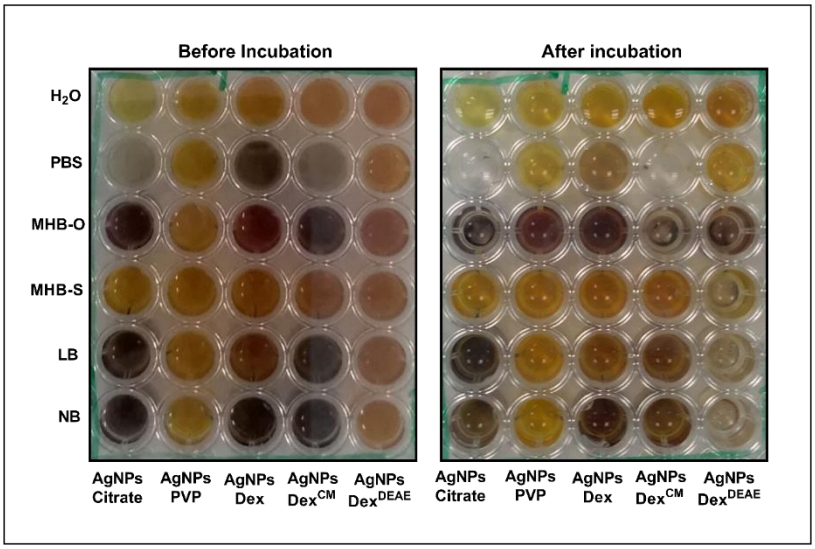

Figure 2-13. AgNPs in ultrapure, type I water (H_2O), PBS and different broths used for bacterial growth: MHB-O, MHB-S, LB and NB, before and after overnight incubation at 37°C.

3.3. Antibacterial activity of the AgNPs

3.3.1. MIC and MBC

The antibacterial activity of the AgNPs was assessed against *E. coli*, MRSA and *P. aeruginosa*, three strains responsible for a high number of healthcare associated infections[205,206].

Figure 2-14 presents the average MIC and MBC of all the AgNPs. The average MIC ranged between 16.9-210 µg.ml^{-1}, 18.8-240 µg.ml^{-1} and 3.8-240 µg.ml^{-1} for *E. coli*, MRSA and *P. aeruginosa*, respectively. The wide ranges demonstrate that the MIC varied considerably between the AgNPs. The uncoated AgNPs were the nanoparticles that presented the lowest activity, caused by the large nanoparticles and broad size distribution. Moreover, the lack of a capping agent made the bare AgNPs more susceptible to agglomeration in the testing medium. The AgNPs capped with Dex^{DEAE} presented the second-highest MIC. This is explained by their instability in the medium, which promoted their agglomeration as demonstrated in the previous section. The formation of clusters is very detrimental to the activity of AgNPs, as the total surface area is reduced, decreasing the interactions with the bacteria and the release of Ag^+, essential to for antibacterial activity[167].

Despite the good stability of the AgNPs-PVP in MHB-S, their antibacterial activity was lower than the activity of the AgNPs coated with Citrate, Dex or Dex^{CM}. This can be explained by the slightly larger diameter (13.4 ± 4.4 nm) of the AgNPs-PVP in comparison

with the AgNPs-Citrate (9.7 ± 2.0 nm), AgNPs-Dex (8.1 ± 2.9 nm) and AgNPs-Dex^{CM} (7.8 ± 3.0 nm). Additionally, PVP itself, and the corona formed on the nanoparticles through the adsorption of biomolecules from the medium, might also play a role, as they can decrease the interactions with the bacteria and the release of Ag^{+}. It is also expectable that PVP forms a tight mesh on the surface of the nanoparticles due to the hydrophobic nature of the carbon chain, decreasing the oxidation of the AgNPs and consequent release of Ag^{+}. On the other hand, the hydrophilic nature of the dextrans and citrate results in a loose protective layer that allows a quicker diffusion of oxygen and Ag^{+}. Interestingly, the AgNPs-PVP and AgNPs Dex^{DEAE} presented similar MICs against *E. coli* and MRSA, despite the AgNPs-Dex^{DEAE} being considerably more unstable. This might be due to the positively charged AgNPs-Dex^{DEAE} presenting stronger interactions with the negatively charged bacterial cell surfaces[207] and to a higher oxidation rate that result in the release of more Ag^{+}. The AgNPs coated with Citrate, Dex and Dex^{CM} presented the lowest MIC values, with the AgNPs-Dex^{CM} presenting the best antibacterial activity against *E. coli* and MRSA, due to being more stable in MHB-S, as shown in **Figure 2-11** and **Figure 2-12**, than the other nanoparticles. Nonetheless, other factors might have also potentiated the antibacterial activity of the AgNPs-Dex^{CM}, like the type of corona formed on their surface, and the release rate of Ag^{+}.

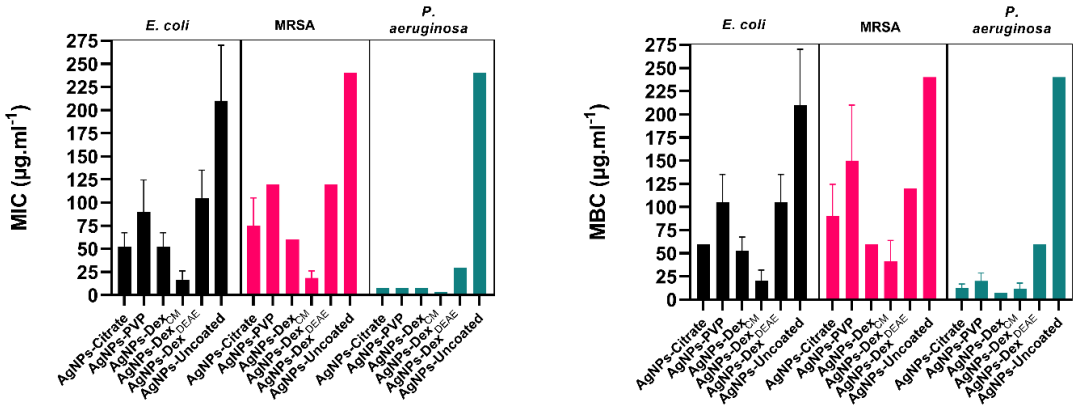

Figure 2-14. Minimum inhibitory concentration (MIC) and minimum biocidal concentration (MBC) of AgNPs. The concentration represents the content of silver in the nanoparticles. The medium used was MHB-S. The experiment was repeated three times, with three replicates per repetition.

The MBC data presented the same trend found in the MIC results, although higher concentrations were needed to kill the bacteria. The average MBC varied between 20-210 µg.ml^{-1}, 41-240 µg.ml^{-1}and 11-240 µg.ml^{-1} for *E. coli*, MRSA and *P. aeruginosa*, respectively. The MIC and MBC of the coated AgNPs were similar to values reported by

other authors[208–211]. Nonetheless, a significant discrepancy between studies in the literature is found due to variations in the AgNPs properties (size, zeta potential, shape, capping agent) and the assay conditions (inoculum density, medium formulation and salts concentration).

To study the effect of the capping agents on the antibacterial activity, all the coatings were tested against the same bacteria at concentrations above their content in the AgNPs dispersions with biocidal activity. As depicted in **Figure 2-15**, the bacteria grew in the presence of the capping agents (cloudy wells), ruling out their bactericidal activity at the concentrations tested. The inert effect of Citrate and PVP against *E. coli* has also been reported by Ivask *et al.*[212]. Therefore, the antibacterial activity described above was associated with AgNPs and not the capping agents as it mainly works as a stabilising coating.

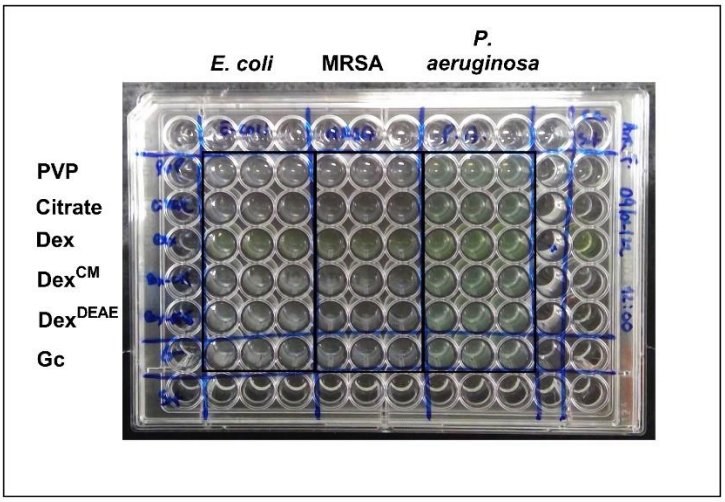

Figure 2-15. Microplate after incubation at 37°C for 20 hours with *E. coli*, MRSA and *P. aeruginosa* exposed to Citrate, PVP, Dex, Dex^{CM} and Dex^{DEAE}. The concentrations tested correspond to the theoretical amount of capping agent in a colloidal dispersion of AgNPs with a concentration of silver equal to 120 µg.ml^{-1} (AgNPs-Dex and AgNPs-Dex^{CM}), 240 µg.ml^{-1} (AgNPs-Citrate and AgNPs-Dex^{DEAE}), and 480 µg.ml^{-1} (AgNPs-PVP). The concentrations tested are above the MBC. The growth control row (no capping agent) is labelled as Gc.

3.3.2. Bacterial growth curves

The growth of the bacteria exposed to the AgNPs was monitored over 21 hours. **Figure 2-16** presents the optical density at 600 nm (OD_{600}) of MRSA, *E. coli* and *P. aeruginosa* exposed to the AgNPs at equivalent silver concentrations. This was 30 µg.ml^{-1} of silver for *E. coli* and MRSA, and 7.5 µg.ml^{-1} for *P. aeruginosa*.

The results show the AgNPs-Citrate, AgNPs-Dex and AgNPs-Dex^{CM} completely inhibited the growth of *E. coli*, with the AgNPs-PVP being able to prolong the lag phase for 10 hours. As expected, the bare AgNPs and AgNPs-Dex^{DEAE} did not decrease the *E. coli* growth rate.

Regarding MRSA, all the AgNPs decreased the bacterial growth rate, except the AgNPs-Dex^{DEAE}, nonetheless just the AgNPs coated with Dex and Dex^{CM} inhibited the bacterial growth. These results agree with the MIC results, except for the AgNPs-Dex, which had a higher MIC (60 $\mu g.ml^{-1}$). The discrepancy probably resulted from the differences in the assay settings. While in the MIC test the bacteria were left in an incubator at 37°C under static conditions, in the growth curves assay, the bacteria were left inside a microplate reader, also at 37°C, but stirred every 20 min for 20 sec before each OD_{600} reading. This helped to increase the oxygenation of the medium, and consequently increase the silver oxidation and release of Ag^+ that exerts the toxic effect. The increased toxicity of AgNPs under aeration conditions has been previously reported by Xiu Z. *et al.*[183] and explained by the aeration increasing the oxygen exposure and promoting the release of higher quantities of Ag^+.

Regarding *P. aeruginosa*, the concentration of AgNPs tested (7.5 $\mu g.ml^{-1}$) was lower than the concentration tested against *E. coli* and MRSA (30 $\mu g.ml^{-1}$), as *P. aeruginosa* is more sensitive to the AgNPs. That was shown in the MIC and MBC results and corroborated by the growth curves, where AgNPs-Uncoated and AgNPs-Dex^{DEAE} were the only nanoparticles that did not inhibit their growth. However, the AgNPs-Dex^{DEAE} prolonged the lag phase for about 13 hours.

Overall, the growth curves highlight the trend presented in the MIC and MBC results, *i.e.*, *P. aeruginosa* is more sensitive to AgNPs than *E. coli*, and *E. coli* is more sensitive to AgNPs than MRSA. This trend was verified for all the coated nanoparticles and is believed to result from structural differences between bacteria, and different mechanisms used to evade the toxic effect of the nanoparticles. Similar trends where the AgNPs present stronger activity against gram-negative than gram-positive have been previously reported and is believed to result from differences in the cell wall [208,213–215]. Moreover, the strong activity of AgNPs against *P. aeruginosa*, a bacterium that has developed an increased resistance to antibiotics is believed to result from AgNPs enhancing the oxidative stress and interfering with the ability of the bacteria to form biofilms by decreasing their adhesion, motility, destroying the iron homeostasis, blocking aerobic and anaerobic respiration, and affecting the quorum sensing systems[216,217].

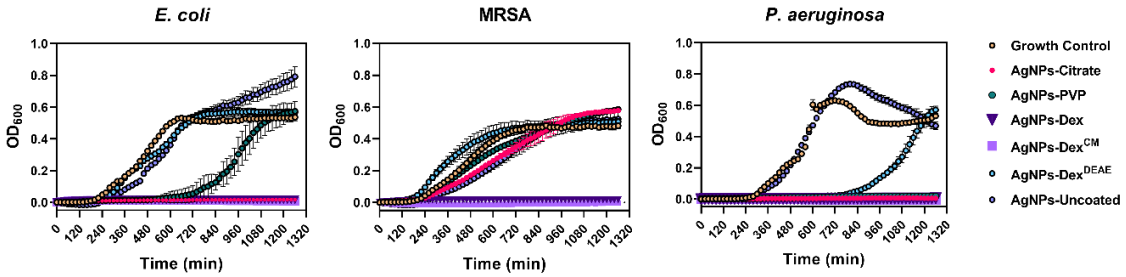

Figure 2-16. Growth curves of *E. coli*, MRSA and *P. aeruginosa* exposed to the AgNPs. The equivalent concentration of silver against *E. coli* and MRSA was 30 µg.ml^{-1}, and against *P. aeruginosa* was 7.5 µg.ml^{-1}.

3.3.3. Biocidal activity against formed biofilm

The effect of AgNPs on the removal of biofilms was assessed against established biofilms of MRSA and *P. aeruginosa*. *E. coli* was not tested as the strain used in this work did not form strong biofilms.

The destruction of biofilms is challenging, as they present additional mechanisms to inactivate and surpass the antimicrobial agents. In the case of metal-containing salts and nanoparticles, the polysaccharides in the extracellular matrix of the biofilm can stop their diffusion via chelation, entrapment, or agglomeration[218]. This reduces the activity of the nanoparticles or metallic ions, and can stimulate the appearance of antimicrobial resistance[219]. Moreover, a considerable number of bacterial cells in the biofilms are in a stationary phase, making them less susceptible to antimicrobials agents that depend on the metabolism of the cells to exert their activity[218–220].

The activity of nanoparticles against biofilms depends on the particle size, composition, charge and surface chemistry. All these factors affect the transport of the nanoparticles into the biofilms, and therefore the antimicrobial acitivty[221]. In the case of AgNPs, it has been shown that smaller nanoparticles are more effective in removing biofilms, due to better penetration into the biofilms and greater silver ions dissolution[222–225].

Figure 2-17 presents the percentage of biofilm mass left after treatment with different concentrations of AgNPs, and **Table 2-4** the MBEC. The minimum concentration of silver that promoted the eradication of 95% or more of the MRSA biofilm was 120 µg.ml^{-1} for the AgNPs coated with Citrate, PVP and Dex, and 60 µg.ml^{-1} for the AgNPs coated with AgNPs-Dex^{CM}. Once again, the AgNPs-Dex^{CM} presented better activity against MRSA, which can be explained by its better stability and diffusion into the biofilm, as smaller nanoparticles tend to travel deeper in the biofilm. The AgNPs-Dex^{DEAE} and AgNPs-Uncoated decreased the biofilm mass at high concentrations however, the remaining

biofilm mass was above the MBEC threshold (<5%). Peulen *et al.* [225] studied the diffusion of nanoparticles into biofilms composed of *P. fluorescens* and found that the diffusion decreased exponentially with the square of the solute radius, and the effective size of the biofilm pores ranged between 10 to 50 nm. Based on these findings, the poor activity of the AgNPs-Dex^{DEAE} and AgNPs-Uncoated can be explained by their larger sizes. While the uncoated AgNPs presented a broad distribution of diameters (**Figure 2-6**) due to their uncontrolled growth during synthesis, the AgNPs-Dex^{DEAE} formed micro-sized clusters in MHB-S (**Figure 2-12**) due to the poor stability in the medium. Moreover, the uncoated AgNPs are more prone to agglomeration due to the lack of a stabilising agent. Due to these reasons, both nanoparticles had poor diffusion into the biofilm, which explains their lower bactericidal activity against formed biofilm.

As expectable, the *P. aeruginosa* biofilms were more sensitive to the AgNPs, with the AgNPs coated with PVP, Dex and Dex^{CM} presenting an MBEC of 15 µg.ml^{-1}, and the AgNPs coated with Citrate of 30 µg.ml^{-1}. Once again, the AgNPs-Dex^{DEAE} and AgNPs-Uncoated did not completely eradicate the biofilm due to their larger sizes and limited diffusion.

Interestingly, at some sub-lethal concentrations, mainly for the AgNPs coated with Dex^{CM} and Dex^{DEAE}, the nanoparticles promoted an increased biofilm formation for both bacteria (**Figure 2-17**). This effect was previously reported by Yan et al. [226] for *P. aeruginosa*, and is believed to be caused by sublethal concentrations of AgNPs stimulating biofilm formation via upregulation of the quorum sensing, lipopolysaccharide biosynthesis, antibiotic resistance genes, and the enhanced production of components of the biofilm matrix like sugars and proteins.

Overall, the data shows that the AgNPs activity against the biofilms is highly dependent on their size and stability, with the capping agent playing an essential role in keeping the antibacterial activity of the AgNPs.

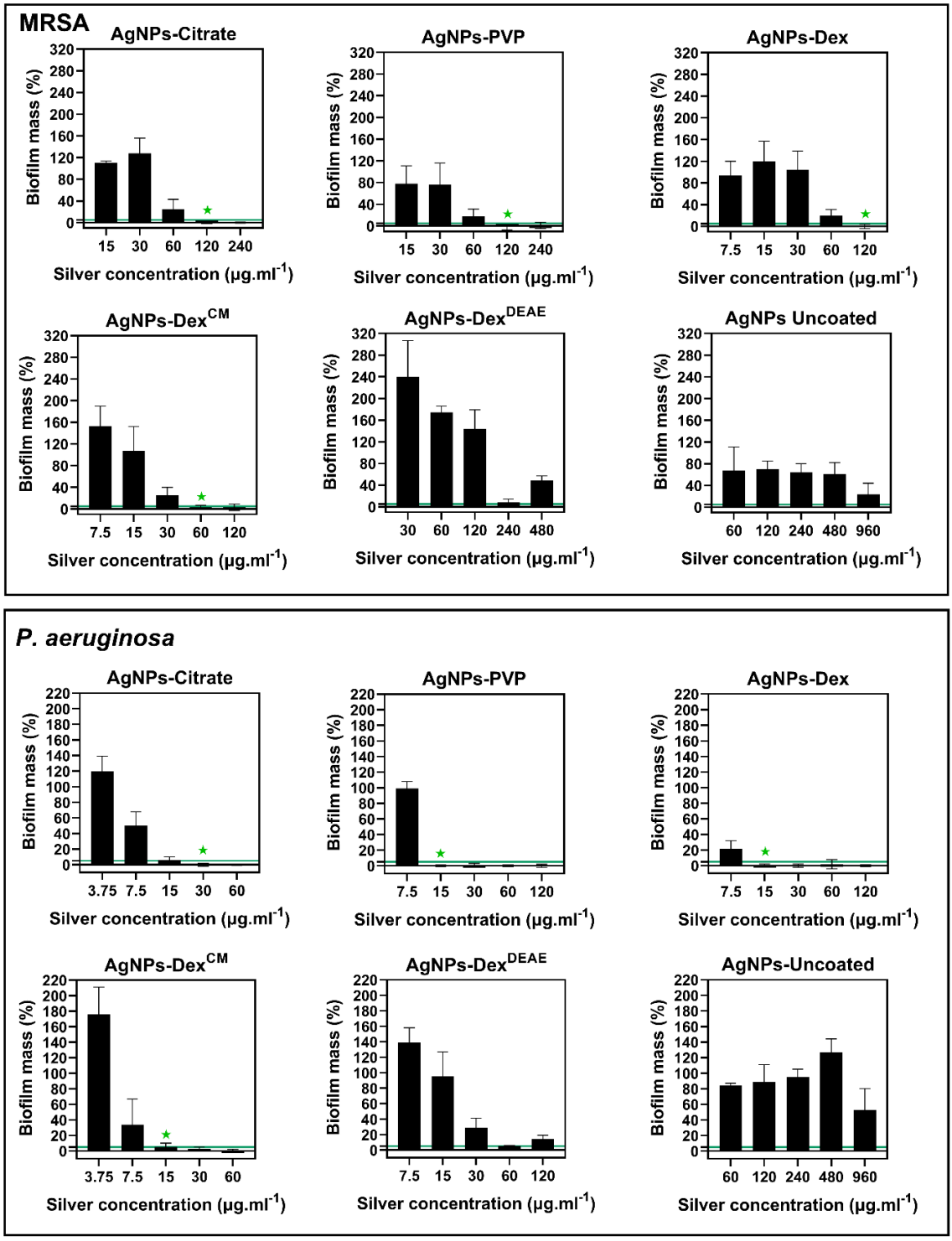

Figure 2-17. Remaining biofilm mass after treatment of the MRSA or *P. aeruginosa* biofilms with AgNPs at different equivalent concentrations of silver. The green line represents the minimum biofilm mass cut-off (≤ 5%) for the definition of the minimum biofilm eradication concentration (MBEC) and the green star marks the MBEC value.

TABLE 2-4. MBEC of the AgNPs against MRSA and *P. aeruginosa* biofilms. The concentration represents the content of silver in the AgNPs.

MBEC (μg.ml^{-1})	MRSA	*P. aeruginosa*
AgNPs-Citrate	120	30
AgNPs-PVP	120	15
AgNPs-Dex	120	15
AgNPs-Dex^{CM}	60	15
AgNPs-Dex^{DEAE}	>480	>120
AgNPs-Uncoated	>960	>960

4. Conclusion

In the present study the effect of five different capping agents (Citrate, PVP, Dex, Dex^{CM} and Dex^{DEAE}) on the physicochemical properties and antibacterial activity of the AgNPs was studied. The results showed that the capping agents are essential to prevent the nanoparticles growth over nanoscale dimensions and endow stability. The nanoparticles synthesised with capping agents presented diameters between 8 and 13 nm, while the uncoated AgNPs presented a larger average diameter (33 nm) due to the uncontrolled growth during synthesis. All the AgNPs, without exception, presented the typical crystalline structure of pure silver, without the presence of the silver oxide peaks. The DLS and FTIR analysis demonstrated that the coated AgNPs acquired the properties of the capping agent in terms of charge and spectral signatures, being more stable during storage than the bare AgNPs, most probably due to the repulsions forces and steric hindrance created by the capping agents.

The stability of the AgNPs in PBS and different media used to grow bacteria was also studied. Overall, the data showed that the AgNPs are highly sensitive to the composition of the media and buffer, with positively charged nanoparticles being extremely unstable in culture media. The higher the content of electrolytes and infusion or extracts in the media, the higher the disruption of the stability, with the nanoparticles stabilised through electrostatic repulsions being more easily destabilised.

The antibacterial activity of the AgNPs was tested against *E. coli*, MRSA and *P. aeruginosa*. The results showed that the antibacterial activity of the AgNPs was dependent on their stability and the interaction with the medium and the bacteria. The AgNPs coated with Dex and Dex^{CM} presented the strongest activity across all the antibacterial tests (MIC, MBC and MBEC) due to their better stability, smaller size, and increased interactions with the bacteria.

In conclusion, this work shows that the capping agents have a crucial role in controlling the physicochemical properties and antibacterial activity of the AgNPs. From production to the final application, the capping agents protect the AgNPs from overgrowth and agglomeration. Importantly, the capping agent must be chosen taking into consideration the final application, as their charge and structure affect the affinity to the AgNPs and their stability. As shown in this work, small variations in the capping agents can considerably improve or deteriorate the antibacterial activity of AgNPs.

Chapter 3

Design of hybrids of vaterite and silver nanoparticles

All the content presented in this chapter has been published in 2023 as a research article titled "Vaterite vectors for the protection, storage and release of silver nanoparticles" in the Journal of Colloid and Interface Science, Volume 631, pages 165 to180 [227].

1. Introduction

Silver nanoparticles (AgNPs) have demonstrated considerable commercial value due to their antimicrobial, optical, thermal, and electrical properties. AgNPs have been incorporated into a wide range of products, such as medical devices, air/water filters, textiles, cosmetics, household appliances, wound dressings, sensors, electronic and photonic devices[9,208,228,229]. Despite the broad spectrum of applications, there are still concerns about the stability of AgNPs. It is well established that changes in pH, light exposure, high ionic strength and high temperature shifts can promote AgNPs agglomeration and loss of their antimicrobial, thermal and optical properties[9,230,231]. Moreover, the increased use of AgNPs has also raised environmental concerns about silver accumulation in the environment and potential adverse effects on different living organisms[10,182,230].

The use of supporting materials for AgNPs has broadened their application possibilities by improving AgNPs stability and tuning silver release. Various materials, such as silica, hydroxyapatite, ceramic, calcium phosphate, polymer matrices, clay, graphene and cellulose have been tested as supporting materials to prevent the agglomeration and control the release of AgNPs[232–243]. Nonetheless, the production of some of these materials requires toxic chemicals and entails expensive and time-consuming production methods.

Vaterite is a calcium carbonate ($CaCO_3$) polymorph with a typical spherical shape and size ranging from nanometres to ten of micrometres[1,5]. It is the least stable anhydrous $CaCO_3$ polymorph, when compared with the other two phases (calcite and aragonite)[5].

Vaterite $CaCO_3$ crystals are typically synthesised on a lab-scale by mixing concentrated calcium and carbonate containing salt solutions[244]. Vaterite crystals have a porous structure, high loading capacity, availability, low price, biocompatibility, biodegradability, high surface area, tuneable and stimuli-responsive properties[5,6,38], making them excellent carriers for the protection and controlled delivery of different compounds.

The combination of $CaCO_3$ with AgNPs ($CaCO_3$/AgNPs) presents an excellent opportunity to protect and control the release of AgNPs, as $CaCO_3$ dissolves in acidic environments, or in the presence of chelating agents like EDTA and citric acid. This property allows the release of the cargo from vaterite in acidic microenvironments such as tumours, inflammation sites and the inner core of biofilms[1,245]. Moreover, vaterite can spontaneously recrystallise to calcite resulting in a drastic reduction of the surface area and the payload release[60]. Therefore, the association of $CaCO_3$ vaterite with AgNPs opens up new ways to store, protect and release AgNPs, improving the overall properties of the final materials. This association also presents new possibilities for the production of platforms with dual action for cancer treatment (photothermal and calcium overload therapy)[246–249] and the photothermal eradication of biofilms[250].

Several groups have reported the association of AgNPs with $CaCO_3$ crystals for the production of antimicrobial materials and surface-enhanced raman scattering (SERS) platforms[1,138,251–253]. Nonetheless, despite this attractive association, there are still unclear points that have not been addressed, or are not entirely understood, such as AgNPs uptake by $CaCO_3$ crystals, the stability of AgNPs before and after loading, the impact of AgNPs capping agents in the affinity to $CaCO_3$, and the nanoparticle loading/release mechanism. Therefore, this work intends to address these points and validate whether vaterite $CaCO_3$ crystals may be used as effective carriers/supporting matrices to store, protect and keep AgNPs intact and active before and after being released. The effect of the capping agents trisodium citrate (Citrate), polyvinylpyrrolidone (PVP), dextran (Dex), diethylaminoethyl–dextran (Dex^{DEAE}), and carboxymethyl–dextran (Dex^{CM}) on AgNPs loading into vaterite *via* co-precipitation has also been studied.

2. Materials and methods

2.1. Materials

Silver nitrate ($AgNO_3$, extra pure crystals, ≥99%), calcium dinitrate tetrahydrate ($Ca(NO_3)_2.4H_2O$, ≥99%), calcium dibromide hydrate ($CaBr_2.xH_2O$, 98%), calcium

diiodide hydrate ($CaI_2.xH_2O$, 98%), sodium borohydride ($NaBH_4$, ≥99% pure), polyvinylpyrrolidone 40 kDa (PVP), trisodium 2-hydroxypropane-1,2,3-tricarboxylate dihydrate (Citrate, $C_6H_5Na_3O_7 \cdot 2H_2O$, ≥99% pure), fluorescein isothiocyanate–dextran 40 kDa (Dex), fluorescein isothiocyanate–diethylaminoethyl–dextran 40 kDa (Dex^{DEAE}), fluorescein isothiocyanate–carboxymethyl–dextran 40 kDa (Dex^{CM}), Mueller Hinton broth Sigma 70192 (MHB-S), Mueller Hinton agar Sigma 70191 (MHA-S), sodium acetate (CH_3COONa, ≥99%), TraceCERT® 10,000 ppm calcium ICP-MS standard in 5% nitric acid and TraceCERT® 1 ppm Silver ICP-MS standard in 2% nitric acid, were obtained from Sigma-Aldrich (Steinheim, Germany). Calcium dichloride dihydrate ($CaCl_2.2H_2O$, ≥99%), disodium carbonate (Na_2CO_3, ≥99.5%), tris buffer saline 10X solution (TBS), 99% ethanol, sodium hydroxide pellets (NaOH, ≥98%), glacial acetic acid (CH_3COOH, ≥99.7 %), 70% nitric acid (HNO_3, analytical grade) and 37% hydrochloric acid (HCl, analytical grade) were obtained from Fisher Scientific (Loughborough, United Kingdom).

2.2. Methods

2.2.1. Synthesis of AgNPs

AgNPs with average sizes ranging between 7 and 13 nm were synthesised *via* a modified chemical reduction methodology adapted from Nau E.*et al*.[9] as described in **Chapter 2**.

2.2.2. Synthesis of bare vaterite $CaCO_3$ crystals

Bare vaterite $CaCO_3$ was synthesised based on the work of Volodkin, D. et al.[254]. Briefly, $CaCl_2.2H_2O$ (150 mM, in water) was mixed with an equal volume of TBS 6x and ultrapure, type I water under intense magnetic stirring (800 rpm) in a polystyrene well (1.5 cm diameter) of a 24 well cell culture plate, using a magnetic stirrer plate and a glass-encased stir bar (1.2 cm length and 0.5 cm diameter). Then Na_2CO_3 (50 mM, in water) was added, and the stirring continued for 30 seconds. The suspension was poured into a polypropylene tube and left for 10 minutes to allow the crystals growth. After this period, the suspension was centrifuged at 1000 *g* for 5 minutes, washed with ultrapure, type I water *via* resuspension, centrifuged for another 5 minutes, and then resuspended in ethanol. The crystals were then dried at 80°C for 1 hour. The initial molar ratio between $CaCl_2.2H_2O$ and Na_2CO_3 was 1. All the syntheses were carried at room temperature, and the reagents solutions pre-filtered through a 0.2 μm syringe-tip filter (Fisherbrand™, Loughborough, United Kingdom).

2.2.3. Synthesis of $CaCO_3$/AgNPs hybrids and adsorption studies

2.2.3.1. Synthesis

AgNPs were loaded into $CaCO_3$ crystals by co-precipitation. Briefly, $CaCl_2.2H_2O$ (150 mM, in water) was mixed with an equal volume of TBS 6x, and then AgNPs colloid and ultrapure, type I water were added under intense magnetic stirring (800 rpm) in a polystyrene well (1.5 cm diameter) of a 24 well cell culture plate, using a magnetic stirrer plate and a glass-encased stir bar (1.2 cm length and 0.5 cm diameter). A few seconds later, Na_2CO_3 (50 mM, in water) was added, and the stirring continued for 30 seconds (the final volume was the same for all the syntheses). The suspension was transferred to a polypropylene tube and left for 10 minutes to allow the crystals growth. After that, the suspension was centrifuged at 1000 *g* for 5 min, and then the supernatant collected for the quantification of free/unloaded silver. The sediment was washed with ultrapure, type I water, centrifuged at 1000 *g* for another 5 minutes, resuspended in ethanol and dried at 80°C for 30 min. The initial molar ratio between $CaCl_2.2H_2O$ and Na_2CO_3 was 1. All the syntheses were performed at room temperature. The free (unloaded) silver was quantified by ICP-MS with three replicates per condition as described below. A control sample was prepared at the same conditions for all the concentrations tested, however Na_2CO_3 was replaced by ultrapure, type I water to prevent the formation of $CaCO_3$ and the entrapment of AgNPs. The amount of silver loaded at equilibrium was calculated using the following equation:

$$qe = \frac{(C_O - C_e) \times V}{\mathrm{m}} \qquad (1)$$

where q_e is the adsorption capacity (mg. g^{-1}); C_O and C_e are the initial and equilibrium silver concentrations, respectively (mg. mL^{-1}); V is the volume (ml) of the supernatant, and m is the mass of $CaCO_3$ (g).

The loading efficiency (LE) was calculated using the following equation:

$$LE = \frac{(m_i - m_f)}{m_i} v \qquad (2)$$

where m_i and m_f are the initial and final silver mass in the supernatant (mg), respectively.

2.2.3.2. Adsorption isotherms fitting

The experimental data of AgNPs adsorption into vaterite $CaCO_3$ was fitted with two-parameter models of adsorption using the linearised functions of the following classical isotherm models:

Langmuir:

$$\frac{c_e}{Q_e} = \frac{1}{K_L Q_m} + \frac{1}{Q_m} c_e \qquad (3)$$

Freundlich:

$$\ln Q_e = \ln K_F + \frac{1}{n} \ln c_e \qquad (4)$$

Dubinin-Radushkevich:

$$\ln Q_e = \ln Q_m - \beta \left[RT \cdot \ln(1 + {}^{1}/_{c_e}) \right]^2 \qquad (5)$$

Temkin:

$$Q_e = \frac{RT}{b} \ln K_T + \frac{RT}{b} \ln c_e \qquad (6)$$

Where c_e corresponds to the equilibrium concentration of AgNPs (mg.ml^{-1}), Q_e and Q_m are the equilibrium and maximum adsorption capacities of the vaterite crystals (mg of AgNPs per g of $CaCO_3$), respectively; K_i (i = L, F, T) is the adsorption constant, β (mol^2/kJ^2) is the constant related to the mean free energy change, and *n*, *b* are other fitting parameters of Freundlich and Temkin isotherms, respectively. Gas constant R = 8.314 J mol^{-1} K^{-1} and temperature T = 293 K.

Non-linear fitting of the experimental data was also performed on Excel using Solver Add-In for the Sips model:

Sips equation:

$$Q_e = \frac{K_S {c_e}^{\beta}}{1 - A \cdot {c_e}^{\beta}} \qquad (7)$$

Where c_e is defined above, K_s (L.g^{-1}) is the adsorption constant, and *A* and β other fitting parameters.

For all the fittings, the R^2, coefficient of linear regression, was calculated as $1 - \frac{\sum(y_{fit} - y)^2}{\sum(y - \bar{y})^2}$ where y and y_{fit} are experimental and predicted (fitted) values of Q_e, respectively, and $\bar{y}$ the mean experimental value of Q_e.

2.2.4. Extraction of AgNPs from the hybrids

To characterise the AgNPs loaded into the $CaCO_3$ crystals, approx. 3 mg of hybrids were dissolved in approx. 2% acetic acid and then centrifuged at 3000 *g* for 5 min to sediment any undissolved $CaCO_3$. The stability of the AgNPs in 2% acetic acid was confirmed by UV-vis spectroscopy, where no shifts in the characteristic maximum absorbance peak of AgNPs were detected (**Figure 3-1**). Then, the supernatant with the released AgNPs was transferred into a centrifugal filter unit with a 30 kDa molecular weight cut-off (Amicon® Millipore, USA) centrifuged at 5000 *g* for 5 min and then washed three times with Milli-Q water. The nanoparticles were then characterised as described below.

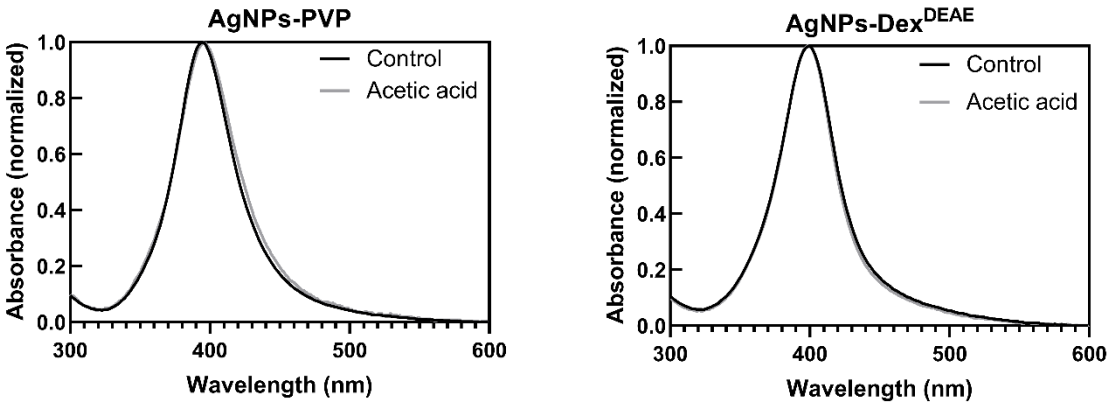

Figure 3-1. UV-vis spectra of AgNPs-PVP and AgNPs-Dex^{DEAE} in water (Control) and in 2% acetic acid (Acetic acid).

2.2.5. Characterisation of the AgNPs, $CaCO_3$ and $CaCO_3$/AgNPs hybrids

Ultraviolet-visible (UV-vis) spectroscopy: AgNPs present size-dependent optical properties, making UV-vis analysis a simple and highly sensitive method to evaluate AgNPs formation, size and stability[184,185]. For analysis, AgNPs were diluted with ultrapure, type I water to an absorbance below one and the UV-vis extinction spectra were recorded in a NanoDrop One spectrophotometer (Thermo Scientific, USA) from 190 to 850 nm. To study the stability of the AgNPs in the presence of $CaCO_3$ precursor salts, AgNPs were added toa mixture of Tris Buffer Saline (6x), ultrapure, type I water and a Ca^{2+} donor salt ($CaCl_2$ $CaBr_2$, CaI_2 or $Ca(NO_3)_2$) and then analysed by UV-vis spectroscopy. The ratios between all the chemicals were kept constant.

Transmission electron microscopy (TEM): To analyse the distribution of AgNPs into $CaCO_3$ crystals, $CaCO_3$/AgNPs hybrids were embedded in LR White Resin (Agar Scientific Ltd, Stansted, UK) and cured for three days at 50°C. Embedded samples were cross-sectioned using an Ultracut E ultramicrotome (Reichert-Jung, Wetzlar, Germany) and mounted on holey carbon film copper grids (Agar Scientific Ltd, Stansted, UK). Around 100 AgNPs, embedded in or released from the hybrids, were analysed using the ImageJ software (NIH, USA), to estimate the average size and distribution of the nanoparticles after being loaded into $CaCO_3$.

Dynamic light scattering (DLS) analysis: DLS analysis was performed to determine the zeta-potential of the hybrids in ultrapure, type I water using a Zetasizer Nano ZS (Malvern, UK). The zeta potential mean value represents the average of 50 runs.

Induced Couple Plasma Mass Spectroscopy (ICP-MS): The samples were digested with a fresh mixture of one part of 70% HNO_3 and three parts of 37% HCl (v/v) to ensure the formation of soluble silver chloride complexes [$AgCl_x^{1-x}$] instead of insoluble AgCl. All the digested samples presented a concentration of silver lower than 10 $\mu g.ml^{-1}$ and HCl content above 10% (v/v). The samples were digested at room temperature in the dark for over 1h and then 25 to 50 µl of digested sample diluted with 1 ml of 2% HNO_3 before analysis. A calibration curve was obtained for each independent ICP analysis with silver and calcium concentrations ranging between 3 $\mu g.L^{-1}$ to 800 $\mu g.L^{-1}$ and 7 $\mu g\ L^{-1}$ to 1800 $\mu g.L^{-1}$, respectively. The coefficient of determination of the standards calibration curve was always superior to 0.99.

Scanning electron microscopy (SEM): The morphology of $CaCO_3$ and $CaCO_3$/AgNPs hybrids was analysed by SEM (JEOL, JSM-7100f, Tokyo, Japan). The samples were mounted on stubs using double-sided carbon tape and then coated with a 5 nm thick layer of gold using a rotary pumped coater (Quorum Q150R ES, UK). Samples were analysed with a secondary electron detector and an acceleration voltage between 2.0 and 10.0 kV. The surface roughness was analysed using the surface plot analysis tool on ImageJ software (NIH, USA). The average size of the nanocrystallites that compose $CaCO_3$ vaterite and the hybrids was estimated by measuring the diameter of 100 nanocrystallites using the ImageJ software (NIH, USA).

SEM coupled with energy-dispersive X-ray spectroscopy (SEM-EDS): To determine the hybrids surface composition, samples were mounted on stubs using double-sided carbon tape and analysed directly with an energy dispersive X-Ray detector. An

accelerating voltage of 10 kV and a working distance of 10 mm was used. The probe current was optimised to give a dead time of approximate 45%.

Fourier transform infrared (FTIR) spectroscopy: The presence of the capping agent on the surface of the AgNPs and the crystalline structure of $CaCO_3$ and $CaCO_3$/AgNPs microparticles was analysed by FTIR spectroscopy (Spectrum Two FTIR spectrometer, PerkinElmer, Uberlingen, Germany). Before analysis, all the residual water from $CaCO_3$ and $CaCO_3$/AgNPs was removed by drying the samples at 30 ºC until constant weight. In the case of the AgNPs, the colloids of concentrated nanoparticles were poured on top of the ATR crystal and then dried with a Dexter® heat air gun before analysis until no water peaks were detectable. The analysis conditions were the same for all the samples*, i.e.*, 32 scans were run for each sample between 500 and 4000 cm^{-1}, with a resolution of 4 cm^{-1}. The ATR (attenuated total reflectance) technique was used in all the measurements.

X-ray diffraction (XRD): The crystalline structure of the samples was analysed in a SmartLab SE X-Ray diffraction system from Rigaku Co. Ltd. (Tokyo, Japan) with a Kβ filter for cupper (λ = 0.1392 nm). Samples were scanned with a θ/2θ scan axis. The scan range varied between 20° and 80°, and the scan mode and speed were 1D and 5°/min, respectively.

Diffusion coefficient estimation: The diffusion coefficient was determined using the Stokes-Einstein equation below:

$$D = \frac{K_B \times T}{6\pi \times \eta \times r} \qquad (8)$$

Where D is the diffusion coefficient ($m^2.s^{-1}$), K_B the Boltzmann constant, T the temperature in kelvin (K), η the dynamic viscosity (Pa.s) and r (m) the radius of the spherical nanoparticles.

2.2.6. Analysis of AgNPs release from the hybrids

The release of AgNPs from the $CaCO_3$/AgNPs hybrids was assessed at three different pH values: 5.0; 7.5 and 9.0. Acetate buffer was used to test the release at pH 5.0 and TBS at pH 7.5 and 9.0. When needed, the pH was adjusted with NaOH (2 M) or HCl (1 M). The $CaCO_3$/AgNPs hybrids were incubated in acetate buffer (pH 5) and TBS (pH 7.5 and 9.0) at 37°C and left under constant stirring (500 rpm) in a ThermoMixer® C with a SmartBlock (Eppendorf, Germany). The final concentration of the hybrids was 2 $mg.ml^{-1}$. After 15 min and 48h, the samples were centrifuged at 2000 *g* for 5 min, and then 35 µl of supernatant taken for calcium and silver quantification by ICP-MS. The aliquots were replaced with 35

µl of fresh buffer solution to maintain the same final volume. All the experiments were done in triplicate.

3. Results and discussion

3.1. Loading of capped AgNPs into vaterite crystals

AgNPs stabilisation is crucial as its agglomeration leads to decreased or complete loss of the optical and antimicrobial properties[255]. In **Chapter 2** the synthesis of AgNPs by chemical reduction in the presence of different capping agents: Citrate, PVP, Dex, Dex^{DEAE} and Dex^{CM} was presented as well as the characterization of the obtained nanoparticles. The capping agents not only helped to control the growth of the nanoparticles during synthesis but also provided colloidal stability after production through steric hindrance and electrostatic repulsions, essential for loading AgNPs into vaterite $CaCO_3$ (**Figure 3-2**).

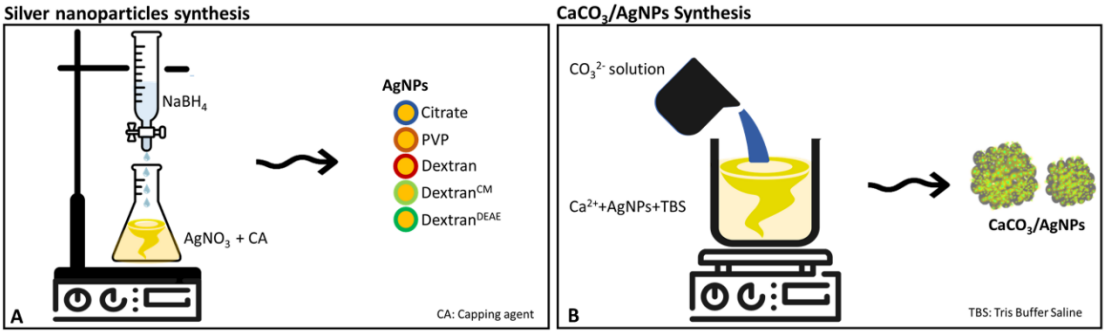

Figure 3-2. Scheme of the AgNPs synthesis and hybrids production. A) silver nanoparticles synthesis with different capping agents. B) $CaCO_3$/AgNPs production by co-precipitation.

In this work, AgNPs were loaded into vaterite by co-precipitation, a well-established approach for effective loading by mixing the compound of interest with the precursor salts of $CaCO_3$[1]. AgNPs were firstly mixed with $CaCl_2$ and TBS, and then Na_2CO_3 was added, triggering the rapid formation of $CaCO_3$. Due to the interaction of AgNPs with the precursor salts possibly affecting the stability of the nanoparticles by shielding or displacing the capping agent, an initial stability screening was carried. To that end, AgNPs were mixed with the same quantities of $CaCl_2$ (150 mM), TBS(6x) and ultrapure, type I water used in the co-precipitation reaction and then analysed by UV-vis spectroscopy. To broaden the AgNPs stability screening, $CaBr_2$, CaI_2 and $Ca(NO_3)_2$ salts were also tested, as they can be used as alternative donors of Ca^{2+} ions. **Figure 3-3** presents the colour changes and absorption spectra of the AgNPs mixed with only water (labelled "Control") or with a mixture of water, TBS and a calcium salt. The results show that AgNPs-Citrate, AgNPs-Dex and AgNPs-Dex^{CM} are highly unstable when mixed with any type of calcium

salt and TBS, clumping together and forming aggregates. This effect is clear by the broadening or disappearance of the typical peak of maximum absorbance (λ_{max}) of AgNPs around 400 nm, and the colour change from amber to greyish. The instability of AgNPs coated with citrate, Dex and Dex^{CM} was caused by the interaction of the salts with the capping agents and consequent loss of the electrostatic repulsions between the nanoparticles. On the other hand, the AgNPs coated with Dex^{DEAE} and PVP were stable in the mixtures with $CaCl_2$ and $Ca(NO_3)_2$, as demonstrated by the presence of the same λ_{max} peak and yellow colour. In the case of the solutions with $CaBr_2$, the data shows that the salt affected the stability of all the nanoparticles, evidenced by λ_{max} peak shift to higher wavelengths or band broadening. CaI_2 had an even bigger impact on the stability of the AgNPs as demonstrated by the UV-vis data. These results show that increasing the calcium counterion atomic number affects the stability of the AgNPs, as they present a higher reducing power and more easily destabilize the nanoparticles.

The AgNPs coated with PVP were the only nanoparticles with a negative zeta potential that did not aggregate when mixed with some of the salts. This resulted from PVP mainly promoting the stability of the AgNPs through repulsive forces, created by the hydrophobic carbon chains, and steric hindrance *via* its bulky structure[190]. Moreover, the silver/PVP ratio (0.3 m/m) was lower than the silver/dextrans ratio (1.7 m/m), and therefore, AgNPs capped with PVP presented a higher steric hindrance effect.

In the case of the AgNPs coated with Dex^{DEAE} the stability in the presence of some of the calcium salts was promoted by the electrostatic repulsions evidenced on the positive zeta potential (47.8±11.7 mV). Unlike AgNPs-Dex and AgNPs-Dex^{CM}, the electrostatic repulsions between the AgNPs were kept (no aggregation of nanoparticles), nonetheless these were disrupted by the calcium counterions that presented higher reducing power, like iodide.

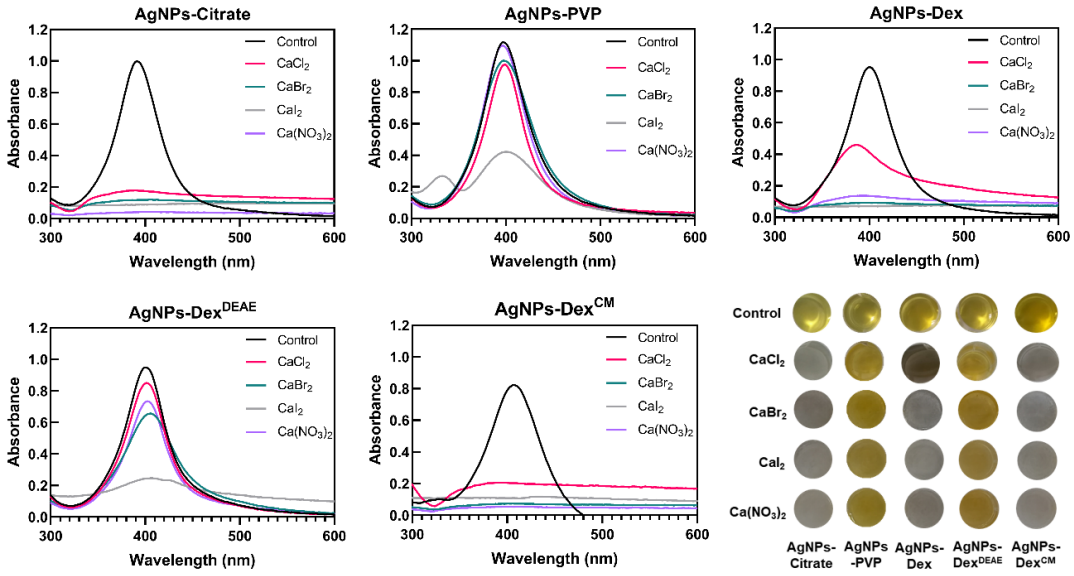

Figure 3-3. UV-vis absorption spectra and colour changes of AgNPs mixed with ultrapure, type I water (Control) or a mixture of Tris Buffer Saline (6x), ultrapure, type I water and a calcium salt ($CaCl_2$ $CaBr_2$, CaI_2 or $Ca(NO_3)_2$, 150mM solution).

To confirm the selection of the best AgNPs to produce $CaCO_3$/AgNPs hybrids, all the capped AgNPs were loaded into the vaterite crystals *via* co-precipitation as described above. **Figure 3-4** presents the transmittance images of vaterite crystals co-precipitated with the different AgNPs. As expected, there was no visible agglomeration during the co-precipitation of $CaCO_3$ crystals with AgNPs-PVP and AgNPs-Dex^{DEAE} as these nanoparticles possess the highest stability. On the other hand, agglomerates were detected when $CaCO_3$ crystals were co-precipitated with AgNPs-Citrate and AgNPs-Dex^{CM}, as these nanoparticles are easily destabilized by the salts used to synthetise the hybrids. In the case of the vaterite crystals co-precipitated with AgNPs-Dex, silver agglomerates were not visible on the transmission images. Nonetheless, the immediate colour change from amber to grey of the reaction medium, and the changes in the UV-vis absorption spectrum in **Figure 3-3**, indicate the formation of agglomerates with diameters below 1 µm, and therefore not detectable under the optical microscope.

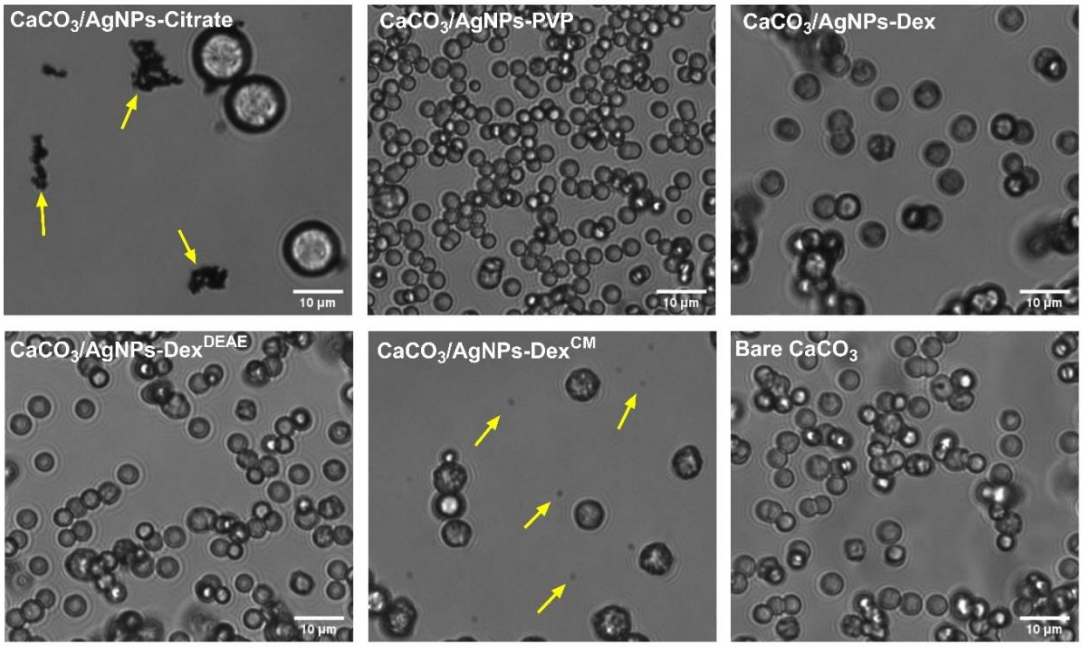

Figure 3-4. Transmittance images of bare $CaCO_3$ and $CaCO_3$ crystals co-precipitated with AgNPs in the reaction medium. The initial AgNPs/$CaCO_3$ ratio was 2% (m/m). Some of the AgNPs agglomerates are pointed with yellow arrows.

The stability screening revealed that the AgNPs coated with PVP and Dex^{DEAE} were the most appropriate candidates for synthesising $CaCO_3$/AgNPs hybrids, and the following sections are focused on their synthesis and characterisation.

3.2. Characterisation of $CaCO_3$/AgNPs hybrids

3.2.1. Morphology

Figure 3-5 depicts the bare $CaCO_3$ crystals and the crystals co-precipitated with 2 % m/m of AgNPs. The colour of the crystals, white for the bare $CaCO_3$ and amber for the loaded ones, demonstrates that the AgNPs were embedded into the crystals. The SEM images show that in both cases, the AgNPs did not affect the formation of vaterite over other $CaCO_3$ polymorphs, and its typical morphology was maintained (spherical shape, composed of nanosized primary crystals, or the so-called nanocrystallites**.** The roughness mapping of the surfaces is present in **Figure 3-5 E, J and O**. All the samples presented rough surfaces due to vaterite crystals being composed of primary nanocrystallites which impart this characteristic. Bare $CaCO_3$, $CaCO_3$/AgNPs-Dex^{DEAE} and $CaCO_3$/AgNPs-PVP hybrids presented nanocrystallites with similar diameters, 96.6 ± 23.4, 69.0 ± 18.7 and 74.1 ± 18.9 nm, respectively; demonstrating that the incorporation of AgNPs coated with PVP

or Dex^{DEAE} into vaterite did not affect the outer surface morphology, size or shape drastically.

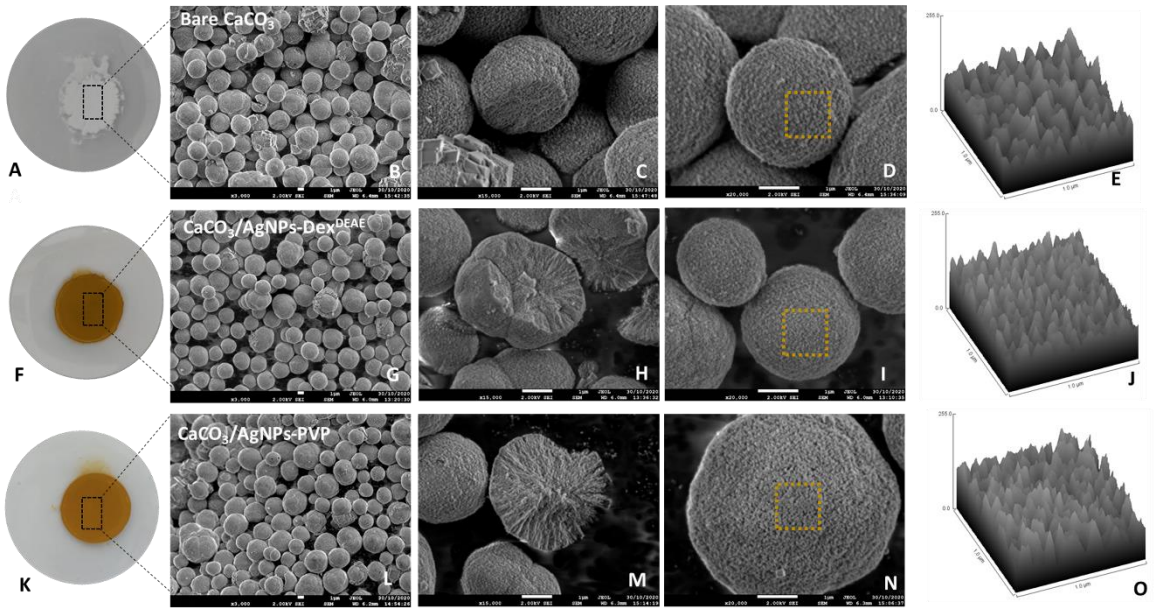

Figure 3-5. Images of the dried crystals (A, F and K) and SEM images of the bare crystals (B, C and D) and the crystals co-precipitated with AgNPs-Dex^{DEAE} (G, H and I) and AgNPs-PVP (L, M and N). The respective surface roughness plots (E, J and O) of the areas marked with amber outline (D, I and N) are also presented. The initial AgNPs/$CaCO_3$ ratio was 2% (m/m).

The average size of the bare $CaCO_3$ crystals, $CaCO_3$/AgNPs-Dex^{DEAE} and $CaCO_3$/AgNPs-PVP was 4.03 ±0.70, 2.84 ± 0.63, and 3.97 ± 1.24 µm, respectively. All the crystals presented sizes in the micrometre range, and overall, the size of the crystals was not affected by the initial concentration of AgNPs (**Figure 3-6**). Nonetheless, it was verified that the size of the crystals co-precipitated with AgNPs-PVP fluctuated more between replicates than the size of the crystals co-precipitated with AgNPs-Dex^{DEAE}, as demonstrated by the larger standard deviations in **Figure 3-6**. These results indicate that Dex^{DEAE} promotes a more homogenous mixing and crystals growth between replicates than PVP.

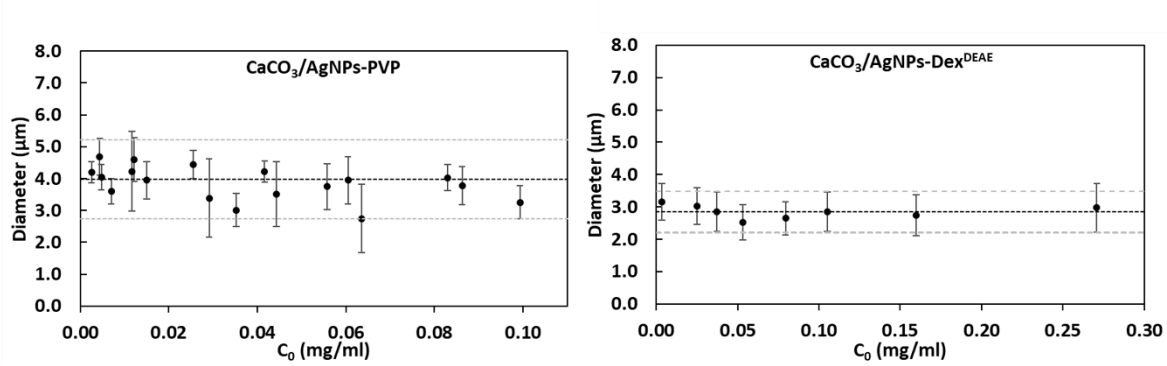

Figure 3-6. Crystals size distribution for different initial concentrations of AgNPs. Data points correspond to three replicates per concentration. C_0 represents the initial concentration of silver. The average size and standard deviations are represented with black and grey dashed lines, respectively.

3.2.2. Structure

Figure 3-7 presents cross-section images of bare $CaCO_3$ (**A, B, C and D**) and $CaCO_3$ loaded with AgNPs-Dex^{DEAE} (**E, F, G and H**) and AgNPs-PVP (**I, J, K and L**). The images of bare $CaCO_3$ clearly show the typical structure of vaterite crystals composed of nanosized crystals. The crystalline structure is confirmed by the lattices of the nanosized crystals (d-spacing 2.72 Å) as depicted in **Image C inset**. The cross-section images of the crystals loaded with AgNPs show that the AgNPs (darker spots) are prevalently present in the region closer to the surface, and regardless of the AgNPs capping agent, there were no AgNPs in the inner core of $CaCO_3$ crystals (**Image H and L**).

The formation of vaterite is a gradual and complex process. Different research groups have studied vaterite formation, and different mechanisms have been proposed[256–259]. Bots, P. et al.[260] proposed a pathway that combines previously proposed mechanisms. Firstly, hydrated and disordered amorphous calcium carbonate (ACC) forms and then rapidly transforms into a more ordered and dehydrated form, which then agglomerates through spherulitic growth and forms vaterite (Stage 1). When the supersaturation of the solution decreases sufficiently, the mechanism changes to ACC dissolution and vaterite crystal growth (Stage 2), followed by vaterite particles Ostwald ripening (Stage 3)[260]. TEM results indicate that AgNPs do not participate in the initial formation of the crystals (Stage 1) due to the supersaturation of the reaction medium with Ca^{2+} and CO_3^{2-} ions. The presence of AgNPs closer to the surface indicates that the AgNPs adsorb to the crystals at a later stage, most probably stages 2 and 3. This may be related to the lower diffusion coefficients of AgNPs (0.38×10^{-10} $m^2.s^{-1}$ and 0.38×10^{-10} $m^2.s^{-1}$ for AgNPs-PVP and AgNPs-

Dex^{DEAE}, respectively) in comparison with Ca^{2+} and CO_3^{2-} diffusion coefficients (7.92×10^{-10} $m^2.s^{-1}$ and 9.20×10^{-10} $m^2.s^{-1}$, respectively)[261]. As a result of this, Ca^{2+} and CO_3^{2-} ions are first consumed during the crystal growth and only at later stages, when the concentration of ions drops, such as during Ostwald ripening, AgNPs are embedded into the crystals. These results demonstrate that diffusion limitations in the reaction medium contributes to the accumulation of AgNPs on the hybrids surface.

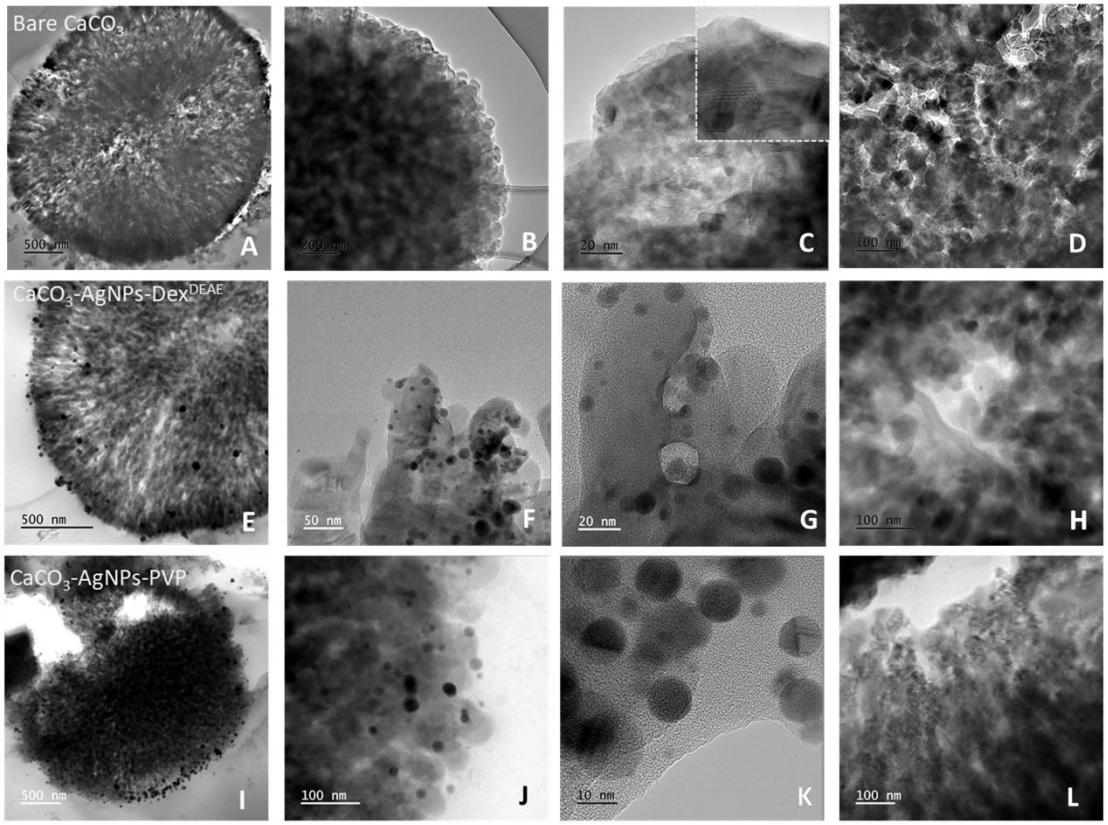

Figure 3-7. TEM images of cross-sectioned bare crystals (A, B, C and D) and crystals co-precipitated with AgNPs-Dex^{DEAE} (E, F, G and H) and AgNPs-PVP (I, K, J and L). The initial AgNPs/$CaCO_3$ ratio was 2% (m/m).

SEM-EDX analysis was carried out to study the elementary composition of the hybrids and the distribution of AgNPs on the surface of the crystals. As depicted in **Figure 3-8**, the mapping images of the hybrids confirm the high contents of oxygen and calcium, as the $CaCO_3$/AgNPs hybrids are mainly composed of $CaCO_3$ (approx. 98%). The mapping images of silver demonstrate that AgNPs are distributed homogeneously on the surface of the crystals, with the $CaCO_3$/AgNPs-Dex^{DEAE} hybrids also presenting AgNPs clusters, highlighted by the brighter areas. The crystals spectrograms also confirm the presence of high contents of calcium and oxygen, and despite the lower intensity of the silver peaks,

these were detectable around the 3 KeV region (2.979 KeV and 3.146 KeV), showing the presence of silver embedded into the $CaCO_3$ hybrids[262–264].

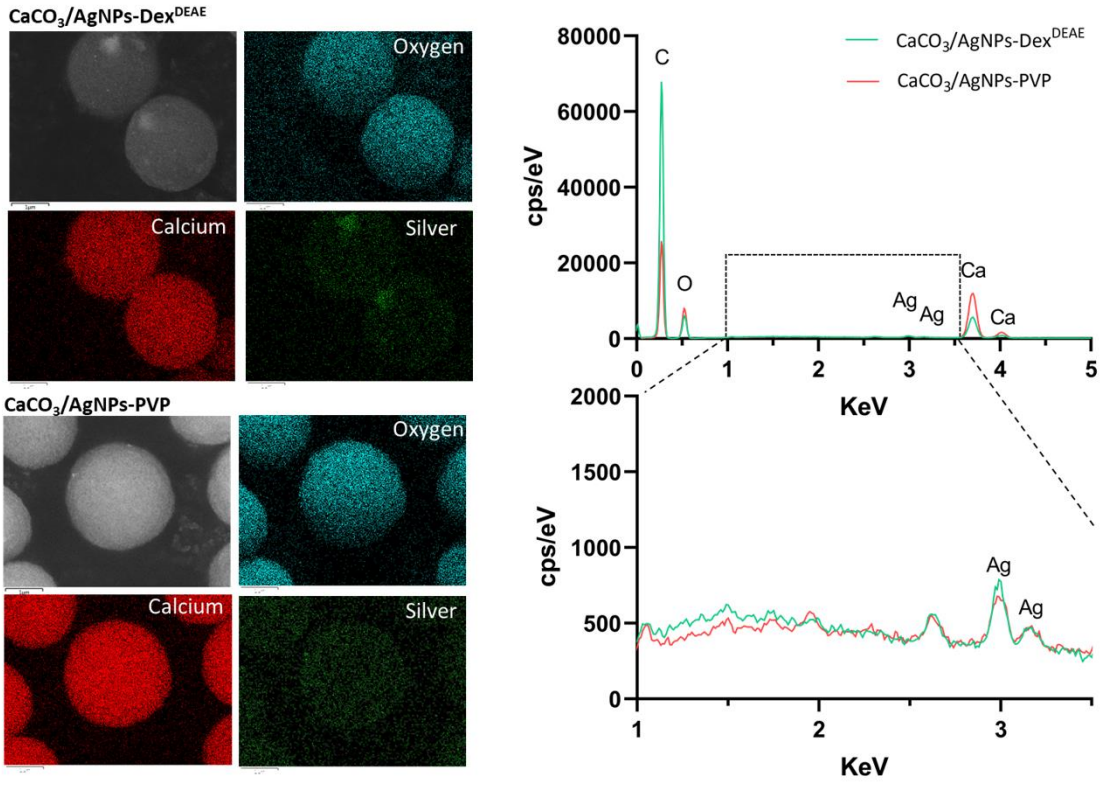

Figure 3-8. SEM-EDX mapping images and respective spectrograms of the hybrids co-precipitated with AgNPs-Dex^{DEAE} and AgNPs-PVP. The initial AgNPs/$CaCO_3$ ratio was 2% (m/m).

3.2.3. Crystallinity

FTIR analysis was conducted to determine the predominant $CaCO_3$ polymorph in the $CaCO_3$/AgNPs hybrids. For a better comparison between samples, the intensities of the obtained spectra were divided by the intensity of a typical band, in this case the band $I_{1400-1396}$, assigned to CO_3^{2-} anti-symmetrical stretching. **Figure 3-9** presents the FTIR spectrum of bare vaterite, bare calcite, $CaCO_3$/AgNPs-Dex^{DEAE} and $CaCO_3$/AgNPs-PVP hybrids. Regardless of the sample, all the crystals presented characteristic bands with similar intensities in the regions 848-849 cm^{-1} and 872-874 cm^{-1} resulting from CO_3^{2-} out-of-plane bending (ν_2 mode) and the region 1397-1407 cm^{-1} originated by CO_3^{2-} anti-symmetrical stretching (ν_3 mode)[265,266]. Shifts in these bands result from the polymorphic composition of the sample and the presence of other components, like silver and the capping agents, that can interact with $CaCO_3$[267].

The bare calcite sample presented the characteristic bands with maximum transmittance at 712, 1795, and 1400 cm^{-1}. These bands correspond to CO_3^{2-} in-plane bending (ν_4 mode),

symmetric stretching (ν_1 mode) + ν_4 mode, and ν_3 mode, respectively[268,269]. Bare vaterite also presented its characteristic bands at 745 cm^{-1} (ν_4 mode), 1088 cm^{-1} (ν_1 mode) and a split and broad band around 1397-1459 cm^{-1} (ν_3 mode) due to the asymmetry around the carbonate ion[270]. The vaterite spectrum also presented a very small band at 713 cm^{-1}, which indicates the presence of minimal quantities of calcite in the sample. Low calcite contents are expectable in vaterite samples, as calcite is the most stable $CaCO_3$ polymorph. The spectra of $CaCO_3$/AgNPs-PVP and $CaCO_3$/AgNPs-Dex^{DEAE} hybrids were very similar to that of bare vaterite, also presenting the same characteristic bands at 745 and 1088 cm^{-1}; as well as a split and broad band around 1397-1459 cm^{-1}. There is also a very low intensity band at 713 cm^{-1}, which indicates the presence of small quantities of calcite in the samples. Overall, the data demonstrate that the main polymorph in the $CaCO_3$ samples loaded with AgNPs is vaterite with a small quantity of calcite being present. These results match the XRD data presented in **Figure 3-10** and the SEM images in**Figure 3-5**, where is possible to mainly detect vaterite crystals (spherical shape) and small contents of calcite (rhombohedral shape). The predominance of vaterite is beneficial, as it has a porous structure with a large surface area[271] that can accommodate, protect and release other compounds of interest in combination with AgNPs.

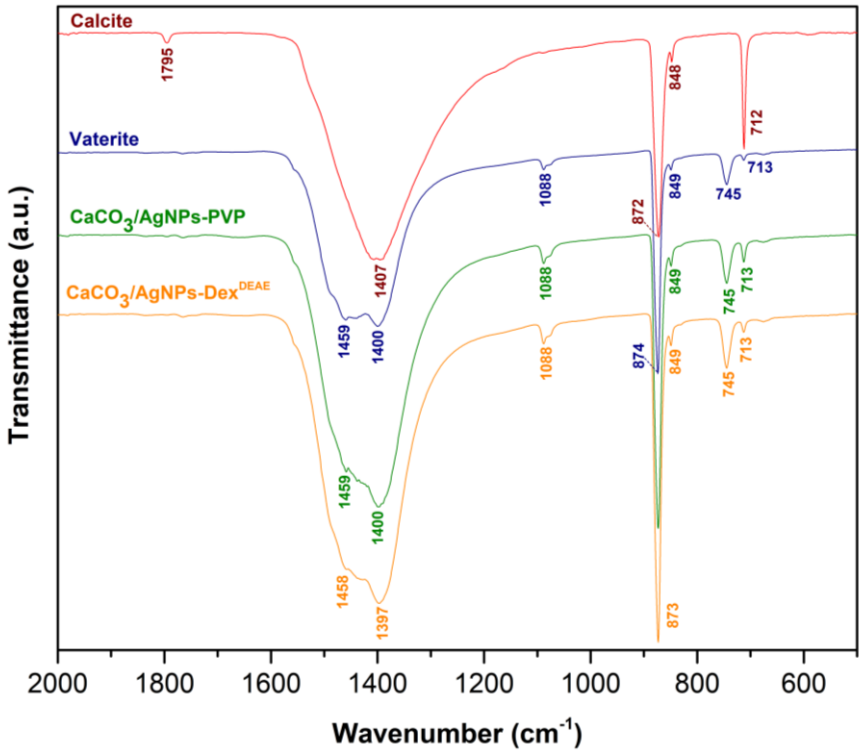

Figure 3-9. FTIR spectra of bare vaterite, bare calcite, $CaCO_3$/AgNPs-Dex^{DEAE} and $CaCO_3$/AgNPs-PVP hybrids. The initial AgNPs/$CaCO_3$ ratio was 2% (m/m).

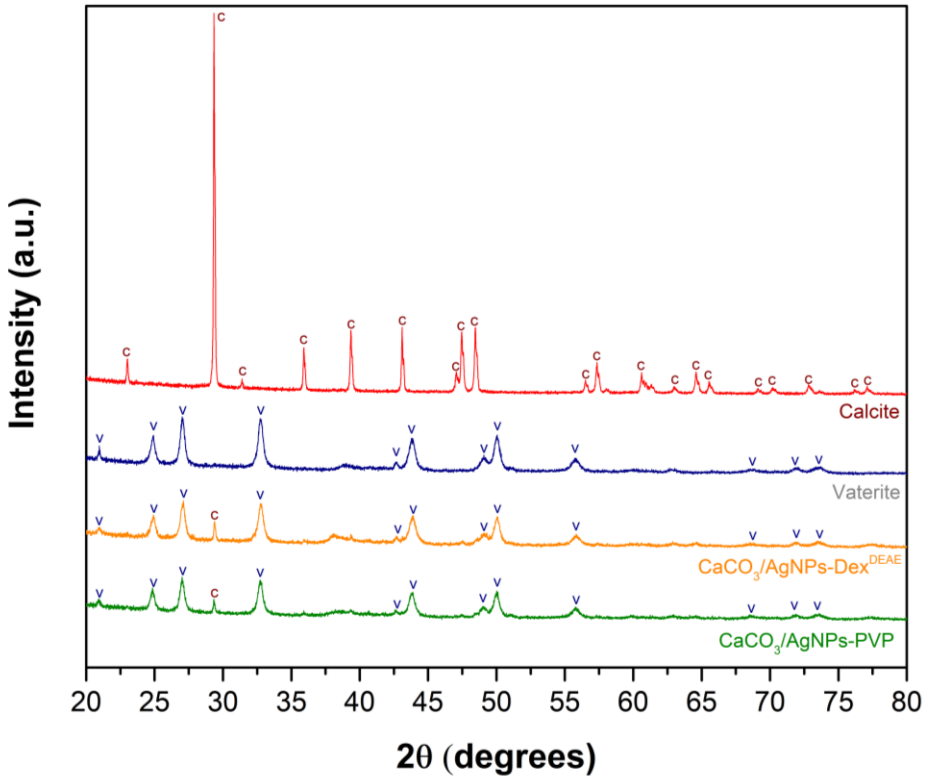

Figure 3-10. XRD spectra of bare vaterite, bare calcite, $CaCO_3$/AgNPs-Dex^{DEAE} and $CaCO_3$/AgNPs-PVP hybrids. The initial AgNPs/$CaCO_3$ ratio was 2% (m/m).

3.2.4. Surface charge

The zeta potential of bare $CaCO_3$ and $CaCO_3$ loaded with AgNPs was determined in ultrapure, type I water (pH 5.28) to study the effect of AgNPs on the electrical potential of the crystals. Bare $CaCO_3$ crystals presented a positive zeta potential (9.66 ± 4.38 mV) which is characteristic of vaterite and has been reported by different authors[102,272,273]. $CaCO_3$/AgNPs-PVP hybrids presented a slightly negative/neutral zeta potential (-2.41 ± 3.98 mV) resultant from the presence of AgNPs capped with PVP, which have a negative zeta potential of -24.0 ± 8.0 mV (**Table 2-2**). Moreover, PVP might also affect the availability and distribution of ions on the surface of $CaCO_3$. On the other hand, $CaCO_3$ loaded with AgNPs-Dex^{DEAE} presented a positively charged surface with a zeta potential of 23.6 ± 4.4 mV, higher than the zeta potential of bare $CaCO_3$ and $CaCO_3$/AgNPs-PVP. This is due to the presence of Dex^{DEAE}, a highly positively charged polymer that is responsible for the positive zeta potential of the AgNPs (45.2 ± 6.9 mV, **Table 2-2**).

The effect of AgNPs on the zeta potential of $CaCO_3$ crystals broadens the range of possibilities for $CaCO_3$ use, including the application of the modified crystals to load drugs with opposite charges. This would help to turn pharmacological treatments simpler by allowing the combination of different therapeutic agents in the same vector.

3.3. Mechanism of AgNPs loading into $CaCO_3$ crystals

Figure 3-11 and **Figure 3-12** present the adsorption isotherms and loading efficiency, respectively, of $CaCO_3$ hybrids loaded with AgNPs-PVP and AgNPs-Dex^{DEAE}. In both figures, the data corresponding to the $CaCO_3$/AgNPs-PVP hybrids presents larger standard deviations as the size of the crystals co-precipitated with AgNPs-PVP fluctuated more between replicates, as referred in **Section 3.2.1.**.

Figure 3-11 depicts an evident difference between the affinity of AgNPs-PVP and AgNPs-Dex^{DEAE} to $CaCO_3$. In both cases, the loaded content of AgNPs into the hybrids increased with the concentration of AgNPs and then reached a plateau. The maximum adsorption capacity of vaterite for the AgNPs coated with Dex^{DEAE} was 35.8 ± 6.0 $mg.g^{-1}$, about two times more than that for the AgNPs coated with PVP (18.5 ± 0.9 $mg.g^{-1}$).

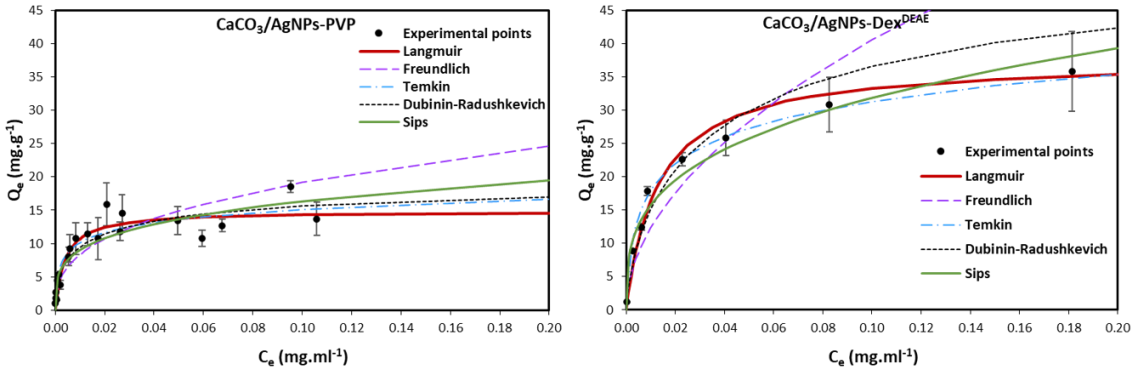

Figure 3-11. Adsorption isotherms of AgNPs-PVP and AgNPs-Dex^{DEAE} loaded by co-precipitation into $CaCO_3$ and respective fitting models. Data points correspond to three (AgNPs/PVP-$CaCO_3$) and one ($CACO_3$/AgNPs-Dex^{DEAE}) independent experiment with three replicates per point. Q_e represents the adsorption capacity of silver into vaterite ($mg.g^{-1}$) at equilibrium, and c_e the supernatant equilibrium concentration of silver ($mg.ml^{-1}$).

The loading efficiency results also demonstrated the different affinities of the AgNPs to vaterite. As shown in **Figure 3-12**, the loading efficiency of AgNPs-PVP and AgNPs-Dex^{DEAE} into $CaCO_3$ decreased inversely with the initial concentration of AgNPs, due to the saturation of $CaCO_3$ with AgNPs. Due to the higher uptake of AgNPs/Dex^{DEAE} into the $CaCO_3$ crystals, the loading efficiency at similar concentrations of AgNPs was higher for AgNPs-Dex^{DEAE}. Yin, W. et al.[274] recently reported that hierarchical mesoporous calcite presents different affinities to AgNPs coated with PVP and poly(vinyl alcohol) (PVA). The authors showed that calcite adsorbs higher contents of AgNPs coated with PVP than with PVA. These results, as well as the results reported in this chapter, show that the capping agents affect the affinity of AgNPs to the substrate/carrier, and therefore, the adsorption capacity.

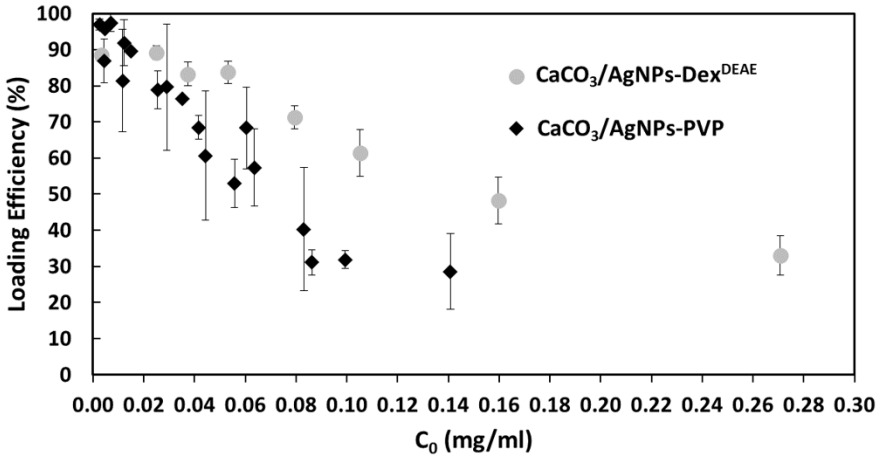

Figure 3-12. Loading efficiency of AgNPs-PVP and AgNPs-Dex^{DEAE} loaded by co-precipitation into $CaCO_3$. Data points correspond to three (AgNPs/PVP-$CaCO_3$) and one ($CACO_3$/AgNPs-Dex^{DEAE}) independent experiment with three replicates per point (C_0). C_0 represents the initial concentration of silver.

The adsorption mechanism was investigated by fitting the experimental data to well-known models of adsorption with two and three-parameters (**Figure 3-11** and **Table 3-1**).

Systems with homogeneous monolayer adsorption obey the Langmuir adsorption model. Mathematical fitting of the experimental data revealed that the adsorption of AgNPs-PVP and AgNPs-Dex^{DEAE} into vaterite crystals obeys the Langmuir equation with an R^2 of 0.951 and 0.996, respectively. Fitting of the experimental data to other adsorption isotherms resulted in lower R^2 coefficients (**Table 3-1**). Importantly, all these models assume different types of repulsive or attractive AgNPs-AgNPs or AgNPs-$CaCO_3$ interactions. The Freundlich model of adsorption is semi-empirical. It describes heterogeneous adsorption in systems where adsorption is accompanied either by AgNPs-AgNPs attraction (n>1) or by AgNPs-AgNPs repulsion (n<1) during adsorption on the surface of $CaCO_3$. Similarly, Dubinin-Radushkevich isotherm is a semi-empirical adsorption model. It describes heterogeneous systems with a Gaussian distribution of the energy of adsorption sites. This model is often applicable to systems where the adsorbent size is comparable with the size of the pores. Temkin isotherm explains AgNPs-$CaCO_3$ interactions in relation to the heat of adsorption, *i.e.*, it assumes that the heat of adsorption of AgNPs decreases linearly with the increased coverage of the $CaCO_3$ surface. None of these models describes the adsorption of AgNPs coated with PVP and Dex^{DEAE} better than the Langmuir isotherm, and therefore the mathematical fitting of the data suggests no or negligible interaction between the AgNPs.

Table 3-1. Mathematical fitting of the adsorption isotherm models for AgNPs-PVP and AgNPs-Dex^{DEAE} loaded by co-precipitation into $CaCO_3$. R^2 - coefficient of linear regression.

		$CaCO_3$/AgNPs-PVP		**$CaCO_3$/AgNPs-Dex^{DEAE}**	
Model	**Equation**	**Fitted parameters**	**R^2**	**Fitted parameters**	**R^2***
Langmuir	$Q_e = \frac{Q_m K_L c_e}{1 + K_L c_e}$	Q_m = 14.8 ± 0.8 mg.g^{-1} K_L = 263 ± 151 L.g^{-1}	0.951	Q_m = 37.6 ± 1.0 mg.g^{-1} K_L = 77 ± 11 L.g^{-1}	0.996
Freundlich	$Q_e = K_F {c_e}^{1/n}$	n = 2.8 ± 0.2 K_F = 44 ± 2	0.877	n = 1.9 ± 0.3 K_F = 134 ± 10	0.974
Dubinin-Radushkevich	$Q_e = Q_m e^{-\beta[RT \ln(1+1/c_e)]^2}$	Q_m = 18.9 ± 0.6 mg.g^{-1} β = (5.5 ± 0.4)·10^{-9}	0.907	Q_m = 50.8 ± 1.4 mg.g^{-1} β = (9.6 ± 0.7)·10^{-9}	0.973
Temkin	$Q_e = \frac{RT}{b} \ln K_T + \frac{RT}{b} \ln c_e$	b = (1.1 ± 0.1)·10^3 K_T = (1.04 ± 0.06)·10^4	0.848	b = (4.2 ± 0.2)·10^2 K_T = (2.19 ± 0.07)·10^3	0.983
Sips	$Q_e = \frac{K_S {c_e}^{\beta}}{1 - A \cdot {c_e}^{\beta}}$	A = 0 K_S = 29.5 β = 0.26	0.822	A = 0 K_S = 64.2 β = 0.30	0.949

3.4. Release of AgNPs from $CaCO_3$/AgNPs hybrids

The entrapment of AgNPs into $CaCO_3$ allows its protection from undesirable external conditions while allowing the association with small molecules able to diffuse through the mesoporous structure of vaterite. At the same time, it presents a way to release AgNPs under different conditions, as vaterite can dissolve in mild biocompatible conditions, e.g. slowly by continuously washing with water, or rapidly under acidic conditions or in the presence of chelating agents that bind to calcium ions.

Before studying the release of AgNPs at different pH values, the stability of the AgNPs loaded into $CaCO_3$ was evaluated, as the loading steps during co-precipitation can disturb the capping agents or bring nanoparticles close to each other, inducing the formation of irreversible AgNPs aggregates inside $CaCO_3$ and consequently deteriorating their antimicrobial, optical, thermal, and electrical properties.

To that end, the stability of AgNPs was evaluated by dissolving $CaCO_3$ with acetic acid and analysing the released AgNPs by UV-vis, DLS and XRD. **Figure 3-13** presents the UV-vis absorption spectra, hydrodynamic diameter determined by DLS and XRD pattern of the AgNPs coated with PVP and Dex^{DEAE} before loading into $CaCO_3$ and after the dissolution of the hybrids. The similar UV-vis spectra and hydrodynamic size distribution of the AgNPs before and after the dissolution of $CaCO_3$ indicate that the nanoparticles did not suffer drastic changes, and that any nanoparticles cluster formed inside $CaCO_3$, as depicted in the TEM and EDS images (**Figure 3-7** and **Figure 3-8**, respectively), disaggregate after being released. Nonetheless, in the case of the AgNPs coated with PVP, the slightly broader UV-vis peak and the disappearance of the peak around 10 nm in the DLS data indicate a size distribution change. Small changes in the size of the AgNPs-Dex^{DEAE} were also detected in the DLS data. To confirm these results the size of the AgNPs loaded into the hybrids was determined by analysing the TEM images of the cross-sectioned hybrids (**Figure 3-7**). The results showed that the loaded AgNPs coated with PVP and Dex^{DEAE} had an average size equal to 17 ± 9.2 and 13 ± 6.5 nm, respectively, being 4 and 3.5 nm larger than the initial nanoparticles (13 ± 4.4 and 9.5 ± 2.9 nm for the AgNPs coated with PVP and Dex^{DEAE}, respectively). This size increment (approx. 30% in both cases) was promoted by the different loading steps conditions and possibly a size-selective entrapment of the AgNPs into the crystals.

The XRD data showed that the AgNPs coated with Dex^{DEAE} and PVP present a face-centred cubic crystal structure (Card No.:9008459. Rigaku database), which is characteristic of silver metallic nanoparticles. The data also shows that the loading and entrapment of AgNPs into vaterite did not change the crystalline structure of the nanoparticles.

Overall the data presented in **Figure 3-13** shows that the co-precipitation steps (exposure to salts, centrifugation and drying at 70°C) did not drastically affect the properties of AgNPs-PVP and AgNPs-Dex^{DEAE}, and $CaCO_3$ can be used to store and protect the nanoparticles.

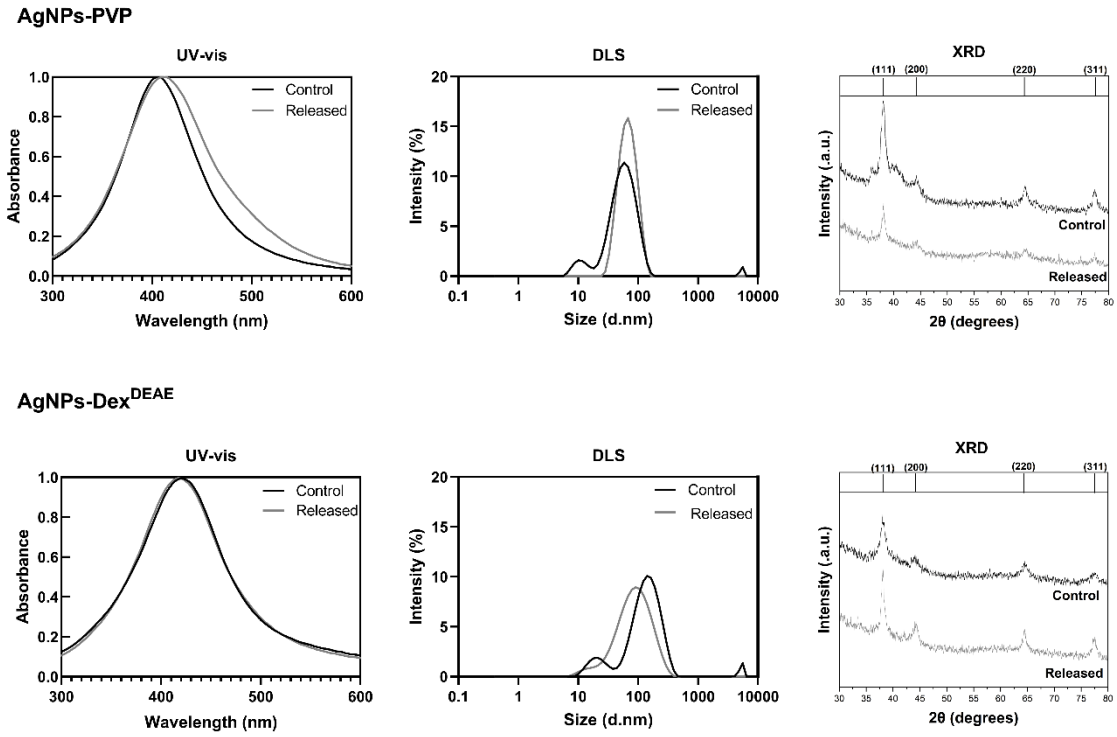

Figure 3-13. UV-vis absorption spectra, size distribution determined by DLS and XRD pattern of AgNPs-PVP and AgNPs-Dex^{DEAE} before loading (Control) into $CaCO_3$ and after being released from the corresponding hybrids (Released). AgNPs loaded into vaterite were analysed after dissolving $CaCO_3$ with acetic acid (ca. 2%).

Figure 3-14 presents the cumulative release of silver from the $CaCO_3$/AgNPs-PVP and $CaCO_3$/AgNPs-Dex^{DEAE} hybrids after 15 minutes and 48 hours at different pH values (5.0, 7.5, and 9.0). Both hybrids presented a burst release at pH 5.0, with ca. 60% and 78% of silver being immediately released from $CaCO_3$/AgNPs-PVP and $CaCO_3$/AgNPs-Dex^{DEAE} hybrids, respectively. This was caused by the dissolution of $CaCO_3$, as confirmed by the high content of calcium released (**Figure 3-15**). Almost no silver was released after 15 min at pH 7.5 and 9.0 due to the low solubility of $CaCO_3$ (**Figure 3-14** and **Figure 3-15**). Interestingly, after 48 hours, the hybrids presented a different release profile at pH 7.5 and 9.0, with $CaCO_3$/AgNPs-PVP hybrids releasing more silver at both pH values, about 40% and 58%, than $CaCO_3$/AgNPs-Dex^{DEAE} hybrids, which only released about 24% and 4%, respectively.

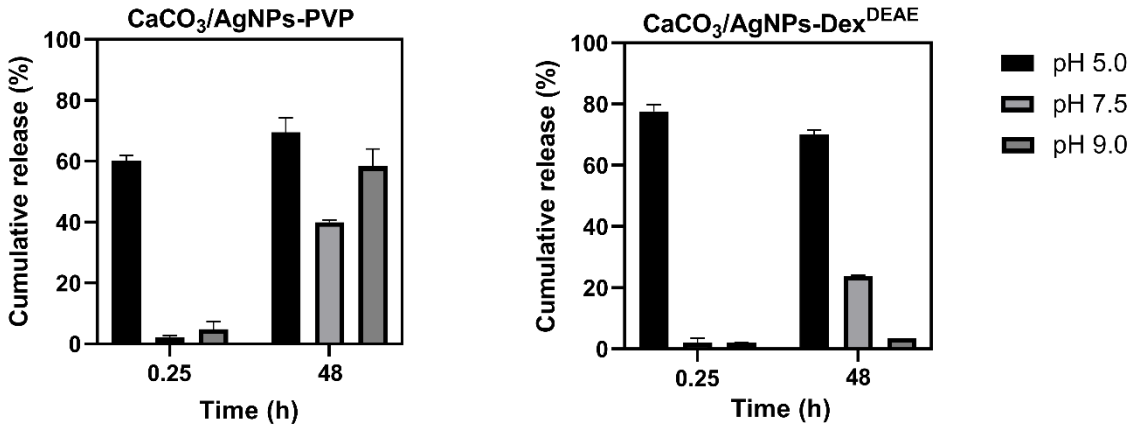

Figure 3-14. Cumulative release of silver from $CaCO_3$/AgNPs-PVP and $CaCO_3$/AgNPs-Dex^{DEAE} hybrids after 15 minutes (0.25 hours) and 48 hours in acetate buffer (pH 5.0) and TBS (pH 7.5 and 9.0). The data represents the average of three replicates.

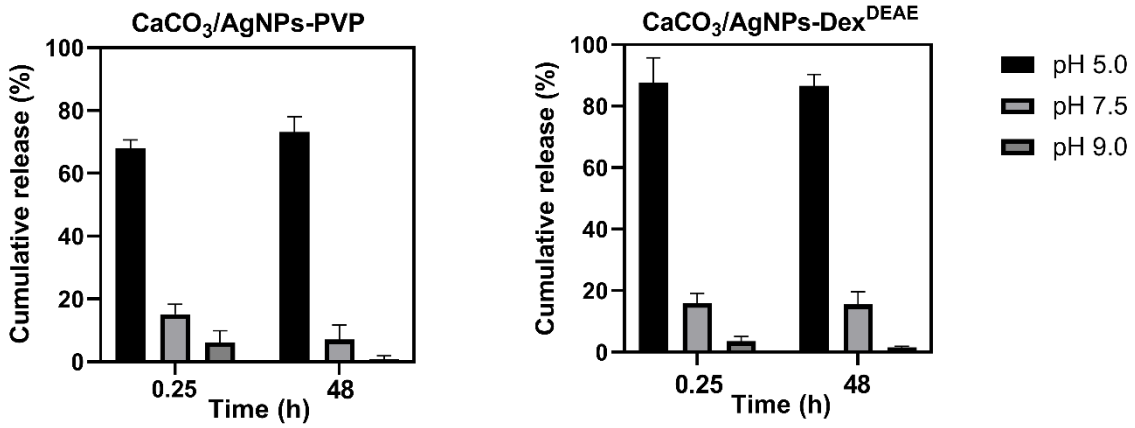

Figure 3-15. Cumulative release of calcium from $CaCO_3$/AgNPs-PVP and $CaCO_3$/AgNPs-Dex^{DEAE} hybrids after 15 minutes (0.25 hours) and 48 hours in acetate buffer (pH 5.0) and TBS (pH 5, 7.5 and 9.0). The data corresponds to the average of three replicates.

The high affinity between $CaCO_3$ and AgNPs-Dex^{DEAE}, as demonstrated in the loading studies, explains the lower contents of AgNPs released at neutral and basic conditions. The images in **Figure 3-16**, where only calcite, instead of vaterite, is present after 48 hours of incubation, show that the release of AgNPs at pH 7.5 and 9.0 is triggered by the recrystallisation of the hybrids into calcite. The calcium release studies (**Figure 3-15**) also corroborate this hypothesis as the content of calcium ions in solution slightly decreased due to the lower solubility of the newly formed calcite hybrids. Surprisingly, the $CaCO_3$/AgNPs-PVP hybrids released more silver at pH 9.0 than 7.5, which can be due to the longer recrystallisation times of vaterite into calcite at basic pH, which favours the exclusion of AgNPs from calcite. While $CaCO_3$/AgNPs-Dex^{DEAE} hybrids presented a more

selective release (mainly at acidic pH), $CaCO_3$/AgNPs-PVP hybrids released AgNPs at a broader range of pH values, with a burst release at acidic conditions and a controlled release at neutral and basic pH values. These results demonstrate that $CaCO_3$/AgNPs hybrids are desirable materials for targeted burst release at acidic environments, like infection sites or the core of biofilms, as well as for controlled release overtime at neutral and basic conditions, making them attractive for different applications like implants, coatings of contact surfaces in hospitals, wound dressings, among others. Moreover, the results demonstrate that the pH, recrystallisation rate and affinity between the cargo and $CaCO_3$, can be used to trigger and control the release of nanoparticles from vaterite.

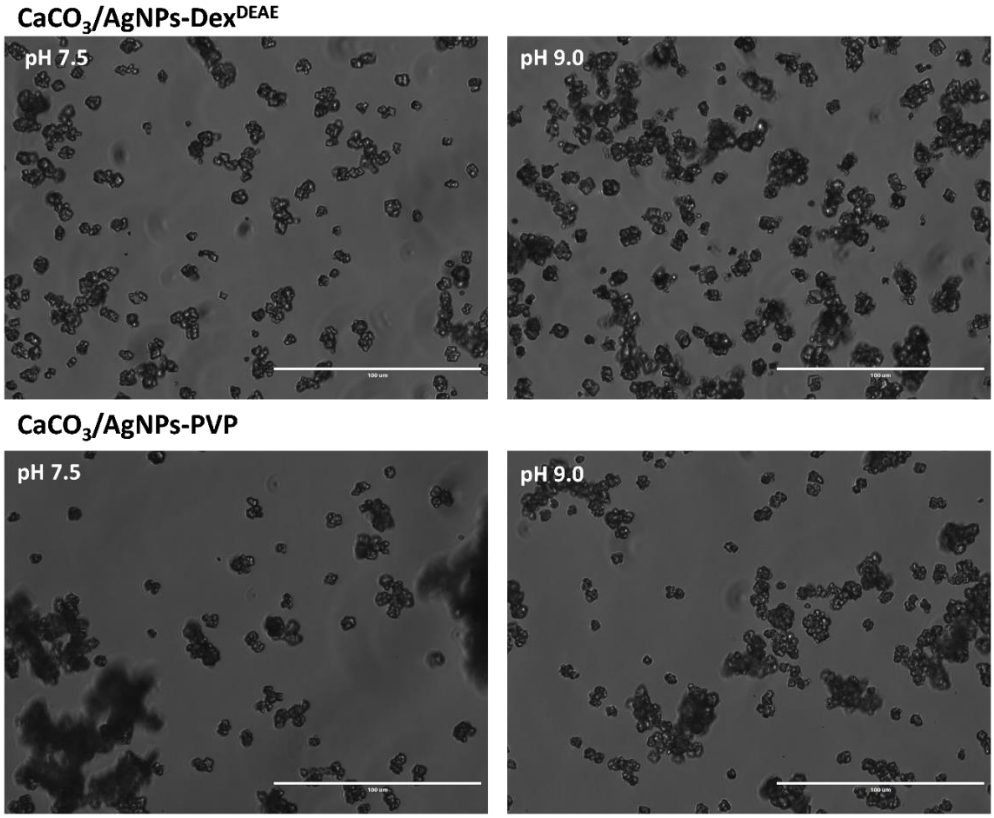

Figure 3-16. Transmittance images of the hybrids recrystallised into calcite after incubation at pH 7.5 and 9.0 at 37°C for 48 hours. Scale bar is 100 µm.

4. Conclusion

This work presents the loading of AgNPs into vaterite $CaCO_3$ crystals through co-precipitation. The effect of different capping agents on the stability of AgNPs, the hybrid properties, nanoparticles loading and release mechanism were also addressed. It was demonstrated that AgNPs coated with PVP and Dex^{DEAE} can be loaded into $CaCO_3$ crystals without losing stability or impairing $CaCO_3$ polymorphism, while the other capping agents

(citrate, Dex and Dex^{CM}) did not endow stability to the AgNPs due to their interaction with $CaCO_3$ precursor salts. AgNPs coated with Dex^{DEAE} had a high affinity to vaterite, resulting in an adsorption capacity (37.6 ± 1.0 mg.g^{-1}) higher than that of the AgNPs coated with PVP (14.8 ± 0.8 mg. g^{-1}), with both AgNPs adsorption profiles being well-described by the Langmuir adsorption model. These results proved the key role of the capping agents in modifying the affinity of AgNPs to $CaCO_3$ and promoting the stability of the nanoparticles. Moreover, the maximum content of AgNPs loaded into vaterite in this work (37.6 mg.g^{-1}) was higher than previously reported for vaterite loaded with AgNPs *via* a similar method (0.15 mg.g^{-1})[138]. The release studies shed light for the first time on the release mechanism of AgNPs from the hybrids. Crystals dissolution was the main trigger at acidic conditions, while at neutral and basic conditions, the recrystallisation of vaterite to non-porous calcite, and the affinity of AgNPs to $CaCO_3$ governed the release. The results presented in this report open new possibilities to handle and protect AgNPs and improve the final application outcome, as their stability is maintained. Moreover, the mild conditions used to load AgNPs into $CaCO_3$ creates the possibility for co-loading AgNPs with sensitive drugs in a quick, simple, and environmentally friendly way. Future work should focus on fine-tuning the release of AgNPs from $CaCO_3$ for a target release, studying the release mechanism further and assess the antibacterial activity of the hybrids.

Chapter 4

Study of silver nanoparticles release from the hybrids and antibacterial activity assessment

All the content presented in this chapter has been published in 2023 as a research article titled "Vaterite-nanosilver hybrids with antibacterial properties and pH-triggered release" in the journal Materials Today Chemistry, Volume 30, article 101586.

1. Introduction

The target and controlled delivery of antimicrobial agents have been the focus of numerous works and carry on being a crucial research area due to the alarming levels of bacterial resistance[1]. Silver nanoparticles (AgNPs) are among the most used antimicrobial agents for coatings due to their good activity against a wide range of microorganisms[275]. Nonetheless, the tenuous stability of AgNPs and concerns about their release in the environment and adverse effects on livings organisms have driven the development of carriers/vectors able to protect and target the release of AgNPs[230].

Calcium carbonate ($CaCO_3$) can be found as three different anhydrous polymorphs: aragonite, vaterite and calcite, with the first two being metastable phases that can rapidly recrystallise to calcite, the most stable phase[53]. All three polymorphs have been studied as carriers for the protection and delivery of antimicrobial and anticancer drugs, enzymes, hormones, and other biomolecules, due to their biocompatibility, availability, easy synthesis, low production costs and pH-sensitive properties[1,40,42,51,52]. In comparison with calcite and aragonite, vaterite has attracted more interest due to its porous structure, which can accommodate significant contents of different compounds[1].

The combination of $CaCO_3$ with AgNPs presents an opportunity to store, protect and deliver AgNPs in a controlled way, especially in acid microenvironments due the high solubility of $CaCO_3$ at low pH values. This association has been studied before to produce

antimicrobial materials and surface-enhanced Raman scattering (SERS) platforms[127,137,138,145,146,251–253], although the mechanisms behind the release of AgNPs from $CaCO_3$ have not been extensively studied, understood and intentionally modulated.

Various works have demonstrated that the cargo release from vaterite can be triggered by the dissolution of $CaCO_3$ at acid pH or the recrystallisation of vaterite into calcite[37,105,141]. Due to vaterite being a metastable polymorph when in solution it recrystallises into calcite. When loaded with a cargo, the transformation of vaterite (porous) into calcite (non-porous) promotes the release of the payload as it entails a dissolution/reprecipitation process and the reduction of the surface area[276]. While the recrystallisation of vaterite can be used to promote a controlled and sustained release of the cargo, when the goal is to achieve a targeted delivery at acid environments (e.g. at infection sites and tumours) the recrystallisation of metastable vaterite can cause an unwanted premature delivery of the payload. Therefore, the inhibition of the recrystallisation can be essential to improve the delivery at acidic sites. Previous studies have reported the partial or complete inhibition of vaterite recrystallisation by adsorbing polymers on its surface through the layer-by-layer (LbL) polymer deposition, or by co-synthesis of vaterite with stabilising agents like mucin and glutamic acid[60,90,105,161,277–279].

In this chapter, the recrystallization of the hybrids composed of $CaCO_3$ and AgNPs ($CaCO_3$/AgNPs) is studied and modulated. To improve the stability of the hybrids, different contents of two additives, poly(sodium 4-styrenesulfonate) (PSS) and carboxymethyl–dextran 40 kDa (Dex^{CM}), were tested and their effect studied. The morphology, composition, and polymorphism of the $CaCO_3$/AgNPs hybrids was assessed, and the release of AgNPs was studied in a closed (no change of the buffer) and open (supernatant periodically replaced with fresh buffer solution) system, also referred as static or continuous system, respectively. The antibacterial activity of the $CaCO_3$/AgNPs hybrids was tested against *Escherichia coli* (*E. coli*), methicillin-resistant *Staphylococcus aureus* (MRSA) and *Pseudomonas aeruginosa* (*P. aeruginosa*), three bacterial isolates responsible for numerous infections in hospital settings.

While this work is centred on AgNPs release from $CaCO_3$, the findings presented here can be extrapolated to other systems and help to understand and modulate the release of different compounds of interest from vaterite.

2. Materials and methods

2.1.Materials

Sodium borohydride ($NaBH_4$, ≥99% pure), polyvinylpyrrolidone 40 kDa (PVP), fluorescein isothiocyanate–carboxymethyl–dextran 40 kDa (Dex^{CM}), poly(sodium 4-styrenosulfonate) 70,000 $g.mol^{-1}$ (PSS), citric acid ($HOC(COOH)(CH_2COOH)_2$, 99.98% pure), Mueller Hinton broth Sigma 70192 (MHB-S), Mueller Hinton agar Sigma 70191 (MHA-S), phosphate buffered saline (PBS) tablets, sodium acetate (CH_3COONa, ≥99% pure), TraceCERT® 10,000 ppm calcium ICP-MS standard in 5% nitric acid and TraceCERT® 1 ppm Silver ICP-MS standard in 2% nitric acid, were obtained from Sigma-Aldrich (Steinheim, Germany). Silver nitrate ($AgNO_3$, ≥99% pure), calcium chloride dihydrate ($CaCl_2.2H_2O$, ≥99% pure), sodium carbonate (Na_2CO_3, ≥99.5%), tris buffer saline 10X solution (TBS), crystal violet ($C_{25}H_{30}N_3Cl$, pure), 99% ethanol, sodium hydroxide pellets (NaOH, ≥98% pure), glacial acetic acid (CH_3COOH, ≥99.7 % pure), 70% nitric acid (HNO_3, analytical grade) and 37% hydrochloric acid (HCl, analytical grade) were obtained from Fisher Scientific (Loughborough, United Kingdom).

2.2. Methods

2.2.1. Synthesis of AgNPs

AgNPs coated with PVP with an average size around 14 nm were synthesised *via* a modified chemical reduction methodology as described in **Chapter 2**.

2.2.2. Synthesis of bare vaterite $CaCO_3$ crystals

Bare vaterite $CaCO_3$ was synthesised based on the work of Volodkin, D. et al.[254]. Briefly, $CaCl_2.2H_2O$ (150 mM, in water) was mixed with an equal volume of TBS 6x and ultrapure, type I water under different magnetic stirring speeds (400, 650, 800 or 1400 rpm) in a 100 mL polypropylene beaker (diameter 4.5 cm), using a magnetic stirrer plate and a glass-encased stir bar (2.5 cm length and 0.6 cm diameter). Then Na_2CO_3 (50 mM, in water) was added, and the stirring continued for 30 seconds. The suspension was poured into a polypropylene tube and left for 10 minutes to allow the growth of the crystals. After that, the suspension was centrifuged at 3000 *g* for 5 minutes, washed with 25 mL of ultrapure, type I water *via* resuspension, centrifuged for another 5 minutes, and resuspended in 300 µl of 99% ethanol. The crystals were then dried at 80°C for 40 min. The initial molar ratio between $CaCl_2.2H_2O$ and Na_2CO_3 was 1:1. All the syntheses were performed at room temperature, and the reagents solutions were pre-filtered with a 0.2 µm syringe-tip filter

(Fisherbrand™, Loughborough, United Kingdom). Three independent syntheses were done per stirring speed. At least 300 particles were analysed to estimate the particle size and distribution using the ImageJ software (NIH, USA).

2.2.3. Synthesis of $CaCO_3$/AgNPs hybrids

AgNPs were loaded into $CaCO_3$ crystals by co-precipitation. Briefly, $CaCl_2.2H_2O$ (150 mM, in water) was mixed with an equal volume of TBS 6x in a 100 mL polypropylene beaker (diameter 4.5 cm), using a magnetic stirrer plate and a glass-encased stir bar (2.5 cm length and 0.6 cm diameter), and then AgNPs colloid and ultrapure, type I water were added. The reaction was repeated at different magnetic stirring speeds: 400, 650, 800, or 1400 rpm. A few seconds later, Na_2CO_3 (50 mM, in water) was added, and the stirring continued for 30 seconds (the final volume was the same for all the syntheses). Then the suspension was poured into a polypropylene tube and left for 10 minutes to allow the growth of the crystals. After that, the suspension was centrifuged at 3000 *g* for 5 minutes, washed with 25 mL of ultrapure, type I water *via* resuspension, centrifuged for another 5 minutes, and resuspended in 300 µl of 99% ethanol. The crystals were then dried at 80°C for 40 min. The molar ratio between $CaCl_2.2H_2O$ and Na_2CO_3 was kept the same in all the syntheses (1:1), as well as the mass ratio between AgNPs and $CaCO_3$ (30 $mg.g^{-1}$). All the synthesises were performed at room temperature, and the reagents solutions were pre-filtered with a 0.2 µm syringe-tip filter (Fisherbrand™, Loughborough, United Kingdom). A minimum of 300 particles were analysed to estimate the particle size and distribution using the ImageJ software (NIH, USA). The mass of silver loaded into $CaCO_3$ ($mg.g^{-1}$) was determined by ICP-MS, and the loading efficiency (LE, %) and yield (%) were calculated with the following equations:

$$LE\ (\%) = \frac{m_1}{m_2} \times 100 \qquad (9)$$

where m_1 is the actual loaded mass of silver (mg) per gram of $CaCO_3$/AgNPs, and m_2 the total theoretical mass of silver (mg) per gram of $CaCO_3$/AgNPs hybrids.

$$Yield\ (\%) = \frac{m_3}{m_4} \times 100 \qquad (10)$$

where m_3 is the actual mass of hybrids (mg) produced per synthesis and m_4 the theoretical mass of hybrids (mg) obtained per synthesis.

2.2.4. Recrystallisation studies of bare vaterite and $CaCO_3$/AgNPs hybrids into calcite

The recrystallisation of bare $CaCO_3$ and $CaCO_3$/AgNPs vaterite crystals to calcite was studied to better understand the stability and release profile of the hybrids in a closed/static and open/continuous system. At static conditions, bare $CaCO_3$ vaterite and $CaCO_3$/AgNPs hybrids were dispersed in TBS at pH 7.4 and 9.0 to a final concentration of 2 $mg.ml^{-1}$. The samples were then incubated at 37°C and left under constant agitation (500 rpm) in a ThermoMixer® C with a SmartBlock (Eppendorf, Germany). Aliquots corresponding to 0.5% of the final volume were taken at different time points for analysis under the microscope (Life Technologies EVOS FL, Invitrogen, USA). In the open-like system, $CaCO_3$/AgNPs hybrids were dispersed in TBS at pH 7.4 and 9.0 to a final concentration of 1.5 $mg.ml^{-1}$ and then incubated at 37°C under constant agitation (500 rpm) in a ThermoMixer® C with a SmartBlock (Eppendorf, Germany). At different time points, the samples were analysed under the microscope (Life Technologies EVOS FL, Invitrogen, USA), and 75% of the supernatant was replaced with fresh buffer after centrifugation at 2000 *g* for 5 min. The recrystallisation of $CaCO_3$/AgNPs hybrids at a concentration equal to 1.5 $mg.ml^{-1}$ was also studied at static conditions and pH 9.0 for comparison with the results obtained at open-like conditions. In all the studies, the crystals were considered fully recrystallised when no more vaterite/spherical particles were visible. The experiment was carried out in triplicate.

2.2.5. Co-synthesis of $CaCO_3$/AgNPs with Dex^{CM} and PSS, and recrystallisation study

$CaCO_3$/AgNPs were co-synthesised with different contents of Dex^{CM} (1, 2,3, 4 and 9%, initial $m_{DexCM}/m_{hybrids}$ ratio) and PSS (1, 2, 3 and 9%, initial $m_{PSS}/m_{hybrids}$ ratio) to promote $CaCO_3$ vaterite stability and prevent its recrystallisation into calcite. The hybrids were co-precipitated as described in **Section 2.2.3** with one exception, PSS or Dex^{CM} solutions (2 $mg.ml^{-1}$) were added just before adding Na_2CO_3. The final volume was the same for all the syntheses. To monitor the recrystallisation, the hybrids were washed with ultrapure, type I water and resuspended in TBS to a final concentration of approximately 3 $mg.ml^{-1}$. The suspensions were then kept at 37°C under constant agitation (500 rpm) in a ThermoMixer® C with a SmartBlock (Eppendorf, Germany). Aliquots corresponding to 0.5% of the total volume were taken at different time points for analyses under the microscope (Life Technologies EVOS FL, Invitrogen, USA). All the syntheses were performed at room

temperature, and the reagents solutions were pre-filtered with a 0.2 μm syringe-tip filter (Fisherbrand™, Loughborough, United Kingdom).

2.2.6. Characterization of the AgNPs, bare $CaCO_3$, $CaCO_3$/AgNPs and $CaCO_3$-PSS/AgNPs hybrids

Ultraviolet-visible (UV-vis) spectroscopy: AgNPs present size-dependent optical properties, making UV-vis analysis a simple and highly sensitive method to evaluate AgNPs formation, size, and stability[184,185]. The samples of AgNPs were diluted with ultrapure, type I water, to an absorbance below one and the UV-vis extinction spectra were recorded in a NanoDrop One spectrophotometer (Thermo Scientific, USA) between 190 and 850 nm. The AgNPs loaded into 7-month-old hybrids were analysed after dissolving $CaCO_3$ with citric acid (1 $mg.ml^{-1}$).

Transmission electron microscopy (TEM): The distribution of AgNPs in $CaCO_3$/AgNPs hybrids was analysed through TEM as described in **Chapter 3**.

Induced couple plasma mass spectroscopy (ICP-MS): The concentration of silver and calcium was determined through ICP-MS as described in **Chapter 3**.

Scanning electron microscopy (SEM): The morphology of bare $CaCO_3$, $CaCO_3$/AgNPs and $CaCO_3$-PSS/AgNPs hybrids was analysed by SEM (JEOL, JSM-7100f, Tokyo, Japan as described in **Chapter 3**.

SEM coupled with energy-dispersive X-Ray spectroscopy (SEM-EDS): SEM-EDS was used to determine the hybrids composition and AgNPs distribution as described in **Chapter 3**. Before analysis the samples were coated with a 5 nm thick layer of gold using a rotary pumped coater (Quorum Q150R ES, UK).

Fourier transform infrared (FTIR) spectroscopy: The crystalline structure of bare $CaCO_3$, $CaCO_3$/AgNPs and $CaCO_3$-PSS/AgNPs microparticles were analysed by FTIR spectroscopy (Spectrum Two FTIR spectrometer, PerkinElmer, Uberlingen, Germany). For each sample, 32 scans were run between 500 and 4000 cm^{-1} with a resolution of 4 cm^{-1}. The ATR (attenuated total reflectance) technique was used in all the measurements, and to compare different samples, the intensities of the obtained spectra were divided by the intensity of the typical band at $I_{1400\text{-}1396}$ assigned to CO_3^{2-} anti-symmetrical stretching. AgNPs incubated in MHB-S were also analysed by FTIR to detect the formation of the corona composed of biomolecules. For the corona formation the AgNPs were incubated at

37 °C under constant stirring (500 rpm) in MHB-S (final concentration 0.38 mg.ml^{-1}) for 2 hours, and then the non-adsorbed biomolecules were removed by washing the AgNPs three times with ultrapure, type I water *via* centrifugation (14,470 *g*, 4 °C for 30 min) and resuspension. After washing the concentrated AgNPs were poured on top of the ATR crystal and then dried with a Dexter® heat air gun until no water peaks were detectable. The analysis conditions were the same as described above.

X-ray diffraction (XRD): The crystalline structures of bare $CaCO_3$, $CaCO_3$/AgNPs and $CaCO_3$-PSS/AgNPs microparticles were analysed on a SmartLab SE X-Ray diffractometer from Rigaku Co. Ltd. (Tokyo, Japan) with a copper Kβ filter (λ = 0.1392 nm). Three independent samples per condition were scanned with a θ/2θ scan axis. The scan range varied between 20° and 80°, and the mode and speed were 1D and 5°/min, respectively. The molar percentage of vaterite and calcite was calculated based on the work of Vagena N. *et al*.[280]. The percentage of aragonite was assumed to be zero, and the equations below were used to determine the polymorphs molar percentage:

$$\frac{I_C^{104}}{I_V^{110}} = 7.691 \times \frac{X_C}{X_V} \qquad (11)$$

$$100 = (X_c + X_V) \times 100 \qquad (12)$$

Where 7.691 is the proportionality constant for mixtures of calcite and vaterite, I_C^{104}/I_v^{110} the ratio of the intensities of calcite and vaterite diffraction planes (104) and (110), respectively, and X_C/X_V the molar fraction ratio of calcite and vaterite.

2.2.7. Release studies of AgNPs from the hybrids

The release of AgNPs from the $CaCO_3$/AgNPs and $CaCO_3$-PSS/AgNPs hybrids was assessed at static (closed-like system) and continuous (open-like) conditions and at different pH values.

At static conditions the release was studied at pH 5.0 (acetate buffer); pH 7.4 (TBS and MHB-S) and pH 9.0 (TBS). Briefly, the hybrids were incubated in the respective buffer/media at 37°C and left under constant stirring (500 rpm) in a ThermoMixer® C with a SmartBlock (Eppendorf, Germany). The final concentration was 2 mg.ml^{-1}. At different time points, the samples were centrifuged at 2000 *g* for 5 min, and then aliquots corresponding to 2.3% of the total volume of supernatant were taken for calcium and silver quantification through ICP-MS. The aliquots were replaced with the same volume of fresh

buffer/media to maintain the same final volume. All the experiments were carried out in triplicate. At open-like conditions, the release was studied at pH 7.4 (TBS buffer) and pH 9.0 (TBS). Briefly, the hybrids were incubated in the respective buffer at 37°C under constant stirring (500 rpm). The final concentration was 1.5 $mg.ml^{-1}$. At different time points, the samples were centrifuged at 2000 *g* for 5 min, and then aliquots equal to 75% of the total volume of the supernatant were taken for calcium and silver quantification through ICP-MS. The aliquots were replaced with the same amount of fresh buffer to maintain the final volume. All the experiments were carried out in triplicate.

2.2.8. Assessment of the antibacterial activity

The antibacterial activity of the AgNPs, $CaCO_3$/AgNPs hybrids and bare $CaCO_3$ was determined against *E. coli* (O157:H7), MRSA and *P. aeruginosa* (PA01). The *E. coli*, MRSA and *P. aeruginosa* isolates were obtained from the American Type Culture Collection (ATCC 43888), National Collection of Type Cultures (NCTC 12493) and Nottingham Trent University Cultures Collection (NTUCC 876), respectively.

2.2.8.1. Inoculum preparation

The bacterial isolates were streaked onto MHA-S plates and incubated at 37°C for 18 to 24 hours. For each isolate, three to four isolated colonies of the same morphological appearance were transferred into a tube containing 5 ml of MHB-S and then incubated overnight in a shaker at 35°C and 225 rpm. Immediately before incubation with the hybrids or bare $CaCO_3$, overnight cultures were diluted to 1×10^6 $CFU.ml^{-1}$.

2.2.8.2. Minimum inhibitory concentration (MIC) and minimum bactericidal concentration (MBC)

The MIC was determined using the broth microdilution method adapted from Wiegand I. *et al.*[186], with some modifications. Briefly, AgNPs, $CaCO_3$/AgNPs and bare $CaCO_3$ were serially diluted in a 96-wells microplate with MHB-S to a final volume per well of 50 µl. Then 50 µl of *E. coli*, MRSA or *P. aeruginosa*, previously diluted with MHB-S to 1×10^6 $CFU.ml^{-1}$, were added to each well. The concentrations of the AgNPs ranged between 480 and 1.875 $\mu g.ml^{-1}$, and the concentrations of $CaCO_3$/AgNPs and bare $CaCO_3$ ranged between 21 and 0.328 $mg.ml^{-1}$. The final bacterial inoculum density was 5×10^5 $CFU.ml^{-1}$. Bacteria in MHB-S at the same density were used as growth controls (positive control) and the medium with and without AgNPs, $CaCO_3$/AgNPs and bare $CaCO_3$ as sterility

controls (negative control). The microplates were incubated at 37°C for 20 hours and then read visually by observing the presence or absence of turbidity. The MIC was defined as the lowest concentration that inhibited the visible growth of the bacteria in all the replicate wells. The MBC was determined after reading the MIC and consisted of plating 10 µl of the wells without visible turbidity onto MHA-S plates. The agar plates were incubated at 37°C for 24 hours, and then read visually. The lower dilution without macroscopic bacterial growth was defined as the MBC. The experiment was repeated three to six times, with three replicates per repetition. To compare the antibacterial activity of the unloaded AgNPs with the activity of the AgNPs released from the hybrids, the amount of silver released from $CaCO_3$/AgNPs hybrids was determined. Briefly, $CaCO_3$/AgNPs were serially diluted with MHB-S on a 96-well microplate to a final volume per well of 50 µl and then 50 µl of MHB-S was added. The plate was incubated at 37°C for 24 hours, and after incubation, the suspensions in each well were transferred to tubes and centrifuged at 2000 *g* for 5 minutes to sediment the hybrids. The content of silver in the supernatant was quantified by ICP-MS, as described in **Chapter 3**, and the morphology of the crystals was analysed under the microscope (Life Technologies EVOS FL, Invitrogen, USA). The experiment was carried out in triplicate and included sterility controls as described above.

2.2.8.3. Minimum inhibitory biofilm concentration (MIBC)

The MIBC determination was based on the method from Ivanova A. et al.[188] with some modifications. Briefly, AgNPs and $CaCO_3$/AgNPs were serially diluted in a 96-wells microplate with MHB-S to a final volume per well of 50 µl. Then 50 µl of MRSA or *P. aeruginosa*, previously diluted with MHB-S to 1×10^6 CFU.ml^{-1}, were added to each well. The concentrations of the AgNPs ranged between 480 and 1.875 µg.ml^{-1}, and the concentrations of $CaCO_3$/AgNPs and bare $CaCO_3$ ranged between 21 and 0.328 mg.ml^{-1}. The final bacterial inoculum density was 5×10^5 CFU.ml^{-1}. The microplates were then incubated for 24 hours at 37°C under static conditions to allow the biofilm formation. After incubation, the non-adhered bacterial cells were gently washed away three times with 150 µl of sterile PBS and then the biofilms were fixated by keeping the microplates at 60°C for 1hour. After fixation, the biofilms were stained with crystal violet (0.1% w/v) for 1 hour and then the excess of crystal violet was removed by washing the wells three times with 150 µl of sterile PBS. Between washes, the microplate was stirred at 100 rpm for 5 min. After washing, the crystal violet was dissolved with acetic acid (30% v/v, 200 µl per well). 100 µl were then transferred into a 96-well microplate, and the absorbance was read at 595

nm. The experiment was repeated at least three times in triplicate and included sterility controls of MHB-S medium. Untreated biofilms were used as positive controls. Bare $CaCO_3$ was also tested in triplicate against MRSA and *P. aeruginosa* at concentrations ranging between 21 and 0.328 $mg.ml^{-1}$. The content of silver released from the $CaCO_3$/AgNPs hybrids was quantified by ICP-MS as described in **Chapter 3**.

3. Results and discussion

3.1. Loading of AgNPs into $CaCO_3$ and hybrids stabilisation

The immobilisation of AgNPs in vectors opens new opportunities to protect, store and release AgNPs. It also presents the chance to co-immobilise silver with other active components or use the vectors as catalytic platforms *per se*. In **Chapter 3**, vaterite crystals were used as vectors to immobilise AgNPs due to their environmentally friendly nature and straightforward synthesis, as well as biocompatibility and easy dissolution in acid environment or with chelating agents like EDTA[1]. In this chapter, the effect of the crystals size on the amount of silver loaded into the hybrids is presented, as well as the recrystallisation studies of the hybrids into calcite. AgNPs coated with PVP were selected as they present better stability in bacterial growth media (**Chapter 2**) and when loaded into vaterite (**Chapter 3**).

3.1.1. Effect of $CaCO_3$/AgNPs hybrids size on AgNPs uptake

The effect of the hybrids size on vaterite loading capacity was studied to improve the uptake of AgNPs. Smaller particles tend to present higher loading capacity due to the larger surface area[281,282], however this correlation is not always found. Size changes can be associated with other alterations, like different pore size distribution or different internal structure, which can alter the capacity of the crystals to adsorb and retain the payload[282,283]. In this work, the effect of the size on the loading capacity of vaterite was analysed by synthesising $CaCO_3$/AgNPs crystals with different sizes.

The size of vaterite crystals can be tuned by varying the precursor salts concentration or ratio, pH, stirring time and speed, or even by adding additives or changing the solvent. Nonetheless, some of these parameters, like pH or salts concentration, can also affect the polymorphism of the crystals. Herein, bare vaterite crystals and $CaCO_3$/AgNPs hybrids with different sizes were synthesised by varying the stirring speeds (400, 650, 800 and 1400 rpm) as it marginally affects the polymorphism of $CaCO_3$. As presented in **Figure 4-1A,** by increasing the stirring speed from 400 to 1400 rpm it was possible to decrease the

size of bare vaterite and $CaCO_3$/AgNPs hybrids by approximately 57% and 43%, respectively. These results show the particle size dependence on the stirring speed, as higher speeds promote the formation of more nuclei and consequently the formation of smaller particles[1].

Figure 4-1B presents the effect of the $CaCO_3$/AgNPs hybrids size on the amount of silver loaded. The smallest crystals (2.0 ± 0.3 µm) presented a significantly higher uptake of AgNPs than the biggest ones (3.4 ± 0.6 µm), *i.e.* 26 and 21 $mg.g^{-1}$, respectively. Moreover, **Figure 4-1B** depicts a clear correlation between the size and amount of AgNPs loaded, showing that when the size of the hybrids decreased, the amount of AgNPs loaded was higher. These results indicate that, although not drastically, it is possible to increase the uptake of AgNPs by reducing the size of the crystals. This is associated with the smaller hybrids presenting a larger surface area, since the variation of the steering speed should only affect the initial number of nuclei formed during the start of the crystallization process[1].

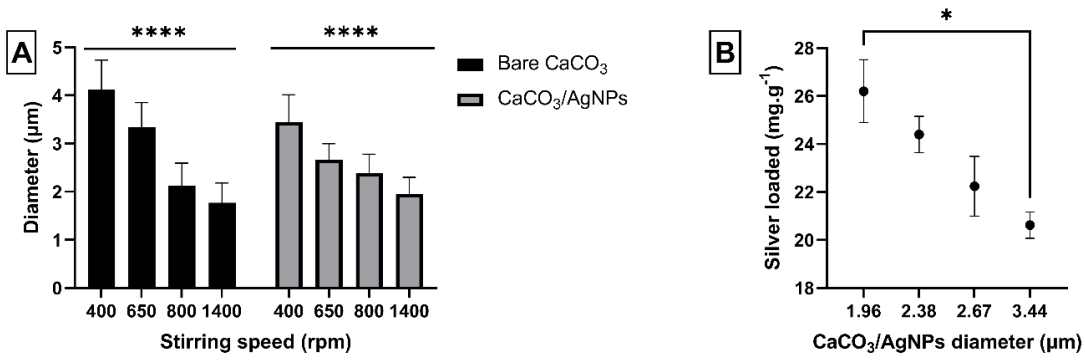

Figure 4-1. Effect of the stirring speed on the size of bare $CaCO_3$ vaterite crystals and $CaCO_3$/AgNPs hybrids (A), and the size of the hybrids versus the content of silver loaded (B). Statistical analysis made using the one-way ANOVA/Tukey's test (A) and Kruskal-Wallis/Dunn's post-test (B) (*$p \leq 0.05$, and ****$p \leq 0.0001$).

3.1.2. Stabilization of $CaCO_3$/AgNPs: Recrystallization modulation

Vaterite is a metastable polymorph of $CaCO_3$, meaning that when in solution, it tends to recrystallise into calcite, the most thermodynamically stable polymorph. When loaded, the transformation of vaterite (porous) into calcite (non-porous) promotes the release of the cargo as it entails a dissolution/reprecipitation process[276] and the reduction of the total surface area. While the recrystallisation triggers and drives the release of the cargo, the affinity between $CaCO_3$ and the loaded compounds defines how much of the payload remains free. Compounds with a high affinity to $CaCO_3$ will be released and largely readsorbed into calcite, if the released content is below the binding capacity of calcite. On

the other hand, compounds with low affinity to $CaCO_3$ will remain partly or completely free.

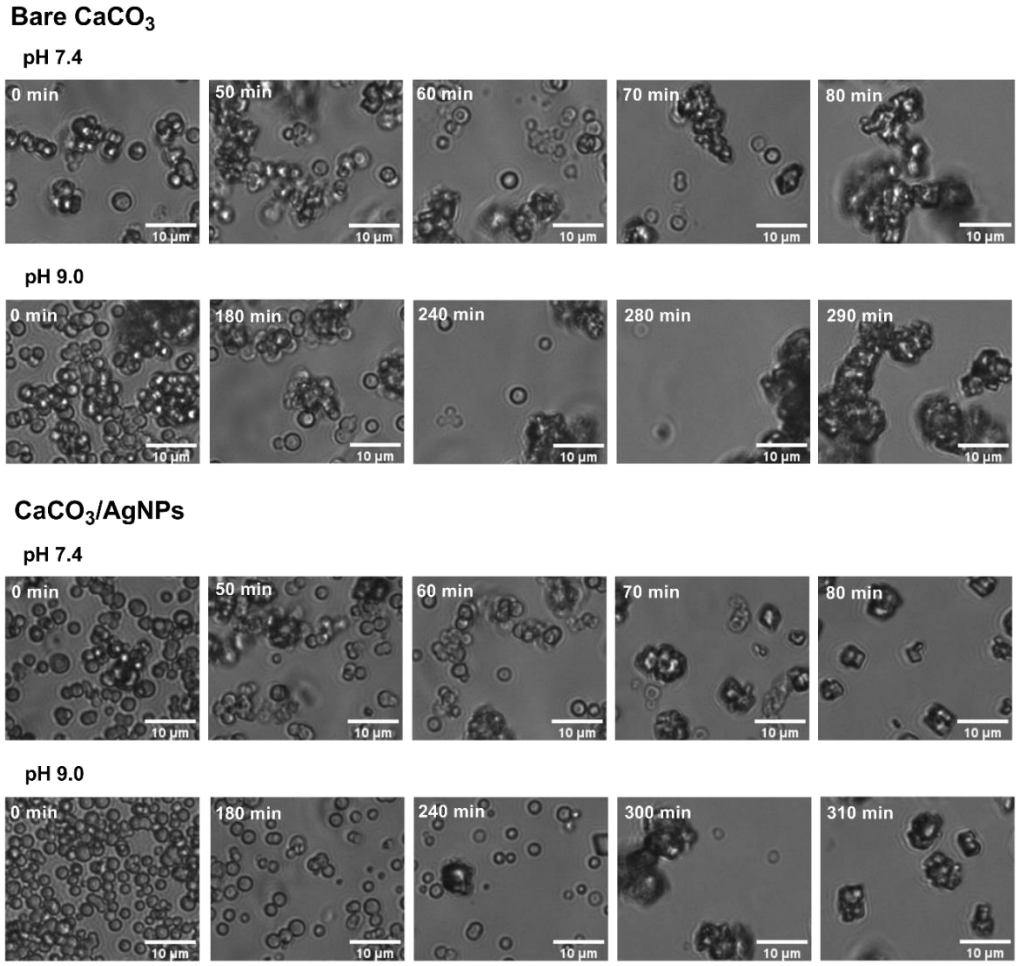

Figure 4-2. Transmittance images of bare $CaCO_3$ and $CaCO_3$/AgNPs hybrids (2.0 $mg.ml^{-1}$) over time at static conditions (pH 7.4 and pH 9.0).

The recrystallisation of bare $CaCO_3$ vaterite and $CaCO_3$/AgNPs hybrids was monitored over time in TBS at pH 7.4 and 9.0 (**Figure 4-2**). The crystals were considered fully recrystallised when there were no more spherical particles (vaterite) visible (**Figure 4-2**). **Figure 4-3** presents the recrystallisation time of bare $CaCO_3$ vaterite and $CaCO_3$/AgNPs hybrids into calcite at pH 7.4 and 9.0. The data shows no differences between bare $CaCO_3$ vaterite and $CaCO_3$/AgNPs hybrids, proving that AgNPs do not affect the recrystallisation of vaterite. As expected, it is confirmed that the transformation of vaterite into calcite is pH-dependent, taking longer times at pH 9.0 (ca. 280 min) than at pH 7.4 (ca. 80 min). This is caused by the lower solubility of $CaCO_3$ at basic pH, which slows down the dissolution/reprecipitation process of vaterite into calcite.

While recrystallisation can be used to control the release of the cargo, it does not enable a targeted release in acidic environments, like infection sites or tumours. Therefore, changing or even halting the recrystallisation of vaterite into calcite is of interest, as it would allow the modulation and controlled release of the cargo. On that front, researchers have been inspired by the occurrence of vaterite in nature. Despite vaterite being a metastable polymorph, it can be found on gastropod eggshells and gallstones, either as a precursor or a structural component[284]. It is believed that such existence is possible through the stabilisation of vaterite with inorganic or organic components[284]. In a biomimicry type approach, vaterite has been stabilized by associating it with ions, macromolecules or polymers[284].

In the present work, the effect of different quantities of PSS (1 to 9%, initial $m_{PSS}/m_{hybrids}$ ratio) and Dex^{CM} (1 to 9%, initial m_{DexCM}/m_{hyrid} ratio) was tested in an attempt to develop stable hybrids.

PSS has been used by numerous researchers as an additive for the synthesis of vaterite, as it favours the growth of vaterite over calcite[278,285–287], while Dex^{CM} has only recently been reported as a good stabiliser for vaterite[288]. In both cases, it is believed that the stabilisation of vaterite is promoted by the interactions of Ca^{2+} with the negatively charged groups on the polymers chains[284,285], which initially work as centres of nucleation (due to the localised high concentration of Ca^{2+} around the polymers chains) and then as stabilisation agents through absorption on vaterite phase[289,290].

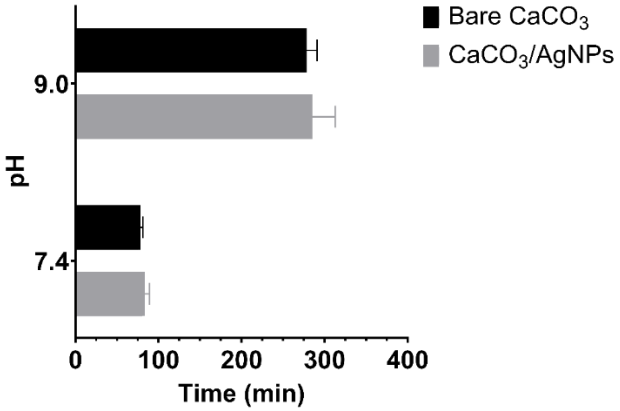

Figure 4-3. Time taken for complete recrystallisation of bare $CaCO_3$ vaterite and $CaCO_3$/AgNPs hybrids into calcite in TBS at pH 7.4 and 9.0.

Table 4-1 summarises the effect of PSS and Dex^{CM} on the recrystallisation of $CaCO_3$/AgNPs hybrids over 15 days. Overall, all the crystals synthesised with Dex^{CM} and PSS presented better stability, with the recrystallisation being delayed or totally prevented.

Dex^{CM} at 2 and 3% prevented the hybrids from fully recrystallising within 7 days, which was extended to 15 days when the crystals were synthesised with 4% of Dex^{CM}. Nonetheless, although the recrystallisation was clearly delayed with 4% of Dex^{CM}, it did not stop the dissolution/reprecipitation of vaterite into calcite, proven by the presence of calcite and depleted vaterite crystals in solution after 9 and 15 days (**Figure 4-4**).

Table 4-1. Recrystallization duration of $CaCO_3$/AgNPs hybrids co-synthesized with different contents of Dex^{CM} and PSS in TBS (pH 7.4, concentration ca. 3 $mg.ml^{-1}$). The 7- and 15-days groups include all the samples that were fully recrystallised within 7 or 15 days, respectively. [a]: not tested due to the low uptake of AgNPs.

Dex^{CM} (%)	**Fully recrystallized?**	
	7 days	**15 days**
1	**Yes**	**-**
2	**No**	**Yes**
3	**No**	**Yes**
4	**No**	**No**
9	**-[a]**	**-[a]**
PSS (%)		
1	**No**	**Yes**
2	**No**	**No**
3	**No**	**No**
9	**No**	**No**

Another intriguing effect of Dex^{CM} on the hybrids was the inhibition of AgNPs uptake by $CaCO_3$. As presented in **Figure 4-4**, by increasing the amount of Dex^{CM} the content of AgNPs loaded into the hybrids dropped, as evidenced by the intensification of the amber colour of the supernatant (more AgNPs in suspension) and whitening of the crystals. This effect might have resulted from Dex^{CM} changing the affinity between $CaCO_3$ and AgNPs and altering the structure of the crystals and consequently decreasing the adsorption of

AgNPs.

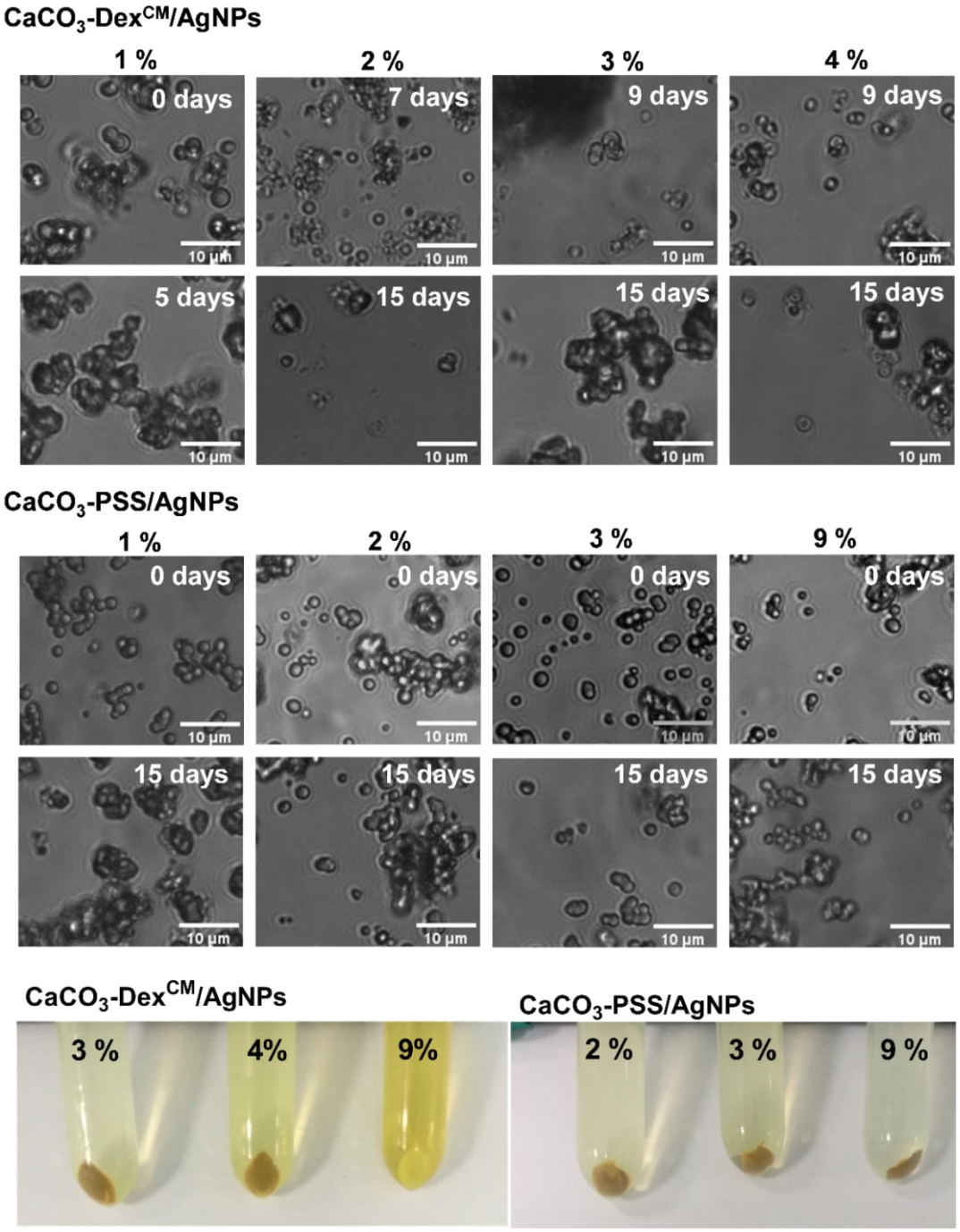

Figure 4-4. Transmittance images of $CaCO_3$-Dex^{CM}/AgNPs (top) and $CaCO_3$-PSS/AgNPs (middle) with different contents of Dex^{CM} and PSS on different days. Images of the sediment and supernatant after synthesis and centrifugation of $CaCO_3$-Dex^{CM}/AgNPs and $CaCO_3$-PSS/AgNPs with different contents of Dex^{CM} and PSS (bottom).

In the case of the $CaCO_3$-PSS/AgNPs hybrids, 1 and 2% of PSS added during synthesis inhibited the complete recrystallisation of the hybrids within 7 and 15 days, respectively. Crystals synthesised with 2% to 9% of PSS, did not present calcite after 15 days nor

depleted vaterite crystals (**Figure 4-4**), which indicates that the recrystallisation was entirely halted. Moreover, PSS did not affect the uptake of AgNPs at the concentrations tested (**Figure 4-4**). These results demonstrate that PSS is a better stabilising agent for the $CaCO_3$/AgNPs hybrids, which can be explained by presenting a much higher density of anionic groups (one sulfonate group per each sodium 4-vinylbenzenesulfonate monomer) than Dex^{CM} (ca. one *O*-carboxymethyl group per every five glucose monomers), resulting on the growth of hybrid vaterite crystals energetically more favourable[289].

Overall, the results here presented highlight the effect of stabilising agents on the recrystallisation of vaterite, and their effect on the loading of AgNPs, demonstrating that the final properties of the crystals must be considered when choosing an ideal stabilising agent.

Due to PSS not affecting the uptake of AgNPs and halting the recrystallisation of $CaCO_3$, the work was further carried on with the hybrids synthesised with 2% of PSS.

3.2. Characterisation of the hybrids

3.2.1. Composition, morphology and stability

$CaCO_3$/AgNPs hybrids, with or without PSS, were synthesised at the optimised synthesis conditions. **Table 4-2** presents the size and content of silver loaded into $CaCO_3$/AgNPs and $CaCO_3$-PSS/AgNPs hybrids, as well as the loading efficiency and yield per synthesis. Overall, $CaCO_3$-AgNPs and $CaCO_3$-PSS/AgNPs hybrids presented similar sizes, *i.e.* around 2 µm, and similar silver contents, *i.e.* ca. 26 $mg.g^{-1}$. This was reflected on the high loading efficiencies, 90 and 89 %, also favoured by the small size of the hybrids, as demonstrated in the sections above. The yield per synthesis was also similar between the hybrids, ca. 68 %, with about 32% being lost due to the synthesis steps (reaction, centrifugation, washing and drying).

Table 4-2. $CaCO_3$/AgNPs and $CaCO_3$-PSS/AgNPs hybrids size (µm), mass of silver loaded into the hybrids ($mg.g^{-1}$), loading efficiency (%) and yield per synthesis (%).

	Diameter (µm)	**Silver content (mg of silver per g of hybrids)**	**Loading efficiency (%)**	**Yield (%)**
$CaCO_3$/AgNPs	1.9 ± 0.8	26.3 ± 2.4	90.4 ± 8.2	68.9 ± 2.3
$CaCO_3$-PSS/AgNPs	2.1 ± 1.0	26.0 ± 3.4	89.1 ± 11.8	68.0 ± 4.9

The data in **Table 4-2.** shows that PSS did not considerably affect the size of the hybrids, content of AgNPs loaded or the yield per synthesis. Moreover, the high loading efficiencies (ca. 87%) demonstrate that the synthesis process presented here can minimise AgNPs waste, an important consideration due to the potential adverse effects of silver in the environment. Moreover, the AgNPs that were not uptaken by the hybrids could be washed and re-used, as no changes on the properties of the surplus AgNPs retrieved from the synthesis medium were detected, as corroborated by the UV-vis absorbance spectra (**Figure 4-5**).

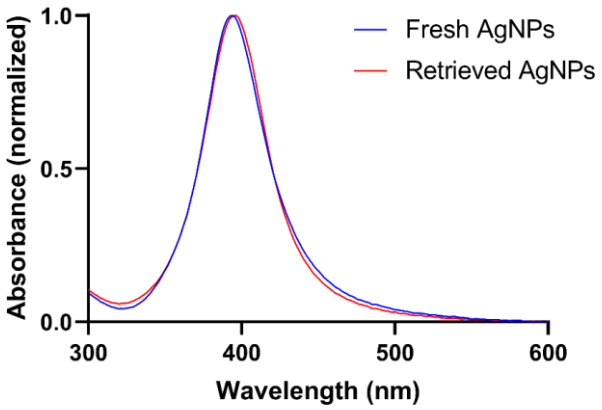

Figure 4-5. UV-vis spectra of fresh AgNPs and surplus AgNPs retrieved after the synthesis of the hybrids (AgNPs – Retrieved).

The stability of AgNPs over time is of significant importance as it assures that the optical and antimicrobial properties are maintained for prolonged periods. To test the suitability of the hybrids to store AgNPs, AgNPs loaded into 7-month-old hybrids were analysed by UV-vis spectrophotometry.

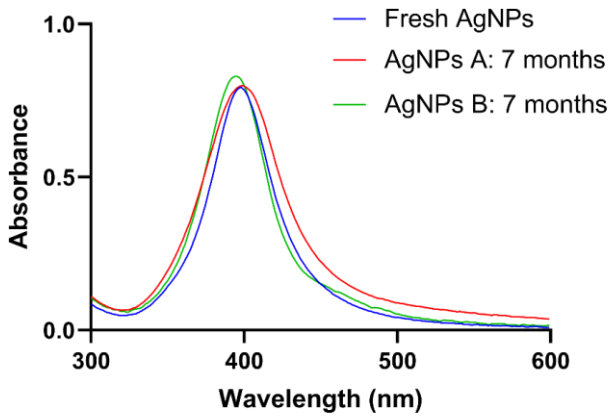

Figure 4-6. UV-vis spectra of fresh AgNPs and AgNPs from 7 months old $CaCO_3$/AgNPs hybrids (AgNPs A: 7 months) and $CaCO_3$-PSS/AgNPs hybrids (AgNPs B: 7 months).

As shown in **Figure 4-6**, the AgNPs loaded in the hybrids for 7 months presented the same characteristic peak with maximum absorbance around 400 nm, without any major shifts, indicating that there were not major changes on the properties of the nanoparticles during storage. This proves that the hybrids are good platforms to store AgNPs at room temperature for at least 7 months, an advantage in comparison with silver colloidal suspensions that must be stored at 4°C to preserve the properties of the nanoparticles.

The hybrids morphology and surface characteristics were also analysed using SEM. As presented in **Figure 4-7**, all the synthesised crystals (bare $CaCO_3$, $CaCO_3$/AgNPs, $CaCO_3$-PSS and $CaCO_3$-PSS/AgNPs) presented a spherical structure composed of small nanocrystallites, a typical feature of $CaCO_3$ vaterite. Interestingly, the crystals co-precipitated with AgNPs presented slightly smaller nanocrystallites, as evidenced in **Figure 4-7B**, although the most significant difference was noticed between the crystals with and without PSS. The crystals co-synthesised with PSS had significantly smaller nanocrystallites (sizes between 43 and 54 nm) than those synthesised without PSS (sizes between 81 and 99 nm). This resulted in the crystals with PSS presenting smoother surfaces, as demonstrated by the surface analysis in **Figure 4-7C.** The smoother surfaces resulted from PSS controlling the nucleation process and adsorbing on the surface of the nanocrystallites preventing further growth[289,290].

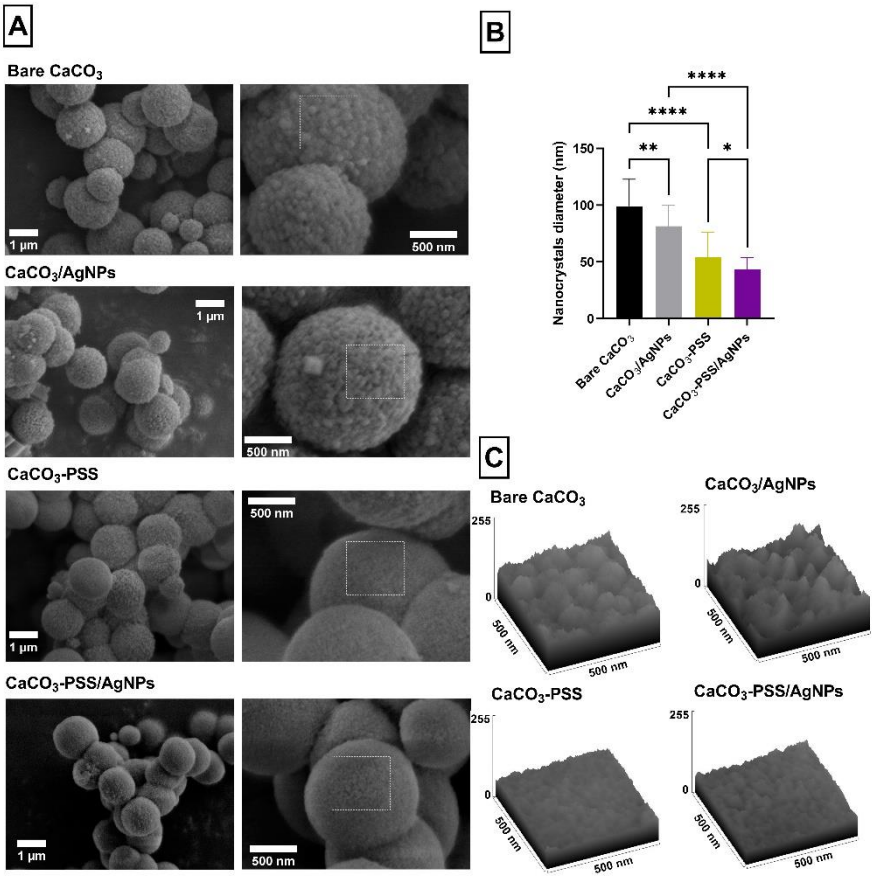

Figure 4-7. SEM images of bare $CaCO_3$, $CaCO_3$/AgNPs, $CaCO_3$-PSS and $CaCO_3$-PSS/AgNPs (A) and the respective average size of the nanocrystallites (B) and surface roughness plots of the areas marked in grey outline on the SEM images (D). Statistical analysis made using the Kruskal-Wallis/Dunn's post-test (*p≤ 0.05, ** p ≤ 0.01 and ****p≤ 0.0001). The scale bar in image A (left) correspond to 1 µm and in image A (right) to 500 nm.

3.2.2. Silver nanoparticles distribution

To understand the distribution of AgNPs within the hybrids and the elementary composition of the hybrids, SEM-EDS analysis was carried out. **Figure 4-8** presents the mapping images and respective spectrograms of $CaCO_3$/AgNPs and $CaCO_3$-PSS/AgNPs hybrids. As expected, the data confirmed that the hybrids are mainly composed of calcium, oxygen and carbon, although the carbon peak also resulted from the carbon tape used to mount the samples. The gold peak in the spectrogram resulted from coating the samples with gold for SEM-EDX analysis. In the mapping images it is possible to see the uniform distribution of AgNPs on the hybrids and confirm that the AgNPs are embedded on the crystals, which is also corroborated by the characteristic peaks of silver on the spectrogram at 2.98 and 3.15 KeV. Once again, it is demonstrated that PSS did not affect the distribution of the AgNPs, although it is not possible to exclude that the nanoparticles might be localised at different depths.

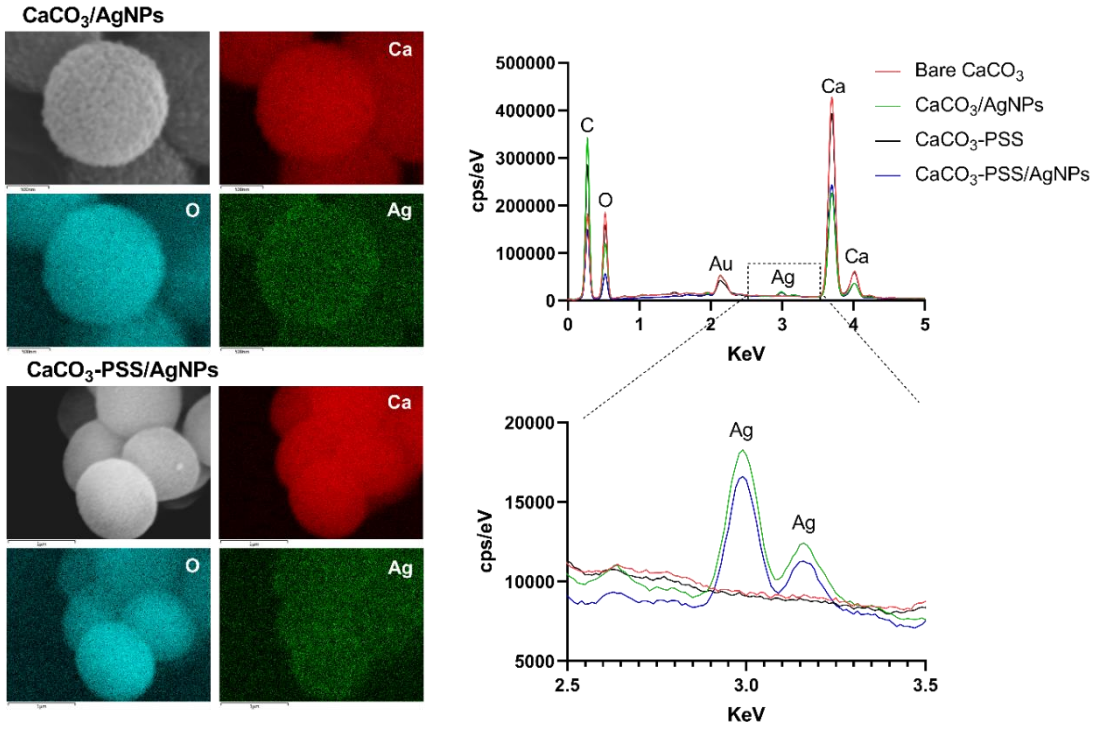

Figure 4-8. SEM-EDS mapping images and respective spectrograms of $CaCO_3$/AgNPs and $CaCO_3$-PSS/AgNPs hybrids. Initial $CaCO_3$/AgNPs ratio equal to 3 % (m/m).

3.2.3. Polymorphism

The polymorphism of $CaCO_3$ is of utmost importance as it affects the surface area and the cargo release mechanism. The polymorphism of the crystals loaded with silver,with or without PSS, was assessed through FTIR and XRD analysis. **Figure 4-9** presents the FTIR spectra of bare vaterite, bare calcite, $CaCO_3$/AgNPs, $CaCO_3$-PSS and $CaCO_3$-PSS/AgNPs hybrids. All the spectra presented three characteristic peaks with similar intensities with maximum transmittance at 848-850 cm^{-1} and 872-874 cm^{-1}, resultant from CO_3^{2-} out-of-plane bending (ν_2 mode), and at 1396-1401 cm^{-1} originated by CO_3^{2-} anti-symmetrical stretching (ν_3 mode)[265,266]. Shifts on these peaks were caused by the main polymorphic identity of the samples, the ratio between the different polymorphs, and interactions of $CaCO_3$ with other components, such as AgNPs, the corresponding capping agents, and PSS[267].

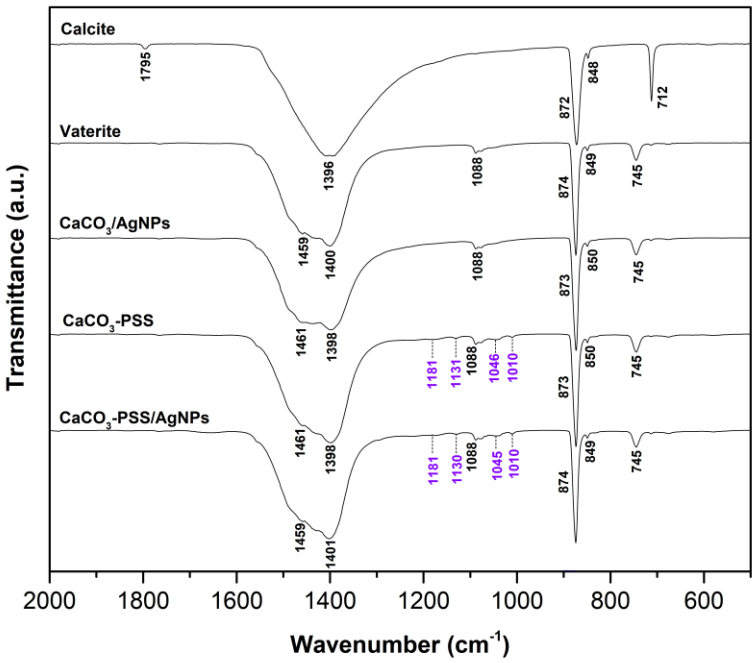

Figure 4-9. FTIR spectra of bare vaterite and calcite crystals, $CaCO_3$-PSS, $CaCO_3$/AgNPs and $CaCO_3$-PSS/AgNPs hybrids. Purple wavenumbers correspond to characteristic bands of PSS.

The bare calcite sample presented the characteristic peaks with maximum transmittance at 712 and 1795 cm^{-1}, and a single peak with maximum transmittance around 1400 cm^{-1}. These bands correspond to CO_3^{2-} in-plane bending (ν_4 mode), symmetric stretching (ν_1 mode) + ν_4 mode, and ν_3 mode, respectively[268,269]. Bare vaterite also presented its characteristic peaks at 745 cm^{-1} (ν_4 mode), 1088 cm^{-1} (ν_1 mode) and a split and broad band around 1400-1459 cm^{-1} (ν_3 mode) due to the asymmetry around the carbonate ion[270].

The spectra of $CaCO_3$/AgNPs and $CaCO_3$-PSS/AgNPs hybrids presented the unique peaks assigned to the vaterite phase at 745 and 1088 cm^{-1}, as well as the split and broad band around 1398-1461 cm^{-1}. A peak with very low intensity was also detected at 713 cm^{-1}, which indicates the presence of small quantities of calcite in both samples. This is corroborated by the XRD data, where is possible to detect a low-intensity peak assigned to calcite (**Figure 4-10**).

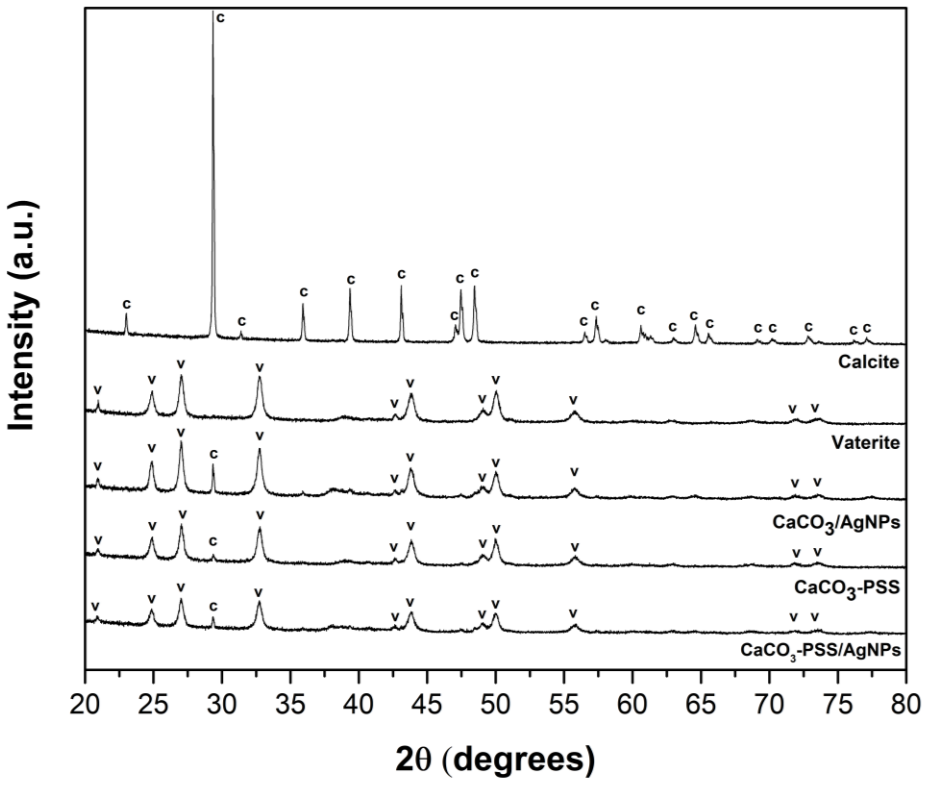

Figure 4-10. XRD spectra of bare vaterite and calcite, $CaCO_3$-PSS, $CaCO_3$/AgNPs and $CaCO_3$-PSS/AgNPs hybrids.

The samples with PSS ($CaCO_3$-PSS and $CaCO_3$-PSS/AgNPs) presented four unique peaks at 1181, 1130/1131, 1045/1046 and 1010 cm^{-1}, which corresponded to PSS (**Figure 4-11**) and evidenced its incorporation into the crystals. The peaks at 1181 and 1045/1046 cm^{-1} corresponded to the SO_3^- group asymmetric and symmetric vibrations, and the peaks at 1130/1131 and 1010 cm^{-1} to in-plane skeleton vibrations and in-plane bending of the benzene ring[291–293]. The band shifts are due to the interaction of $CaCO_3$ with PSS, mainly the sulfonate group, which are responsible for vaterite stability.

Table 4-3. Vaterite molar percentage (mol%).

	Vaterite (mol%)
Vaterite/Bare $CaCO_3$	93.8 ± 2.1
$CaCO_3$/AgNPs	86.2 ± 7.5
$CaCO_3$-PSS	93.5 ± 0.2
$CaCO_3$-PSS/AgNPs	91.8 ± 1.7

Table 4-3 presents the vaterite molar percentage (mol%) of bare $CaCO_3$, $CaCO_3$/AgNPs, $CaCO_3$-PSS and $CaCO_3$-PSS/AgNPs samples determined from the XRD data (**Figure 4-10**). The results show that all the synthesised crystals present a high content of vaterite,

between 86% and 94%, proving that the main phase of $CaCO_3$/AgNPs and $CaCO_3$-PSS/AgNPs hybrids is vaterite. Moreover, the data shows that AgNPs and PSS did not affect the predominant $CaCO_3$ phase, as corroborated by the SEM images (**Figure 4-7A**) where mainly vaterite crystals are visible (spherical shape particles).

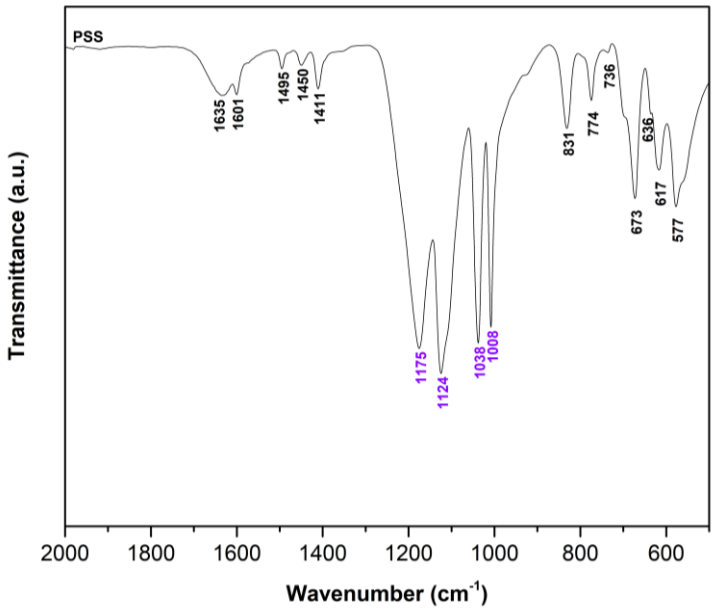

Figure 4-11. FTIR spectra of PSS. Peaks assigned in purple correspond to the peaks found in the hybrids co-precipitated with PSS.

3.3. AgNPs release

The use of vectors/carriers to store and protect active compounds, as well as to control and target their release, opens the possibility to increase the cargo activity and consequently improve the therapeutical effect of the payload. When it comes to nanoparticles, the use of carriers is even more crucial, as they can help to solve two major problems in nanomedicine: the low efficacy on nanoparticles delivery and potential toxicity[294].

$CaCO_3$ has been studied in the past decades as a carrier for different compounds due to its biocompatibility, easy synthesis, and pH-sensitive properties. In some of studies published so far, it is proposed that the release of the cargo from $CaCO_3$ vaterite crystals results from the recrystallisation of vaterite into calcite, diffusion, or the dissolution of $CaCO_3$ at low pH values or in the presence of calcium chelating agents[1,246,295]. The predominant release mechanism is triggered and/or affected by the properties of the cargo, the cargo-vector interactions, and external conditions (composition of the media, pH, temperature, etc.). Moreover, different release mechanisms can occur concomitantly. Although there has been a lot of progress in understanding the release of the payload from vaterite crystals, there are still areas that need further clarification, like to which extent the recrystallisation drives

the release of the cargo and the effect of external factors, like the media composition. In the following sections, the different release mechanisms of AgNPs from the hybrids are studied, as well as the effect of pH, type of release system and media composition on the cargo release.

3.3.1. Release of AgNPs in saline buffer

Figure 4-12 and **Figure 4-14** present the release of silver and calcium ions from $CaCO_3$/AgNPs and $CaCO_3$-PSS/AgNPs hybrids, respectively, in saline buffers at different pH values. The release was assessed at closed and open-like conditions to study the main release mechanisms of AgNPs at static (no buffer change) and continuous conditions (supernatant periodically replaced with a fresh buffer solution), respectively.

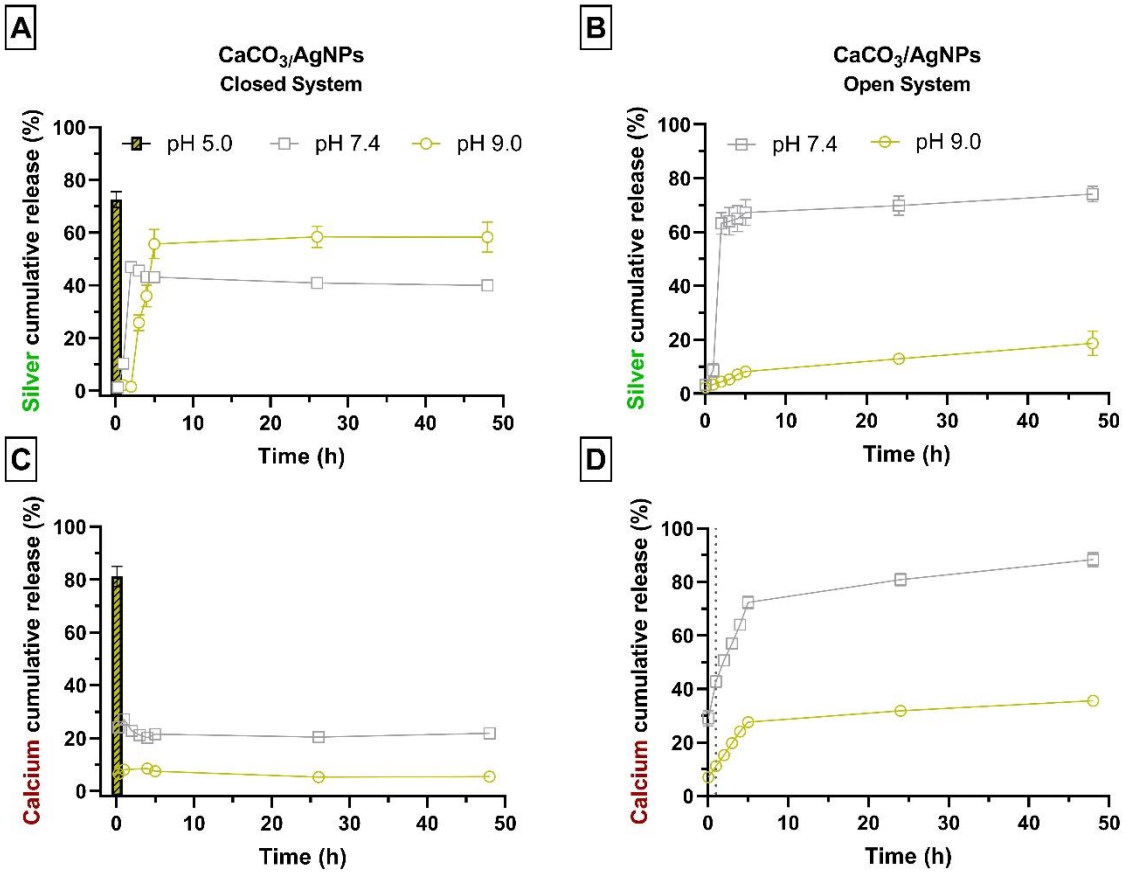

Figure 4-12. Cumulative release over time of silver (A and B) and calcium ions (C and D) from $CaCO_3$/AgNPs hybrids at pH 5.0, 7.4 and 9.0 at closed (A and C) and open-like (B and D) conditions.

At static conditions, $CaCO_3$/AgNPs presented a burst release of AgNPs at pH 5.0, which was promoted by the dissolution of the crystals, as corroborated by the high amount of calcium ions released, ca. 80% of the total calcium in the hybrids. At pH 7.4 and 9.0 there was a slower release, with the maximum amount of AgNPs being released within 2 (47 ±

1%) and 5 hours (56 ± 6%), respectively. This was not accompanied by the dissolution of $CaCO_3$, and the maximum release coincided with the end of the crystals recrystallisation (**Figure 4-2** and **Figure 4-3**), demonstrating that the transformation of vaterite into calcite promoted the partial release of the cargo. The hybrids released more silver at pH 9.0 than at pH 7.4, due to the longer recrystallisation times, which made the process more selective and therefore, lower contents of AgNPs were entrapped into calcite as mentioned in the previous chapter. It is noteworthy that calcite crystals can also work as carriers for AgNPs. After vaterite recrystallisation, the newly formed calcite crystals retained around 53 and 44% of AgNPs at pH 7.4 and 9.0, respectively, with no further significant release of AgNPs being detected in the following hours. Therefore, it is demonstrated that the vaterite-to-calcite recrystallisation promotes the partial release of the cargo, and although the recrystallisation triggers the release of the payload, calcite can also uptake the cargo and prevent a complete release. The amount of the payload that remains free depends on the affinity between the cargo and $CaCO_3$ as demonstrated in **Chapter 3**. These results show that at static conditions, the pH and recrystallization are the main factors governing the release mechanism of AgNPs from $CaCO_3$.

The release of AgNPs and calcium ions at pH 7.4 and 9.0 was also studied at open-like conditions (**Figure 4-12, B and D),** where the supernatant was periodically removed and replaced with fresh buffer. This was not done at pH 5.0, as the results from the experiment at static conditions demonstrated that at low pH values the crystals dissolve and have an immediate burst release of AgNPs.

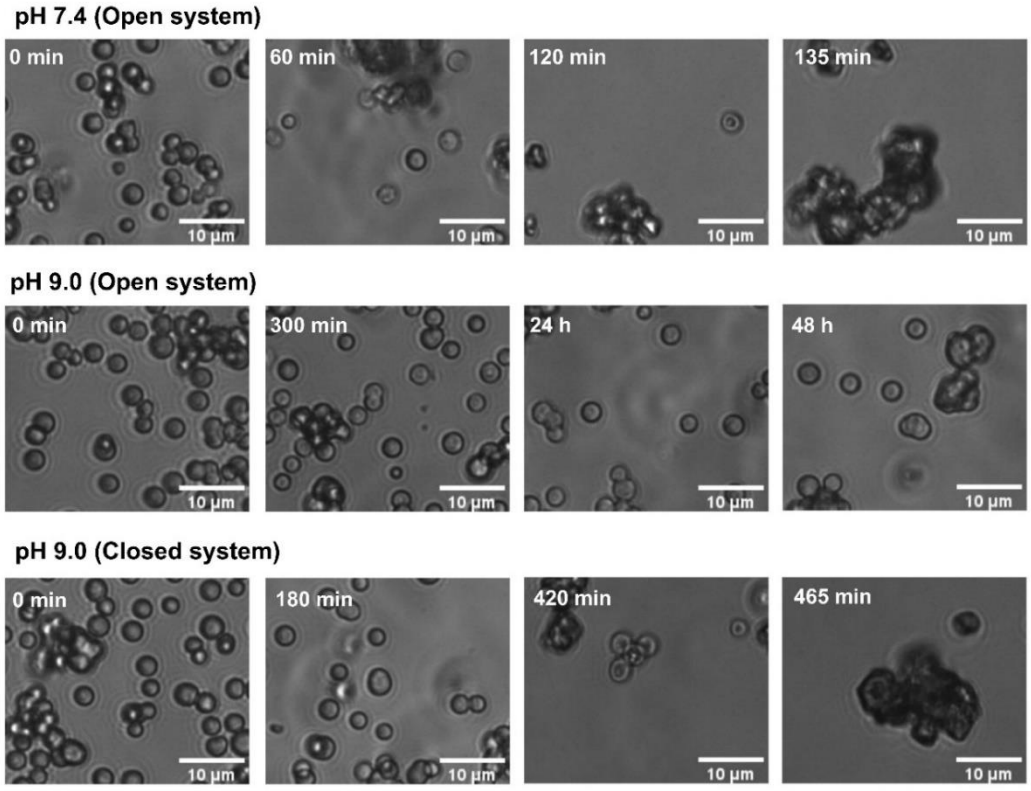

Figure 4-13. Transmittance images of $CaCO_3$/AgNPs hybrids (1.5 $mg.ml^{-1}$) over time at open (pH 7.4 and pH 9.0) and closed-like conditions (pH 9.0).

The data presented in **Figure 4-12, B and D,** shows that at pH 7.4 the release was mainly driven by the dissolution of the hybrids (81% of calcium released), and to a lower extent, by the transformation of vaterite into calcite, as demonstrated by the recrystallisation studies at open-like conditions (**Figure 4-13**). This resulted in approximately 74% of silver being released after 48 hours. On the other hand, at pH 9.0 almost no silver was released despite the continuous replacement of the buffer due to the low solubility of $CaCO_3$ at basic pH. Moreover, the continuous removal of dissolved $CaCO_3$ when replacing the supernatant with fresh buffer delayed the recrystallisation of vaterite into calcite. This was corroborated by the recrystallisation studies at open-like conditions (**Figure 4-13**), where via the continuous replacement of the buffer, the recrystallisation of vaterite into calcite was prolonged. This was more drastically noticed at pH 9.0, where the recrystallisation of the hybrids into calcite took more than 48 hours (**Figure 4-13**).

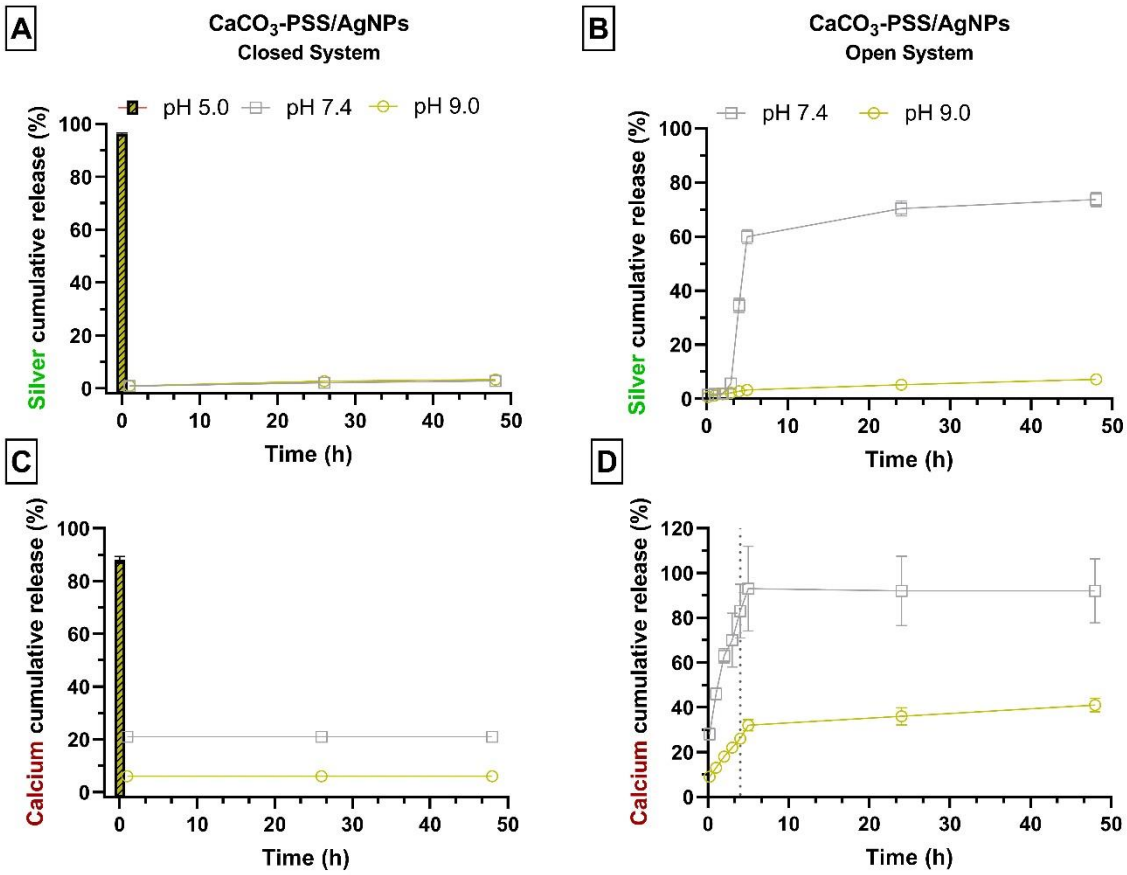

Figure 4-14. Cumulative release over time of silver (A and B) and calcium (C and D) from $CaCO_3$-PSS/AgNPs hybrids at pH 5.0, 7.4 and 9.0 at closed (A and C) and open-like (B and D) conditions.

The effect of PSS on the release of AgNPs from the hybrids was also analysed under the same conditions. As mentioned in the previous sections, PSS is a negatively charged polymer that can stabilise vaterite crystals and prevent the recrystallisation into calcite.

As shown in **Figure 4-14**, at static conditions, the hybrids synthesised with PSS did not release AgNPs at pH 7.4 and pH 9.0 as they did not recrystallise (**Figure 4-15**). On the other hand, at pH 5.0 there was an immediate burst release, with over 90% of AgNPs being released. This was promoted by the dissolution of $CaCO_3$ at acidic pH, demonstrated by the high amount of calcium ions in the solution (ca. 90%). These results highlight the importance of recrystallisation in triggering the release of AgNPs, and that by controlling it, is possible to target the cargo release at acidic conditions. This is a highly desirable property for the target release of drugs at infection and inflammation sites, as well as at the core of biofilms or tumours, where an acidic microenvironment is mostly predominant.

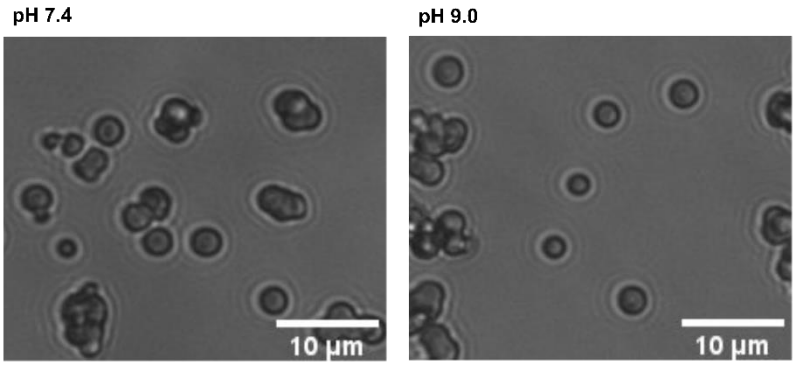

Figure 4-15. Transmittance images of $CaCO_3$-PSS/AgNPs after 48 hours in TBS at pH 7.4 (left) and pH 9.0 (right).

The release of silver and calcium from the $CaCO_3$-PSS/AgNPs hybrids was also studied at open-like conditions (**Figure 4-14, B and D)**. At pH 9.0 there was no release of silver, once again due to the low solubility of $CaCO_3$ at basic pH. At pH 7.4 about 60% of silver was released after 6 hours due to the continuous dissolution of the crystals promoted by the frequent replacement of the buffer. Interestingly, the release profile of calcium at pH 7.4 demonstrated that ca. 80% of $CaCO_3$ had to be dissolved for a significant release of silver to happen. This was lower for the hybrids synthesised without PSS, for which about 40% of the crystals had to be dissolved before a significant release of AgNPs. This difference might be due to the recrystallisation also playing a role in the release of silver from the $CaCO_3$/AgNPs hybrids and the lower stability of the hybrids without PSS. Nonetheless, despite these differences, the data show that the hybrids just released AgNPs when their structure was significantly affected by the dissolution of $CaCO_3$, which can be explained by the unique structure of vaterite and the good affinity between $CaCO_3$ and AgNPs. **Figure 4-16** presents an outline of the main release mechanism of AgNPs in buffer saline.

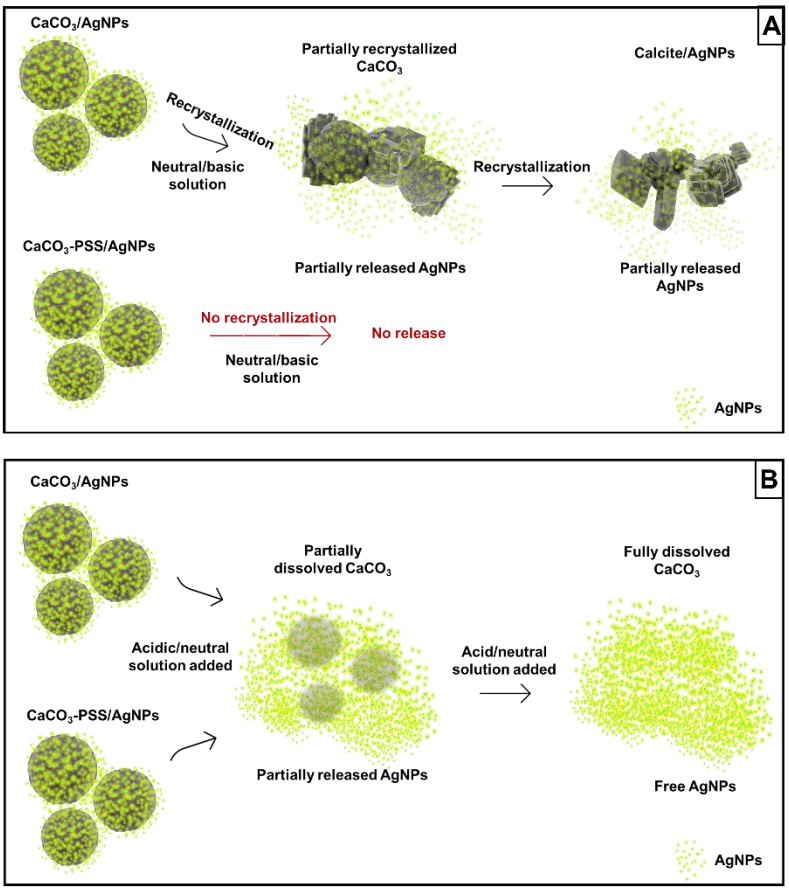

Figure 4-16. AgNPs main release mechanisms in saline buffer solutions: recrystallisation (A) and dissolution (B).

3.3.2. Release of AgNPs in the presence of proteins and carbohydrates

The recrystallisation of vaterite is a complex process that, as demonstrated before, can be affected by several factors. Less than twenty years ago, the "corona effect" on nanoparticles was reported. It describes the adsorption of proteins, carbohydrates, lipids, nucleic acids, and other molecules onto the surface of nanoparticles when they are mixed with biologic fluids or media rich in biomolecules[294]. Herein, MHB-S, the medium used to perform the antibacterial tests, was used to study the release behaviour of the hybrids when exposed to high contents of proteins and carbohydrates at pH 7.4.

As depicted in **Figure 4-17**, 39 and 18% of silver was released from $CaCO_3$/AgNPs and $CaCO_3$-PSS/AgNPs within 1 hour, and 53% and 34% after 96 hours, respectively. Although it is clear that PSS retarded the release of the AgNPs, and that both types of hybrids presented a very slow release in MHB-S, the hybrids with PSS did not present a release profile similar to that in saline buffer at pH 7.4, where almost all the silver remained embedded in the hybrids. Interestingly, the hybrids presented good stability in MHB-S, with no recrystallisation detected within 96 hours (**Figure 4-18**), even for the crystals

without PSS. This evidenced that recrystallisation was not the driving force for the release of AgNPs, but instead the interactions between the biomolecules in the medium and the hybrids and AgNPs. The need for the microparticles to decrease the surface energy, and the proteins and carbohydrates in the medium to minimise the free enthalpy, favoured the adsorption on the surface of $CaCO_3$ and AgNPs, forming a corona through electrostatic, hydrophobic and van der Walls interactions[294].

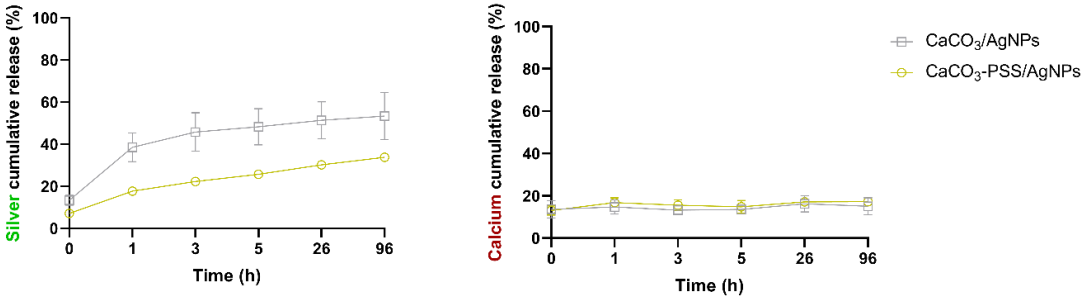

Figure 4-17. Cumulative release over time of silver (left) and calcium (right) from $CaCO_3$/AgNPs and $CaCO_3$-PSS/AgNPs hybrids in MHB-S.

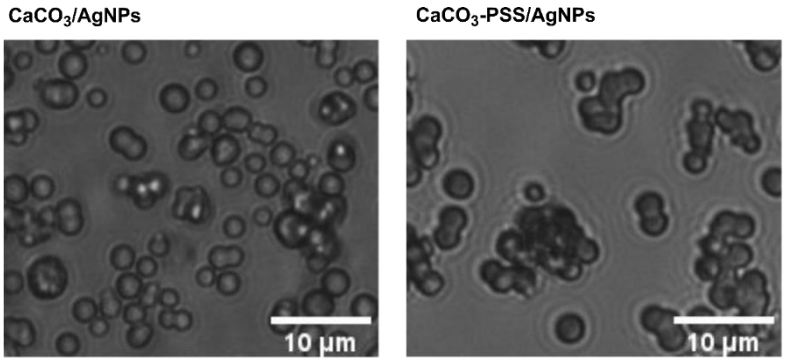

Figure 4-18. Transmittance images of $CaCO_3$/AgNPs and $CaCO_3$-PSS/AgNPs after 96 hours in MHB-S.

The formation of a corona on $CaCO_3$ surface has previously been reported and used to prevent or retard the recrystallisation of vaterite and therefore, the cargo release[164,296,297]. Nonetheless, to the best of our knowledge, the opposite effect, *i.e.*, the corona triggering the cargo release from vaterite has not been reported before. We believe, that while the biomolecules that compose the corona promote the stability of vaterite and halt the recrystallisation, which is desirable, they are also adsorbed onto the surface of the AgNPs, as demonstrated by the FTIR data in **Figure 4-19**, decreasing the affinity between the AgNPs and $CaCO_3$. Therefore, poorly entrapped AgNPs are eventually released due to the low affinity to $CaCO_3$. This is potentiated by the depletion of 13 to 17% of calcium (**Figure**

4-17) from the surface of some of the hybrids, as demonstrated in **Figure 4-20**, which facilitated the release of AgNPs.

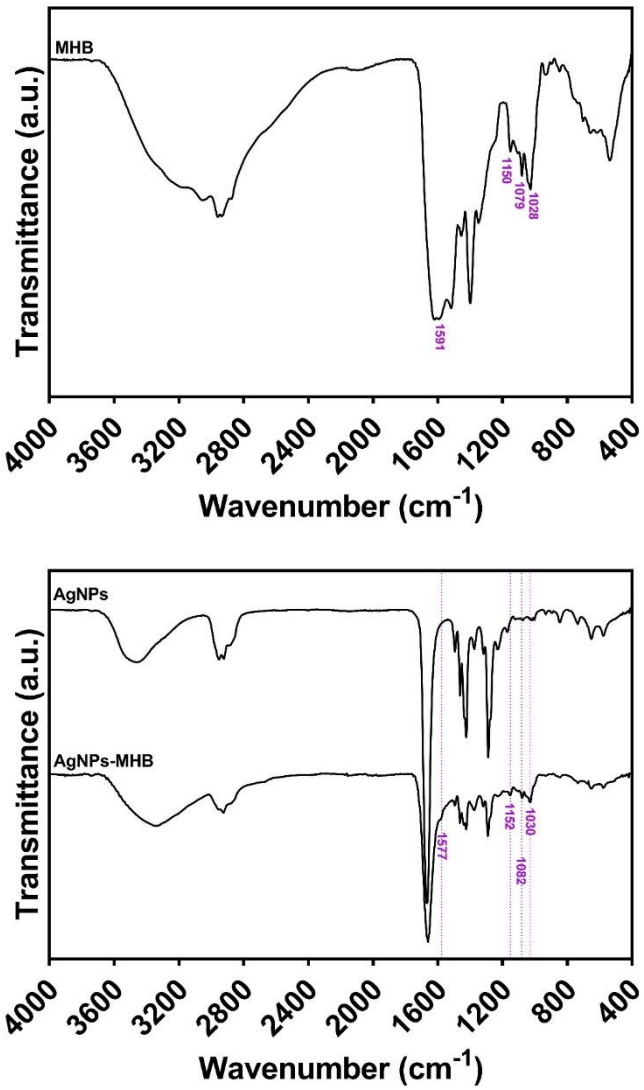

Figure 4-19. FTIR spectra of AgNPs before (AgNPs) and after (AgNPs-MHB) being mixed with MHB-S. The AgNPs mixed with MHB-S were washed three times with ultrapure, type I water before the FTIR analysis. Peaks assigned in purple represent the characteristic bands of MHB-S found in the AgNPs spectrum.

Although the release of AgNPs was more accentuated in the first hour, it slowly carried on throughout the incubation period. This might be due to the corona formation steps, which entail the development of a "soft" corona composed of biomolecules that exist in high abundance, which then evolves to a "hard" corona composed of biomolecules with high affinity to the surface[203,294,298]. The formation of the "soft" corona is believed to occur within seconds to minutes, and the "hard" corona, within hours[203]. This might explain the

higher contents of AgNPs released in the first hour and then the slow release over the next 96 hours.

The results presented here demonstrate that the proteins and carbohydrates in MHB-S changed the hybrids surface properties, as well as the interactions between $CaCO_3$ and AgNPs, resulting in a slow release over time. Although these results cannot be extrapolated to situations where the cargo and/or the medium are different, as the corona might potentiate or decrease the interactions between $CaCO_3$ and the cargo, it shows that vaterite is highly sensitive to the surrounding environment and that the release is not only controlled by recrystallisation and dissolution at low pH, but also by the medium composition which can promote or halt the cargo release. **Figure 4-21** outlines the release route of AgNPs from vaterite in the presence of biomolecules.

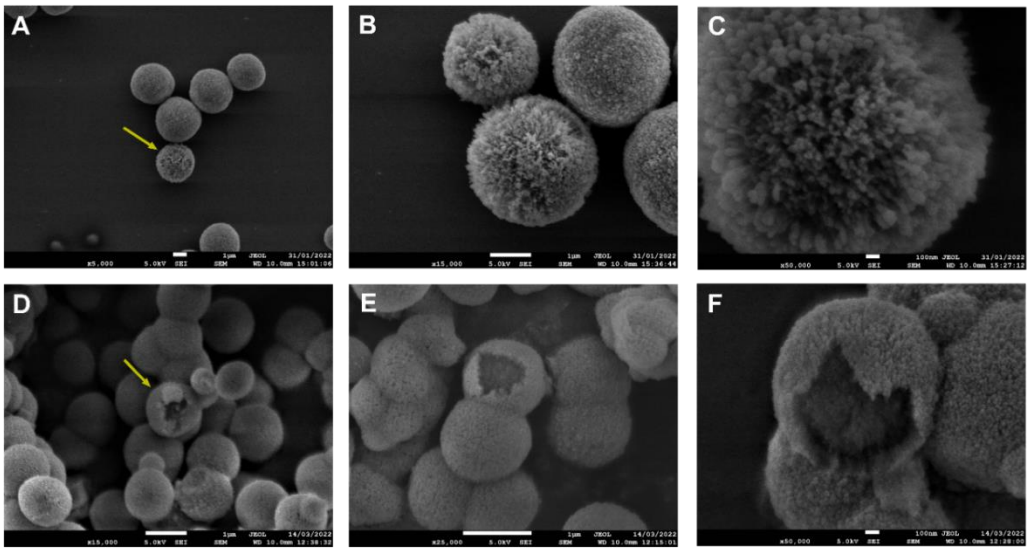

Figure 4-20. SEM images of $CaCO_3$/AgNPs (A-C) and $CaCO_3$-PSS/AgNPs (D-F) after 2 hours in MHB-S at 37°C. The yellow arrows in images A and D point to the hybrids with partially dissolved surfaces (higher magnification images allow to see this in more detail).

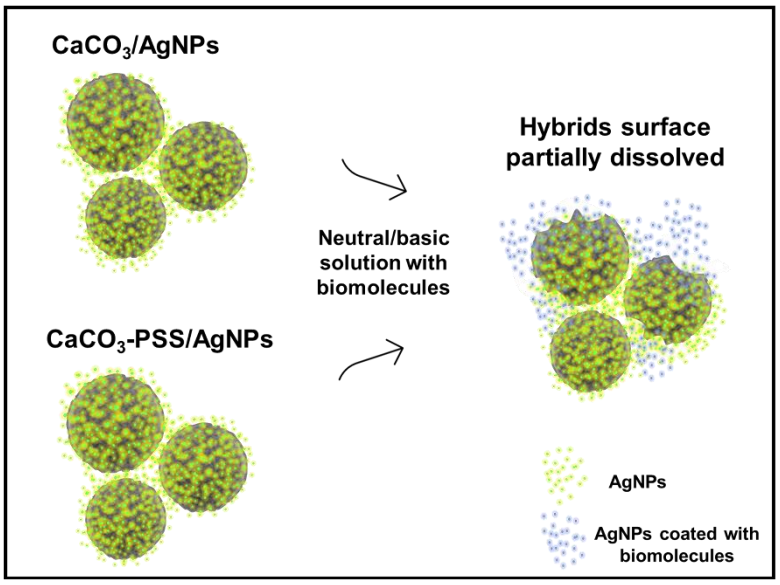

Figure 4-21. Scheme of AgNPs release mechanism at neutral to basic pH in the presence of biomolecules.

3.4. Antibacterial activity

The alarming levels of antimicrobial resistance and decreasing number of drugs capable of eradicating the evolved microorganisms have raised awareness to control the release of antimicrobial agents and improve their delivery for better effectiveness and therapeutical outcomes. Herein, $CaCO_3$/AgNPs hybrids were developed to store, protect, carry and release AgNPs more efficiently.

To assess the antibacterial activity of $CaCO_3$/AgNPs hybrids, and find out whether the activity of the AgNPs loaded into $CaCO_3$ was affected by the loading process, antibacterial tests were carried out against E. *coli*, MRSA and *P. aeruginosa*, three bacterial isolates responsible for a high number of infections in hospital settings. $CaCO_3$/AgNPs hybrids were chosen instead of $CaCO_3$-PSS/AgNPs hybrids, as the last ones present a lower release of AgNPs in MHB-S at pH 7.4.

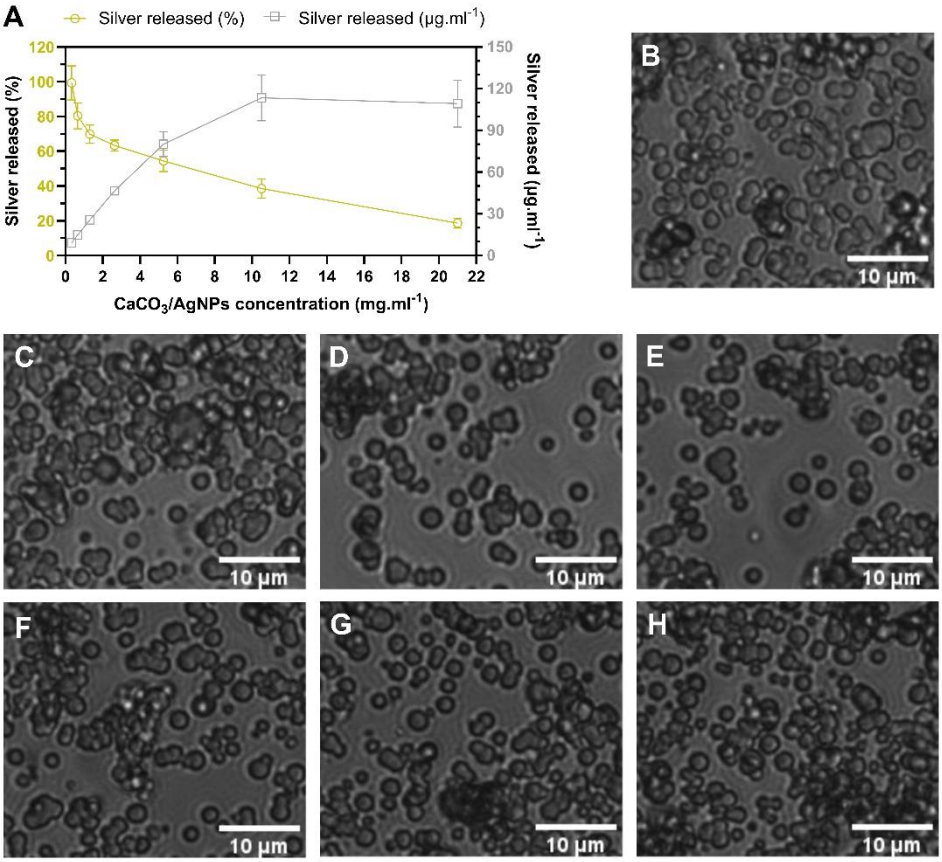

Figure 4-22. Content of silver released after the incubation of $CaCO_3$/AgNPs hybrids in MHB-S at different concentrations for 24 hours at 37°C (A). Transmittance images from B to H of $CaCO_3$/AgNPs hybrids at 0.33, 0.66, 1.31, 2.63, 5.25, 10.5 and 21 $mg.ml^{-1}$, respectively, after incubation.

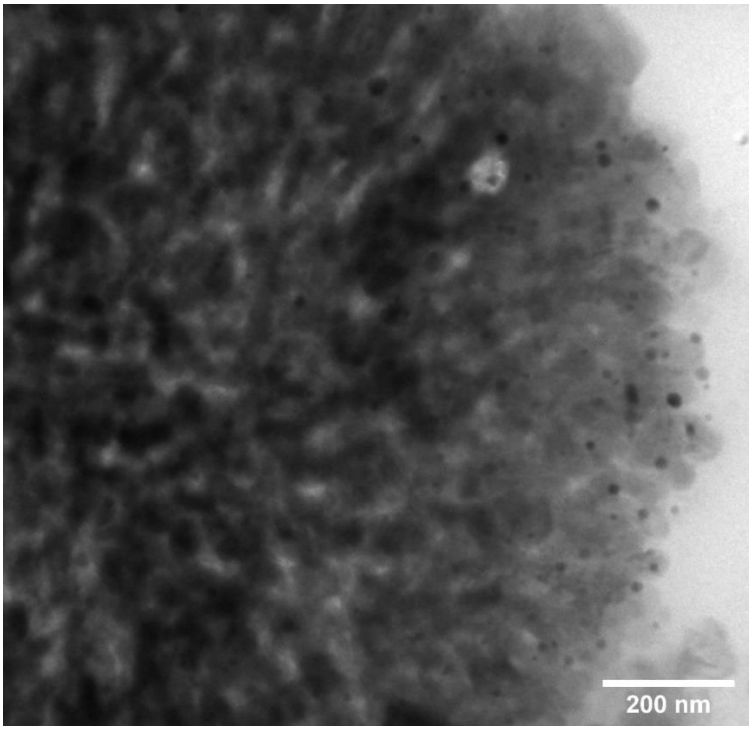

Figure 4-23. TEM images of cross-sectioned AgNPs/$CaCO_3$ hybrid.

Before assessing the antibacterial activity of the hybrids, the content of AgNPs released from the $CaCO_3$/AgNPs hybrids in MHB-S was determined. As presented in **Figure 4-22**, the amount of silver released ranged between 9.1 and 109.4 $\mu g.ml^{-1}$, corresponding to 99.4% and 18.6% of the total amount of silver loaded into the hybrids at the concentrations ranging between 0.33 and 21 $mg.ml^{-1}$, respectively. Similarly to the release studies in MHB-S, no recrystallisation of the hybrids was detected after 24 hours, as shown in the transmittance images in **Figure 4-22**. It was also verified that the amount of silver released increased with the concentration of hybrids, and then a plateau was reached when the hybrids concentration was above 10 $mg.ml^{-1}$.

AgNPs are mainly found on the surface or close to the surface of $CaCO_3$ (**Figure 4-23**), therefore when the concentration of $CaCO_3$/AgNPs increases, more hybrids are in suspension, which increases the surface area and release of AgNPs through the partial dissolution of the surface (**Figure 4-20**), instead of the entire or more profound areas of the hybrids which do not carry AgNPs. This exposes more nanoparticles to the proteins and carbohydrates present in MHB-S, which tends to form a corona on their surface, decreasing the affinity to $CaCO_3$. The reduced affinity, associated with the fact that the nanoparticles become poorly entrapped on the partially dissolved surfaces, promotes the release of the AgNPs. When there is an excess of hybrids, and the dissolution of the crystals necessary to reach the equilibrium only affects the surfaces of the $CaCO_3$/AgNPs hybrids, a plateau is reached, and the amount of silver released does not change with increasing concentrations of hybrids.

Figure 4-24 presents the minimum concentration of silver required to inhibit the growth of planktonic bacteria and biofilms (MIC and MIBC, respectively) and kill the bacteria (MBC). Unloaded AgNPs were used as a control for comparison with the AgNPs released from the hybrids. The results show that the AgNPs released from the $CaCO_3$/AgNPs hybrids inhibited the growth of *E. coli*, MRSA and *P. aeruginosa* at 34 ± 12, 38 ± 22 and 17 ± 10 $\mu g.ml^{-1}$, respectively. The AgNPs were also effective in killing and inhibiting the growth of biofilms.

The bare $CaCO_3$ crystals did not present bactericidal activity at concentrations equal to or below 21 $mg.ml^{-1}$, which shows that the bactericidal activity of the hybrids was mostly promoted by the AgNPs.

Interestingly, the AgNPs presented better activity against *E. coli* and *P. aeruginosa* than against MRSA. Despite the reason behind this effect not being fully understood and the lack of consensus, similar results have been reported elsewhere, and is believed to result

from structural differences between the membrane of gram-positive and gram-negative bacteria[299–301].

Importantly, in all the antibacterial tests performed, there were no significant differences between the antibacterial activity of the unloaded AgNPs and the AgNPs released from the hybrids, which demonstrates that the loading steps and vaterite itself did not impair the activity of the AgNPs. The good antibacterial activity of the developed hybrids, allied with the controlled and targeted release, offers new opportunities to use and deliver active AgNPs more efficiently, and contribute to a more rational use of silver.

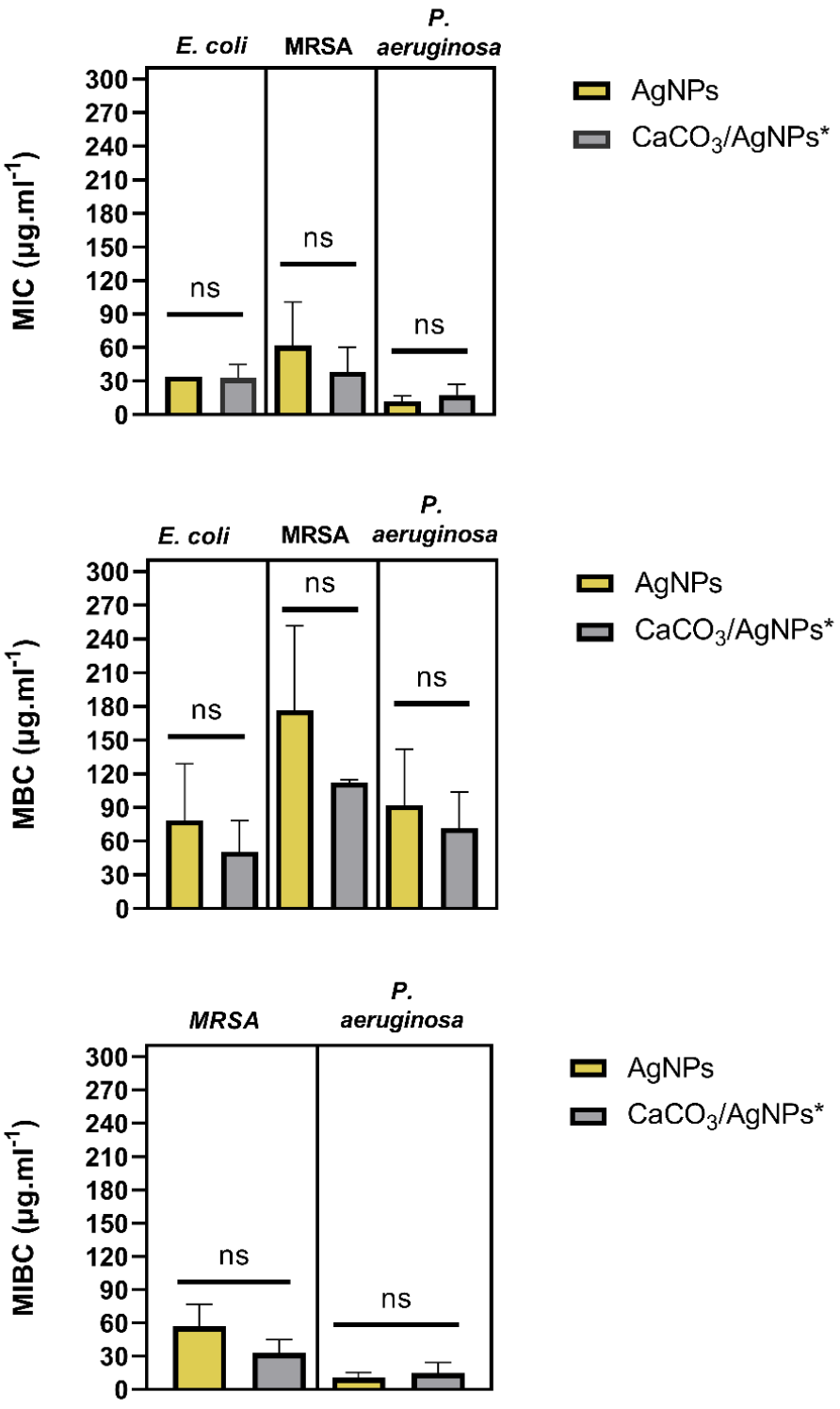

Figure 4-24. MIC, MBC and MIBC (µg/ml) of AgNPs and $CaCO_3$/AgNPs against *E. coli*, MRSA and *P. aeruginosa*. Data represented the average of three to six repeats with three replicates each. Statistical analysis made using the t-test (normal distribution) and Mann-Whitney test (non-normal distribution). ns: not significant difference. $CaCO_3$/AgNPs*: concentration of silver released from $CaCO_3$/AgNPs hybrids determined based on preliminary studies where the amount of silver released in MHB-S was quantified.

4. Conclusion

In this chapter, hybrids composed of vaterite $CaCO_3$ and AgNPs were produced for the protection and storage of AgNPs. To control the release of the cargo, Dex^{CM} and PSS were used to stabilise the hybrids by preventing the recrystallisation of vaterite to calcite and consequent cargo release. Dex^{CM} partially prevented the recrystallisation at contents equal to 4%, although it affected the uptake of AgNPs. On the other hand, 2% of PSS prevented the recrystallisation of the hybrids without impairing the uptake of AgNPs.

The release of AgNPs from $CaCO_3$/AgNPs and $CaCO_3$-PSS/AgNPs hybrids was studied at different pH values, at static and open-like conditions, and in the presence of high contents of biomolecules for a detailed elucidation of the release mechanisms. The results showed that dissolution of $CaCO_3$ is the primary release mechanism at acid pH, while at neutral and basic pH, the recrystallisation is responsible for the release of AgNPs. Nonetheless, the interaction of AgNPs with the newly formed calcite crystals dictates the amount of AgNPs that remains free. The hybrids stabilised with PSS presented a targeted release at acid environments, with a burst release at pH 5 and no AgNPs being released at pH 7.4 and 9.0. New insights were also introduced about the effect of biomolecules on the release of AgNPs from the hybrids.

The antibacterial studies demonstrated that the hybrids developed protect the AgNPs without impairing their activity. It was also demonstrated that the antibacterial activity of the hybrids against *E. coli,* MRSA and P. *aeruginosa,* resulted mainly from the release of AgNPs.

Overall, this work presents a simple approach to control the recrystallisation of vaterite and consequent cargo (AgNPs) release. The detailed analysis of the release mechanism gives a complete insight into the challenges and viable solutions for the targeted and controlled release of active compounds from vaterite vectors, and highlights the impact of biomolecules in changing the affinity between the cargo and the vector, and consequently the release mechanism. While this work is focused on AgNPs, the findings can be extrapolated to other types of compounds loaded into $CaCO_3$, and will help future works on the design of vaterite vectors with features of controlled and targeted release.

Chapter 5

Antibacterial coatings based on $CaCO_3$/AgNPs hybrids

1. Introduction

Antimicrobial materials are crucial to decrease the spread of pathogenic microorganisms through contaminated surfaces, with their importance being even more emphatic in hospital settings where the spread of dangerous microorganisms through contaminated surfaces is a real threat to patients[302]. Different antimicrobial agents, predominantly metals and metal oxides, including silver, copper, zinc and titanium dioxide, have been incorporated into antibacterial coatings, with silver being the most used one[303,304]. While silver nanoparticles (AgNPs) and silver salts present a broad antimicrobial activity, the unwanted release of silver in the environment raises concerns about its toxicity on living organisms[227,305,306]. Moreover, AgNPs present a tenuous stability, and once disrupted the effectiveness of the nanoparticles decreases. Therefore, different platforms have been used to immobilise AgNPs, including calcium carbonate ($CaCO_3$) vaterite[227]. Vaterite crystals are metastable polymorphs of $CaCO_3$ that, due to their porous structure, can accommodate AgNPs, protecting them from external factors[227]. Moreover, the dissolution of vaterite at acidic pH makes these carriers ideal for releasing AgNPs in acidic microenvironments, like inflammation sites and the core of biofilms[1].

As referred in the previous chapters, the mechanism of AgNPs release from vaterite is based either on pH-mediated dissolution or vaterite recrystallisation into calcite in aqueous solutions. The release of AgNPs is also controlled by the medium composition and the affinity between $CaCO_3$ and the AgNPs.

The production of coatings entails the use of polymers that promote the coating adhesion to the substrate, either through mechanical interlocking, electrostatic interactions, polymer chain entanglement or intermolecular bonding like van der Waals forces and covalent and

hydrogen bonds[307–309]. Polyvinylpyrrolidone (PVP) is a non-toxic, water-soluble polymer with excellent binding and film-forming properties[310]. PVP also presents a good affinity to both hydrophilic and hydrophobic compounds due to its hydrophilic pyrrolidone moiety and hydrophobic alkyl groups[172,311]. Due to these properties, PVP has been used to produce coatings and adhesives[311].

An important parameter when developing coatings with vaterite is selecting polymers that can also halt the recrystallisation of vaterite into calcite, giving an option for controlled and sustained release. Mucins are large bioactive extracellular glycoproteins mainly composed of carbohydrates, with the main functions being lubrication, hydration, barrier properties and regulation of biological responses[312]. Adding to that, mucins present good adhesive properties, and their bulky structure with a rich chemistry can work as a stabilising agent for vaterite by suppressing the diffusion of ions from the surface of the crystals[107,313]. Moreover, materials coated with some mucins present improved compatibility and anti-fouling properties[312].

In this chapter, hybrids composed of vaterite and AgNPs ($CaCO_3$/AgNPs) were used for the production of antibacterial coatings. A simple method was developed to produce the coatings, and a formulation composed of hybrids, PVP and mucin developed. The drop casting technique was selected to coat polystyrene due to the simplicity of the method and lower wastage of sample compared with other methods like spin coating[314].

The coatings were prepared on 96-well plates, which minimised the quantity of sample required, and then characterised through different techniques, including scanning electron microscopy (SEM), X-ray diffraction (XRD) and Fourier-transform infrared spectroscopy (FTIR). The release of AgNPs was tested to evaluate the role of the coatings in preventing the premature release of the nanoparticles. The antibacterial activity of the coatings was assessed against *Escherichia coli* (*E. coli)*, methicillin-resistant *Staphylococcus aureus* (MRSA) and *Pseudomonas aeruginosa* (*P. aeruginosa*). The additives influence on the antibacterial activity was also studied, as well as the *in vitro* cytotoxicity of the hybrids at bactericidal concentrations on human cells.

Overall, this chapter examines the potential of $CaCO_3$/AgNPs hybrids as active components for the production of surfaces with strong antibacterial activity. A simple approach to rapidly produce coatings and test their antibacterial activity is presented, opening new routes to accelerate the development of novel antibacterial coatings, crucial to reduce the spread of dangerous bacteria through contact with surfaces.

2. Materials and methods

2.1. Materials

Sodium borohydride ($NaBH_4$, ≥99% pure), polyvinylpyrrolidone M_w 40 kDa and 150-300 kDa (PVP), Mueller Hinton broth Sigma 70192 (MHB-S), Mueller Hinton agar Sigma 70191 (MHA-Sigma), phosphate buffer saline (PBS) tablets, Calbiochem® mucin from the bovine submaxillary gland, trypsin-EDTA solution, heat-inactivated foetal bovine serum (FBS), and TraceCERT® 1 ppm Silver ICP-MS standard in 2% nitric acid, were obtained from Sigma-Aldrich (Steinheim, Germany). MSCGM™ mesenchymal stem cell growth medium Bullet Kit™ was purchased from Lonza (Walkersville, MD USA). Silver nitrate ($AgNO_3$, ≥99% pure), calcium chloride dihydrate ($CaCl_2.2H_2O$, ≥99% pure), sodium carbonate (Na_2CO_3, ≥99.5%), tris buffer saline 10X solution (TBS), 99% ethanol, hexamethyldisiloxane 98% (HMDS), dimethyl sulfoxide, high purity resazurin sodium salt (80% min.), 3-(4,5-Dimethylthiazol-2-yl)-2,5-Diphenyltetrazolium Bromide (MTT), Gibco™ Penicillin-Streptomycin (10,000 $U.mL^{-1}$), Gibco™ low glucose-GlutaMAX supplement Dulbecco's Modified Eagle Medium (DMEM), sodium hydroxide pellets (NaOH, ≥98% pure), glacial acetic acid (CH_3COOH, ≥99.7 % pure), 70% nitric acid (HNO_3, analytical grade) and 37% hydrochloric acid (HCl, analytical grade) were obtained from Fisher Scientific (Loughborough, United Kingdom).

2.2. Methods

2.2.1. Synthesis of AgNPs

AgNPs with an average size around 14 nm and coated with PVP 40 kDa were synthesised *via* a modified chemical reduction methodology as described in **Chapter 2**.

2.2.2. Synthesis of bare $CaCO_3$ and $CaCO_3$/AgNPs hybrids

Bare vaterite $CaCO_3$ and $CaCO_3$/AgNPs hybrids were synthesised as described in **Chapter 4.**

2.2.3. Characterization of the $CaCO_3$/AgNPs hybrids

Inductively coupled plasma mass spectrometry (ICP-MS): The content of silver loaded into the hybrids was determined by ICP-MS as described in **Chapter 3**.

SEM: The morphology of $CaCO_3$ and $CaCO_3$/AgNPs hybrids was analysed by SEM (JEOL, JSM-7100f, Tokyo, Japan) as described in **Chapter 3**.

2.2.4. Coatings production

The drop casting technique was selected to coat flat bottom hydrophilic polystyrene wells of a 96-well microplate (SARSTEDT, Germany) due to the simplicity of the method and lower wastage of hybrids. The formulation and coating steps were optimised to produce uniform surfaces and prevent the recrystallisation of the hybrids.

2.2.4.1. Method optimisation

Dispersions of $CaCO_3$/AgNPs hybrids in ultrapure, type I water, with and without PVP, were prepared by mixing all the components at 2000 rpm for 5 min in a ThermoMixer® C with a SmartBlock (Eppendorf, Germany), followed by sonication at 30 Hz, power 30%, for 5 min in a Fisherbrand™ Transsonic TI-H-10 ultrasonic batth (Fisher Scientific, USA) and then mixed for 3 min. After that, 60 and 90 µl of the dispersions were poured on the wells of a 96-well microplate and dried in the oven (Heratherm™ oven, Thermo Scientific, USA) at 50 and 37°C for 2 and 20 hours, respectively. The concentrations of $CaCO_3$/AgNPs hybrids and PVP in the coating dispersions were 6 and 8 $mg.ml^{-1}$, respectively. After drying, the adhesion of the coatings to the wells was tested by scraping the formed coatings with a spatula. The coatings were also analysed under the microscope (Life Technologies EVOS FL, Invitrogen, USA) to study the effect of the coating preparation steps on the polymorphism of the hybrids. Different drying conditions were also tested for the wells coated with 90 µl of $CaCO_3$/AgNPs coating dispersion. After pouring the dispersion into the wells, these were dried at 80°C for 2 hours, instead of the 50/37°C temperature cycle.

2.2.4.2. Optimised method

Due to the recrystallisation of the hybrids during the coatings production, mucin was added to the formulation to halt the transformation of vaterite into calcite. To that end, $CaCO_3$/AgNPs hybrids were mixed with a water-based solution of mucin for 10 min at 2000 rpm, and then PVP and ultrapure, type I water were added and mixed at 2000 rpm for another 5 min. After that, the dispersion was sonicated for 5 min at 35 Hz, power 30%, to break apart any clusters of hybrids, and then mixed for 3 min before being poured into the wells of a 96-well microplate (90 µl/well). Formulations with different concentrations of hybrids were prepared by replacing the hybrids with equal quantities of bare $CaCO_3$ vaterite. Regardless of the $CaCO_3$/AgNPs hybrids concentration, the PVP and mucin concentrations were kept constant, *i.e.*, at 8 and 1 $mg.ml^{-1}$, respectively, as well as the total

concentration of vaterite (6 mg.ml^{-1}, bare $CaCO_3$ plus $CaCO_3$/AgNPs hybrids). The coating pattern is depicted in **Figure 5-1.** This layout was chosen as it allowed to quickly test the antibacterial activity of the coatings with different concentrations of hybrids and respective replicates, without adding extra steps, or the need to set up a new layout.

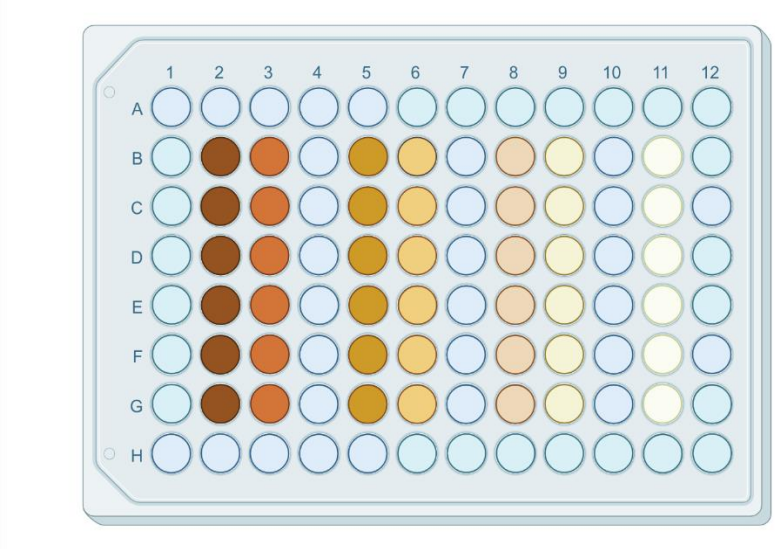

Figure 5-1. Scheme of the coatings in the 96-well microplate. The brown/yellow wells represent the wells coated with different concentrations of hybrids, with the dark brown wells representing the coatings with the highest concentrations of hybrids. The blue wells represent the wells that were filled with PBS to prevent the dehydration of the bacteria. Created with BioRender.com

2.2.5. Characterisation of the coatings

SEM: The coatings were cut out from the microplates with a laser cutter and then mounted on stubs using double-sided carbon tape. To determine the thickness of the coatings, cross-sections were also analysed. All the samples were coated with a 5 nm thick layer of gold using a rotary pumped coater (Quorum Q150R ES, UK) and then analysed on a field emission electron microscope (JEOL, JSM-7100f, Tokyo, Japan) with a secondary electron detector and an acceleration voltage of 5.0 kV. Three independent samples were analysed to determine the average thickness of the coatings.

SEM coupled with energy dispersive X-Ray spectroscopy (SEM-EDS): Samples of the cross-sectioned coatings were mounted on stubs using double-sided carbon tape and then coated with a 5 nm thick layer of gold. An accelerating voltage of 10 kV and a working distance of 10 mm was used. The probe current was optimised to give a dead time of around 45%.

Fourier transform infrared (FTIR) spectroscopy: Previously formed coatings were humidified with ultrapure, type I water, and portions were scratched out and placed on the

FTIR spectrometer (Spectrum Two FTIR spectrometer, PerkinElmer, Uberlingen, Germany). The sample was quickly dried with a Dexter® air gun until no water peaks were present in the spectrum, and then the spectrum was recorded. Mucin, PVP and $CaCO_3$/AgNPs were also analysed. The analysis settings were 32 scans per sample between 500 and 4000 cm^{-1} with a resolution of 4 cm^{-1}. The ATR (attenuated total reflectance) technique was used in all the measurements.

X-ray diffraction (XRD): The crystallinity of the coatings was analysed in a SmartLab SE X-Ray diffraction system from Rigaku Co. Ltd. (Tokyo, Japan) with a Kβ filter for copper ($\lambda = 0.1392$ nm). Samples were scanned with a $\theta/2\theta$ scan axis. The scan range varied between 20° and 80°, and the scan mode and speed were 1D and 5°/min, respectively.

2.2.6. Analysis of AgNPs release from the coatings

The release of AgNPs from the coating only composed of hybrids, and the coating composed of hybrids mucin and PVP, was assessed in MHB-S and TBS (unless otherwise specified TBS is TBS 1x, *i.e.*, ten times diluted from TBS 10x). Briefly, 200 µl of TBS or MHB-S were added to the coated wells and then incubated at 37°C overnight (ca. 19 hours). The next day, TBS and MHB-S were aspirated from the wells and centrifuged at 2350 *g* for 5 min to sediment any possibly detached hybrids from the coating. After that, the supernatant was analysed by UV-vis spectrophotometry (NanoDrop One spectrophotometer, Thermo Scientific, USA) to detect any released AgNPs. TBS and MHB-S were used as blanks. For comparison, the exact content of AgNPs on the coatings was dispersed in the same volume of TBS or MHB-S (200 µl) and analysed on the UV-vis spectrophotometer. All samples were diluted with ultrapure, type I water till the absorbance was below one. The data was multiplied by the dilution factor and then divided by the maximum absorbance for better comparison.. The coatings were also analysed under the microscope (Life Technologies EVOS FL, Invitrogen, USA) to investigate the effect of MHB-S and TBS on the hybrids.

2.2.7. Assessment of the antibacterial activity

The antibacterial activity of coatings with different concentrations of $CaCO_3$/AgNPs hybrids was determined against *E. coli* (O157:H7), MRSA and *P. aeruginosa* (PA01). The *E. coli*, MRSA and *P. aeruginosa* isolates were obtained from the American Type Culture Collection (ATCC 43888), National Collection of Type Cultures (NCTC 12493) and Nottingham Trent University Cultures Collections (NTUCC 876), respectively.

2.2.7.1. Inoculum preparation

The bacterial isolates were streaked onto MHA-S plates and incubated at 37°C for 18 to 24 hours. For each isolate, three to four isolated colonies of the same morphological appearance were transferred into a tube containing 5 ml of MHB-S and then incubated for 18 to 24 hours in a shaker at 35°C and 225 rpm. Overnight cultures were diluted to 5×10^5 CFU.ml^{-1} with MHB-S right before incubation with the coatings.

2.2.7.2. Bacterial viability after contact with the coated surfaces

The antibacterial activity of the coatings only composed of $CaCO_3$/AgNPs hybrids (coating A), and the coatings composed of $CaCO_3$/AgNPs hybrids, PVP and mucin (coating B) was tested. The final concentration of hybrids was equivalent between the two coating formulations and ranged between 7 µg/cm^2 and 1862 µ/cm^2. The assay conditions were selected and optimised based on the reports of Minor L. et al., García-Cañas V. et al. and Bittne M. et al.[315–317] and comprised the measurement of the bacterial viability using the resazurin reduction assay. Before testing the coatings, the sensitivity of the resazurin reduction assay to different concentrations of viable cells of *E. coli*, MRSA and *P. aeruginosa* was tested. Briefly, overnight cultures were serially diluted with PBS and then 150 µl of the bacterial suspensions were mixed with 30 µl of resazurin (0.15 mg.ml^{-1} in PBS). The bacteria were then incubated at 37°C for 2 to 3 hours, after which the fluorescence was measured using a 560 nm excitation/590 nm emission filter set (Cytation 3, BioTek, Vermont, USA).

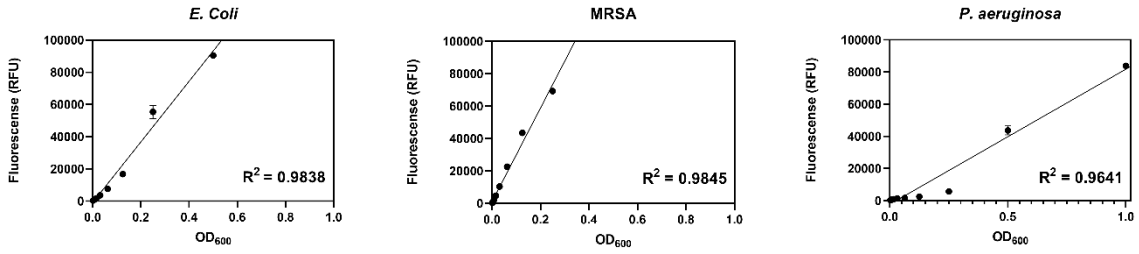

Figure 5-2. Resorufin fluorescence versus the bacterial concentration represented by increasing optical densities at 600 nm (OD_{600}).

As shown in **Figure 5-2**, the fluorescence emitted by resorufin (the product of resazurin reduction by the bacteria) was proportional to the concentration of the bacteria, with *E. coli* and MRSA presenting better correlation coefficients, 0.9838 and 0.9845, respectively, than *P. aeruginosa* (0.9641). Due to the sensitivity of the resazurin assay to the concentration of viable cells, the antibacterial activity of the coatings was tested using this method.

Briefly, 20 µl of *E. coli*, MRSA or *P. aeruginosa*, previously diluted with MHB-S to 5.0×10^5 CFU.ml^{-1}, were added to each well. The final bacterial inoculum density was approximately 3.4×10^4 CFU/cm^2. The microplates were incubated at 37°C for 20 hours. After that, 200 µl of PBS was added to the wells, followed by 30 µl of resazurin (0.15 mg.ml^{-1} in PBS). The microplates were then incubated at 37°C for 2.5 hours, and then 100 µl of each well transferred to a new microplate for measuring the fluorescence using a 560 nm excitation/590 nm emission filter set. Coated wells were also incubated with an equal volume of sterile MHB-S to check for any potential bacterial contamination or unwanted reduction of resazurin. These controls were used as blanks and repeated for all the tested concentrations. To confirm the eradication of the bacteria, 10 µl of the suspension from the wells without detectable bacterial growth were plated onto MHA-S plates. The agar plates were incubated at 37°C for 24 hours and then read visually.

Bacterial growth controls were included in each experiment and consisted in pouring 20 µl of bacterial suspension (5×10^5 CFU.ml^{-1}) into the uncoated wells followed by incubation at the same conditions. The sterility of the MHB-S medium was controlled by incubating it at the same conditions on uncoated wells. Coatings of bare $CaCO_3$ with mucin and PVP and coatings of just bare $CaCO_3$, mucin or PVP were also prepared and tested against the bacteria under the same conditions. All the microplates were sterilised with ethanol (70% v/v), and then dried at 80°C for 2 hours prior to the antibacterial assay. The microplate layout is present in **Figure 5-1**. Each tested condition included four to five replicates.

2.2.8. SEM of the bacteria after contact with the coatings

Polystyrene discs coated with the hybrids, PVP and mucin were put inside a 12-well microplate and then 20 µl of *E. coli*, MRSA or *P. aeruginosa* suspension, previously diluted with MHB-S to 5.0×10^5 CFU.ml^{-1}, was poured on top. The concentration of $CaCO_3$/AgNPs-PVP hybrids was 29 µg/cm^2, and the final bacterial inoculum density was approximately 3.4×10^4 CFU/cm^2. The coated discs were then incubated at 37°C for 2 hours. After that, 1.5 ml of formalin (4% formaldehyde) was added to the wells and left for 10 min to fixate the bacteria. Formalin was then removed, and the discs washed thrice with ultrapure, type I water. After washing, the coatings were dehydrated in graded ethanol solutions (50, 60, 70, 80, 90 and 100%), 5 min per concentration. After dehydration, the samples were infiltrated with HMDS (5 min, twice) to further enhance the drying of the samples without the risk of collapsing. The samples were left drying overnight inside a fume hood for complete evaporation of the HMDS, and then mounted on stubs and coated

with a 5 nm layer of gold before analysis. An accelerating voltage of 10 kV and a working distance of 10 mm was used for SEM imaging.

2.2.9. *In vitro* cytotoxicity assessment

The cytotoxicity of the hybrids was tested on two cell lines, normal human dermal fibroblasts (NHDFs) and human mesenchymal stem cells (hMSCs) acquired from the ATCC and Lonza collections, respectively.

2.2.9.1. Cell culture

The NHDFs were cultured in DMEM media supplemented with 10% FBS and 1% penicillin-streptomycin. The hMSCs were cultured on MSCBM™ hMSC basal medium supplemented with MSCGM™ SingleQuots™ kit of supplements and growth factors. The cells were maintained at 37°C in a humidified incubator and an atmosphere of 5% CO_2.

2.2.9.2. Cell viability assay

The MTT reduction assay was used to study the cytotoxicity of $CACO_3$/AgNPs hybrids, bare $CaCO_3$ and AgNPs. Briefly, the cells were seeded into 96-well plates at a density of approximately 24,000 and 7,500 cells/well, for the NHDFs and hMSCs, respectively. The final volume was 150 µl per well. The cells were incubated for 18 hours before treatment to allow their adherence to the plate. After that, the media was gently aspirated and replaced with fresh media with $CaCO_3$/AgNPs hybrids, bare $CaCO_3$ or AgNPs. The final volume was 200 µl, and the concentration of $CaCO_3$/AgNPs hybrids and bare $CaCO_3$ 29 µg/cm^2. The concentration of AgNPs was 0.87 µg/cm^2, *i.e.*, equivalent to the amount of AgNPs loaded into de hybrids. The cells were incubated at 37°C in a humidified incubator and an atmosphere of 5% CO_2 for 24 hours. After the incubation period, 14 µl of MTT in PBS (5 mg.ml^{-1}) was added to the wells to a final concentration of 0.3 mg.ml^{-1}. Subsequently, the cells were incubated at 37°C for 2 hours. After incubation, the cell culture media was gently aspirated, and the formed formazan crystals dissolved with 200 µl of dimethyl sulfoxide. The absorbance was measured at 550 and 620 nm in a multi-well plate reader (Cytation 3, BioTek, Vermont, USA). To reduce the effect of interferences from the media and crystals, the final absorbance (Abs_{final}) was calculated with the following equation:

$$Abs_{final}=Abs_{550}-Abs_{620} \qquad (13)$$

Where, Abs_{550} and Abs_{620} represent the absorbance and 550 and 620 nm, respectively.

Each experiment was carried out in triplicate or quadruplicate, and replicates of untreated cells were used as positive control.

3. Results and discussion

3.1. Coatings design

In this work, we intended to develop a simple method to produce coatings composed of $CaCO_3$/AgNPs hybrids and ultimately test their potential as an active ingredient for antimicrobial coatings. The hybrids used for the production of the coatings were synthesised *via* co-precipitation of vaterite in the presence of AgNPs with an average diameter of 14 nm (**Figure 5-3A**). The formed hybrids had an average diameter of 2.3 ± 0.8 µm and were composed of ca. 3% (m/m) of silver **(Figure 5-3B)**.

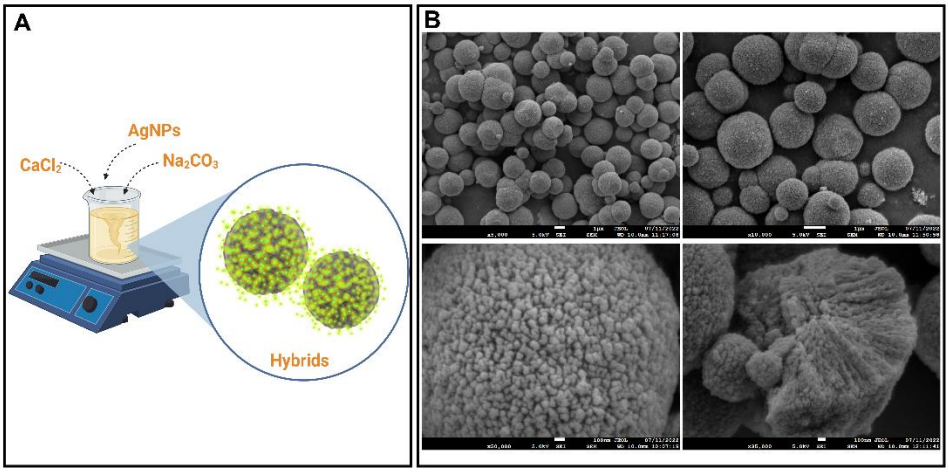

Figure 5-3. Schematic representation of the $CaCO_3$/AgNPs hybrids synthesis (A) and SEM images of the $CaCO_3$/AgNPs hybrids. Scale bar is 1 µm and 100 nm for the top and bottom images, respectively (B). Image A created with BioRender.com.

The drop casting technique was selected to coat the bottom of flat polystyrene wells in a 96-well microplate. This method was selected due to its simplicity and lower wastage of sample in comparison with other techniques like spin coating. Polystyrene microplates were chosen as the coating substrate as they offer the possibility to rapidly produce different coatings and present an easy way to run the antibacterial tests. In one single microplate is possible to assess the antibacterial activity of different coatings, and corresponding replicates, without requiring a new set up or layout.

While the drop-casting technique offers an unbeatable simplicity, it also presents some drawbacks, including the formation of uneven surfaces, with the appearance of the so-called "coffee rings" being common. These rings are formed due to differences between

the solvent evaporation rates in the periphery and centre of the "drop", which promotes the flow of more solvent and solute to the periphery and consequent concentration of non-volatile components in the edges[318]. An effect called "coffee-eye" can also occur when drying coatings at temperatures above 40°C on substrates with low conductivity, like glass and polystyrene[319]. This pattern forms due to the Marangoni flow, which is created by temperature differences between the droplet edge and the apex[319]. This effect creates a surface tension gradient which drives inward the particles and promotes their accumulation in the centre of the droplet[319]. Adding to the complexity of the coatings formation, the hybrids present unique challenges, as they can recrystallise into calcite and partially release the AgNPs when in solution[227].

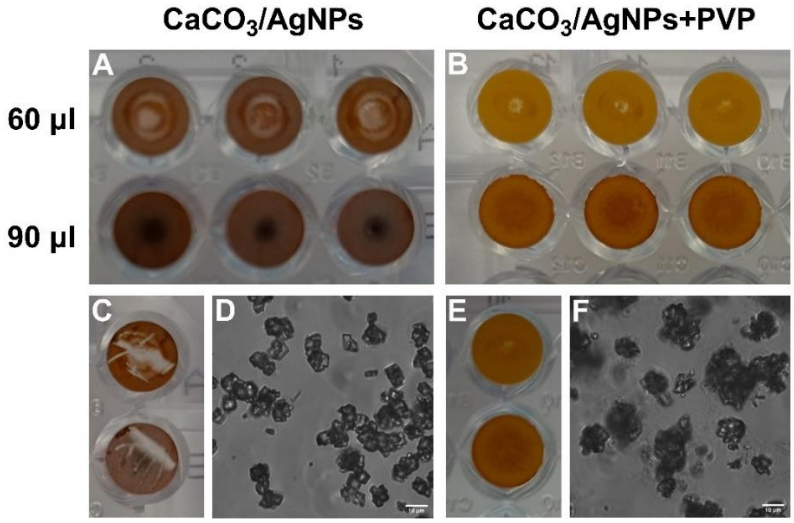

Figure 5-4. Images A and B depict the wells coated with different volumes (60 and 90 µl) of $CaCO_3$/AgNPs hybrids (Hybrids) or $CaCO_3$/AgNPs hybrids with PVP (Hybrids + PVP) by drop casting. The coatings after the scratch test are presented in images C and D and the transmittance images of the coatings after drying at 50/37°C or 80°C are presented in images D and F, respectively. Scale bar is 10 µm for Images D and F.

Figure 5-4 presents the coatings produced with two different volumes, 60 and 90 µl, of $CaCO_3$ hybrids dispersions in water, with and without PVP as an additive. The coatings produced with the lowest volume (60 µl) presented an irregular distribution of particles, which can be explained by the insufficient number of crystals added, and an outward flow of the hybrids during the drying step. When the dispersion volume added to the wells increased to 90 µl, the wells surface became fully coated. Nonetheless, the coating components concentrated in the centre of the wells, as a result of the "coffee eye" effect, which was more attenuated in the formulation with PVP, as it increased the viscosity and wettability of the dispersion, resulting in more uniform coatings due to the slower hybrids flow.

The adhesion of the coatings to polystyrene was tested by scrapping the bottom of the wells after drying. As shown in **Figure 5-4C**, the coatings without PVP presented poor adhesion to the polystyrene wells and were easily detached from the surface. On the other hand, the coatings with PVP were resistant to scraping, showing that PVP worked as a binder, improving the coatings adhesion to polystyrene. The adhesion promoted by PVP resulted from the interactions between PVP/hybrids and PVP/substrate, as well as the entanglement of PVP and possible interlocking with the hybrids due to their porous structure[320,321].

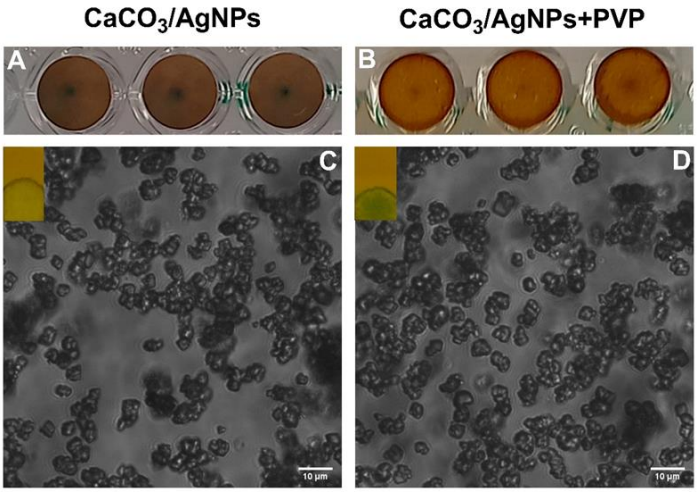

Figure 5-5. Wells coated with 90 µl of $CaCO_3$/AgNPs dispersion (A) or $CaCO_3$/AgNPs hybrids with PVP (Hybrids + PVP) by drop casting (B) and transmittance images of the coatings after drying at 80°C for 2 hours (C and D). Insets in the transmission images correspond to the universal indicator tape (pH 1-14) after dipping into the dispersions. Scale bar is 10 µm for Images C and D.

As depicted in **Figure 5-4 (images D and F)**, regardless of the formulation, the hybrids became unstable during the coatings production and transformed into calcite (rhombohedral shape). This was caused by the exposure of the hybrids to water for a long period, mostly during the drying step, which promoted the recrystallisation of metastable vaterite to stable calcite. To decrease the duration of the drying step, the dispersions were dried at 80°C instead of the 50/37°C cycle. The obtained coatings are presented in **Figure 5-5 (images A and B)**. Regardless of the formulation, all the coatings presented a "coffee ring" or "coffee eye", which was promoted by outflow or inflow forces, respectively. **Figure 5-5**, **images C and D**, show that despite the shorter exposure to water by increasing the drying temperature, the hybrids still recrystallised into calcite.

To rule out the effect of the formulation pH on the recrystallisation rate, as low pH values accelerate the transformation of vaterite into calcite, the pH of the formulation was analysed with universal indicator tape. As depicted on the insets in **Figure 5-5 (images C**

and D), the formulations presented a neutral to basic pH, indicating that the pH did not accelerate the recrystallisation.

Due to the quick recrystallization of vaterite and consequent premature release of AgNPs, the $CaCO_3$/AgNPs crystals were pre-coated with mucin in an attempt to halt the transformation into calcite (**Figure 5-6A)**. The precoated hybrids were then mixed with PVP as it improves the adhesion of the coating and its uniformity.

As shown in **Figure 5-6B,** the formulation composed of hybrids, mucin and PVP (coating B) resulted in uniform coatings as PVP in combination with mucin increased the viscosity and wettability of the formulation, and consequently decreased the outflow and inflow of the hybrids. Moreover, pre-coating the hybrids with mucin prevented the crystals recrystallisation, as shown by the transmittance image in **Figure 5-6C**, where the typical spherically shaped vaterite hybrids are visible. Overall, mucin not only formed a protective layer on the hybrids that suppressed the diffusion of ions and their recrystallisation, but also helped to form uniform coatings. For these reasons, the formulation with PVP and mucin was selected to produce the final coatings with the $CaCO_3$/AgNPs hybrids.

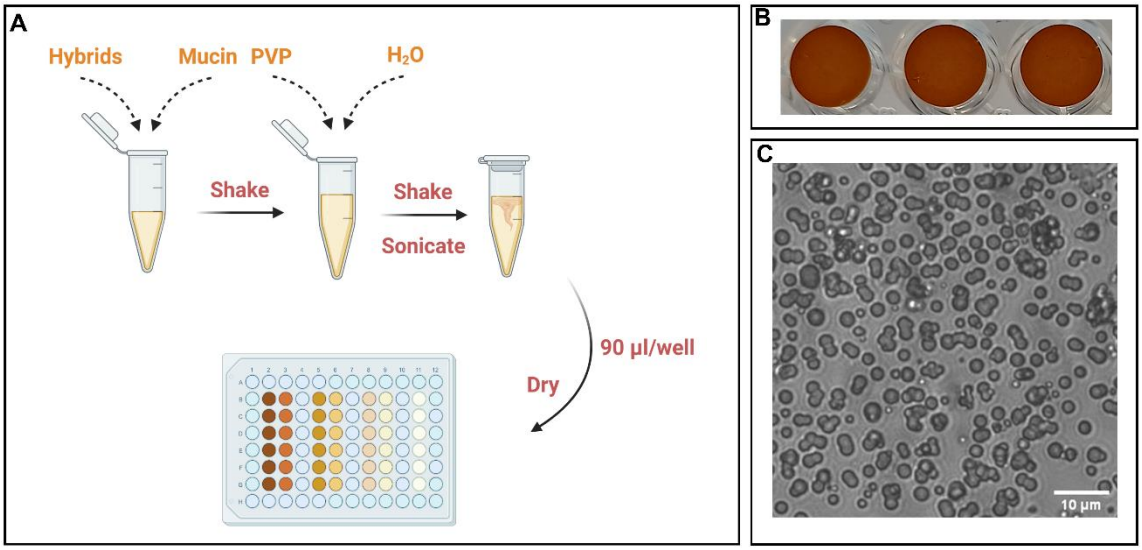

Figure 5-6. Schematic representation of the coating B production with hybrids, PVP and Mucin, (A). Image B and C depict the coatings after drying and respective transmittance images, respectively. Scale bar is 10 µm for image C. Image A created with Biorender.com.

3.2. Characterisation of the coatings

After the formulation development and optimisation, coating B was characterised by SEM, EDS, FTIR and XRD to investigate the coating at a microscopic level, study its crystallinity, composition, and silver distribution.

Figure 5-7AF depict SEM images of the surface of coating B. The coating presented an uneven distribution of PVP, with a gradient from the periphery to the centre, with the highest contents of PVP being at the edges. This was reflected on the smooth surface in the regions rich in PVP (**Figure 5-7B)** that gradually became more coarse with the proximity to the centre (**Figure 5-7C-F)**. The arrows in **Figure 5-7A** present the ring that marks the transition between the region with high (lighter grey) and low (darker grey) contents of PVP. The irregular distribution of PVP seems to have been promoted by an evaporation-driven outflow of PVP to the periphery that compactly packed the hybrids in the centre. As PVP has a higher diffusion coefficient than the hybrids, it diffused more rapidly to the edges of the well, accumulating there and consequently increasing the compactness of the hybrids in the centre. **Figure 5-7F** shows that the centre of the coated surface is composed of compacted hybrids connected to each other through polymer membranes (yellow arrow). Despite the non-uniform distribution of PVP, the thickness of the coatings, 15.2 ± 1.4 µm, was similar between replicates and along the coating cross-sections, regardless of the presence of more (**Figure 5-7G to I)** or less PVP **(Figure 5-7J to L)**. These results demonstrate the reproducibility of the produced coatings, nonetheless, with an uneven distribution of PVP.

Although not tested in this work, as the primary goal was to study the suitability of the $CaCO_3$/AgNPs hybrids to produce antibacterial coatings, a possible solution to improve the distribution of PVP would be drying the coatings at room temperature instead of at 80°C. This would decrease the evaporation rate at the edges, thereby minimising the outward flow of PVP to the periphery.

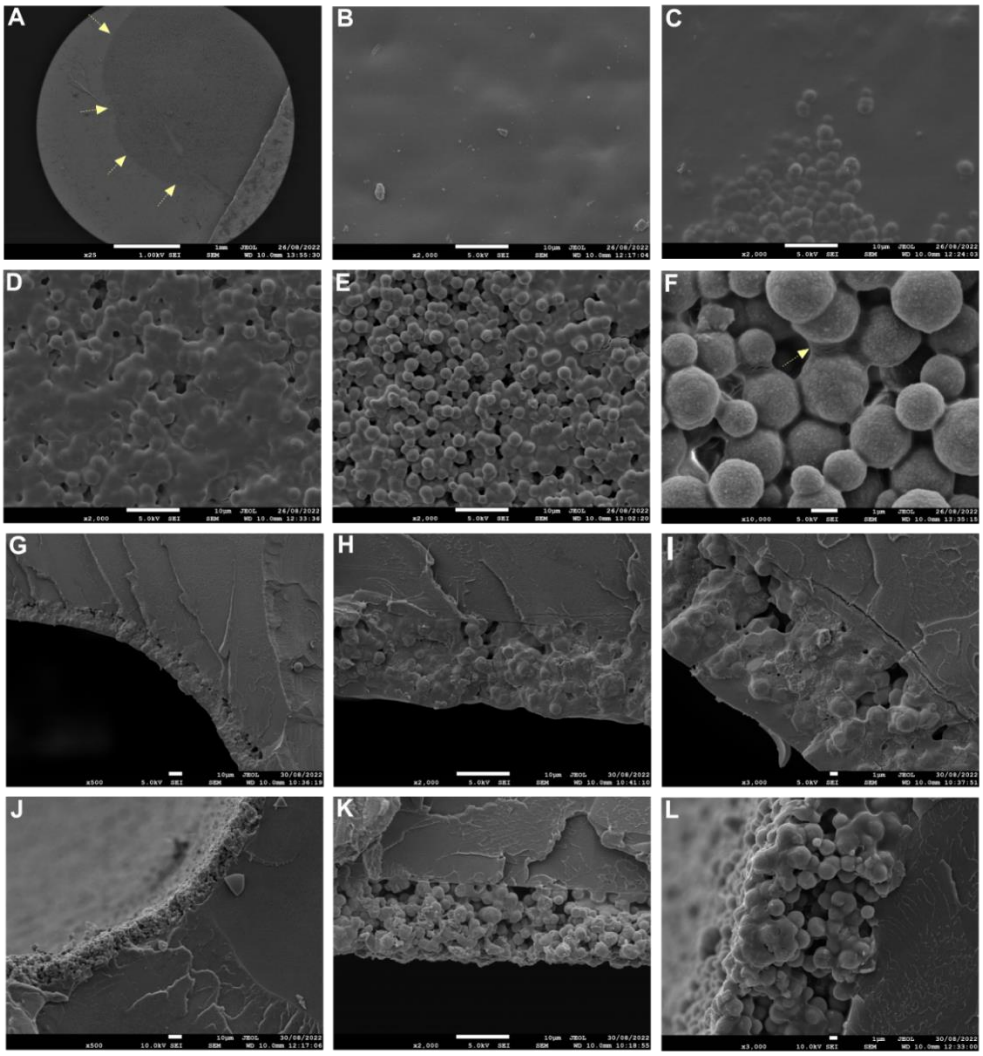

Figure 5-7. SEM images of the surface (A to F), and cross-sections of coating B (G to L). Scale bar is 1 mm for image A, 10 µm for images B, C, D, E, G, H, J and K and 1 µm for images F, I and L.

To analyse the elemental composition of the coatings and silver distribution, cross-sections of the coating were analysed by SEM-EDS. **Figure 5-8** depicts mapping images of calcium, oxygen and silver, and the spectrogram of the coating. As expected, the spectrogram demonstrates that the developed coating is mainly composed of carbon, oxygen and calcium. Nitrogen and silver peaks resultant from the polymers (mucin and PVP) and AgNPs were also present, although the peaks presented lower intensities due to the low contents of nitrogen in PVP and mucin, and silver in the hybrids (ca. 3%).

The mapping image of silver (**Figure 5-8**) shows that the AgNPs were uniformly distributed in the coating, important to assure a good antimicrobial performance.

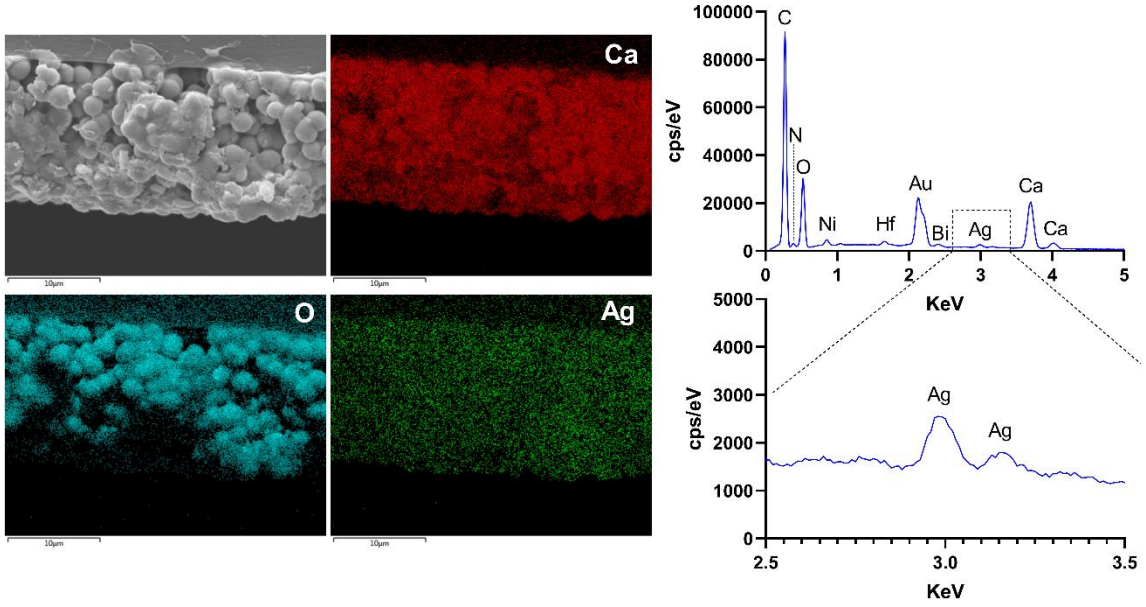

Figure 5-8. SEM-EDS mapping images and respective spectrogram of coating B.

Figure 5-9 depicts the infra-red spectra and XRD pattern of coating B and all the respective components: PVP, mucin and $CaCO_3$/AgNPs hybrids. The FTIR spectrum of the coating presents the characteristic bands of all the components. The typical bands of PVP, mucin and $CaCO_3$/AgNPs hybrids are assigned in orange, green and violet, respectively, with the bands assigned in black resulting from the overlap of bands characteristic of more than one of the components.

The band at 1652 cm^{-1} resulted from C=O stretching of the amide group present in PVP and mucin (amide I band)[190,322]. The low-intensity band at 1538 cm^{-1} resulted from N-H bending and C-N stretching vibrations of the proteins that compose mucin (amide II band)[322]. The region between 1490 cm^{-1} and 1370 cm^{-1} resulted from an overlay of bands from all the components in the coatings, corresponding to C-H vibrations, anti-symmetrical stretching, and vibration of the tertiary nitrogen and CO_3^{2-} [172,268,322,323]. The other bands in the spectra resulted from amide group vibrations, O–P=O antisymmetric stretch, C-C, C-H, C-O and C-O-H vibrations, with the last two being originated by the carbohydrates present in mucin[322]. The characteristic bands of $CaCO_3$ were present at 1088, 874, 848, 742 and 712 cm^{-1}. These bands resulted from vibrational modes of CO_3^{2-}. The bands at 1088 and 742 cm^{-1} are characteristic of the vaterite polymorph, and the band at 712 cm^{-1} corresponds to calcite[266,268]. This last band had a very low intensity, indicating the presence of low contents of calcite in the coating. These results show that vaterite was the main polymorph in coating B, which was corroborated by the SEM and transmittance images

(**Figure 5-6** and **Figure 5-7**). The XRD data in **Figure 5-9** also shows that vaterite is the main polymorph, with the diffraction pattern of the coating presenting the typical peaks of vaterite and a few low intensity peaks assigned to calcite.

Overall, the data shows that mucin prevents the recrystallisation of the hybrids into calcite, with the peaks assigned to $CaCO_3$ in the FTIR spectra and XRD diffraction pattern being similar between coating B and the hybrids. This data demonstrates that during the coating production there was not a premature release of AgNPs from the hybrids triggered by their recrystallisation into calcite. Assuring that there is not an early release of AgNPs is crucial, as it can affect the stability of the AgNPs and antibacterial activity.

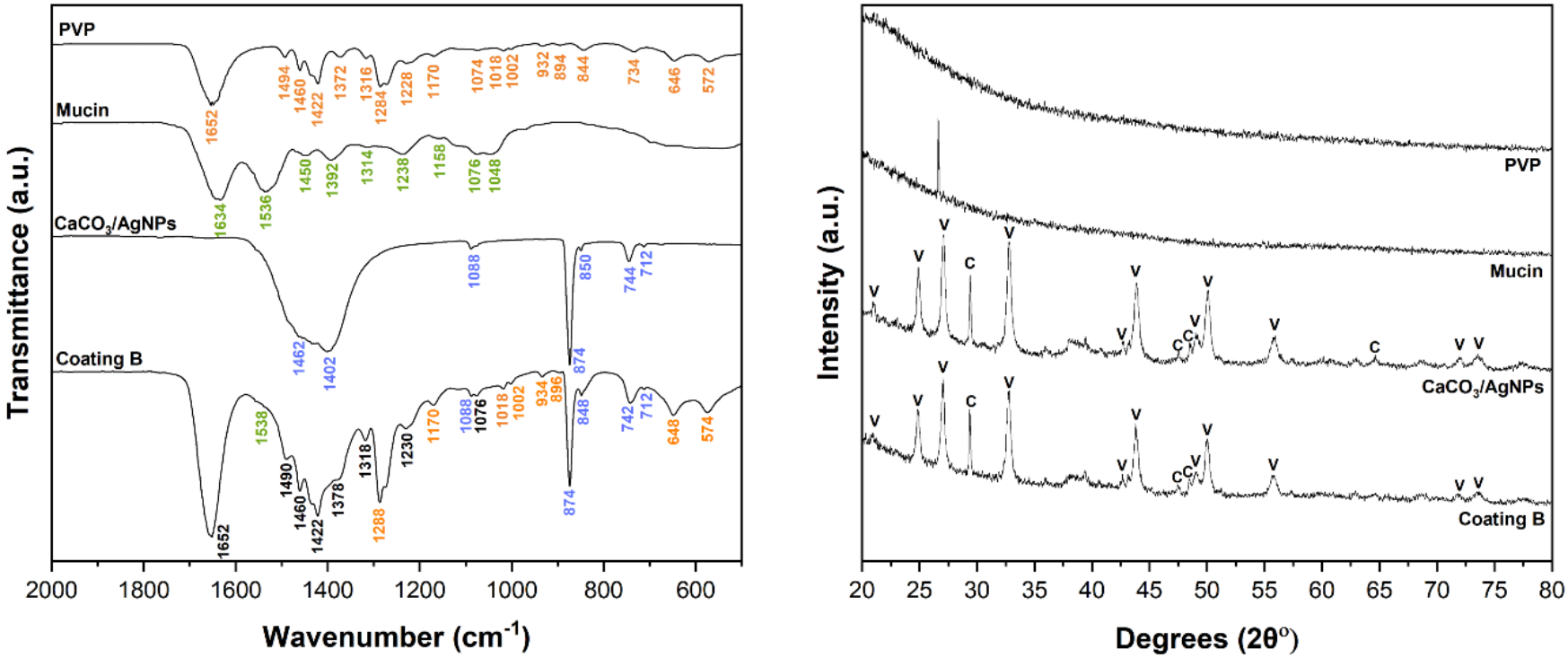

Figure 5-9. FTIR spectra (left) and XRD patterns (right) of PVP, mucin, $CaCO_3$/AgNPs hybrids and Coating B. The bands assigned in orange, green and violet result from vibrational modes of PVP, Mucin and $CaCO_3$/AgNPs hybrids. The band assigned in black in the FTIR spectra correspond to bands that result from the overlap of peaks from different compounds.

3.3. Release of AgNPs from the coatings

The unwanted leaching of AgNPs or other active agents from antimicrobial coatings without contact with bacteria is undesirable as it decreases the antimicrobial activity of the surfaces and unnecessarily releases into the environment active ingredients that can have a toxic effect on living organisms and potentiate the appearance of antimicrobial resistance. In this work, the release of AgNPs from the developed coatings was studied in TBS buffer and MHB-S. The effect of mucin and PVP on the release of AgNPs was also analysed, by testing the coatings produced only with hybrids and the coatings produced with hybrids, PVP and mucin, coating A and B, respectively.

Figure 5-10 A, B, D and E depicts the transmittance images of the coatings after being exposed to TBS and MHB-S. As expected, the coatings without PVP and mucin were composed of calcite (rhombohedral shape) as the hybrids recrystallised during the coatings production. On the other hand, the coatings with PVP and mucin did not recrystallise even after incubation in TBS and MHB-S for approximately 19 hours, demonstrating the good stabilising properties of mucin. **Figure 5-10 C and F** present the UV-vis spectra of TBS and MHB-S after incubation with the coatings. UV-vis spectrophotometry is a good method to detect the presence of AgNPs and their concentration, as it is highly sensitive to AgNPs due to their surface plasmon-resonance property[185,189].

Interestingly, none of the coatings released AgNPs in TBS. While this would be more expectable for the coatings with additives, as the hybrids did not recrystallise, the same was not expectable for the coating only composed of hybrids. This result can be explained by the fact that calcite adsorbs AgNPs, retaining the AgNPs on the coating. The capacity of calcite to adsorbed AgNPs after the hybrids recrystallisation has been demonstrated in the previous chapters, and was shown to be controlled by the affinity between the AgNPs and $CaCO_3$, as well as the medium composition[227]. When the medium is rich in biomolecules that adsorb to AgNPs and decreases the affinity to $CaCO_3$, AgNPs can be released. This effect is demonstrated in this work by the partial release of AgNPs from coating A in MHB-S, as shown by the UV-vis results (**Figure 5-10F)** and the colour of MHB-S solution after incubation with coating A(**Figure 5-10G)**, where AgNPs are visually detectable due to their characteristic amber colour. As MHB-S is rich in biomolecules, like casein and starch, it triggers the partial release of AgNPs by decreasing their affinity to $CaCO_3$. Nonetheless, coating B did not release AgNPs in MHB-S, as shown by the image of MHB-S after

incubation (**Figure 5-10H)**, and the UV-vis spectra where AgNPs were not detected (**Figure 5-10C)**. This data shows the crucial role of mucin not only in protecting the hybrids from recrystallisation but also in preventing the interactions of the AgNPs loaded into the hybrids with the medium constituents. Due to the high content of PVP in the coating it is also expectable that PVP plays a role in preventing the release of AgNPs.

Overall, the results show PVP and mucin help to decrease the unwanted release of AgNPs, and highlight the potential of coating B for applications where a pH-triggered release is desired, like the core of biofilms and inflammation sites, as the low pH in these microenvironments[1,245] can promote the dissolution of $CaCO_3$ and consequent release of AgNPs.

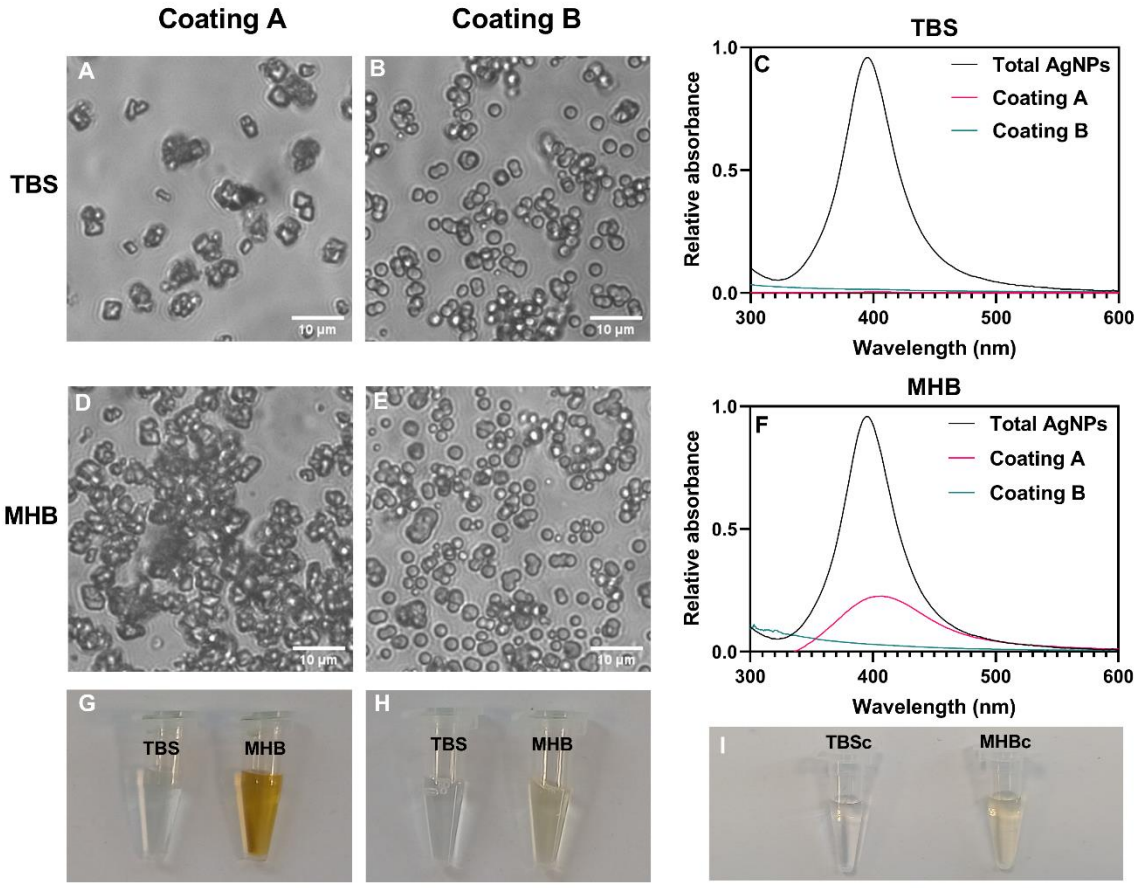

Figure 5-10. Transmittance images of the coating only composed of hybrids (coating A) and composed of hybrids, PVP and mucin (coating B) after being exposed for ca. 19 hours to TBS (A and B) and MHB-S (D and E). Images G and H present the supernatant of TBS and MHB-S after incubation with coating A and coating B, respectively. The TBS and MHB-S controls, TBSc and MHB-Sc, respectively, are presented in Image I. Graphs C and F present the UV-vis spectra of MHB-S and TBS after incubation with coating A and coating B. The control spectrum corresponds to the equivalent concentration of the total content AgNPs (total AgNPs) in the coatings.

3.4. Antibacterial activity

To test the antibacterial activity of the coatings developed in this work in a consistent and rapid way, the resazurin reduction assay was used. This method consists in determining the bacterial viability by measuring the fluorescence of resorufin, a molecule produced via the reduction of resazurin by the viable bacteria. Before testing the coatings, the applicability of this method in assessing the viability of *E. coli*, MRSA and *P. aeruginosa* was studied by incubating different concentrations of bacteria with resazurin and then measuring the fluorescence. **Figure 5-2** presents the developed fluorescence after incubation with different concentrations of bacteria, expressed as increasing optical density values (OD_{600}). The data shows that this assay is sensitive to the concentration of bacteria, with the fluorescence increasing linearly with the concentration of bacteria.

The antibacterial activity of coating A and B was tested to study the effect of PVP and mucin in the overall activity of the coatings. **Figure 5-11** presents the relative fluorescence for *E. coli*, MRSA and *P. aeruginosa* after incubation with coatings containing different concentrations of hybrids. Overall, the coatings with PVP and mucin presented better antibacterial activity than those only composed of hybrids. Coating B inhibited the growth of *E. coli* and *P. aeruginosa* at a density of 15 µg/cm^2 and MRSA at twice this density, *i.e.*, 29 µg/cm^2. On the other hand, coating A required higher concentrations of hybrids to inhibit the growth of the bacteria, inhibiting *E. coli* and MRSA growth at a density equal to 233 and 931 µg/cm^2, respectively. The lowest concentration of hybrids in coating A tested against *P. aeruginosa* effectively inhibited the bacteria, demonstrating that the minimum concentration with bacteriostatic activity against *P. aeruginosa* is below 58 µg/cm^2.

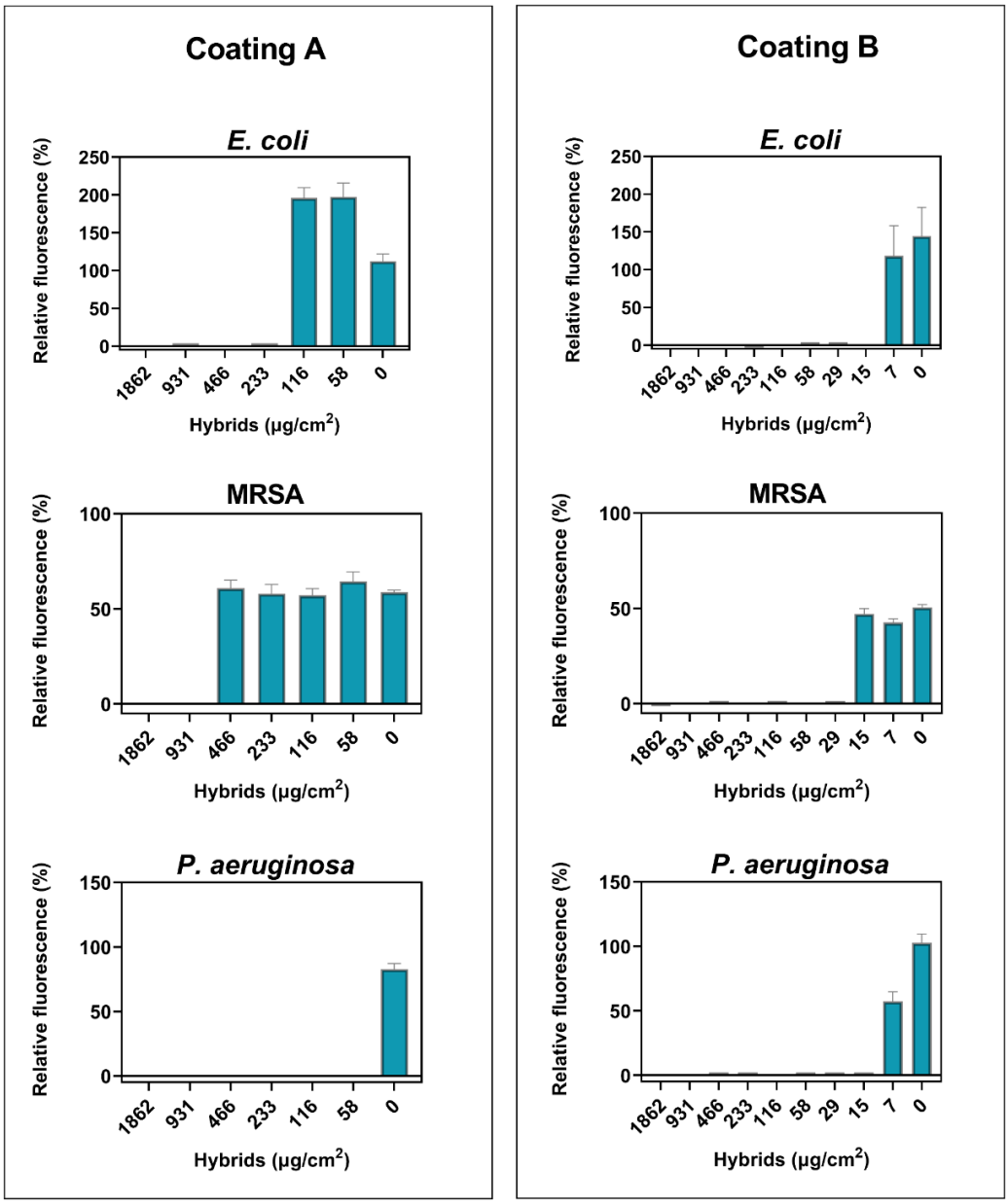

Figure 5-11. Relative fluorescence after incubation of *E. coli*, MRSA and *P. aeruginosa* on coatings A and B at different concentrations for 24 hours. Coating A corresponds to the coatings only composed of hybrids and coating B to the coatings composed of hybrids, mucin and PVP. The fluorescence is relative to the growth control. The results correspond to an average of four to five replicates.

To confirm the eradication of the bacteria by coating B, the bacteria inoculum exposed to the three lowest concentrations of hybrids was spot plated onto MHA-S plates. As shown in **Figure 5-12**, the density of hybrids with biocidal activity was 15 µg/cm^2 for *P. aeruginosa* and 29 µg/cm^2 for *E. coli* and MRSA which matched the data in **Figure 5-11**, except for *E. coli*, which presented viable bacteria for one of the replicates. Based on these results, the density of AgNPs in coating B with bactericidal activity was 0.9 and 0.4 µg/cm^2,

which corresponded to the AgNPs loaded into the coatings with 29 and 15 µg/cm^2 of hybrids, respectively.

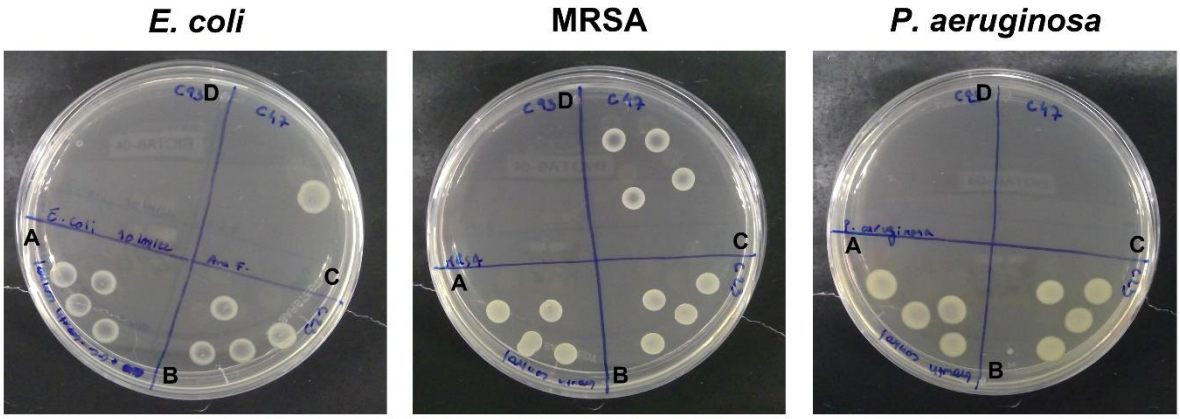

Figure 5-12. Spot plating of the bacterial inoculum after incubation with coating B. The growth controls of the bacteria incubated on uncoated wells are represented by the letter A. The coatings presented the following hybrids densities: 7, 15 and 29 µg/cm^2, which are represented by the letters B, C and D, respectively. The labels 23, 47 and 93 in the plate are respective to the concentration of the hybrids (µg.ml^{-1}) in the formulation dispersions used to produce the coatings, which resulted in hybrids densities equal to 7, 15 and 29 µg/cm^2, respectively.

The low concentrations of AgNPs needed to kill the bacteria demonstrate that the coatings have strong antibacterial activity against *E. coli*, MRSA and *P. aeruginosa*, three bacteria responsible for numerous infections in hospital settings.

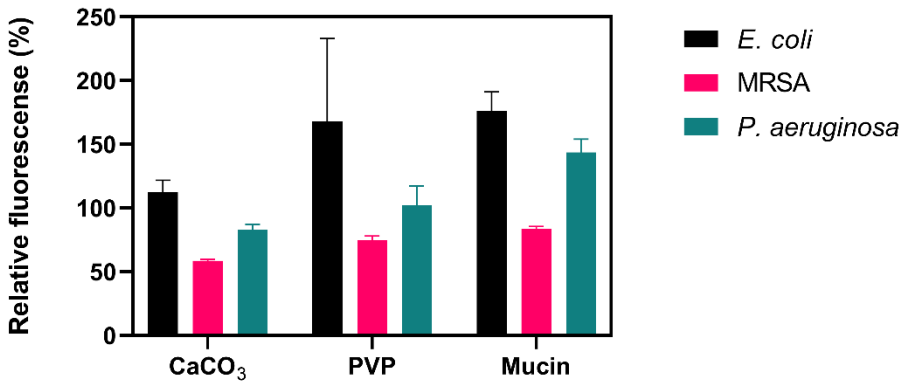

Figure 5-13. Relative fluorescence after incubating the bacteria for 24 hours with the control coatings composed of bare $CaCO_3$, PVP or Mucin. The fluorescence is relative to the growth control. The results correspond to an average of four to five replicates.

To analyse the effect of PVP, mucin and bare $CaCO_3$ against the bacteria, coatings with these components were produced, and their antibacterial activity assessed. **Figure 5-13** presents the relative fluorescence after incubation with these coatings. The data shows that PVP and mucin do not halt the growth of the bacteria, with PVP even promoting the growth of *E. coli*, possibly due to increasing the hydration of the batceria[324]. Mucin also promoted the growth of *E. coli* and *P. aeruginosa* as it can work as an additional energy source for

these bacteria[325–327]. In the case of the bacteria incubated with the coatings composed of bare $CaCO_3$, the growth of *E. coli* and *P. aeruginosa* was not considerably affected, but there was an evident reduction of the MRSA bacterium (41% less than the control). This was also evidenced in the tests carried out with coatings A and B against MRSA (**Figure 5-11**), where the coatings without bactericidal activity reduced the growth of the MRSA to around 60%.

It has been demonstrated by Xie et al.[328] that calcium ions (Ca^{2+}) can kill *Staphylococcus aureus* (*S. aureus)*, by promoting the destabilisation of the membrane via the formation of complexes with cardiolipin (CL), a major lipid component in *S. aureus* membranes. The same researchers also demonstrated that Ca^{2+} does not present activity against *E. coli* due to the low contents of CL on their membranes. The same trend has also been reported by Thanakkasaranee et al.[329]. These findings explain the results obtained in this work, with $CaCO_3$ working as a source of Ca^{2+}, which then interacts with the CL present in the membrane of MRSA disrupting the bacteria.

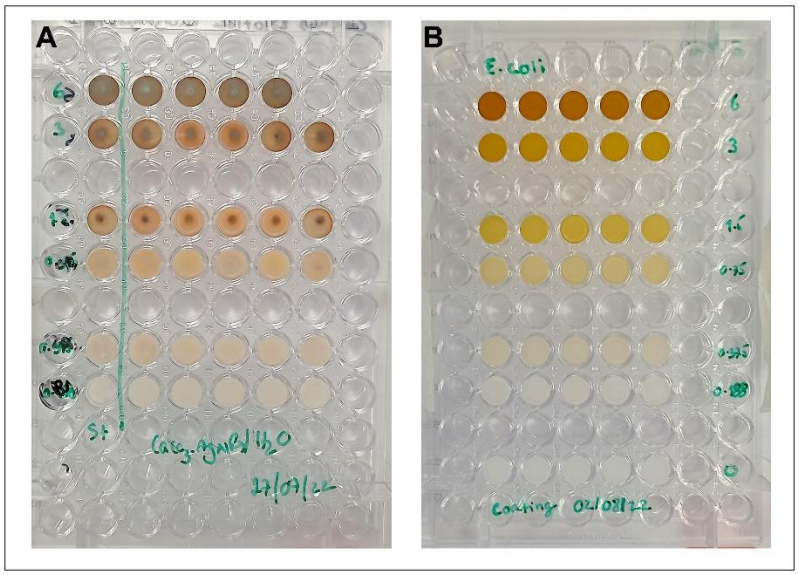

Figure 5-14. Example of microplates coated with different concentrations of $CaCO_3$/AgNPs hybrids without mucin and PVP, coating A (Image A) and coated with different concentrations of $CaCO_3$/AgNPs hybrids and the additives mucin and PVP, coating B (Image B).

The antibacterial activity test results for bare $CaCO_3$, mucin and PVP demonstrate that the difference between the antibacterial activity of coating A and B is not caused by PVP, mucin or bare $CaCO_3$, as the first two do not have antibacterial activity, and bare $CaCO_3$ is present at equal concentrations in both coatings. The better antibacterial activity of the coatings with PVP and mucin, 8 to 32 times stronger against *E. coli* and MRSA, respectively, seems to be promoted by the better uniformity of the coatings (**Figure 5-14**)

which resulted in an even distribution of AgNPs, the main component with antibacterial activity. Moreover, the coating with PVP and mucin prevented the recrystallisation of the hybrids and consequent release of AgNPs, helping to maintain their stability and preventing the formation of clusters when exposed to high temperatures (80°C) during the drying step. As shown in **Figure 5-14**, the coating without PVP and mucin presented darker colours, an indicator of AgNPs agglomeration. One of the major problems associated with AgNPs agglomeration is the reduction of the surface area, which decreases the release of silver ions (Ag^+), crucial for the antibacterial activity of AgNPs[183].

Figure 5-15 presents SEM images of coating B (29 µg/cm^2) after incubation with *E. coli*, MRSA and *P. aeruginosa* for 2 hours, and the respective controls.

The bacteria in the control samples presented a well-preserved cell membrane without any damage or cell deformation. Nonetheless, after contact with the coated surface, the bacteria presented severely damaged and perforated membranes. These results are in agreement with previous reports and demonstrate that the toxicity mechanism of the AgNPs includes the disruption of the cell membrane[330–332]. Regardless of the bacteria type, no cells with intact membranes were found on the coated surfaces, showing that the coating exerts its antibacterial activity within 2 hours of contact with bacteria.

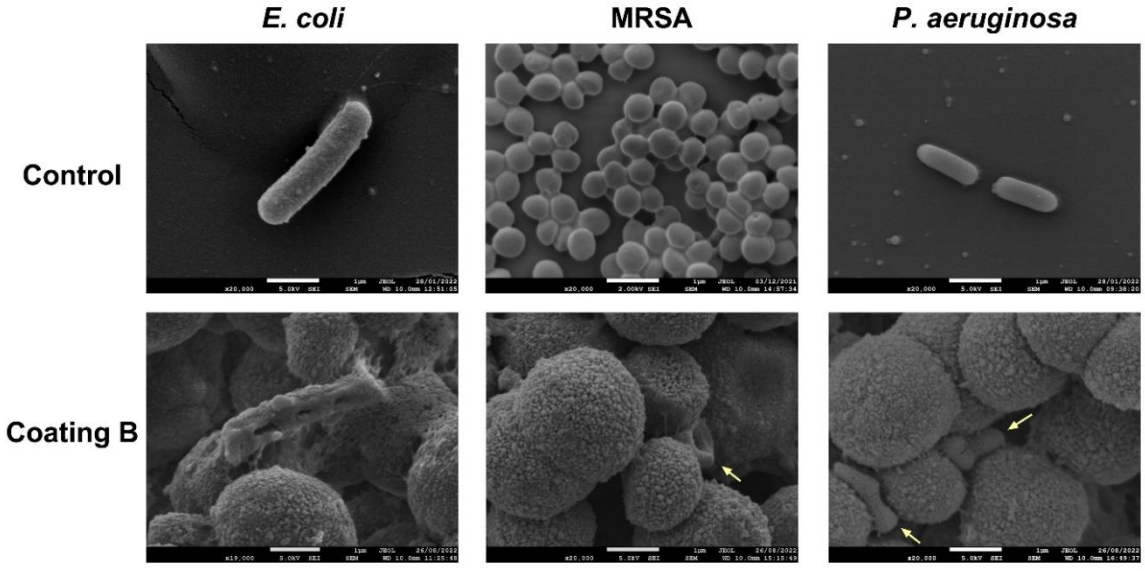

Figure 5-15. SEM images of *E. coli*, MRSA and *P. aeruginosa* controls (Control), and after being exposed to coating B for 2 hours.

3.5. *In vitro* cytotoxicity

While a strong toxicity effect against bacteria is wanted, the same is undesirable against mammalian cells. To evaluate the toxicity effect of the hybrids on human cells, NHDFs and hMSCs were exposed to the same concentration of hybrids that showed bactericidal

activity (29 µg/cm^2). The equivalent concentration of bare $CaCO_3$ and AgNPs was also tested. As shown in **Figure 5-16**, the hybrids did not significantly affect the viability of both cell lines nor the bare $CaCO_3$ crystals. On the other hand, while the equivalent concentration of AgNPs did not affect the viability of hMSCs, they reduced the survival of NHDFs. The enhanced resistance of hMSCs to lethal compounds has previously been demonstrated with studies showing that hMSCs are highly resistant to apoptosis after exposure to DNA-damaging agents, with senescence being one of the mechanisms to evade drug-induced apoptosis[333]. The capacity of hMSCs to evade toxic compounds explains their survival when exposed to AgNPs. In the case of NHDFs, the hybrids decreased the toxicity of the AgNPs. As the AgNPs are immobilised on $CaCO_3$, the interactions between AgNPs and the cells are minimised, and therefore the toxicity of AgNPs is decreased. Transmittance images of the cells after incubation with the hybrids, bare $CaCO_3$ and AgNPs are presented in **Figure 5-17**.

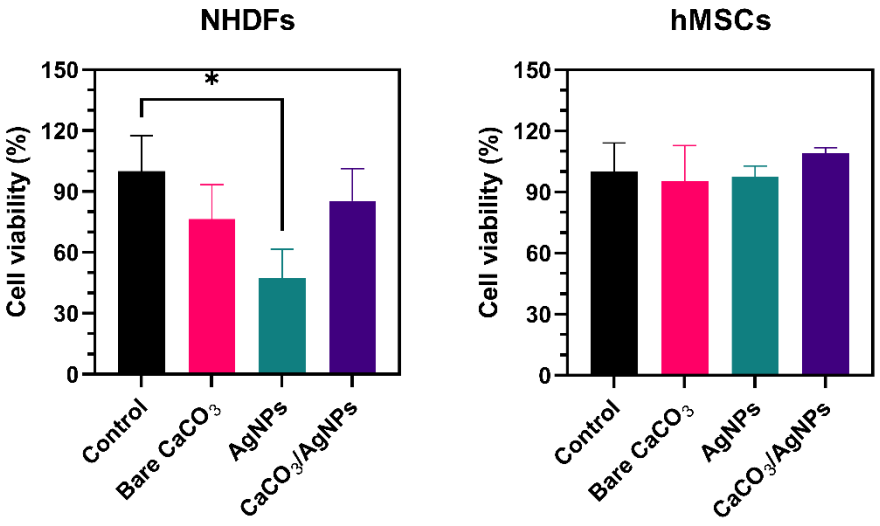

Figure 5-16. NHDFs and hMSCs cell viability after incubation for 24 h with $CaCO_3$/AgNPs hybrids with bactericidal activity and the equivalent concentration of bare $CaCO_3$ and AgNPs. The cell viability was determined via the MTT reduction assay. Statistical analysis was made using the Kruskal-Wallis test/Dunn's post-test (*$p < 0.05$ vs control). The results correspond to an average of three to four replicates.

Overall, these results show that the hybrids do not affect the viability of human cells at concentrations used to induce bactericidal effect, indicating the safety of the coatings.

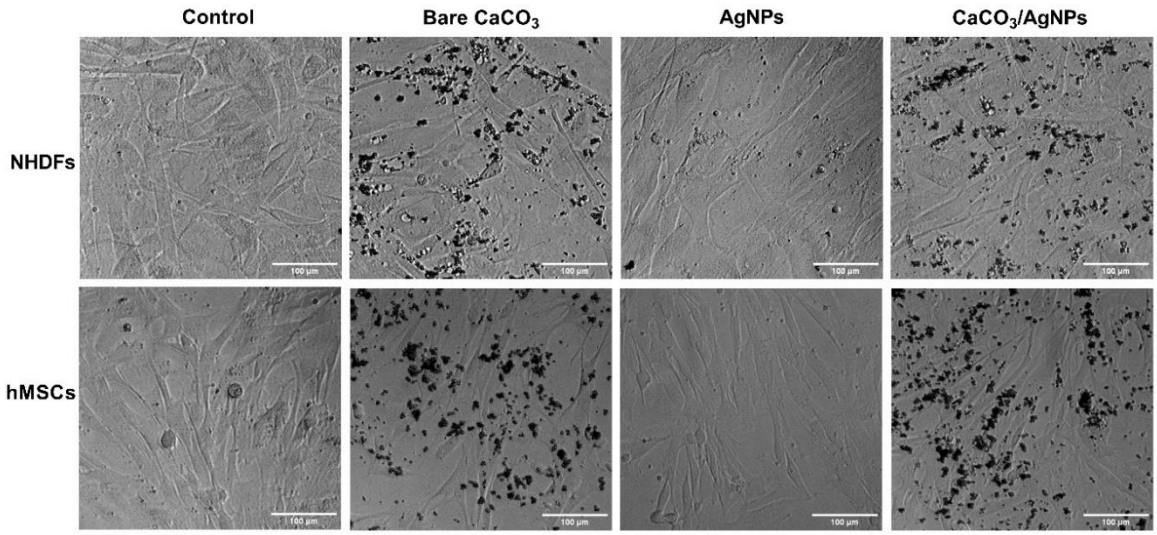

Figure 5-17. Transmittance images of the NHDFs and hMSCs cells after being exposed for 24 hours to $CaCO_3$/AgNPs hybrids (29 µg/cm^2) and the equivalent concentration of bare $CaCO_3$ (29 µg/cm^2) and AgNPs (0.87 µg/cm^2). Dark regions in the images correspond to the hybrids.

4. Conclusion

In this chapter, coatings composed of $CaCO_3$/AgNPs hybrids, with approximately 3% (m/m) of AgNPs, were developed. The production steps were optimised, and a formulation consisting of hybrids, PVP and mucin developed. The optimised formulation resulted in macroscopically uniform coatings, with mucin playing a crucial role in preventing the recrystallisation of the hybrids into calcite and the consequent release of AgNPs. Further characterisation of the coating showed that PVP accumulated more in the periphery and the hybrids in the centre. Nonetheless, all the coatings presented a uniform thickness, 15 µm, which was reproducible between replicates. The SEM-EDS analysis showed that AgNPs were homogeneously distributed in the coating, and the XRD and FTIR analysis proved that mucin prevented the recrystallisation of the hybrids, with the main polymorph in the coating being vaterite. The release of AgNPs from the coatings was tested. The results showed that the coatings with PVP and mucin did not release AgNPs, an important feature in preventing the unwanted release of the active component. The antibacterial studies of the coatings showed that PVP and mucin play an important role in enhancing the antibacterial activity of the AgNPs by improving the uniformity of the coating and halting the recrystallisation of the hybrids and consequent premature release of AgNPs that can cause their agglomeration. This coating presented a strong bactericidal activity against *E. coli*, MRSA and *P. aeruginosa*, killing the bacteria at hybrids concentrations between 15 and 29 µg/cm^2. The antibacterial tests also demonstrated that Ca^{2+} can supress the growth of MRSA bacteria. The in vitro cytotoxicity tests showed that the hybrids at bactericidal

concentrations do not affect the viability of human cells. Overall, the coating developed in this work demonstrates the enormous potential of $CaCO_3$/AgNPs hybrids for the production of surfaces with antibacterial properties, as long as their premature recrystallisation is halted. The methods proposed in this work for the rapid production of coatings and straightforward assessment of their antibacterial activity present new alternatives to accelerate the analysis of materials with antibacterial activity.

Chapter 6

Conclusion and future work

1. Concluding remarks

The work presented in this thesis explores the potential of vaterite $CaCO_3$ as carriers for the storage, protection, transport and controlled delivery of silver nanoparticles (AgNPs) and ultimately, the development of antimicrobial coatings.

The research work was divided into four main parts. The first part covers the synthesis of the cargo, *i.e.*, AgNPs; the second and third parts cover the co-precipitation of vaterite with AgNPs, the release mechanisms and antibacterial activity of the produced hybrids, and the last part covers the design of an antimicrobial coating with the hybrids.

In the first part, the results showed that the capping agents play a key role in maintaining the physicochemical properties and antibacterial activity of the AgNPs. The results showed that the capping agents have a substantial impact on the antibacterial activity of the AgNPs. The AgNPs coated with Dex and Dex^{CM} were the most effective against the bacteria, due to their better stability which resulted in the release of more silver ions, better interactions with the bacteria and diffusion into the biofilms. It is hypothesized that the antibacterial activity of capped AgNPs is governed by a balance between the AgNPs stability and their ability to release silver ions. Strong adsorption of capping agents like PVP on the AgNPs endows higher colloidal stability in culture media; however, it can decrease the rate of Ag^+ release from the AgNPs and reduce the antibacterial performance.

In the second part, crystals of vaterite were loaded with AgNPs, and once again the AgNPs surface chemistry affected the stability of the nanoparticles. Only the AgNPs coated with PVP and Dex^{DEAE} could be loaded into vaterite without forming irreversible clusters. The capping agent dictated the affinity between $CaCO_3$ and the nanoparticles and the uptake efficiency and release. Due to the higher affinity between the AgNPs coated with Dex^{DEAE} and $CaCO_3$, the resultant hybrids presented higher contents of AgNPs and a lower release

of silver. Nonetheless, the results showed that regardless of the affinities differences between the AgNPs and $CaCO_3$, the adsorption profiles were well-described by the Langmuir adsorption model.

In the third part, the developed hybrids composed of $CaCO_3$ and AgNPs were stabilized with poly(sodium 4-styrenesulfonate) (PSS) and carboxymethyl-dextran (Dex^{CM}) in an attempt to stop the recrystallization and premature release of AgNPs. The results demonstrated that PSS is a good stabilizing agent for the hybrids, preventing the recrystallization into calcite. The release studies showed that the dissolution of $CaCO_3$ is the primary release mechanism at acid pH, while at neutral and basic pH, the recrystallisation is responsible for the release of AgNPs. Nonetheless, the interaction of AgNPs with the newly formed calcite crystals determines the amount of AgNPs that remains free. The hybrids stabilised with PSS presented a targeted release in acid environments, with a burst release at pH 5 and no AgNPs being released at pH 7.4 and 9.0. New insights were also introduced about the effect of biomolecules on the release of AgNPs from the hybrids. The antibacterial studies demonstrated that the hybrids developed protect the AgNPs from agglomerating without impairing their antibacterial properties.

In the last part of the thesis, $CaCO_3$/AgNPs hybrids were used to produce antibacterial coatings. The production steps were optimised, and a formulation consisting of hybrids, PVP and mucin was developed. The results showed that PVP and mucin prevent the unwanted release of AgNPs. The coating presented a strong antibacterial activity against *E. coli*, MRSA and *P. aeruginosa*, with the *in vitro* cytotoxicity tests showing that the hybrids at bactericidal concentrations do not affect the viability of human cells. Overall, the results demonstrated the enormous potential of $CaCO_3$/AgNPs hybrids for the production of surfaces with antibacterial properties.

2. Original contribution

The research work presented in this thesis comprises an original contribution to knowledge, helping to understand the particularities of vaterite as carriers for the delivery of antimicrobials, and how these can be potentiated or tuned for better storage and controlled release. The original contributions are summarised below:

Chapter 1: This chapter is not an original contribution to knowledge *per se*, as it consists of a literature review that resulted in a publication in 2020[1]. Nonetheless, it was the first review to compile the findings on $CaCO_3$ crystals as carriers for antimicrobials. It also presents a review of vaterite synthesis routes, how to modulate its features and the existing

loading approaches. Overall, this chapter is a concise source of knowledge for researchers starting their work on the delivery of antimicrobials using $CaCO_3$ crystals as vectors.

Chapter 2: This chapter presents the synthesis of AgNPs with different capping agents and studies how they affect their stability and antibacterial activity. This is the first report where the activity and stability of AgNPs coated with trisodium citrate (Citrate), PVP, dextran (Dex), Dex^{CM} and Dex^{DEAE} is compared. It presents important insights into the stabilization of AgNPs, how the type of bacterial growth media can originate discrepant results, and the importance of running stability screenings. This chapter also presents a detailed method to quantify silver in the presence of chloride salts, and a more efficient way to wash nanoparticles, rarely reported elsewhere. Overall, this chapter presents an array of considerations and tips that can help to accelerate the production of AgNPs and assure their stability.

Chapter 3: This chapter presents the first study about the adsorption mechanism of AgNPs into vaterite synthesized *via* co-precipitation, and how the affinity of the AgNPs to $CaCO_3$ (either vaterite or calcite) affects the loaded and released contents. Overall, the findings presented in this chapter highlight the importance of the capping agents on AgNPs loading into vaterite and clarifies the adsorption mechanism of AgNPs.

Chapter 4: This chapter presents a detailed study of the release mechanisms of AgNPs from vaterite and how they can be tuned. Although the release mechanisms of vaterite have been studied before, the findings presented in this chapter expand the knowledge about the triggers that promote the cargo release, and how the release mechanisms can be tuned. The role of calcite on AgNPs release is acknowledged for the first time, as well as the affinity effect between the medium components and the cargo. It is also demonstrated that vaterite does not decrease the antibacterial activity of AgNPs. In sum, the results presented in this chapter clarify essential points in the release mechanisms of vaterite, helping to better understand vaterite features and how they can be tuned to design carriers with a controlled and targeted release.

Chapter 5: This chapter demonstrates the potential of $CaCO_3$/AgNPs hybrids to produce antibacterial coating. One of the most important contributions was the development of a novel formulation composed of hybrids, PVP and mucin that potentiate the antibacterial activity of the hybrids and prevent the premature release of AgNPs. A simple and rapid coating method was proposed, as well as a straightforward approach to assess the

antibacterial activity of the hybrids. Both methods present new alternatives to accelerate the analysis of materials with antibacterial activity.

3. Directions for future work

$CaCO_3$ crystals present a set of characteristics desirable for drug carriers, including pH sensitivity, low toxicity and simple synthesis. Several works have studied the application of $CaCO_3$ crystals loaded with antimicrobial agents for different applications. Some of these research studies propose the use of $CaCO_3$ vectors for antimicrobial coatings, fillers for polymeric composite materials[138,144,146], water filtration[145], treatment of respiratory infections[130,131], antimicrobial filler for paints[127], oral infections treatment[141], biocides delivery into olive trees[139], treatment of skin burns[137] or osteomyelitis and bone grafting[19,57,129,132,334]. The diverse applications reported up to now demonstrate the versatility of $CaCO_3$ crystals.

While $CaCO_3$ crystals can work as vectors that protect the cargo from external conditions, they can also be designed to release the cargo in a controlled way and at specific conditions. One of the most exciting characteristics of the $CaCO_3$ crystals is their sensitivity to different pH values, allowing the cargo to be released in specific sites or conditions. This is a fascinating topic, and more work on **fine-tuning the pH sensitivity** of $CaCO_3$ would be desirable, including the assessment of new polymers with the potential to control the recrystallization of vaterite and increase the cargo adsorption.

$CaCO_3$ presents three anhydrous polymorphs (calcite, vaterite and aragonite), which have been applied as carriers for the delivery of antimicrobial agents with promising results[1]. Interestingly, despite vaterite being one of the most attractive polymorphs for drug delivery, a high number of works reporting the use of $CaCO_3$ crystals as antimicrobial carriers do not show a preference for this polymorph. While in some works the use of a polymorph is deliberated, in other reports it is unclear why a certain polymorph or a mixture of polymorphs is chosen. Research work where the three **polymorphs** are **compared as carriers** for the same drug at similar experimental conditions is highly desirable.

Another topic not systematically studied is the **effect of $CaCO_3$ crystal size on the antimicrobial activity**. The size of the carriers is an important characteristic as it affects the interactions with the microorganisms. There are various works where $CaCO_3$ crystals with micro- and nano-sizes are used for antimicrobials delivery[1], but there are no reports where the effect of the crystals size is assessed. Studies on this topic would help to optimise the therapeutic effect of $CaCO_3$ crystals as antimicrobial carriers.

More efforts on the **evaluation of the cytotoxicity**, **pharmacokinetics and** possible **side effects** of $CaCO_3$-based delivery vectors are also necessary. In this work, the coatings composed of hybrids demonstrated good antibacterial activity and low cytotoxicity. Future work should focus on **studying the biocompatibility** of the coatings *in vivo* as they present the potential to be used in medical devices including implants.

Finally, some critically ill patients require the use of different antimicrobial agents concomitantly[335,336]. It would be of interest to produce **multicomponent hybrids** to increase the chances of treatment success.

Future efforts should also evaluate the potential of the developed coating in eradicating bacteria through **photothermal therapy** due to AgNPs high thermal conductivity.

Despite the challenges still ahead, the positive results reported so far sign the potential of $CaCO_3$ crystals as extremely attractive and efficient antimicrobial carriers. The research towards $CaCO_3$-based carriers with multiple antimicrobials, and externally triggered or/and programmed release, will fill the gap in the development of antimicrobial delivery systems, and allow to overcome the serious problem of antimicrobial resistance.

References

1. A. M. Ferreira, A. S. Vikulina and D. Volodkin, *Journal of Controlled Release*, 2020, **328**, 470–489.
2. OECD Health Division, *Health at a Glance: Europe 2018: State of Health in the EU cycle*, Paris, 2018.
3. M. Esme, A. Topeli, B. B. Yavuz and M. Akova, *Frontiers Medicine*, 2019, **6**, 118.
4. K. A. Kline and D. M. E. Bowdish, *Current Opinion in Microbiology*, 2016, **29**, 63–67.
5. D. Volodkin, *Advances in Colloidal Interface Science*, 2014, **207**, 306–324.
6. A. S. Vikulina, N. A. Feoktistova, N. G. Balabushevich, A. G. Skirtach and D. Volodkin, *Physical Chemistry Chemical Physics*, 2018, **20**, 8822–8831.
7. S. Temizel-Sekeryan and A. L. Hicks, *Resources Conservation Recycling*, 2020, **156**, 1–11.
8. S. Agnihotri, S. Mukherji and S. Mukherji, *RSC Advances*, 2014, **4**, 3974–3983.
9. E. Izak-Nau, A. Huk, B. Reidy, H. Uggerud, M. Vadset, S. Eiden, M. Voetz, M. Himly, A. Duschl, M. Dusinska and I. Lynch, *RSC Advances*, 2015, **5**, 84172–84185.
10. S. S. Khan, A. Mukherjee and N. Chandrasekaran, *Water Research*, 2011, **45**, 5184–5190.
11. R. Vazquez-Muñoz, N. Bogdanchikova and A. Huerta-Saquero, *ACS Omega*, 2020, **5**, 28441–28451.
12. World Health Organization, *Global Action Plan on Antimicrobial Resistance*, Geneva, Switzerland, 2015.
13. CDC, *Antibiotic resistance threats in the United States 2019*, Atlanta, GA: U.S, 2019.
14. Public Health England, Health matters: antimicrobial resistance, https://www.gov.uk/government/publications/health-matters-antimicrobial-resistance/health-matters-antimicrobial-resistance, (accessed 27 March 2020).
15. L. Rizzello and P. P. Pompa, *Chemical Society Reviews*, 2014, **43**, 1501–1518.
16. D. H. Deck and L. G. Winston, in *Basic and Clinical Pharmacology*, eds. B. Katzung and A. Trevor, McGraw-Hill Education, San Francisco, 13th edn., 2015, pp. 1126–1214.
17. G. H. Talbot, A. Jezek, B. E. Murray, R. N. Jones, R. H. Ebright, G. J. Nau, K. A. Rodvold, J. G. Newland and H. W. Boucher, *Clinical Infectious Diseases*, 2019, **69**, 1–11.
18. R. Y. Pelgrift and A. J. Friedman, *Advanced Drug Delivery Reviews*, 2013, **65**, 1803–1815.
19. S. Maleki Dizaj, F. Lotfipour, M. Barzegar-Jalali, M. H. Zarrintan and K. Adibkia, *Artificial Cells Nanomedicine, and Biotechnology*, 2017, **45**, 535–543.

20. N. Kavanagh, E. J. Ryan, A. Widaa, G. Sexton, J. Fennell, S. O'Rourke, K. C. Cahill, C. J. Kearney, F. J. O'Brien and S. W. Kerrigana, *Clinical Microbiology Reviews*, 2018, **31**, e00084-17.

21. S. Kumar, S. Bandyopadhyay, P. Das, I. Samanta, P. Mukherjee, S. Roy and B. Kundu, *Biotechnology Advances*, 2016, **34**, 1305–1317.

22. S. Maleki Dizaj, F. Lotfipour, M. Barzegar-Jalali, M. H. Zarrintan and K. Adibkia, *Journal of Drug Delivery Science and Technology*, 2016, **35**, 16–23.

23. R. Nordström and M. Malmsten, *Advances in Colloid and Interface Science*, 2017, **242**, 17–34.

24. V. M. Gupta, A.; Mumtaz, S.; Li, C.-H.; Hussain, I.; Rotello, *Chemical Society Reviews*, 2019, **48**, 415−427.

25. B. Singh, J. Na, M. Konarova, T. Wakihara, Y. Yamauchi, C. Salomon and M. B. Gawande, *Bulletin of the Chemical Society of Japan*, 2020, **93**, 1459–1496.

26. A. Gonzalez Gomez and Z. Hosseinidoust, *ACS Infectious Diseases*, 2020, **6**, 896–908.

27. A. Simonazzi, A. G. Cid, M. Villegas, A. I. Romero, S. D. Palma and J. M. Bermúdez, in *Drug Targeting and Stimuli Sensitive Drug Delivery Systems*, eds. Grumezescu, A. M., William Andrew Publishing, New York, 1st edn., 2018, pp. 81–108.

28. I. Negut, V. Grumezescu, G. Dorcioman and G. Socol, in *Nano- and Microscale Drug Delivery Systems: Design and Fabrication*, eds. Grumezescu, A. M., Elsevier, Amsterdam, 1st edn., 2017, pp. 1–10.

29. A. C. Anselmo and S. Mitragotri, *Journal of Controlled Release*, 2014, **190**, 15–28.

30. J. Siepmann and F. Siepmann, *Progress in Colloid and Polymer Science*, 2006, **133**, 15–21.

31. A. M. Pisoschi, A. Pop, C. Cimpeanu, V. Turcuş, G. Predoi and F. Iordache, *European Journal of Medicinal Chemistry*, 2018, **157**, 1326–1345.

32. D. B. Trushina, T. V. Bukreeva, M. V. Kovalchuk and M. N. Antipina, *Materials Science and Engineering C*, 2014, **45**, 644–658.

33. Y. Boyjoo, V. K. Pareek and J. Liu, *Journal of Materials Chemistry A*, 2014, **2**, 14270–14288.

34. M. Brito, E. Case, W. M. Kriven and A. Zhu, Tas, *Engineering and Science Proceedings*, 2008, **28**, 135–150.

35. J. Vuola, H. Göransson, T. Böhling and S. Asko-Seljavaara, *Biomaterials*, 1996, **17**, 1761–1766.

36. N. Feoktistova, J. Rose, V. Z. Prokopović, A. S. Vikulina, A. Skirtach and D. Volodkin, *Langmuir*, 2016, **32**, 4229–4238.

37. G. Begum, T. N. Reddy, K. P. Kumar, K. Dhevendar, S. Singh, M. Amarnath, S. Misra, V. K. Rangari and R. K. Rana, *ACS Applied Materials & Interfaces*, 2016, 8, 22056–22063.

38. S. V. German, M. V. Novoselova, D. N. Bratashov, P. A. Demina, V. S. Atkin, D. V. Voronin, B. N. Khlebtsov, B. V. Parakhonskiy, G. B. Sukhorukov and D. A. Gorin, *Scientific Reports*, 2018, **8**, 17763.

39. B. Aguilar, P. Dusemund, P. Galtier, J. Gilbert, D. Gott, S. Grilli, R. Gurtler, J. Konig, C. Lambre, J.-C. Larsen, J.-C. Leblanc, A. Mortensen, D. Parent-Massin, I. Pratt, I. Rietjens, I. Stankovic, P. Tobback, T. Verguieva and R. Woutersen, *EFSA Journal*, 2011, **9**, 1–73.

40. M. Maleki Dizaj, M. Barzegar-Jalali, Zarrintan, K. Adibkia and F. Lotfipour, *Expert Opinion on Drug Delivery*, 2015, **12**, 1649–1660.

41. N. G. Balabushevich, A. v. Lopez De Guerenu, N. A. Feoktistova and D. Volodkin, *Physical Chemistry Chemical Physics*, 2015, **17**, 2523–2530.

42. A. S. Vikulina, N. A. Feoktistova, N. G. Balabushevich, A. G. Skirtach and D. Volodkin, *Physical Chemistry Chemical Physics*, 2018, **20**, 8822–8831.

43. P. V. Binevski, N. G. Balabushevich, V. I. Uvarova, A. S. Vikulina and D. Volodkin, *Colloids and Surfaces B: Biointerfaces*, 2019, **181**, 437–449.

44. T. Yang, Z. Wan, Z. Liu, H. Li, H. Wang, N. Lu, Z. Chen, X. Mei and X. Ren, *Materials Science & Engineering C*, 2016, **63**, 384–392.

45. S. A. Kamba, M. Ismail, S. H. Hussein-al-ali, T. Azmi, T. Ibrahim, Z. Abu and B. Zakaria, *Molecules*, 2013, **18**, 10580–10598.

46. X. Ma, L. Li, L. Yang, C. Su, Y. Guo and K. Jiang, *Materials Letters*, 2011, **65**, 3176–3179.

47. V. E. Bosio, M. L. Cacicedo, B. Calvignac, I. León, T. Beuvier, F. Boury and G. R. Castro, *Colloids and Surfaces B: Biointerfaces*, 2014, **123**, 158–169.

48. Y. Ueno, H. Futagawa, Y. Takagi, A. Ueno and Y. Mizushima, *Journal of Controlled Release*, 2005, **103**, 93–98.

49. S. Haruta, T. Hanafusa, H. Fukase, H. Miyajima and T. Oki, *Diabetes Thechnology & Therapeutics*, 2003, **5**, 1–9.

50. D. Green, D. Walsh, X. Yang and R. O. C. Oreffo, *Journal of Materials Chemistry*, 2004, **14**, 2206–2212.

51. X. He, T. Liu, Y. Chen, D. Cheng, X. Li, Y. Xiao and Y. Feng, *Cancer Gene Therapy*, 2008, **15**, 193–202.

52. S. Chen, F. Li, R. Zhuo and S. Cheng, *Molecular BioSystems*, 2011, **7**, 2841–2847.

53. R. Beck and J. P. Andreassen, *Journal of Crystal Growth*, 2010, **312**, 2226–2238.

54. Y. G. Bushuev, A. R. Finney and P. M. Rodger, *Crystal Growth & Design*, 2015, **15**, 5269–5279.

55. A. M. Chaka, *ACS Earth and Space Chemistry*, 2018, 2, 210–224.

56. K. K. Sand, J. D. Rodriguez-Blanco, E. Makovicky, L. G. Benning and S. L. S. Stipp, *Crystal Growth & Design*, 2012, 12, 842–853.

57. A. Lucas, J. Gaudé, C. Carel, J. F. Michel and G. Cathelineau, *International Journal of Inorganic Materials*, 2001, **3**, 87–94.

58. D. V. Volodkin, N. I. Larionova and G. B. Sukhorukov, *Biomacromolecules*, 2004, **5**, 1962–1972.

59. D. Konopacka-Łyskawa, *Crystals*, 2019, **9**, 223.

60. A. Sergeeva, R. Sergeev, E. Lengert, A. Zakharevich, B. Parakhonskiy, D. Gorin, S. Sergeev and D. Volodkin, *ACS Applied Materials & Interfaces*, 2015, **7**, 21315–21325.

61. G. Wu, Y. Wang, S. Zhu and J. Wang, *Powder Technology*, 2007, **172**, 82–88.

62. C. Wang, Y. Sheng, X. Zhao, Y. Pan, Hari-Bala and Z. Wang, *Materials Letters*, 2006, **60**, 854–857.

63. Y. Wen, L. Xiang and Y. Jin, *Materials Letters*, 2003, **57**, 2565–2571.

64. S. Houngaloune, K. S. Ariffin, H. Bin Hussin, K. Watanabe and V. Nhinxay, *Malaysian Journal of Microscopy*, 2010, **6**, 53–57.

65. L. Xiang, Y. Wen, Q. Wang and Y. Jin, *Materials Letters*, 2006, **60**, 1719–1723.

66. W. Chuajiw, K. Takatori, T. Igarashi, H. Hara and Y. Fukushima, *Journal of Crystal Growth*, 2014, **386**, 119–127.

67. L. B. Gower and D. J. Odom, *Journal of Crystal Growth*, 2000, **210**, 719–734.

68. M. Faatz, F. Gröhn and G. Wegner, *Materials Science and Engineering C*, 2005, **25**, 153–159.

69. C. K. Ahn, H. W. Lee, M. W. Lee, Y. S. Chang, K. Han, C. H. Rhee, J. Y. Kim, H. D. Chun and J. M. Park, *Energy Procedia*, 2011, **4**, 541–547.

70. H. S. Liu, K. A. Chen and C. Y. Tai, *Chemical Engineering Journal*, 2012, **197**, 101–109.

71. D. B. Trushina, T. V. Bukreeva and M. N. Antipina, *Crystal Growth & Design*, 2016, **16**, 1311–1319.

72. Ç. M. Oral and B. Ercan, *Powder Technology*, 2018, **339**, 781–788.

73. C. Y. Tai and F. Chen, *AIChE Journal*, 1998, **44**, 1790–1798.

74. Y. Sheng Han, G. Hadiko, M. Fuji and M. Takahashi, *Journal of Crystal Growth*, 2006, **289**, 269–274.

75. M. Ma, Y. Wang, X. Cao, W. Lu and Y. Guo, *Crystal Growth & Design*, 2019, **19**, 6972–6988.

76. T. Ogino, T. Suzuki and K. Sawada, *Geochimica et Cosmochimica Acta*, 1987, **51**, 2757–2767.

77. J. Chen and L. Xiang, *Powder Technology*, 2009, **189**, 64–69.

78. R. Ševčík, M. Pérez-Estébanez, A. Viani, P. Šašek and P. Mácová, *Powder Technology*, 2015, **284**, 265–271.

79. M. Ma, Y. Wang, X. Cao, W. Lu and Y. Guo, *Crystal Growth & Design*, 2019, **19**, 6972–6988.

80. N. Spanos and P. G. Koutsoukos, *Journal of Physical Chemistry B*, 1998, **102**, 6679–6684.

81. M. Kitamura, *CrystEngComm*, 2009, **11**, 949–964.

82. C. Y. Tai and P. Chen, *AIChE Journal*, 1995, **41**, 68–77.

83. B. Njegić-Džakula, G. Falini, L. Brečević, Ž. Skoko and D. Kralj, *Journal of Colloid and Interface Science*, 2010, **343**, 553–563.

84. H. Bahrom, A. A. Goncharenko, L. I. Fatkhutdinova, O. O. Peltek, A. R. Muslimov, O. Yu. Koval, I. E. Eliseev, A. Manchev, D. Gorin, I. I. Shishkin, R. E. Noskov, A. S. Timin, P. Ginzburg and M. v. Zyuzin, *ACS Sustainable Chemistry & Engineering*, 2019, **7**, 19142–19156.

85. D. V. Volodkin, S. Schmidt, P. Fernandes, N. I. Larionova, G. B. Sukhorukov, C. Duschl, H. Möhwald and R. Von Klitzing, *Advanced Functional Materials*, 2012, **22**, 1914–1922.

86. S. Maleki Dizaj, F. Lotfipour, M. Barzegar-Jalali, M. H. Zarrintan and K. Adibkia, *Artificial Cells, Nanomedicine, and Biotechnology*, 2016, **44**, 1475–1481.

87. Y. Mori, T. Enomae and A. Isogai, *Materials Science and Engineering C*, 2009, **29**, 1409–1414.

88. Y. Wang, Y. X. Moo, C. Chen, P. Gunawan and R. Xu, *Journal of Colloid and Interface Science*, 2010, **352**, 393–400.

89. M. L. P. Vidallon, F. Yu and B. M. Teo, *Crystal Growth & Design*, 2020, **20**, 645–652.

90. B. V. Parakhonskiy, A. Haase and R. Antolini, *Angewandte Chemie - International Edition*, 2012, **51**, 1195–1197.

91. F. Manoli and E. Dalas, *Journal of Crystal Growth*, 2000, **218**, 359–364.

92. X.-H. Guo, S.-H. Yu and G.-B. Cai, *Angewandte Chemie - International Edition*, 2006, **118**, 4081–4085.

93. D. Gebauer, H. Cölfen, A. Verch and M. Antonietti, *Advanced Materials*, 2009, **21**, 435–439.

94. R.-Q. Song and H. Colfen, *CrystEngComm*, 2011, **13**, 1227–1712.

95. G. Begum and R. K. Rana, *Chemical Communications*, 2012, **48**, 8216–8218.

96. A. G. Skirtach, A. M. Yashchenok and H. Möhwald, *Chemical Communications*, 2011, **47**, 12736–12746.

97. A. Vikulina, D. Voronin, D. Voronin, R. Fakhrullin, V. Vinokurov and D. Volodkin, *New Journal of Chemistry*, 2020, 44, 5638–5655.

98. N. A. Feoktistova, N. G. Balabushevich, A. G. Skirtach, D. Volodkin and A. S. Vikulina, *Physical Chemistry Chemical Physics*, 2020, **22**, 9713–9722.

99. S. Schmidt, M. Behra, K. Uhlig, N. Madaboosi, L. Hartmann, C. Duschl and D. Volodkin, *Advanced Functional Materials*, 2013, **23**, 116–123.

100. N. G. Balabushevich, A. V. Lopez De Guerenu, N. A. Feoktistova, A. G. Skirtach and D. Volodkin, *Macromolecular Bioscience*, 2016, **16**, 95–105.

101. A. I. Petrov, D. V. Volodkin and G. B. Sukhorukov, *Biotechnology Progress*, 2005, **21**, 918–925.

102. N. A. Feoktistova, A. S. Vikulina, N. G. Balabushevich, A. G. Skirtach and D. Volodkin, *Materials and Design*, 2020, **185**, 108223.

103. N. G. Balabushevich, A. V. Lopez De Guerenu, N. A. Feoktistova, A. G. Skirtach and D. Volodkin, *Macromolecular Bioscience*, 2016, **16**, 95–105.

104. N. G. Balabushevich, A. V. Lopez De Guerenu, N. A. Feoktistova and D. Volodkin, *Physical Chemistry Chemical Physics*, 2015, **17**, 2523–2530.

105. N. G. Balabushevich, E. A. Kovalenko, I. M. Le-Deygen, L. Y. Filatova, D. Volodkin and A. S. Vikulina, *Materials and Design*, 2019, **182**, 108020.

106. N. G. Balabushevich, E. A. Sholina, E. V. Mikhalchik, L. Y. Filatova, A. S. Vikulina and D. Volodkin, *Micromachines*, 2018, **9**, 307.

107. N. G. Balabushevich, E. A. Kovalenko, E. v. Mikhalchik, L. Y. Filatova, D. Volodkin and A. S. Vikulina, *Journal of Colloid and Interface Science*, 2019, **545**, 330–339.

108. B. O. Guillame-gentil, O. Semenov, A. S. Roca, T. Groth, R. Zahn, J. Vörös and M. Zenobi-wong, *Advanced Materials*, 2010, **22**, 5443–5462.

109. N. Madaboosi, K. Uhlig, S. Schmidt, A. S. Vikulina, H. Möhwald, C. Duschl and D. Volodkin, *Macromolecular Bioscience*, 2018, **18**, 1700319.

110. D. Volodkin, R. Von Klitzing and H. Moehwald, *Polymers*, 2014, **6**, 1502–1527.

111. C. Üzüm, J. Hellwig, N. Madaboosi, D. Volodkin and R. Von Klitzing, *Beilstein Journal of Nanotechnology*, 2012, **3**, 778–788.

112. D. G. Shchukin and D. V Volodkin, *ACS Applied Materials & Interfaces*, 2017, **9**, 38908–38918.

113. N. Velk, K. Uhlig, A. Vikulina, C. Duschl and D. Volodkin, *Colloids and Surfaces B: Biointerfaces*, 2016, **147**, 343–350.

114. V. Z. Prokopović, A. S. Vikulina, D. Sustr, C. Duschl and D. Volodkin, *ACS Applied Materials & Interfaces*, 2016, **8**, 24345–24349.

115. A. S. Vikulina, Y. G. Anissimov, P. Singh, V. Z. Prokopovic, K. Uhlig, M. S. Jaeger, R. von Klitzing, C. Duschl and D. Volodkin, *Physical Chemistry Chemical Physics*, 2016, **18**, 9–14.

116. D. V. Volodkin, N. G. Balabushevitch, G. B. Sukhorukov and N. I. Larionova, *Biochemistry (Moscow)*, 2003, **68**, 283–289.

117. D. V. Volodkin, N. G. Balabushevitch, G. B. Sukhorukov and N. I. Larionova, *S.T.P. Pharma Sciences*, 2003, **13**, 163–170.

118. C. S. Peyratout and L. Dähne, *Angewandte Chemie - International Edition*, 2004, **43**, 3762–3783.

119. L. Jeannot, M. Bell, R. Ashwell, D. Volodkin and A. S. Vikulina, *Micromachines*, 2018, **9**,547.

120. A. S. Vikulina, S. T. Aleed, T. Paulraj, Y. A. Vladimirov, C. Duschl, R. Von Klitzing and D. Volodkin, *Physical Chemistry Chemical Physics*, 2015, **17**, 12771–12777.

121. A. S. Vikulina, A. G. Skirtach and D. Volodkin, *Langmuir*, 2019, **35**, 8565–8573.

122. A. Sergeeva, A. S. Vikulina and D. Volodkin, *Micromachines*, 2019, **10**, 357.

123. A. Sergeeva, N. Feoktistova, V. Prokopovic and D. Gorin, *Advanced Materials Interfaces*, 2015, **2**, 1500386.

124. A. S. Sergeeva, D. A. Gorin and D. v Volodkin, *Langmuir*, 2015, **31**, 10813–10821.

125. T. Paulraj, N. Feoktistova, N. Velk, K. Uhlig, C. Duschl and D. Volodkin, *Macromolecular Rapid Communications*, 2014, **35**, 1408–1413.

126. X. Pan, S. Chen, D. Li, W. Rao, Y. Zheng, Z. Yang, L. Li, X. Guan and Z. Chen, *Frontiers in Chemistry*, 2018, **5**, 130.

127. P. C. Sahoo, F. Kausar, J. H. Lee and J. I. Han, *RSC Advances*, 2014, **4**, 32562–32569.

128. K. Qian, T. Shi, T. Tang, S. Zhang, X. Liu and Y. Cao, *Microchimica Acta*, 2011, **173**, 51–57.

129. M. Y. Memar, K. Adibkia, S. Farajnia, H. S. Kafil, S. Maleki-Diza and R. Ghotaslou, *Journal of Drug Delivery Science and Technology*, 2019, **54**, 101307.

130. G. A. Islan, M. L. Cacicedo, V. E. Bosio and G. R. Castro, *Journal of Colloid and Interface Science*, 2015, **439**, 76–87.

131. G. A. Islan, M. E. Ruiz, J. F. Morales, M. L. Sbaraglini, A. V. Enrique, G. Burton, A. Talevi, L. E. Bruno-Blanch and G. R. Castro, *Journal of Materials Chemistry B*, 2017, **5**, 3132–3144.

132. A. Lucas-girot, O. Tribut and J. Sangleboeuf, *Journal of Biomedical Materials Research - Part B Applied Biomaterials*, 2005, **73**, 164–170.

133. H. Yang, Y. Wang, T. Liang, Y. Deng, X. Qi, H. Jiang, Y. Wu and H. Gao, *Progress in Natural Science: Materials International*, 2017, **27**, 674–677.

134. M. Mihai, S. Racovita, A. L. Vasiliu, F. Doroftei, C. Barbu-Mic, S. Schwarz, C. Steinbach and F. Simon, *ACS Applied Materials & Interfaces*, 2017, 9, 37264–37278.

135. S. Racovita, A. L. Vasiliu, A. Bele, D. Schwarz, C. Steinbach, R. Boldt, S. Schwarz and M. Mihai, *RSC Advances*, 2018, **8**, 23274–23283.

136. F. Ali Said, N. Bousserrhine, V. Alphonse, L. Michely and S. Belbekhouche, *International Journal of Pharmaceutics*, 2020, **579**, 119175.

137. C. Matei, D. Berger, A. Dumbrava, M. D. Radu and E. Gheorghe, *Journal of Sol-Gel Science and Technology*, 2020, **93**, 315–323.

138. M. Długosz, M. Bulwan, G. Kania, M. Nowakowska and S. Zapotoczny, *Journal of Nanoparticle Research*, 2012, **14**, 1313.

139. F. Baldassarre, A. de Stradis, G. Altamura, V. Vergaro, C. Citti, G. Cannazza, A. L. Capodilupo, L. Dini and G. Ciccarella, *Pure and Applied Chemistry*, 2020, **92**, 429-444.

140. L. D. Tessarolo, R. R. P. P. B. De Menezes, C. P. Mello, D. B. Lima, E. P. Magalhães, E. M. Bezerra, F. A. M. Sales, I. L. Barroso Neto, M. D. F. Oliveira, R. P. Dos Santos, E. L. Albuquerque, V. N. Freire and A. M. Martins, *Parasitology*, 2018, **145**, 1191–1198.

141. K. H. Min, E. Y. Jang, H. J. Lee, Y. S. Hwang, J. I. Ryu, J. H. Moon and S. C. Lee, *Journal of Industrial and Engineering Chemistry*, 2019, **71**, 210–219.

142. J. Xue, X. Li, Q. Li, J. Lyu, W. Wang, L. Zhuang and Y. Xu, *Journal of Physics D: Applied Physics*, 2020, **53**, 245401.

143. T. Isa, Z. A. B. Zakaria, Y. Rukayadi, M. N. M. Hezmee, A. Z. Jaji, M. U. Imam, N. I. Hammadi and S. K. Mahmood, *International Journal of Molecular Sciences*, 2016, **17**, 713.

144. R. V. Padmanabhuni, J. Luo, Z. Cao and Y. Sun, *Industrial & Engineering Chemistry Research*, 2012, **51**, 5148–5156.

145. V. Apalangya, V. Rangari, B. Tiimob, S. Jeelani and T. Samuel, *Applied Surface Science*, 2014, **295**, 108–114.

146. B. J. Tiimob, G. Mwinyelle, W. Abdela, T. Samuel, S. Jeelani and V. K. Rangari, *Journal of Agricultural and Food Chemistry*, 2017, **65**, 1967–1976.

147. C. Ferreira, A. M. Pereira, M. C. Pereira, M. Simões and L. F. Melo, *Heat Transfer Engineering*, 2013, **34**, 712–718.

148. A. Lucas, J. F. Michel, J. Gaude, C. Carel, *French Patent*, 1997, 2743496.

149. M. Kitamura, H. Konno, A. Yasui and H. Masuoka, *Journal of Crystal Growth*, 2002, **236**, 323–332.

150. Y. I. Svenskaya, H. Fattah, O. A. Inozemtseva, A. G. Ivanova, S. N. Shtykov, D. A. Gorin and B. V. Parakhonskiy, *Crystal Growth & Design*, 2018, **18**, 331–337.

151. C. Dhand, M. P. Prabhakaran, R. W. Beuerman, R. Lakshminarayanan, N. Dwivedi and S. Ramakrishna, *RSC Advances*, 2014, 4, 32673–32689.

152. S. Mao, C. Guo, Y. Shi and L. C. Li, *Expert Opinion on Drug Delivery*, 2012, **9**, 1161–1176.

153. R. Ferrari, M. Sponchioni, M. Morbidelli and D. Moscatelli, *Nanoscale*, 2018, **10**, 22701–22719.

154. E. J. Begg, M. L. Barclay and C. J. M. Kirkpatrick, *British Journal of Clinical Pharmacology*, 1999, **47**, 23–30.

155. C. L. Ventola, *Pharmacy&Therapeutics*, 2015, **40**, 277–283.

156. V. P. Torchilin, in *Stimuli-responsive Drug Delivery Systems*, eds. A. Singh and M. M. Amiji, The Royal Society of Chemistry, Croydon, 1st edn., 2018, p. 2.

157. Z. Dong, L. Feng, W. Zhu, X. Sun, M. Gao, H. Zhao, Y. Chao and Z. Liu, *Biomaterials*, 2016, **110**, 60–70.

158. Z. Wang, X. Zhang, G. Huang and J. Gao, in *Stimuli-responsive Drug Delivery Systems*, eds. A. Singh and M. M. Amiji, Royal Society of Chemistry, Croydon, 1st edn., 2018, p. 52.

159. A. F. Radovic-moreno, T. K. Lu, V. A. Puscasu, C. J. Yoon, R. Langer and O. C. Farokhzad, *ACS Nano*, 2012, **6**, 4279–4287.

160. S. Mura, J. Nicolas and P. Couvreur, *Nature Materials*, 2013, **12**, 991–1003.

161. B. V. Parakhonskiy, C. Foss, E. Carletti, M. Fedel, A. Haase, A. Motta, C. Migliaresi and R. Antolini, *Biomaterials Science*, 2013, **1**, 1273–1281.

162. Y. I. Svenskaya, A. M. Pavlov, D. A. Gorin, D. J. Gould, B. V. Parakhonskiy and G. B. Sukhorukov, *Colloids and Surfaces B: Biointerfaces*, 2016, **146**, 171–179.

163. D. B. Trushina, T. N. Borodina, S. N. Sulyanov, J. V. Moiseeva, N. V. Gulyaeva and T. V. Bukreeva, *Crystallography Reports*, 2018, **63**, 998–1004.

164. O. Gusliakova, E. N. Atochina-Vasserman, O. Sindeeva, S. Sindeev, S. Pinyaev, N. Pyataev, V. Revin, G. B. Sukhorukov, D. Gorin and A. J. Gow, *Frontiers in Pharmacology*, 2018, **9**, 559.

165. Y. I. Svenskaya, E. A. Genina, B. V. Parakhonskiy, E. V. Lengert, E. E. Talnikova, G. S. Terentyuk, S. R. Utz, D. A. Gorin, V. V. Tuchin and G. B. Sukhorukov, *ACS Applied Materials & Interfaces*, 2019, **11**, 17270–17282.

166. A. Som, R. Raliya, L. Tian, W. Akers, J. E. Ippolito, S. Singamaneni, P. Biswas and S. Achilefu, *Nanoscale*, 2016, **8**, 12639–12647.

167. S. Anees Ahmad, S. Sachi Das, A. Khatoon, M. Tahir Ansari, M. Afzal, M. Saquib Hasnain and A. Kumar Nayak, *Materials Science for Energy Technologies*, 2020, **3**, 756–769.

168. J. Hühn, C. Carrillo-Carrion, M. G. Soliman, C. Pfeiffer, D. Valdeperez, A. Masood, I. Chakraborty, L. Zhu, M. Gallego, Z. Yue, M. Carril, N. Feliu, A. Escudero, A. M. Alkilany, B. Pelaz, P. del Pino and W. J. Parak, *Chemistry of Materials*, 2017, 29, 399–461.

169. R. Khursheed, K. Dua, S. Vishwas, M. Gulati, N. K. Jha, G. M. Aldhafeeri, F. G. Alanazi, B. H. Goh, G. Gupta, K. R. Paudel, P. M. Hansbro, D. K. Chellappan and S. K. Singh, *Biomedicine & Pharmacotherapy*, 2022, **150**, 112951.

170. H. S. Toh, K. Jurkschat and R. G. Compton, *Chemistry - A European Journal*, 2015, **21**, 2998–3004.

171. C. V. Restrepo and C. C. Villa, *Environmental Nanotechnology, Monitoring & Management*, 2021, **15**, 100428.

172. K. M. Koczkur, S. Mourdikoudis, L. Polavarapu and S. E. Skrabalak, *Dalton Transactions*, 2015, **44**, 17883–17905.

173. M. A. Hussain, A. Shah, I. Jantan, M. N. Tahir, M. R. Shah, R. Ahmed and S. N. A. Bukhari, *Journal of Nanobiotechnology*, 2014, **12**, 53.

174. S. Davidović, V. Lazić, I. Vukoje, J. Papan, S. P. Anhrenkiel, S. Dimitrijević and J. M. Nedeljković, *Colloids and Surfaces B: Biointerfaces*, 2017, **160**, 184–191.

175. R. Eising, A. M. Signori, S. Ebastien Fort and J. B. Domingos, *Langmuir*, 2011, **27**, 11860–11866.

176. R. Wang, S. Zuo, W. Zhu, S. Wu, W. Nian, J. Zhang and J. Fang, *Plasma Processes and Polymers*, 2014, **11**, 44–51.

177. L. Mikac, M. Ivanda, • M. Gotic, T. Mihelj and L. Horvat, *Journal of Nanoparticles Research*, 2014, **16**, 2748.

178. S. Glišić, M. Cakić, G. Nikolić and B. Danilović, *Journal of Molecular Structure*, 2015, **1084**, 345–351.

179. S. Davidović, M. Miljković, V. Lazić, D. Jović, B. Jokić, S. Dimitrijević and M. Radetić, *Carbohydrate Polymers*, 2015, **131**, 331–336.

180. S. Azhar, N. F. Rana, A. S. Kashif, T. Tanweer, I. Shafique and F. Menaa, *Polymers*, 2022, **14**, 3143.

181. I. Vukoje, V. Lazić, D. Sredojević, M. M. Fernandes, S. Lanceros-Mendez, S. P. Ahrenkiel and J. M. Nedeljković, *International Journal of Biological Macromolecules*, 2022, **194**, 461–469.

182. C. Liao, Y. Li and S. C. Tjong, *International Journal of Molecular Sciences*, 2019, **20**, 449.

183. Z. M. Xiu, Q. B. Zhang, H. L. Puppala, V. L. Colvin and P. J. J. Alvarez, *Nano Letters*, 2012, **12**, 4271–4275.

184. I. Khan, K. Saeed and I. Khan, *Arabian Journal of Chemistry*, 2019, **12**, 908–931.

185. D. Paramelle, A. Sadovoy, S. Gorelik, P. Free, J. Hobley and D. G. Fernig, *Analyst*, 2014, **139**, 4855–4861.

186. I. Wiegand, K. Hilpert and R. E. W. Hancock, *Nature Protocols*, 2008, 3, 163–175.

187. J. D. Brewster, *Journal of Microbiological Methods*, 2003, 53, 77–86.

188. A. Ivanova, K. Ivanova, A. Tied, T. Heinze and T. Tzanov, *Advanced Functional Materials*, 2020, **30**, 2001284.

189. S. D. Solomon, M. Bahadory, A. v. Jeyarajasingam, S. A. Rutkowsky, C. Boritz and L. Mulfinger, *Journal of Chemical Education*, 2007, **84**, 322–325.

190. K. M. Koczkur, S. Mourdikoudis, L. Polavarapu, S. E. Skrabalak, K. M. Koczkur, S. Mourdikoudis, L. Polavarapu and S. E. Skrabalak, *Dalton Transactions*, 2015, **44**, 17883–17905.

191. F. Weigert, A. Müller, I. Häusler, D. Geißler, D. Skroblin, M. Krumrey, W. Unger, J. Radnik and U. Resch-Genger, *Scientific Reports*, 2020, **10**, 20712.

192. R. P. Carney, J. Y. Kim, H. Qian, R. Jin, H. Mehenni, F. Stellacci and O. M. Bakr, *Nature Communications*, 2011, **2**, 335.

193. C. M. Maguire, M. Rösslein, P. Wick and A. Prina-Mello, *Science and Technology of Advanced Materials*, 2018, **19**, 732–745.

194. A. K. Jamting, J. Cullen, V. A. Coleman, M. Lawn, J. Herrmann, J. Miles and M. J. Ford, *Advanced Powder Technology*, 2011, **22**, 290–293.

195. C. Holder and R. Schaak, *ACS Nano*, 2019, **13**, 7359–7365.

196. K. L. Cheng, *Microchemical Journal*, 2006, **82**, 119–120.

197. K. L. Cheng, *Microchemical Journal*, 2007, **86**, 257–257.

198. J.-W. Park and J. S. Shumaker-Parry, *Journal of the American Chemical Society*, 2014, **136**, 1907–1921.

199. C. H. Munro, W. E. Smith, M. Garner, J. Clarkson and P. C. White, *Langmuir*, 1995, **11**, 3712–3720.

200. M. H. P. B. Vettori, S. M. M. Franchetti and J. Contiero, *Carbohydrate Polymers*, 2012, **88**, 1440–1444.

201. K. I. Shingel, *Carbohydrate Research*, 2002, **337**, 1445–1451.

202. E. Wiercigroch, E. Szafraniec, K. Czamara, M. Z. Pacia, K. Majzner, K. Kochan, A. Kaczor, M. Baranska and K. Malek, *Spectrochimica Acta, Part A: Molecular and Biomolecular Spectroscopy*, 2017, **185**, 317–335.

203. J. S. Gebauer, M. Malissek, S. Simon, S. K. Knauer, M. Maskos, R. H. Stauber, W. Peukert and L. Treuel, *Langmuir*, 2012, **28**, 9673–9678.

204. C. Levard, S. Mitra, T. Yang, A. D. Jew, A. R. Badireddy, G. v. Lowry and G. E. Brown, *Environmental Science & Technology*, 2013, **47**, 5738–5745.

205. European Centre for Disease Prevention and Control, Healthcare-associated infections acquired in intensive care units. *Annual Epidemiological Report for 2016*, Stockholm, 2018.

206. European Centre for Disease Prevention and Control, *Healthcare-associated infections: surgical site infections*. Annual epidemiological report for 2016, Stockholm, 2018.

207. A. P. V. Ferreyra Maillard, J. C. Espeche, P. Maturana, A. C. Cutro and A. Hollmann, *BBA - Biomembranes*, 2021, 1863, 183597.

208. S. Agnihotri, S. Mukherji and S. Mukherji, *RSC Advances*, 2014, 4, 3974–3983.

209. N. V. Ayala-Núñez, H. H. Lara Villegas, L. del Carmen Ixtepan Turrent and C. Rodríguez Padilla, *NanoBiotechnology*, 2009, **5**, 2–9.

210. E. K. Saeki, A. Y. Yamada, L. A. de Araujo, L. Anversa, D. de O. Garcia, R. L. B. de Souza, H. M. Martins, R. K. T. Kobayashi and G. Nakazato, *Frontiers in Cellular and Infection Microbiology*, 2021, **11**, 656984.

211. A. Bhargava, V. Pareek, S. Roy Choudhury, J. Panwar and S. Karmakar, *ACS Applied Materials & Interfaces*, 2018, **10**, 29325–29337.

212. A. Ivask, A. Elbadawy, C. Kaweeteerawat, D. Boren, H. Fischer, Z. Ji, C. H. Chang, R. Liu, T. Tolaymat, D. Telesca, J. I. Zink, Y. Cohen, P. A. Holden and H. A. Godwin, *ACS Nano*, 2014, **8**, 374–386.

213. A. A. Ashkarran, M. Ghavami, H. Aghaverdi, P. Stroeve and M. Mahmoudi, *Chemical Research in Toxicology*, 2012, **25**, 1231–1242.

214. G. Yang, Q. Lin, C. Wang, J. Li, J. Wang, J. Zhou, Y. Wang and C. Wang, *Journal of Nanoscience and Nanotechnology*, 2012, **12**, 3766–3774.

215. P. Singh and I. Mijakovic, *Frontiers in Microbiology*, 2022, **13**, 820048.

216. S. Liao, Y. Zhang, X. Pan, F. Zhu, C. Jiang, Q. Liu, Z. Cheng, G. Dai, G. Wu, L. Wang and L. Chen, *International Journal of Nanomedicine*, 2019, 1469–1487.

217. Y. Zhang, X. Pan, S. Liao, C. Jiang, L. Wang, Y. Tang, G. Wu, G. Dai and L. Chen, *Journal of Proteome Research*, 2020, **19**, 3109–3122.

218. P. Thuptimdang, T. Limpiyakorn, J. McEvoy, B. M. Prüß and E. Khan, *Journal of Hazardous Materials*, 2015, **290**, 127–133.

219. H.-C. Flemming, J. Wingender, U. Szewzyk, P. Steinberg, S. A. Rice and S. Kjelleberg, *Nature Reviews Microbiology*, 2016, **14**, 563–75.

220. A. M. Königs, H. C. Flemming and J. Wingender, *Front Microbiol*, 2015, **6**, 1–11.

221. K. Ikuma, A. W. Decho and B. L. T. Lau, *Frontiers in Microbiology*, 2015, **6**, 395.

222. M. B. Habash, A. J. Park, E. C. Vis, R. J. Harris and C. M. Khursigara, *Antimicrobial Agents and Chemotherapy*, 2014, **58**, 5818–5830.

223. B. Malaekeh-Nikouei, B. S. Fazly Bazzaz, E. Mirhadi, A. S. Tajani and B. Khameneh, *Journal of Drug Delivery Science and Technology*, 2020, **60**, 101880.

224. Y. Liu, L. Shi, L. Su, H. C. van der Mei, P. C. Jutte, Y. Ren and H. J. Busscher, *Chemical Society Reviews*, 2019, 48, 428–446.

225. T.-O. Peulen and K. J. Wilkinson, *Environmental Science & Technology*, 2011, 45, 3367–3373.

226. Y. Yang and P. J. J. Alvarez, *Environmental Science & Technology Letters*, 2015, 2, 221–226.

227. A. M. Ferreira, A. Vikulina, G. W. V. Cave, M. Loughlin, V. Puddu and D. Volodkin, J *Journal of Colloid and Interface Science*, 2023, 631, 165–180.

228. S. Prasath and K. Palaniappan, *Environmental Geochemistry and Health*, 2019, **41**, 2295–2313.

229. J. Pulit-Prociak and M. Banach, *Open Chemistry*, 2016, **14**, 76–91.

230. A. M. El Badawy, T. P. Luxton, R. G. Silva, K. G. Scheckel, M. T. Suidan and T. M. Tolaymat, *Environmental Science & Technology*, 2010, **44**, 1260–1266.

231. V. V. Pinto, M. J. Ferreira, R. Silva, H. A. Santos, F. Silva and C. M. Pereira, *Colloids and Surfaces A: Physicochemical and Engineering Aspects*, 2010, **364**, 19–25.

232. W. Cai and L. Zhang, *Journal of Physics: Condensed Matter*, 1997, **9**, 7257–7267.

233. W. Cai, H. Hofmeister, T. Rainer and W. Chen, *Journal of Nanoparticle Research*, 2001, **3**, 443–453.

234. Y. Lv, H. Liu, Z. Wang, S. Liu, L. Hao, Y. Sang, D. Liu, J. Wang and R. I. Boughton, *Journal of Membrane Science journal*, 2009, **331**, 50–56.

235. R. N. Faheem, A. S. Muzafar and H. Y. Kim, *Journal of Nanoparticle Research*, 2011, **13**, 1917–1927.

236. Z. Ni, X. Gu, Y. He, Z. Wang, X. Zou, Y. Zhao and L. Sun, *RSC Advances*, 2018, **8**, 41722–41730.

237. S. Kellici, J. Acord, A. Vaughn, N. P. Power, D. J. Morgan and T. Heil, *Applied Materials & Interfaces*, 2016, **8**, 19038–19046.

238. W. Shao, X. Liu, H. Min, G. Dong, Q. Feng and S. Zuo, *Applied Materials & Interfaces*, 2015, **7**, 6966–6973.

239. J. Chen, L. Sun, Y. Cheng, Z. Lu, K. Shao, T. Li, C. Hu and H. Han, *Applied Materials & Interfaces*, 2016, **8**, 24057–24070.

240. X. Wang, S. Zhu, L. Liu and L. Li, *Applied Materials & Interfaces*, 2017, **9**, 9051–9058.

241. S. Borse, M. Temgire, A. Khan and S. Joshi, *RSC Advances*, 2016, **1**, 56674-56683.

242. P. Ma, L. Jiang, M. Yu, W. Dong and M. Chen, *ACS Sustainable Chemistry & Engineering*, 2016, **4**, 6417–6426.

243. S. Loher, O. D. Schneider, T. Maienfisch, S. Bokorny and W. J. Stark, *Small*, 2008, 4, 824–832.

244. R. Vogel, M. Persson, C. Feng, S. J. Parkin, T. A. Nieminen, B. Wood, N. R. Heckenberg and H. Rubinsztein-Dunlop, *Langmuir*, 2009, 25, 11672–11679.

245. S. Fulaz, D. Hiebner, C. H. N. Barros, H. Devlin, S. Vitale, L. Quinn and E. Casey, *ACS Applied Materials & Interfaces*, 2019, **11**, 32679–32688.

246. Y. Li, S. Zhou, H. Song, T. Yu, X. Zheng and Q. Chu, *Biomaterials*, 2021, **277**, 121080.

247. Z. Wang, Z. Chang, M. Lu, D. Shao, J. Yue, D. Yang, M. Li and W. F. Dong, *ACS Applied Materials & Interfaces*, 2017, **9**, 30306–30317.

248. S. Boca-Farcau, M. Potara, T. Simon, A. Juhem, P. Baldeck and S. Astilean, *Molecular Pharmaceutics*, 2014, **11**, 391–399.

249. P. Bose, A. Priyam, R. Kar and S. P. Pattanayak, *RSC Advances*, 2020, **10**, 31961–31978.

250. P. Merkl, S. Zhou, A. Zaganiaris, M. Shahata, A. Eleftheraki, T. Thersleff and G. A. Sotiriou, *ACS Applied Nano Materials*, 2021, **4**, 5330–5339.

251. N. E. Markina, A. V. Markin, A. M. Zakharevich and I. Y. Goryacheva, *Microchimica Acta*, 2017, **184**, 3937–3944.

252. M. Saveleva, E. Prikhozhdenko, D. Gorin, A. G. Skirtach, A. Yashchenok and B. Parakhonskiy, *Frontiers in Chemistry*, 2020, **7**, 888.

253. I. Y. Stetciura, A. V. Markin, A. N. Ponomarev, A. V. Yakimansky, T. S. Demina, C. Grandfils, D. V. Volodkin and D. A. Gorin, *Langmuir*, 2013, **29**, 4140–4147.

254. D. V. Volodkin, A. I. Petrov, M. Prevot and G. B. Sukhorukov, *Langmuir*, 2004, **20**, 3398–3406.

255. I. E. Bordianu, G. David, B. Simionescu, M. Aflori, C. Ursu, A. Coroaba, G. Hitruc, C. Cotofana and M. Olaru, *Journal of Materials Chemistry B*, 2015, **3**, 723–727.

256. J. D. Rodriguez-Blanco, S. Shaw and L. G. Benning, *Nanoscale*, 2011, **3**, 265–271.

257. M. Saharay and R. James Kirkpatrick, *Chemical Physics Letters*, 2014, **591**, 287–291.

258. J. P. Andreassen, *Journal of Crystal Growth*, 2005, **274**, 256–264.

259. R. Beck and J. P. Andreassen, *Crystal Growth & Design*, 2010, **10**, 2934–2947.

260. P. Bots, L. G. Benning, J. D. Rodriguez-Blanco, T. Roncal-Herrero and S. Shaw, *Crystal Growth & Design*, 2012, **12**, 3806–3814.

261. J. Buffle, Z. Zhang and K. Startchev, *Environmental Science & Technology*, 2007, **41**, 7609–7620.

262. A. Abdelmoteleb, B. Valdez-Salas, C. Ceceña-Duran, O. Tzintzun-Camacho, F. Gutiérrez-Miceli, O. Grimaldo-Juarez and D. González-Mendoza, *Chemical Speciation and Bioavailability*, 2017, 29, 1–5.

263. Y. Zheng and A. Wang, *Journal of Materials Chemistry*, 2012, 22, 16552–16559.

264. T. Jayaramudu, G. M. Raghavendra, K. Varaprasad, G. V. S. Reddy, A. B. Reddy, K. Sudhakar and E. R. Sadiku, *Journal of Applied Polymer Science*, 2016, **133**, 43027.

265. M. Sato and S. Matsuda, *Zeitschrift fur Kristallographie*, 1969, **129**, 405–410.

266. F. A. Andersen and L. Brečević, *Acta Chemica Scandinavica*, 1991, **45**, 1018–1024.

267. L. Pérez-Villarejo, F. Takabait, L. Mahtout, B. Carrasco-Hurtado, D. Eliche-Quesada and P. J. Sánchez-Soto, *Ceramics International*, 2018, **44**, 5291–5296.

268. P. Sow, Masters thesis, University of Konstanz, 2016.

269. F. A. Andersen and L. Brečević, *Acta Chemica Scandinavica*, 1991, **45**, 1018–1024.

270. L. Addadi, S. Raz and S. Weiner, *Advanced Materials*, 2003, **15**, 959–970.

271. A. D. Trofimov, A. A. Ivanova, M. v. Zyuzin and A. S. Timin, *Pharmaceutics*, 2018, **10**, 167.

272. K. Sawada, *Pure and Applied Chemistry*, 1997, **69**, 921–928.

273. K. Y. Chong, C. H. Chia, S. Zakaria and M. S. Sajab, *Journal of Environmental Chemical Engineering*, 2014, **2**, 2156–2161.

274. W. Yin, M. Liu, T. L. Zhao, F. J. Qian, H. Li, Q. Z. Yao, S. Q. Fu and G. T. Zhou, *Environmental Research*, 2020, **187**, 109699.

275. M. Ahonen, A. Kahru, A. Ivask, K. Kasemets, S. Kõljalg, P. Mantecca, I. V. Vrček, M. M. Keinänen-Toivola and F. Crijns, *International Journal of Environmental Research and Public Health*, 2017, **14**, 366.

276. P. Bots, L. G. Benning, J. D. Rodriguez-Blanco, T. Roncal-Herrero and S. Shaw, *Crystal Growth & Design*, 2012, **12**, 3806–3814.

277. M. A. Hood, K. Landfester and R. Muñoz-Espí, *Crystal Growth & Design*, 2014, **14**, 1077–1085.

278. E. F. Souza, J. A. R. Ambrósio, B. C. S. Pinto, M. Beltrame, K. K. Sakane, J. G. Pinto, J. Ferreira-Strixino, E. P. Gonçalves and A. R. Simioni, *Photodiagnosis and Photodynamic Therapy*, 2020, **31**, 101913.

279. G. Choukrani, B. Maharjan, C. H. Park, C. S. Kim and A. R. Kurup Sasikala, *Materials Science and Engineering C*, 2020, **106**, 110226.

280. C. G. Kontoyannis and N. V. Vagenas, *Analyst*, 2000, **125**, 251–255.

281. B. V. Parakhonskiy, A. M. Yashchenok, S. Donatan, D. V. Volodkin, F. Tessarolo, R. Antolini, H. Möhwald and A. G. Skirtach, *ChemPhysChem*, 2014, **15**, 2817–2822.

282. A. Vikulina, J. Webster, D. Voronin, E. Ivanov, R. Fakhrullin, V. Vinokurov and D. Volodkin, *Materials and Design*, 2021, 197, 109220.

283. D. B. Trushina, T. N. Borodina, S. Belyakov and M. N. Antipina, *Materials Today Advances*, 2022, 14, 100214.

284. X. Wang, R. Kong, X. Pan, H. Xu, D. Xia, H. Shan and J. R. Lu, *Journal of Physical Chemistry B*, 2009, **113**, 8975–8982.

285. S. S. Wang, A. Picker, H. Cölfen and A. W. Xu, *Angewandte Chemie - International Edition*, 2013, **52**, 6317–6321.

286. M. Yang, X. Jin and Q. Huang, *Colloids and Surfaces A: Physicochemical and Engineering Aspects*, 2011, **374**, 102–107.

287. Y. Wang, Y. X. Moo, C. Chen, P. Gunawan and R. Xu, *Journal of Colloid and Interface Science*, 2010, **352**, 393–400.

288. J. Campbell, A. M. Ferreira, L. Bowker, J. Hunt, D. Volodkin and A. Vikulina, *Advanced Materials Interfaces*, 2022, **9**, 2201196.

289. P. J. M. Smeets, K. R. Cho, R. G. E. Kempen, N. A. J. M. Sommerdijk and J. J. De Yoreo, *Nature Materials*, 2015, **14**, 394–399.

290. Z. Zhang, B. Yang, H. Tang, X. Chen and B. Wang, *Journal of Materials Science*, 2015, **50**, 5540–5548.

291. J. C. Yang, M. J. Jablonsky and J. W. Mays, *Polymer*, 2002, **43**, 5125–5132.

292. Y. B. Song, S. N. Lv, C. J. Cheng, G. L. Ni, X. W. Xie, W. Huang and Z. G. Zhao, *Applied Surface Science*, 2015, **324**, 854–863.

293. M. Braglia, I. V. Ferrari, T. Djenizian, S. Kaciulis, P. Soltani, M. L. Di Vona and P. Knauth, *ACS Applied Materials & Interfaces*, 2017, **9**, 22902–22910.

294. P. C. Ke, S. Lin, W. J. Parak, T. P. Davis and F. Caruso, *ACS Nano*, 2017, **11**, 11773–11776.

295. O. Gusliakova, R. Verkhovskii, A. Abalymov, E. Lengert, A. Kozlova, V. Atkin, O. Nechaeva, A. Morrison, V. Tuchin and Y. Svenskaya, *Materials Science and Engineering C*, 2021, **119**, 111428.

296. Y. I. Svenskaya, A. M. Pavlov, D. A. Gorin, D. J. Gould, B. V. Parakhonskiy and G. B. Sukhorukov, *Colloids and Surfaces B: Biointerfaces*, 2016, **146**, 171–179.

297. D. B. Trushina, T. N. Borodina, V. V. Artemov and T. V. Bukreeva, *Technical Physics*, 2018, **63**, 1345–1351.

298. A. Lesniak, F. Fenaroli, M. P. Monopoli, C. Åberg, K. A. Dawson and A. Salvati, *ACS Nano*, 2012, **6**, 5845–5857.

299. J. S. Kim, E. Kuk, K. N. Yu, J. H. Kim, S. J. Park, H. J. Lee, S. H. Kim, Y. K. Park, Y. H. Park, C. Y. Hwang, Y. K. Kim, Y. S. Lee, D. H. Jeong and M. H. Cho, *Nanomedicine*, 2007, **3**, 95–101.

300. J. Lopez-Esparza, L. Francisco Espinosa-Cristobal, A. Donohue-Cornejo and S. Y. Reyes-Lopez, *Industrial & Engineering Chemistry Research*, 2016, 55, 12532–12538.

301. C. H. Chen, S. H. Chen, K. T. Shalumon and J. P. Chen, *Acta Biomaterialia*, 2015, 26, 225–235.

302. J. A. Otter Phd, S. Yezli Phd, J. A. G. Salkeld Bsc and G. L. French, *American Journal of Infection Control*, 2013, **41**, 6–11.

303. D. C. Mullen, X. Wan, T. M. Takala, P. E. Saris and V. M. Moreira, *Frontiers in Medical Technology*, 2021, **3**, 640929.

304. P. D. Rakowska, M. Tiddia, N. Faruqui, C. Bankier, Y. Pei, A. J. Pollard, J. Zhang and I. S. Gilmore, *Communications Materials*, 2021, **2**, 53.

305. P. v. AshaRani, G. L. K. Mun, M. P. Hande and S. Valiyaveettil, *ACS Nano*, 2009, **3**, 279–290.

306. M. Akter, M. T. Sikder, M. M. Rahman, A. K. M. A. Ullah, K. F. B. Hossain, S. Banik, T. Hosokawa, T. Saito and M. Kurasaki, *Journal of Advanced Research*, 2018, **9**, 1–16.

307. G. Raos and B. Zappone, *Macromolecules*, 2021, **54**, 10617–10644.

308. N. Pandey, L. F. Soto-Garcia, J. Liao, P. Zimmern, K. T. Nguyen and Y. Hong, *Biomaterials Science*, 2020, **8**, 1240–1255.

309. X. Jin, L. Heepe, J. Strueben, R. Adelung, S. N. Gorb and A. Staubitz, *Macromolecular Rapid Communications*, 2014, **35**, 1551–1570.

310. P. Franco and I. de Marco, *Polymers*, 2020, **12**, 1114.

311. M. Teodorescu and M. Bercea, *Polymers-Plastics Technology and Engineering*, 2015, **54**, 923–943.

312. G. Petrou and T. Crouzier, *Biomaterials Science*, 2018, **6**, 2282–2297.

313. N. G. Balabushevich, E. A. Sholina, E. v. Mikhalchik, L. Y. Filatova, A. S. Vikulina and D. Volodkin, *Micromachines*, 2018, **9**, 1–16.

314. V. Vohra, N. T. Razali, R. Wahi, L. Ganzer and T. Virgili, *Optical Materials: X*, 2022, **13**, 100127.

315. T. Riss, R. Moravec, A. Niles, S. Duellman, H. Benink, T. Worzella and L. Minor, in *Assay Guidance Manual*, eds. S. Markossian, A. Grossman, K. Brimacombe, M. Arkin, D. Auld, C. Austin, J. Baell, T. Chung and N. Coussens, Eli Lilly & Company and the National Center for Advancing Translational Sciences, Bethesda (MD), 2004, pp. 361–363.

316. C. Simó, T. Fornari, M. R. García-Risco, A. Peña-Cearra, L. Abecia, J. Anguita, H. Rodríguez and V. García-Cañas, *Food and Function*, 2022, **13**, 5640–5653.

317. E. Travnickova, P. Mikula, J. Oprsal, M. Bohacova, L. Kubac, D. Kimmer, J. Soukupova and M. Bittner, *AMB Express*, 2019, **9**, 183.

318. A. K. S. Kumar, Y. Zhang, D. Li and R. G. Compton, *Electrochemistry Communications*, 2020, **121**, 106867.

319. Y. Li, C. Lv, Z. Li, D. Qué and Q. Zheng, *Soft Matter*, 2015, 11, 4669–4673.

320. J. Comyn, in *Woodhead Publishing Series in Welding and Other Joining Technologies, Adhesive Bonding*, eds. R. D. Adams, Woodhead Publishing, Cambridge, 2nd edn., 2021, pp. 41–78.

321. N. Feoktistova, J. Rose, V. Z. Prokopović, A. S. Vikulina, A. Skirtach and D. Volodkin, *Langmuir*, 2016, **32**, 4229–4238.

322. P. Lasch, M. Boese, A. Pacifico and M. Diem, *Vibrational Spectroscopy*, 2002, **28**, 147–157.

323. A. Slistan-Grijalva, R. Herrera-Urbina, J. F. Rivas-Silva, M. Ávalos-Borja, F. F. Castillón-Barraza and A. Posada-Amarillas, *Materials Research Bulletin*, 2008, **43**, 90–96.

324. P. Maitra, J. Al-Rashid, D. Mandal, M. S. Azam and N. M. Rasul, *Agronomy*, 2021, **11**, 1009.

325. M. Derrien, M. W. J. van Passel, J. H. B. van de Bovenkamp, R. Schipper, W. de Vos and J. Dekker, *Gut Microbes*, 2010, **1**, 254–296.

326. L. P. Aristoteli and M. D. P. Willcox, *Infection and Immunity*, 2003, **71**, 5565–5575.

327. T. Sauvaitre, J. van Landuyt, C. Durif, C. Roussel, A. Sivignon, S. Chalancon, O. Uriot, F. van Herreweghen, T. van de Wiele, L. Etienne-Mesmin and S. Blanquet-Diot, *Biofilms and Microbiomes*, 2022, **8**, 86.

328. Y. Xie and L. Yang, *Scientific Reports*, 2016, **6**, 20628.

329. S. Thanakkasaranee, K. Sadeghi, I. J. Lim and J. Seo, *Materials Science and Engineering: C*, 2020, **111**, 110781.

330. N. Ameera Rosli, Y. Haan Teow and E. Mahmoudi, *Science and Technology of Advanced Materials*, 2021, **22**, 885–907.

331. A. P. Ananda, · N B Krishnamurthy, · K R Savitha and · B S Nagendra, *SN Applied Sciences*, 2019, **1**, 800–813.

332. J. C. Ontong, S. Paosen, S. Shankar and S. P. Voravuthikunchai, *Journal of Microbiological Methods*, 2019, **165**, 105692.

333. A. Rühle, P. E. Huber, R. Saffrich, R. Lopez Perez and N. H. Nicolay, *International Journal of Cance*, 2018, **143**, 2628–2639.

334. S. Maleki Dizaj, F. Lotfipour, M. Barzegar-Jalali, M. H. Zarrintan and K. Adibkia, *Journal of Drug Delivery Science and Technology*, 2016, **35**, 16–23.

335. S. Kappagoda, U. Singh and B. G. Blackburn, *Mayo Clinic Proceedings*, 2011, **86**, 561–583.

336. P. D. Tamma, S. E. Cosgrove and L. L. Maragakis, *Clinical Microbiology Reviews*, 2012, **25**, 450–470.